VALERIA FANTI

GLOBAL ASSESSMENT OF COASTAL STORM HAZARDS ON BARRIER ISLANDS

UNIVERSIDADE DO ALGARVE

Faculdade de Ciências e Tecnologia

2025

VALERIA FANTI

GLOBAL ASSESSMENT OF COASTAL STORM HAZARDS ON BARRIER ISLANDS

PhD in Marine, Earth and Environmental Sciences
Major in Marine Sciences

Performed under the supervision of:
Óscar Ferreira
Carlos Loureiro

UNIVERSIDADE DO ALGARVE

Faculdade de Ciências e Tecnologia

2025

GLOBAL ASSESSMENT OF COASTAL STORM HAZARDS ON BARRIER ISLANDS

Declaration of authorship

I hereby declare to be the author of this work, which is original and unpublished. Authors and papers consulted are duly cited in the text and are listed in the included references.

Signature: Valeria Fanti
Date: 31/01/2025

Acknowledgments

I started thinking about these acknowledgments long before my thesis was finished, as this life chapter was coming to an end. It is not easy to find the right words to conclude and celebrate the past four years.

I would like to start by thanking the people who gave me this opportunity in the first place and without whom I wouldn't be here, my supervisors Óscar Ferreira and Carlos Loureiro. Your continuous support, meticulous guidance and endless enthusiasm have been invaluable. Every time I walked out of your door I had a smile on my face and a few new ideas or solutions up my sleeve. You have been an inspiring example of passion and dedication and I have deeply valued your extreme empathy in guiding me through the ups and downs (mostly ups thanks to your help) of the PhD. It has been a privilege to learn from you. You have helped me shape a career path that I love and cannot wait to continue.

To my colleagues at CIMA, who have been a constant source of encouragement - Vincent, Luísa, Maziar, Jacqueline and all the incredible members of the CIMA Day committee - thank you for sharing this journey with me. Luísa, I will miss your good mood and your "vamos almoçar?". Jacqueline, I don't know how you manage to be so active and productive, I wish you an exciting PhD experience. Vincent, letting me come along on your trip to the Outer Hebrides to help with your fieldwork was an experience I will never forget. Being able to hold a GPS in the stormy Scottish weather and retrieve PTDs in the middle of the night on a dark, empty, rumbling beach are skills I will always be proud of.

Special thanks also to Erwan Garel for organizing the best summer course on the dynamics of semi-enclosed basins. This experience showed me that the skills learned during a PhD on a very specific topic can be transferred to a completely new one, which boosted my confidence and sparked my interest in the world of ADCPs.

A heartfelt thank you to my lifelong friends, for whom time and distance never mattered: Valentina, Annalisa, Elena, Sara, Giulia, Gloria, Marco, Stefano, Gabriele and Gabriele. To those I have met along the way and are here to stay: Sara, Emilia, Lahja, Fabi, Emiel, the little

Vince, Lucas, Blanca, Niklas, Robert, Jonas and Franzi. To all the wonderful people who came to visit us to share bits of this Portuguese journey.

To Albrecht and Elisabeth, for being a second family, always sending love, strength, good energy and, of course, delicious food our way.

To my parents, Liliana and Mauro, who would follow me to the moon and back. You taught me enthusiasm and curiosity, two qualities that define our family. My greatest certainty has always been your unconditional love, your open arms waiting for me and Mum's never-ending supply of Parmigiano. Dad, I will never forget that day in Scotland when I came out of the university and found you hidden behind a tree just to surprise me. Your positivity and love for life are gifts I treasure. Mum, you knew I would do a PhD long before I did. You have always been my biggest motivation and inspiration.
To my sister Alessia, the person who can make me laugh the hardest and whom I have missed the most during these years of distance. You are my example of determination and perseverance, even though I was born first, you have always been my most trusted advisor. You never judged me, even though sometimes we couldn't have made more different choices.
To my grandparents, Nonno Leo, whom I would offer a dinner and a good wine to celebrate. Nonna Ara, who always asked me to bring her more shells, and bigger ones if possible. Nonna Bruna, who, at the end of every phone call, still asks why it is so hard for me to find a job in Rome.

Vinni, you have filled these years with sunshine. You were there from the very beginning and stayed through the good days and the bad. Sometimes you were my strength and sometimes I was yours. Overall, we had great adventures, which will make incredible bedtime stories for our future children. In Italian, we say "o la va, o la spacca", meaning make it or break it. I think we made it. And also to Tala and our free joyful runs on the beach. She greeted us with happiness and excitement every day of this journey.

Finally, to the last but not least love of my life: Praia de Faro. This place has inspired and shaped me in ways I could never have imagined. A piece of my heart will always remain lost somewhere in the sandbanks of Barrinha, in a sunset reflecting on the water, in an orange full moon rising on the Ria Formosa or riding a turquoise crystal clear wave.

Abstract

The vulnerability of barrier islands to coastal storm hazards is a growing challenge, exacerbated by climate change. Local high-resolution information on storm forcing and geomorphology has allowed the development of early warning systems to predict hazards and implement preparedness strategies. However, collecting high-resolution pre- and post-storm data can be costly, challenging and unfeasible at many coastal locations. The use of global low-resolution topo-bathymetry and wave reanalysis datasets presents an unprecedented opportunity to expand coastal hazard assessments, even if at the cost of introducing errors and uncertainties. Aiming to evaluate the response of wave-dominated barrier islands to extreme storms at a global scale, this study validated the latest global wave reanalyses and digital elevation models against high-resolution data. The validation confirmed biases associated with the resolution of global datasets and their inability to resolve complex features of wave propagation and morphology at local scales. Underestimation of extreme wave conditions in coastal areas was observed, and calibration equations were developed to reduce this negative bias. For the topo-bathymetry of barrier islands, an underestimation of the dune crest was identified, and gaps at the land-ocean interface were filled by merging the topo-bathymetry datasets using an equilibrium profile. The best performing global datasets were selected for the first global assessment of erosion and flooding hazards of natural barrier islands. This was achieved simulating the impact of a coastal storm with 50-year return period wave heights using the XBeach process-based model. Based on the implementation of process-based indicators, the strong control that storm hydrodynamics exert on the erosional response was highlighted, allowing the identification of erosion and flooding hotspots that coincided with areas of extra-tropical and tropical cyclone impact. These findings highlight the global patterns of barrier island vulnerability and provide a framework for prioritizing risk mitigation efforts in the face of intensifying coastal hazards.

Keywords: Barrier islands, Coastal storm hazards, Global models, XBeach, Process-based indicators

Resumo

A vulnerabilidade das ilhas-barreira aos efeitos de tempestades costeiras é um desafio crescente, exacerbado pelas alterações climáticas. Para prever e mitigar riscos costeiros, têm sido desenvolvidos sistemas de alerta precoce baseados em informação local detalhada. No entanto, a obtenção de dados de alta resolução pré e pós-tempestade pode ser dispendiosa, difícil e inviável para muitas áreas costeiras. A utilização de dados globais de baixa resolução representa uma oportunidade sem precedentes para desenvolver avaliações dos riscos costeiros, embora introduza incertezas. Tendo como objetivo geral a análise da resposta de ilhas-barreira aos impactos de tempestades à escala global, este estudo validou as recentes reanálises globais de ondulação e os modelos topo-batimétricos contra dados de alta resolução nas ilhas-barreira. A validação confirmou erros associados à resolução dos dados globais e a sua incapacidade para resolver caraterísticas complexas à escala local. Foi observada uma subestimação das condições extremas de ondulação nas zonas costeiras, tendo sido desenvolvidas equações de calibração para reduzir este erro. Relativamente à topo-batimetria, verificou-se uma subestimação da crista dunar e lacunas na interface terra-oceano que foram preenchidas através da fusão dos dados de topo-batimetria com um perfil de equilíbrio. Os dados globais com melhor desempenho foram selecionados para a primeira avaliação à escala global dos riscos de erosão e inundação em ilhas-barreira. Com o modelo XBeach, foi simulado o impacto de uma tempestade costeira com período de retorno de 50 anos para a altura da onda. Implementando indicadores baseados em processos, verificou-se o controlo dominante do forçamento hidrodinâmico sobre a resposta erosiva, permitindo a identificação de sectores críticos de erosão e inundação que coincidem com áreas expostas aos ciclones extra-tropicais e tropicais. Este estudo evidencia os padrões globais de vulnerabilidade de ilhas-barreira e fornecem um quadro de prioridades para os esforços de mitigação dos riscos face à intensificação dos perigos costeiros.

Palavras chave: Ilhas-barreira, Tempestades costeiras, Modelos globais, XBeach, Indicadores baseados em processos

Resumo alargado

A vulnerabilidade das ilhas-barreira aos efeitos de tempestades costeiras é um desafio de importância crescente, que tem vindo a ser investigado de forma mais abrangente nas últimas décadas. Antecipa-se que os eventos extremos costeiros serão exacerbados pelas alterações climáticas, o que levará a uma maior exposição das zonas costeiras e a um potencial aumento das consequências. As barreiras sedimentares costeiras proporcionam uma proteção essencial aos ecossistemas costeiros e às povoações humanas relativamente à ação das ondas, e inundação durante tempestades. No entanto, a sua resiliência está a ser progressivamente posta à prova pela subida do nível do mar, pela intensificação das tempestades e pelo aumento das pressões humanas. As avaliações dos impactos locais, com recurso a informação de alta resolução das características das tempestades (com base em ondógrafos e marégrafos) e das caraterísticas geomorfológicas das ilhas-barreira (com base em levantamentos LiDAR), permitiram o desenvolvimento de sistemas de alerta precoce para prever os perigos e implementar estratégias de minimização de riscos. Apesar destes progressos, a recolha de dados de alta resolução antes e depois das tempestades continua a ser dispendiosa, complexa e muitas vezes inviável para a maioria das áreas costeiras, especialmente em regiões com recursos técnicos e financeiros limitados. A utilização de conjuntos de dados de baixa resolução disponíveis a nível mundial, nomeadamente para a topografia, batimetria e ondulação, representa uma oportunidade única e sem precedentes para desenvolver avaliações de perigos costeiros à escala global, embora a utilização destes dados introduza alguns erros e incertezas. Aproveitando os avanços no acesso e qualidade de conjuntos de dados globais e no desenvolvimento de ferramentas computacionais, este estudo tem como objetivo melhorar a compreensão da dinâmica das ilhas-barreira e a sua resposta a eventos extremos.

Para atingir este objetivo, as características das tempestades costeiras obtidas a partir dos modelos globais de reanálise da ondulação mais recentes, ERA5 e WAVERYS, foram comparadas com as características obtidas a partir das observações de 326 boias ondógrafo costeiras. Esta análise revelou uma subestimação generalizada nos modelos de reanálise de ondulação, tanto para as alturas extremas das ondas como dos períodos médios, provavelmente devido à incapacidade de resolver a propagação das ondas em zonas costeiras complexas e pouco profundas. Estes erros foram significativamente reduzidos através da aplicação de equações de calibração. Foi desenvolvida uma calibração específica para cada local para os casos em que estão disponíveis dados de boias ondógrafo, bem como uma equação de calibração global para a altura significativa de onda e para o período médio, para as zonas que

não dispõem de dados in situ. Esta abordagem reduziu a subestimação da altura significativa das ondas com um período de retorno de 50 anos que, em média, representa cerca de 55% para a calibração específica, ou atinge25% para a calibração global aplicada aos dados da reanálise WAVERYS.

A caraterização morfológica das ilhas-barreira foi obtida com recurso a um conjunto de modelos digitais globais de topografia (Copernicus GLO-30 DEM, AW3D30, TanDEM-X, Euro-Maps 3D) e batimetria (GEBCO_2023, SRTM15+, ETOPO 2022). Estes foram validados com dados topo-batimétricos obtidos com LiDAR para cinco ilhas-barreira distribuídas globalmente. Esta validação forneceu informações essenciais sobre o potencial e as limitações destes modelos, revelando erros relacionados com a resolução dos dados, em especial relacionados com a correta identificação das cristas das dunas, que foram constantemente subestimadas. A inexistência de dados na interface terra-oceano foi colmatada através da determinação de um perfil transversal à costa médio em áreas morfologicamente homogéneas das ilhas-barreira, juntamente coma fusão dos dados topográficos e batimétricos utilizando um perfil de equilíbrio. Os perfis topo-batimétricos das ilhas barreira que integram os dados dos modelos TanDEM-X e ETOPO 2022 evidenciaram o menor erro, com um RMSE vertical de 0.76 m e uma subestimativa média da crista da duna de 1.14 m. Esta abordagem permitiu definir um perfil representativo para cada ilha barreira, adequado para utilização em estudos costeiros regionais e globais.

Após a caraterização das incertezas nos conjuntos de dados, os modelos globais com melhor desempenho - WAVERYS para a reanálise da ondulação, TanDEM-X para a topografia e ETOPO 2022 para a batimetria - foram selecionados para efetuar a primeira avaliação à escala global dos riscos de erosão e inundação em ilhas-barreira. Para tal, o modelo numérico XBeach foi utilizado para simular erosão e inundação induzidas por tempestades costeiras com um período de retorno de 50 anos para a altura da onda em 30 ilhas-barreira distribuídas globalmente. O modelo foi implementado em modo surfbeat para simular impactos de erosão e em modo não-hidrostático para simular impactos de inundação. A resposta das ilhas barreira à erosão e à inundação foi caracterizada através de indicadores baseados em processos. Para determinar a importância relativa das variáveis morfológicas e hidrodinâmicas na resposta das ilhas-barreira a tempestades extremas, foi efetuada uma análise de regressão multilinear. Esta análise evidenciou o controlo dominante do forçamento hidrodinâmico de tempestade na resposta erosiva das ilhas-barreira, com 87% da variabilidade no alcance máximo do espraio e 65% da variabilidade no volume dunar erodido a serem explicadas apenas por parâmetros

hidrodinâmicos. Foi ainda observada uma variabilidade espacial significativa na resposta das ilhas-barreira, com sectores críticos de erosão e inundação predominantemente localizados em regiões frequentemente afetadas por ciclones extra-tropicais e tropicais. Estas conclusões não só evidenciam padrões globais de vulnerabilidade de ilhas-barreira, como também o enquadramento para definir prioridades em termos de mitigação de riscos de erosão e inundação num contexto de intensificação dos perigos costeiros.

A integração de futuros dados topo-batimétricos de alta resolução obtidos a partir de satélites, bem como de novas técnicas para calibrar e validar de forma robusta os modelos morfodinâmicos e de abordagens estatísticas mais avançadas que permitam reduzir os custos computacionais da modelação numérica, possuem elevado potencial para ultrapassar as limitações não só de dados como de métodos e permitir a avaliação precisa dos riscos costeiros à escala global.

Considerando a expansão das populações costeiras e a aceleração das alterações climáticas, a necessidade de metodologias robustas e globalmente aplicáveis para avaliar e mitigar os riscos costeiros torna-se ainda mais premente. Este estudo representa assim um passo significativo no sentido de colmatar a lacuna entre a utilização de dados globais e a avaliação de risco localizada, lançando as bases para um planeamento e tomada de decisão mais eficazes para as zonas costeiras.

Palavras chave: Ilhas-barreira, Tempestades costeiras, Modelos globais, XBeach, Indicadores baseados em processos

Table of contents

Declaration of authorship ..... **v**

Acknowledgments ..... **vii**

Abstract ..... **ix**

Resumo ..... **x**

Resumo alargado ..... **xi**

Table of contents ..... **xiv**

List of figures ..... **xvii**

List of tables ..... **xxi**

Abbreviations ..... **xxii**

Chapter 1 Introduction **1**

1.1 Motivation **1**

1.2 Thesis objective **5**

1.3 Outline **6**

1.4 References **7**

Chapter 2 Improved estimates of extreme wave conditions in coastal areas from calibrated global reanalyses **13**

Abstract **13**

2.1 Introduction **13**

2.2 Materials and methods **16**

2.2.1 Wave reanalysis data 17

2.2.2 Wave buoy data 18

2.2.3 Evaluation 19

2.2.4 Calibration 20

2.2.5 Calculation of return periods 22

2.3 Results **23**

2.3.1 Overview 23

2.3.2 Evaluation of global wave reanalysis 23

2.3.3 Calibration of reanalyses for individual buoy locations 27

2.3.4 Global reanalysis calibration 30
2.4 Discussion 33
2.5 References 38
2.6 Data availability 44
2.7 Code availability 45
2.8 Acknowledgments 45
2.9 Appendix A. Supplementary figures 46
2.10 Appendix B. Supplementary tables 55
Chapter 3 Development of topo-bathymetric continuum profiles for coastal barriers with global open-access data 57
Abstract 57
3.1 Introduction 58
3.2 Materials and Methods 61
3.2.1 Topography 61
3.2.2 Bathymetry 64
3.2.3 Study sites 66
3.2.4 Horizontal and vertical datum correction 68
3.2.5 Cleaning of spikes and water bodies removal 68
3.2.6 DEM resampling 69
3.2.7 Error metrics 70
3.2.8 Merging of topo-bathymetry 71
3.3 Results 72
3.3.1 Evaluation of GDEMs' elevation accuracy 72
3.3.2 Evaluation of GBMs' depth accuracy 76
3.3.3 Merging of topo-bathymetry and profile elevation accuracy 77
3.4 Discussion 78
3.4.1 Performance of global and regional models 78
3.4.2 Challenges for the topo-bathymetric continuum in poorly surveyed areas 80
3.5 Conclusion 84
3.6 Acknowledgements 84
3.7 Appendix A. Supplementary data 85
3.8 References 88

Chapter 4 Barrier island response to energetic storms: a global view 99

Abstract 99

4.1 Introduction 100

4.2 Methods 103

4.2.1 Selection of barrier islands 103

4.2.2 Synthetic barrier island profiles 104

4.2.3 Synthetic storm identification 105

4.2.4 Nearshore downscaling 108

4.2.5 Storm impact modelling 109

4.2.6 Statistical analysis of barrier island characteristics and storm response 110

4.3 Results 113

4.3.1 Storm hydrodynamic forcing 113

4.3.2 Barrier island morphology 114

4.3.3 Relationships between morphological, hydrodynamic and process-based variables 116

4.3.4 Storm-induced barrier erosion 119

4.3.5 Storm-induced barrier flooding 121

4.4 Discussion 123

4.4.1 Assumptions of the global data and modelling-based methodology 123

4.4.2 Controls on the barrier island morphodynamic response 125

4.4.3 Recommendations for assessing global erosion and flooding using global models 129

4.5 Conclusion 130

4.6 Appendix A. Location and hydrodynamic characteristics of the barrier islands 131

4.7 Appendix B. Characteristics of the morphological and hydrodynamic variables 132

4.8 Appendix C. Process-based indicators 135

4.9 Acknowledgments 137

4.10 References 137

Chapter 5 General conclusions 145

List of figures

Figure 1.1 Global distribution of modern barrier islands according to the database of Mulhern et al. (2021) (dark grey) and location of barrier islands where XBeach was implemented to model storm impacts (black dots). 5

Figure 2.1 Example of original (a, c, e, g, i, k) wave parameters (H_s, T_m and T_p) and calibrated for individual buoy locations (b, d, f, h, j, l). Results shown for the Belmullet buoy location, in western Ireland, for WAVERYS (a, b, c, d, e, f) and ERA5 (g, h, i, j, k, l). Results for mean wave direction (in °) are shown for original (light red) and calibrated for individual buoy locations (light blue) for WAVERYS (m) and ERA5 (n) and compared to the buoy data (grey). The black dots indicate the percentiles (from 1st to 99th). 25

Figure 2.2 Global distribution of relative bias (in %) for extreme (above the 95th percentile) values of H_s between wave buoys and original reanalysis data (a-b), individual calibration (c-d) and percentual improvement obtained with the calibration (e-f) for WAVERYS (a, c, e) and ERA5 (b, d, f). Red (blue) values represent an underestimation (overestimation) from the reanalysis (in a, b, c, d). 26

Figure 2.3 Effect of individual and global calibration on H_s 50-year return periods. a) Return period values for original WAVERYS reanalysis (red) and buoy data (black), and with the individual (light blue) and global (dark blue) calibration for the location in the coast of South Carolina, USA. b) Box plot of differences in H_s 50-years return period between buoy data (only buoys with negative relative bias for extreme H_s) and reanalysis data, estimated with the original reanalysis data, individual calibration, and global calibration for WAVERYS and ERA5. The bottom and top of each box plot are the 25th and 75th percentile, the line in the middle the median, the whiskers correspond to 99.3% of the data and the outliers are reported as circles. 29

Figure 2.4 Global distribution of the relative improvement (in %) for the 50-year return period H_s calculated for the wave buoys and individual calibration (a-b) and global calibration (c-d) for WAVERYS (a-c) and ERA5 (b-d). 30

Figure S2.5 Correlation coefficient. Global distribution of Pearson's correlation coefficient (R) for H_s (a-b), Tm (c-d), T_p (e-f) and Dir_m (g-h) between the wave buoys and WAVERYS (left column, a-c-e-g) and ERA5 (right column, b-d-f-h) reanalyses. 46

Figure S2.6 Global distribution of RMSE for H_s (a-b, in meters), T_m (c-d, in seconds), T_p (e-f, in seconds) and Dir_m (g-h, in degrees) between wave buoys and WAVERYS (left column, a-c-e-g) and ERA5 (right column, b-d-f-h) reanalyses. 47

Figure S2.7 Global distribution of SI (in %) for H_s (a-b), T_m (c-d), T_p (e-f) and Dir_m (g-h) between wave buoys and WAVERYS (left column, a-c-e-g) and ERA5 (right column, b-d-f-h) reanalyses. 48

Figure S2.8 Global distribution of relative bias (in %) for H_s (a-b), T_m (c-d), T_p (e-f) and Dir_m (g-h) between wave buoys and WAVERYS (left column, a-c-e-g) and ERA5 (right column, b-d-f-h) reanalysis. Red (blue) values represent an underestimation (overestimation) from the reanalysis. 49

Figure S2.9 Global distribution of the mean difference for extreme values (above the 95th percentile) values of H_s (a-b in meters), T_m (c-d, in seconds) and T_p (e-f, in seconds) between wave buoys and WAVERYS (left column, a-c) and ERA5 (right column, b-d) reanalysis. Red (blue) values represent an underestimation (overestimation) from the reanalysis. 50

Figure S2.10 Global distribution of the mean difference for extreme values (above the 99th percentile) values of H_s (a-b in meters), T_m (c-d, in seconds) and T_p (e-f, in seconds) between wave buoys and WAVERYS (left column, a-c) and ERA5 (right column, b-d) reanalysis. Red (blue) values represent an underestimation (overestimation) from the reanalysis. 51
Figure S2.11 Global distribution of H_s 50-year return period difference between wave buoy data and WAVERYS (a) and ERA5 (b) reanalysis. Red (blue) values represent an underestimation (overestimation) from the reanalysis. 51
Figure S2.12 Global distribution of relative bias (in %) for extreme (>95th percentile) values of T_m (a-b) and T_p (c-d) between wave buoys and WAVERYS (left column, a-c-e) and ERA5 (right column, b-d-f) reanalyses. Red (blue) values represent an underestimation (overestimation) from the reanalysis. 52
Figure S2.13 Global distribution of difference (in degrees) between mean direction estimated with wave buoys data and with WAVERYS (a) or ERA5 (b) reanalysis data. 52
Figure S2.14 Box plot of R, RMSE (in meters), SI (in meters) and difference of extreme H_s (in meters) estimated with buoy data and original (a) and calibrated (b) reanalysis data from WAVERYS and ERA5. 53
Figure S2.15 Box plot of relative bias (in %) for H_s and for the extreme H_s (above the 95th percentile) estimated with buoy data and original (a) and calibrated (b) reanalysis data from WAVERYS and ERA5. 53
Figure S2.16 Sensitivity analysis of global calibration for H_s. Error metrics for the comparison of H_s between the buoys and global calibration of WAVERYS and ERA5 applied to the validation group (in red, ranging from 50% to 10% of the total buoys in bins of 0.01%) and the group of buoys used to determine the global calibration equations (in black, ranging from 50% to 90% of the total buoys). The parameters represented are R (a), RMSE (b), SI (c), relative bias (d), extreme (>95th percentile) relative bias (e), mean difference between buoy and reanalysis for values above the 95th (f) and 99th (g) percentile and difference between the H_s 50-years return period (h). 54
Figure S2.17 Sensitivity analysis of global calibration for T_m. Error metrics for the comparison of T_m between the buoys and global calibration of WAVERYS and ERA5 applied to the validation group (in red, ranging from 50% to 10% of the total buoys in bins of 0.01%) and the group of buoys used to determine the global calibration equations (in black, ranging from 50% to 90% of the total buoys). The parameters represented are R (a), RMSE (b), SI (c), relative bias (d), extreme (>95th percentile) relative bias (e), mean difference between buoy and reanalysis for values above the 95th (f) and 99th (g) percentile. 55
Figure 3.1 Location of coastal barriers and analysed 2 km-long sectors in: a) the Outer Banks in the USA, b) Fire Island in the USA, c) Terschelling in the Netherlands, d) Ria Formosa in southern Portugal and e) Myalup in Australia. Source: ESRI World Imagery. 67
Figure 3.2 Visualisation of topographic (a-e) and bathymetric (f-j) data at the Outer Banks, USA, displaying the different resolutions according to the data source. All GDEMs and GBMs are reprojected into the same horizontal (EPSG:3631 NAD83) and vertical (NAVD88) datum. 69
Figure 3.3 Error metrics between GDEMs and high-resolution LiDAR-derived DEMs for cross-shore profiles extracted at the Outer Banks in the USA (a), Fire Island in the USA (b), Terschelling in the Netherlands (c), Ria Formosa in southern Portugal (d) and Myalup in Australia (e). 73

Figure 3.4 Comparison between LiDAR-derived elevation and GDEMs for a) TanDEM-X, b) Copernicus GLO-30), c) AW3D30 and d) Euro-Maps 3D. Linear regression lines (forced through the origin) are shown along with their equation for each location. The dashed black line represents a perfect fit. 74
Figure 3.5 Averaged topographic profiles aligned at the dune top (x = 0 m) derived from LiDAR and GDEMs at the Outer Banks in the USA (a), Fire Island in the USA (b), Terschelling in the Netherlands (c), Ria Formosa in southern Portugal (d) and Myalup in Australia (e). The ocean is to the right of the profiles. 75
Figure 3.6 Error metrics between GBMs and RBMs (CUDEM, EMODnet, 2023 bathymetry of Australia) and high-resolution LiDAR-derived DEMs for cross-shore profiles extracted at the Outer Banks in the USA (a), Fire Island in the USA (b), Terschelling in the Netherlands (c), Ria Formosa in southern Portugal (d) and Myalup in Australia (e). 76
Figure 3.7 Averaged bathymetric profiles derived from LiDAR, RBMs and GBMs at the Outer Banks in the USA (a), Fire Island in the USA (b), Terschelling in the Netherlands (c), Ria Formosa in southern Portugal (d) and Myalup in Australia (e). 77
Figure 3.8 Top (a to e): Merged topo-bathymetric profiles obtained from LiDAR topography and regional bathymetries (blue line) compared with profiles obtained from merging the equilibrium profile with the TanDEM-X topography and ETOPO 2022 bathymetry (red line). Bottom (f to j): Plot of differences (in meters) between the higher resolution topo-bathymetry derived from merging LiDAR and RBMs and the topo-bathymetry derived from merging TanDEM-X GDEM with ETOPO 2022 GBM. The profiles refer to the coastal barriers at the Outer Banks in the USA (a, f), Fire Island in the USA (b, g), Terschelling in the Netherlands (c, h), Ria Formosa in southern Portugal (d, i) and Myalup in Australia (e, j). 78
Figure S3.9 Source ID grids from ETOPO 2022 (a to e) and Type Identifier grids from GEBCO 2022 (f to j) for the Outer Banks in the USA (a-f), Fire Island in the USA (b-g), Terschelling in the Netherlands (c-h), Ria Formosa in Portugal (d-i), Myalup in Australia (e-j). For each coastal barrier the extracted cross-shore profiles until 30 m depth are represented in white. 87
Figure 4.1 Global distribution of modern barrier islands from the Mulhern et al. (2021) database (dark grey) and 30 barrier islands selected for the present study (black). 104
Figure 4.2 Topo-bathymetric profiles of the barrier islands aligned at the dune crest (x = 0). Negative values represent distances seaward the dune crest and depths below mean sea level. 105
Figure 4.3 Parameters used to determine the synthetic storm forcing for Hog Island from WAVERYS and GTSM global data. (a) Return period for H_s. (b) Linear relationship between storm H_s and storm duration, (c) T_p and (d) storm surge (d). (e) Average spring tidal cycle and synthetic profile of the 50-year return period storm, including (f) H_s (g), T_p and (h) storm surge. 108
Figure 4.4 Storm hydrodynamic forcing scaled to the 50-year return period H_s. (a) 50-year return period H_s (in m) and modal storm direction; (b) T_p (in s), (c) storm duration (in h), (d) total water level (in m). 114
Figure 4.5 Morphologic characteristics of barrier islands: (a) dune height (in m) and (b) dune volume (in m^3/m), both estimated from the dune toe to the dune crest. 115
Figure 4.6 Heatmap of cross-correlations between morphological, hydrodynamic and process-based variables. All morphological parameters refer to the pre-storm conditions. The larger (smaller) black dots show relationships that are significant at the 99% (95%) significance level. The red (blue) colors represent positive

(negative) correlation between variables. The vertical and horizontal lines separate the response variables from the explanatory variables. 118
Figure 4.7 Coefficient of determination estimated through multilinear regression between the response variables (indicated in the x-axis) and the explanatory variables as a whole and separated between morphologic and hydrodynamic variables. The large (small) dots on top show when the regression is significant at 99 % (95 %) confidence level. 119
Figure 4.8 Pre- (dotted line) and post- (continuous line) storm profiles simulated with XB-SB. The dune crest (black dot), dune toe before the storm (blue dot) and dune toe after the storm (red dot) are reported. 120
Figure 4.9 Erosional response of synthetic barrier island profiles to a 50-year return period storm simulated with XBeach in surfbeat mode. (a) Eroded volume (in m^3/m), (b) relative volume loss (in %), (c) maximum dune horizontal retreat (in m) and (d) average dune retreat (in m). 121
Figure 4.10 Flooding due to overwash events for a 50-year return period storm simulated with XBeach in non-hydrostatic mode. (a) Maximum run-up simulated with XB-NH only shown for overwashed barrier islands (in m), (b) number of overtopping waves, (c) overtopping volume (in m^3/m), (d) overwash extent (in m). 122
Figure 4.11 Total barrier volume (in m^3/m, calculated from MSL to the dune crest) normalized by the product of the maximum H_s (in m) and maximum water level (in m). The horizontal threshold corresponds to 42. Barrier islands that experienced overwash are highlighted with a blue dot. 123
Figure 4.12 Linear regression (red line) between eroded dune volume (in m3/m) and the combination of maximum H_s (in m) and maximum water level (in m) at the offshore boundary of XBeach. The barrier islands located in areas typically affected by extratropical cyclones are represented with triangles, by tropical cyclones with dots and none of them by a diamond. 127

List of tables

Table 2.1 Error metrics for original and calibrated WAVERYS and ERA5 global wave reanalyses. Calibration results including the correlation coefficient R, relative bias of the values above the 95th percentile, mean differences for values above the 95th and 99th percentiles determined from the buoys and the original, individual and global calibrated reanalysis data, considering the randomly selected 70% of buoys used to find the global equations and the remaining 30% buoys used to validate the equations. 32
Table 3.1 Specifications for global topographic models. 62
Table 3.2 Specifications for local topographic models. 63
Table 3.3 Specifications for global and regional bathymetric models. 65
Table 3.4 Specifications for local bathymetric models (N/A where not available). 66
Table 3.5 Statistical comparison of LiDAR-derived topography and bathymetry against GDEMs/GBMs (from 0 m to ~10 m depth) averaged over all study sites for three cases: a) estimated for all profiles, b) for the average profiles and c) for the merged topo-bathymetric profile obtained from TanDEM-X and ETOPO 2022. Euro-Maps 3D is not included here as data were only available for 2 of the 5 sites. 75
Table S3.6 Average GDEM performance statistics. All GDEMs are averaged only for two sites, Outer Banks in the USA and Ria Formosa in Portugal due to the restricted availability of Euro-Maps3D. 85
Table S3.7 Average GBM performance statistics. All GBMs are averaged only for two sites, Outer Banks and Fire Islands in the USA due to the availability of CUDEM data only for the USA. 85
Table S3.8 Average GBM performance statistics. All GBMs are averaged only for two sites, Praia de Faro in Portugal and Terschelling in the Netherlands due to the availability of EMODnet data only for the European coast. 85
Table S3.9 Depth of closure (Dc) calculated with wave height and peak period from the entire WAVERYS series ($H12h/y$, $T12h/y$), median grain size (D50) from the literature and statistical results from the comparison of the profiles obtained merging of GDEMs and GBMs and the profile obtained from LiDAR-derived DEMs and RBMs. D50 values in red are out of the acceptable range of fine (0.125 - 0.25 mm) to medium (0.25 - 0.5 mm) sand. The colour scale (blue for higher accuracy, red for lower accuracy) of the mean absolute error (MAE) and root mean squared error (RMSE) is based on the highest and lowest values amongst all sites. The colour scale of the bias is based on the highest and lowest absolute values. 86
Table 4.1 Selected morphological and hydrodynamic variables characterizing the barrier islands. 111
Table 4.2 Process-based indicators of barrier island erosion and flooding response to an extreme storm, derived with XB-SB and XB-NH respectively. 112
Table S4.3 Barrier islands name, location, coordinates of the analyzed sector, depth of closure (Dc), and offshore wave characteristics extracted from WAVERYS global wave reanalysis and GTSM. 131

Abbreviations

CMEMS	Copernicus Marine Environment Monitoring Service
DEM	Digital elevation model
Dir_m	Mean wave direction (°)
ECMWF	European Centre for Medium-Range Weather Forecasts
ETC	Extratropical cyclones
GBM	Global bathymetric model
GDEM	Global digital elevation model
GTSM	Global Tide and Surge Model
H_s	Significant wave height (m)
LiDAR	Light Detection and Ranging
MSL	Mean sea level
RBM	Regional bathymetric model
TC	Tropical cyclones
T_m	Mean wave period (s)
T_p	Peak wave period (s)
XB-NH	Non-hydrostatic mode of XBeach
XB-SB	Surfbeat mode of XBeach

Chapter 1 Introduction

1.1 Motivation

Barrier islands systems are low-lying coastal landforms characterized by a combination of sedimentary environments that include islands and peninsulas comprised of sand or gravel that often extends parallel to the mainland. Barrier islands are separated from the mainland by a backbarrier lagoon and often form a barrier system with inlets in between islands (Oertel, 1985). Their global distribution (Mulhern et al., 2019; Stutz and Pilkey, 2011) and associated dynamic behaviour contribute to significant variability in their physical characteristics, exposure and response to environmental and anthropogenic stressors (Stutz and Pilkey, 2005). Their formation mechanisms are diverse, with their occurrence determined by sediment supply, tectonic setting and sea level change history at each specific location (Otvos, 2020, 2012). Key factors influencing their morphology and evolution include coastal gradient, sediment availability, tidal regime, wave climate and storm frequency, vegetation and sea level fluctuations (Stutz and Pilkey, 2011). Depending on the specific context, one or more of these factors may dominate, making barrier islands highly complex and dynamically evolving systems. Barrier islands provide multiple beneficial services for society and the environment (Otvos, 2012). They act as natural buffers, dissipating wave and storm energy, protecting inland areas, and supporting diverse ecosystems within their back-barrier bays, lagoons, and marshes (Barbier et al., 2011; FitzGerald et al., 2008). These areas are not only ecologically vital but also serve as habitats for numerous species. Additionally, many barrier islands are economically significant, hosting tourism-intensive recreational activities (Stutz and Pilkey, 2005).

Despite the important role of barrier islands as natural coastal buffers to storms, their sedimentary nature and narrow barrier width backed and fronted by water, makes them vulnerable to a variety of natural hazards. Coastal storms and longer-term changes in sediment supply and sea level can cause episodic erosion and flooding, as well as widespread inundation. The response of barrier islands to these hazards can vary depending on the specific morphological characteristics (e.g. dune, beach and nearshore) and hydrodynamic processes (e.g. alongshore wave energy variability, total water levels, extreme storm surge). This response has been extensively characterized and classified with field monitoring (e.g., Matias et al., 2010;

Morton and Sallenger, 2003), laboratory experiments (e.g., van Wiechen et al., 2023; Williams et al., 2012), morphodynamic modelling (e.g., Cohn et al., 2019; McCall et al., 2010) and the use of storm impact scales (e.g. Leaman et al., 2021; Sallenger, 2000).

In the context of global climatic change, storm impacts on barrier islands are expected to intensify. Global sea level rise is projected to increase between 0.5 m and 1 m by 2100 in case of unmitigated growth of emissions (SSP5-RCP8.5), when compared to the period 1986-2005 (Horton et al., 2020), and extreme wind-wave events are expected to change in magnitude and frequency (Meucci et al., 2020). With rising sea levels, the severity of coastal hazards such as floods and storm-induced erosion on coastal barriers is likely to increase (Masselink and van Heteren, 2014), leading to potential damage to ecosystems and populations. Presently, more than 10% of the world's population lives in coastal areas that are lower than 10 meters above MSL (Athanasiou et al., 2024), and this is projected to increase, especially in the low-elevation coastal zones of the Southern Hemisphere (Reimann et al., 2023). Fenster et al. (2022) highlighted the widespread coastal development on barrier islands, with approximately 59% of wave-dominated and mixed-energy barrier islands showing evidence of infrastructure and building development between 2015 and 2017. These developments are primarily residential single- and multi-family units and are located predominantly in North America, followed by Asia, Africa, and South America.

Exploring the complex interactions between sediment transport, hydrodynamics, morphology, vegetation and rigid infrastructures on barrier islands at different spatial and temporal scales has been the focus of a significant body of research. Multiple techniques have been developed over the years, ranging from simple conceptual models relating the antecedent morphology and hydrodynamic forcing with barrier response (e.g. Sallenger, 2000) to a variety of numerically more complex models relating temporally variable wave forcing with dune and beach erosion (e.g. SBEACH by Larson and Kraus, 1989; DUROS by Vellinga, 1986; CSHORE by Kobayashi et al., 2007; XBeach by Roelvink et al., 2009). According to a recent review by Sherwood et al. (2022) on process-based numerical models for assessing the impact of extreme storms on sandy coasts, one of the most significant advances has been the incorporation of infragravity waves into the physics of coastal morphodynamics models. One such model is XBeach (Roelvink et al., 2009), a state-of-the-art process-based model that has been widely applied and validated for simulating beach and dune erosion, demonstrating its skillful

predictions, particularly when site-specific calibration is incorporated (Schweiger et al., 2020). However, despite considerable advances on the modelling of coastal processes, the availability of accurate data for implementing models and for comparison of results remains the main challenge. XBeach relies on pre-storm topo-bathymetric information, hydrodynamic inputs of wave characteristics during storm events and boundary conditions such as water levels, currents, and sediment transport parameters to simulate coastal responses such as erosion, accretion, and flooding under extreme weather conditions. In addition, post-storm information on observed impacts is essential to determine the model skill and assess uncertainty. All of these requirements can be difficult to meet for many remote and data-poor areas along the world's coasts.

Therefore, even though there is an urgent need to understand and quantify erosional and flooding hazards on barrier islands worldwide, data limitations hinder efforts in many regions. For instance, wave buoys are heavily concentrated in the Northern Hemisphere (Copernicus Marine In Situ Team, 2020; Data Buoy Cooperation Panel, 2018) as are tide gauges (Haigh et al., 2023). High-resolution topo-bathymetric data are also unavailable for numerous coastal regions worldwide (Archer et al., 2018; Simpson et al., 2015; Wechsler, 2007), with very poor coverage of intertidal zones (Tseng et al., 2017), while high-resolution multibeam datasets are mostly restricted to economically significant areas (Mayer et al., 2018; Wölfl et al., 2019). Considering such data limitations, it is unsurprising that, to date, all storm-impact assessments performed for barrier islands using the process-based numerical model XBeach have focused on the Northern Hemisphere (Figure 1.1). This means that research on data-poor areas, and even some studies on areas with data availability, are forced to rely at least partially on coarse-resolution, globally available datasets (Alves, 2009; Escudero-Castillo et al., 2018; Garzo et al., 2023; Garzon et al., 2023; Silva et al., 2021).

Global datasets describing elevation, depth, waves and water levels, still lack adequate resolution for local scale assessments. In terms of the topo-bathymetric data, there is still the need for an openly available global digital elevation model with high spatial resolution and vertical accuracy (Schumann and Bates, 2018). Regarding global hydrodynamic datasets, although the representation of average conditions is nowadays quite accurate, predicting extremes remains challenging due to persistent underestimation of wave and wind parameters from most reanalyses (Morim et al., 2023), especially in areas prone to extratropical cyclones

(Lodise et al., 2024), which can lead to an underestimation of the impacts. While waiting for next-generation global digital elevation and hydrodynamic datasets, which will improve the representation of physical processes, provide increasing spatial and temporal resolution and address sources of uncertainty, applying the global datasets available nowadays remains both possible and necessary. However, to maximize their usefulness, it is essential to first acknowledge the inherent uncertainties, then to quantify them and, whenever feasible, to integrate these uncertainties into risk assessments (e.g., Toimil et al., 2021). This can enhance the credibility of present and future impact assessments, especially in relation to extreme events (Bricheno and Wolf, 2018; Morim et al., 2023). Additional uncertainties stem from the unpredictability of human-driven coastal adaptation and its interaction with future risks, as highlighted in an extensive review of uncertainties and biases in global-scale coastal flood risk assessments by Hinkel et al. (2021).

Despite these challenges, global datasets offer unparalleled possibilities to investigate coastal processes at unprecedented spatial and temporal scales. Recent studies have already characterized coastal areas using global datasets for metrics such as depth of closure, nearshore slope, sediment grain size and coastal geomorphic characteristics (Athanasiou et al., 2019, 2024). Furthermore, global flood hazards (Vousdoukas et al., 2018) and beach erosion trends (Luijendijk et al., 2018; Mentaschi et al., 2018) have been explored. A solution for providing information on coastal erosion and flooding hazards in areas lacking high-resolution information may therefore lie in the integration of open-access global datasets with the most advanced coastal modelling techniques, combining global coverage with the simulation capabilities of process-based models. While this approach may be readily applicable and constitute a promising way forward, there are still significant challenges to address. These include the incorporation of the uncertainties associated with global datasets and the determination of the robustness and skill of process-based models, such as XBeach, when data for calibration are unavailable. Nevertheless, such an approach based on global datasets and process-based models would allow a first-level characterization of event-scale coastal hazards, aided by the implementation of process-based indicators (Ferreira et al., 2017), which would help identify and prioritize vulnerable coastal areas. Process-based indicators integrate physical forcings with their morphological effects and can enable a more nuanced identification of exposed coastal areas. Prioritizing these areas for mitigation and adaptation efforts can be

further informed by coastal vulnerability indices, such as those reviewed by Nguyen et al. (2016), ensuring effective responses to future coastal risks.

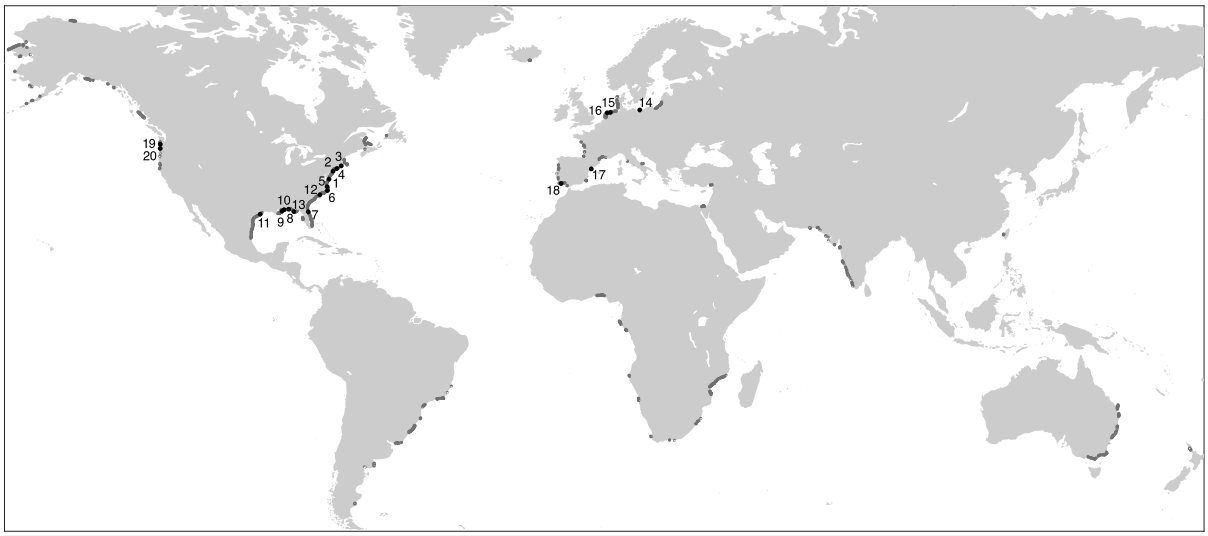

Figure 1.1 Global distribution of modern barrier islands according to the database of Mulhern et al. (2021) (dark grey) and location of barrier islands where XBeach was implemented to model storm impacts (black dots).

1.2 Thesis objective

This study aims to *evaluate, on a global scale, the response of wave-dominated barrier islands to extreme storm events*. By integrating global datasets and process-based models, it seeks to overcome the challenges posed by limited data availability while addressing the uncertainties and limitations inherent in existing methodologies. To achieve this overarching goal, the study focuses on the following objectives:

- The assessment of coastal storm forcing by evaluating the suitability and reliability of openly available global wave reanalysis datasets for large-scale storm impact assessments in coastal areas. This involves investigating the accuracy of these datasets in representing extreme storm events and ensuring that they effectively capture critical wave parameters such as height, period, and direction.

- The characterization of barrier island morphology by developing methodologies to assess and integrate coarse resolution global topo-bathymetric datasets. This involves identifying and analyzing key morphological parameters such as dune height and nearshore configuration, which are critical for understanding the response of barrier islands to storm events.

- The characterization of coastal storm impacts, including erosion and flooding, on barrier islands at a global scale using process-based modelling to determine process-based indicators, allowing to evaluate the variability of the storm induced impacts. This combines the hydrodynamic forcing and morphologic characterization of barrier islands carried out with the previously selected global datasets.

By addressing these objectives, this study contributes to advance global-scale methodologies for assessing storm impacts on barrier islands, particularly in underreported and data-scarce regions.

1.3 Outline

The thesis is structured as follows, with Chapters 2, 3 and 4 addressing respectively the three objectives mentioned above:

- Chapter 1 provides a general introduction that frames the main topics that will be addressed in the thesis and outlines the motivation for the global assessment of coastal storm hazards in barrier islands.

- Chapter 2 is a scientific paper that was published in Communication Earth and Environment as Fanti, V., Ferreira, Ó., Kümmerer, V. & Loureiro, C., Improved estimates of extreme wave conditions in coastal areas from calibrated global reanalyses. *Communication Earth and Environment* 4, 151 (2023). https://doi.org/10.1038/s43247-023-00819-0.

- Chapter 3 is a scientific paper that was published in Remote Sensing Applications: Society and Environment as Fanti, V., Loureiro, C. & Ferreira, Ó., Development of topo-bathymetric continuum profiles for coastal barriers with global open-access data. *Remote Sensing Applications: Society and Environment* 38, 101528 (2025).

- Chapter 4 has been partially published as Fanti, V., Ferreira, Ó., & Loureiro, C. (2023). Application of global datasets for storm impact assessment in barrier island systems. In Coastal Sediments 2023: The Proceedings of the Coastal Sediments 2023 (pp. 12-23). The chapter was submitted as Fanti, V., Ferreira, Ó., Kümmerer V., & Loureiro, C. Barrier island response to energetic storms: a global view.

- Chapter 5 provides a final synthesis and general conclusions of the thesis.

1.4 References

Alves, A.R., 2009. Long-term erosional hot spots in the southern Brazilian coast. J. Geophys. Res. Ocean. 114, 1–11. https://doi.org/10.1029/2008JC004933

Archer, L., Neal, J.C., Bates, P.D., House, R.J., 2018. Comparing TanDEM-X data with frequently-used DEMs for flood inundation modeling. Water Resour. Res. 54, 10–205. https://doi.org/https://doi.org/10.1029/2018WR023688

Athanasiou, P., van Dongeren, A.R., Giardino, A., Vousdoukas, M.I., Gaytan-Aguilar, S., Ranasinghe, R., 2019. Global distribution of nearshore slopes with implications for coastal retreat. Earth Syst. Sci. Data 11, 1515–1529. https://doi.org/10.5194/essd-11-1515-2019

Athanasiou, P., van Dongeren, A.R., Pronk, M., Giardino, A., Vousdoukas, M., Ranasinghe, R., 2024. Global Coastal Characteristics (GCC): A global dataset of geophysical, hydrodynamic and socioeconomic coastal indicators (submitted for publication). Earth Syst. Sci. Data Discuss. 8200199, 3433–3452.

Barbier, E.B., Hacker, S.D., Kennedy, C., Koch, E.W., Stier, A.C., Silliman, B.R., 2011. The value of estuarine and coastal ecosystem services. Ecol. Monogr. 81, 169–193. https://doi.org/10.1890/10-1510.1

Beckman, J.N., Long, J.W., Hawkes, A.D., Leonard, L.A., Ghoneim, E., 2021. Investigating controls on barrier island overwash and evolution during extreme storms. Water (Switzerland) 13. https://doi.org/10.3390/w13202829

Bricheno, L.M., Wolf, J., 2018. Future Wave Conditions of Europe, in Response to High-End Climate Change Scenarios. J. Geophys. Res. Ocean. 123, 8762–8791. https://doi.org/10.1029/2018JC013866

Bugajny, N., Furmańczyk, K., Dudzińska-Nowak, J., Paplińska-Swerpe, B., 2013. Modelling morphological changes of beach and dune induced by storm on the Southern Baltic coast using XBeach (case study: Dziwnow Spit). J. Coast. Res. 672–677. https://doi.org/10.2112/SI65-114

Cohn, N., Ruggiero, P., García-Medina, G., Anderson, D.L., Serafin, K.A., Biel, R.G., 2019. Environmental and morphologic controls on wave-induced dune response. Geomorphology 329, 108–128. https://doi.org/10.1016/j.geomorph.2018.12.023

Copernicus Marine In Situ Team, 2020. Copernicus In Situ TAC, Real Time Quality Control for WAVES. https://doi.org/https://doi.org/10.13155/46607

Data Buoy Cooperation Panel, 2018. Global Data Buoy Observations, a DBCP Implementation Strategy.

de Vet, L., McCall, R.T., Den Bieman, J.P., Stive, M.J.F., van Ormondt, M., 2015. Modelling Dune Erosion, Overwash and Breaching At Fire Island (NY) During Hurricane Sandy 1–10. https://doi.org/10.1142/9789814689977_0006

Erikson, L.H., Larson, M., Hanson, H., 2007. Laboratory investigation of beach scarp and dune recession due to notching and subsequent failure. Mar. Geol. 245, 1–19. https://doi.org/10.1016/j.margeo.2007.04.006

Escudero-Castillo, M., Felix-Delgado, A., Silva, R., Mariño-Tapia, I., Mendoza, E., 2018. Beach erosion and loss of protection environmental services in Cancun, Mexico. Ocean Coast. Manag. 156, 183–197. https://doi.org/10.1016/j.ocecoaman.2017.06.015

Fenster, M.S., Hughes, C.P., Stutz, M.L., 2022. A Survey of Global Mixed-Energy and Wave-Dominated Barrier Island Distribution and Development. J. Coast. Res. 38, 795–806. https://doi.org/10.2112/JCOASTRES-D-19-00144.1

Ferreira, Ó., Plomaritis, T.A., Costas, S., 2017. Process-based indicators to assess storm induced coastal hazards. Earth-Science Rev. 173, 159–167. https://doi.org/10.1016/j.earscirev.2017.07.010

FitzGerald, D.M., Fenster, M.S., Argow, B.A., Buynevich, I. V., 2008. Coastal impacts due to sea-level rise. Annu. Rev. Earth Planet. Sci. 36, 601–647. https://doi.org/10.1146/annurev.earth.35.031306.140139

Garzo, P.A., Sánchez-Caro, L., Mojica, M., 2023. Coastal erosion in temperate barriers: an anthropized sandy beach in Buenos Aires, Argentina. J. South Am. Earth Sci. 128. https://doi.org/10.1016/j.jsames.2023.104453

Garzon, J.L., Ferreira, Ó., Plomaritis, T.A., 2022. Modeling of Coastal Erosion in Exposed and Groin-Protected Steep Beaches. J. Waterw. Port, Coastal, Ocean Eng. 148, 1–16. https://doi.org/10.1061/(asce)ww.1943-5460.0000719

Garzon, J.L., Ferreira, Ó., Reis, M.T., Ferreira, A., Fortes, C.J.E.M., Zózimo, A.C., 2023. Conceptual and quantitative categorization of wave-induced flooding impacts for pedestrians and assets in urban beaches. Sci. Rep. 13, 1–12. https://doi.org/10.1038/s41598-023-32175-6

Gharagozlou, A., Dietrich, J.C., Karanci, A., Luettich, R.A., Overton, M.F., 2020. Storm-driven erosion and inundation of barrier islands from dune-to region-scales. Coast. Eng. 158, 103674. https://doi.org/10.1016/j.coastaleng.2020.103674

Gharagozlou, A., Dietrich, J.C., Massey, T.C., Anderson, D.L., Gorski, J.F., Overton, M.F., 2021. Formation of a barrier island breach and its contributions to lagoonal circulation. Estuar. Coast. Shelf Sci. 262, 107593. https://doi.org/10.1016/j.ecss.2021.107593

Gracia, V., García, M., Grifoll, M., Sánchez-Arcilla, A., 2013. Breaching of a barrier under extreme events. The role of morphodynamic simulations. J. Coast. Res. 65, 951–956. https://doi.org/10.2112/si65-161.1

Haigh, I.D., Marcos, M., Talke, S.A., Woodworth, P.L., Hunter, J.R., Hague, B.S., Arns, A., Bradshaw, E., Thompson, P., 2023. GESLA Version 3: A major update to the global higher-frequency sea-level dataset. Geosci. Data J. 10, 293–314. https://doi.org/10.1002/gdj3.174

Harter, C., Figlus, J., 2017. Numerical modeling of the morphodynamic response of a low-lying barrier island beach and foredune system inundated during Hurricane Ike using XBeach and CSHORE. Coast. Eng. 120, 64–74. https://doi.org/10.1016/j.coastaleng.2016.11.005

Hinkel, J., Feyen, L., Hemer, M., Le Cozannet, G., Lincke, D., Marcos, M., Mentaschi, L., Merkens, J.L., de Moel, H., Muis, S., Nicholls, R.J., Vafeidis, A.T., van de Wal, R.S.W., Vousdoukas, M.I., Wahl, T., Ward, P.J., Wolff, C., 2021. Uncertainty and Bias in Global to Regional Scale Assessments of Current and Future Coastal Flood Risk. Earth's Futur. 9, 1–28. https://doi.org/10.1029/2020EF001882

Horton, B.P., Khan, N.S., Cahill, N., Lee, J.S.H., Shaw, T.A., Garner, A.J., Kemp, A.C., Engelhart, S.E., Rahmstorf, S., 2020. Estimating global mean sea-level rise and its uncertainties by 2100 and 2300 from an expert survey. npj Clim. Atmos. Sci. 3, 1–8. https://doi.org/10.1038/s41612-020-0121-5

Larson, M., Erikson, L., Hanson, H., 2004. An analytical model to predict dune erosion due to wave impact. Coast. Eng. 51, 675–696. https://doi.org/10.1016/j.coastaleng.2004.07.003

Larson, M., Kraus, N.C., 1989. SBEACH: numerical model for simulating storm-induced beach change; report 1: empirical foundation and model development. Tech. Rep. - US Army Coast. Eng. Res. Cent. 89–9.

Leaman, C.K., Harley, M.D., Splinter, K.D., Thran, M.C., Kinsela, M.A., Turner, I.L., 2021. A storm hazard matrix combining coastal flooding and beach erosion. Coast. Eng. 170, 104001. https://doi.org/10.1016/j.coastaleng.2021.104001

Lindemer, C.A., Plant, N.G., Puleo, J.A., Thompson, D.M., Wamsley, T. V., 2010. Numerical simulation of a low-lying barrier island's morphological response to Hurricane Katrina. Coast. Eng. 57, 985–995. https://doi.org/10.1016/j.coastaleng.2010.06.004

Lodise, J., Merrifield, S., Collins, C., Behrens, J., Terrill, E., 2024. Performance of ERA5 wind speed and significant wave height within Extratropical cyclones using collocated satellite radar altimeter measurements. Coast. Eng. J. 66, 89–114. https://doi.org/10.1080/21664250.2023.2301181

Luijendijk, A., Hagenaars, G., Ranasinghe, R., Baart, F., Donchyts, G., Aarninkhof, S., 2018. The State of the World's Beaches. Sci. Rep. 8, 1–11. https://doi.org/10.1038/s41598-018-24630-6

Ma, M., Huang, W., Vijayan, L., Jung, S., 2024. Modeling wave-surge effects on barrier-island breaching in St. Joseph Peninsula during Hurricane Michael. Nat. Hazards 14199–14226. https://doi.org/10.1007/s11069-024-06768-x

Masselink, G., van Heteren, S., 2014. Response of wave-dominated and mixed-energy barriers to storms. Mar. Geol. 352, 321–347. https://doi.org/10.1016/j.margeo.2013.11.004

Matheen, N., Harley, M.D., Turner, I.L., Splinter, K.D., Simmons, J.A., Thran, M.C., 2021. Bathymetric data requirements for operational coastal erosion forecasting using xbeach. J. Mar. Sci. Eng. 9. https://doi.org/10.3390/jmse9101053

Matias, A., Ferreira, Ó., Vila-Concejo, A., Morris, B., Dias, J.A., 2010. Short-term morphodynamics of non-storm overwash. Mar. Geol. 274, 69–84. https://doi.org/10.1016/j.margeo.2010.03.006

Mayer, L., Jakobsson, M., Allen, G., Dorschel, B., Falconer, R., Ferrini, V., Lamarche, G., Snaith, H., Weatherall, P., 2018. The Nippon Foundation-GEBCO seabed 2030 project: The quest to see the world's oceans completely mapped by 2030. Geosci. 8. https://doi.org/10.3390/geosciences8020063

McCall, R.T., van Thiel de Vries, J.S.M., Plant, N.G., van Dongeren, A.R., Roelvink, J.A., Thompson, D.M., Reniers, A.J.H.M., 2010. Two-dimensional time dependent hurricane overwash and erosion modeling at Santa Rosa Island. Coast. Eng. 57, 668–683. https://doi.org/10.1016/j.coastaleng.2010.02.006

Mentaschi, L., Vousdoukas, M.I., Pekel, J.F., Voukouvalas, E., Feyen, L., 2018. Global long-term observations of coastal erosion and accretion. Sci. Rep. 8, 1–11. https://doi.org/10.1038/s41598-018-30904-w

Meucci, A., Young, I.R., Hemer, M., Kirezci, E., Ranasinghe, R., 2020. Projected 21st century changes in extreme wind-wave events. Sci. Adv. 6. https://doi.org/10.1126/sciadv.aaz7295

Morim, J., Wahl, T., Vitousek, S., Santamaria-aguilar, S., Young, I., Hemer, M., 2023. Understanding uncertainties in contemporary and future extreme wave events for broad-scale impact and adaptation planning. Sci. Adv. 9, 1–13. https://doi.org/10.1126/sciadv.ade3170

Morton, R.A., Sallenger, A.H., 2003. Morphological impacts of extreme storms on sandy beaches and barriers. J. Coast. Res. 19, 560–573.

Mulhern, J.S., Johnson, C.A., Martin, J.M., 2021. Dataset for: Is barrier island morphology a function of tidal and wave regime? https://doi.org/https://doi.org/10.1016/j.margeo.2017.02.016.

Mulhern, J.S., Johnson, C.L., Martin, J.M., 2019. Modern to ancient barrier island dimensional comparisons: Implications for analog selection and paleomorphodynamics. Front. Earth Sci. 7, 1–22. https://doi.org/10.3389/feart.2019.00109

Nguyen, T.T.X., Bonetti, J., Rogers, K., Woodroffe, C.D., 2016. Indicator-based assessment of climate-change impacts on coasts : A review of concepts , methodological approaches and vulnerability indices. Ocean Coast. Manag. 123, 18–43. https://doi.org/10.1016/j.ocecoaman.2015.11.022

Oertel, G.F., 1985. The barrier island system. Mar. Geol. 63, 1–18. https://doi.org/10.1016/0025-3227(85)90077-5

Otvos, E.G., 2020. Coastal barriers - fresh look at origins, nomenclature and classification issues. Geomorphology 355, 107000. https://doi.org/10.1016/j.geomorph.2019.107000

Otvos, E.G., 2012. Coastal barriers - Nomenclature, processes, and classification issues. Geomorphology 139–140, 39–52. https://doi.org/10.1016/j.geomorph.2011.10.037

Passeri, D.L., Dalyander, P.S., Long, J.W., Mickey, R.C., Jenkins, R.L., Thompson, D.M., Plant, N.G., Godsey, E.S., Gonzalez, V.M., 2020. The Roles of Storminess and Sea Level Rise in Decadal Barrier Island Evolution. Geophys. Res. Lett. 47, 1–8. https://doi.org/10.1029/2020GL089370

Reimann, L., Vafeidis, A.T., Honsel, L.E., 2023. Population development as a driver of coastal risk: Current trends and future pathways. Cambridge Prism. Coast. Futur. 1. https://doi.org/10.1017/cft.2023.3

Roelvink, D., Reniers, A., van Dongeren, A.R., van Thiel de Vries, J., McCall, R.T., Lescinski,

J., 2009. Modelling storm impacts on beaches, dunes and barrier islands. Coast. Eng. 56, 1133–1152. https://doi.org/10.1016/j.coastaleng.2009.08.006

Rutten, J., Torres-Freyermuth, A., Puleo, J.A., 2021. Uncertainty in runup predictions on natural beaches using XBeach nonhydrostatic. Coast. Eng. 166, 103869. https://doi.org/10.1016/j.coastaleng.2021.103869

Sallenger, J., 2000. Storm impact scale for barrier islands. J. Coast. Res. 16, 890–895.

Schambach, L., Grilli, A.R., Grilli, S.T., Hashemi, M.R., King, J.W., 2018. Assessing the impact of extreme storms on barrier beaches along the Atlantic coastline: Application to the southern Rhode Island coast. Coast. Eng. 133, 26–42. https://doi.org/10.1016/j.coastaleng.2017.12.004

Schumann, G.J.-P., Bates, P.D., 2018. The Need for a High-Accuracy, Open-Access Global DEM. Front. Earth Sci. 6, 1–5. https://doi.org/10.3389/feart.2018.00225

Schweiger, C., Kaehler, C., Koldrack, N., Schuettrumpf, H., 2020. Spatial and temporal evaluation of storm-induced erosion modelling based on a two-dimensional field case including an artificial unvegetated research dune. Coast. Eng. 161, 103752. https://doi.org/10.1016/j.coastaleng.2020.103752

Sherwood, C.R., Long, J.W., Dickhudt, P.J., Dalyander, P.S., Thompson, D.M., Plant, N.G., 2014. Inundation of a barrier island (Chandeleur Islands, Louisiana, USA) during a hurricane: Observed water-level gradients and modeled seaward sand transport. J. Geophys. Res. Earth Surf. 119, 300–316. https://doi.org/10.1002/2013JF002871.Received

Sherwood, C.R., van Dongeren, A.R., Doyle, J., Hegermiller, C.A., Hsu, T.J., Kalra, T.S., Olabarrieta, M., Penko, A.M., Rafati, Y., Roelvink, D., Van Der Lugt, M., Veeramony, J., Warner, J.C., 2022. Modeling the Morphodynamics of Coastal Responses to Extreme Events: What Shape Are We In? Ann. Rev. Mar. Sci. 14, 457–492. https://doi.org/10.1146/annurev-marine-032221-090215

Silva, M.S., Guedes, C.C.F., da Silva, G.A.M., Ribeiro, G.P., 2021. Active mechanisms controlling morphodynamics of a coastal barrier: Ilha comprida, brazil. Ocean Coast. Res. 69, 1–24. https://doi.org/10.1590/2675-2824069.20-338mss

Simpson, A.L., Balog, S., Moller, D.K., Strauss, B.H., Saito, K., 2015. An urgent case for higher resolution digital elevation models in the world's poorest and most vulnerable countries. Front. Earth Sci. 3, 50. https://doi.org/10.3389/feart.2015.00050

Smallegan, S.M., Irish, J.L., van Dongeren, A.R., Den Bieman, J.P., 2016. Morphological response of a sandy barrier island with a buried seawall during Hurricane Sandy. Coast. Eng. 110, 102–110. https://doi.org/10.1016/j.coastaleng.2016.01.005

Splinter, K.D., Palmsten, M.L., 2012. Modeling dune response to an East Coast Low. Mar. Geol. 329–331, 46–57. https://doi.org/10.1016/j.margeo.2012.09.005

Stutz, M.L., Pilkey, O.H., 2011. Open-ocean barrier islands: Global influence of climatic, oceanographic, and depositional settings. J. Coast. Res. 27, 207–222. https://doi.org/10.2112/09-1190.1

Stutz, M.L., Pilkey, O.H., 2005. The relative influence of humans on barrier islands: Humans versus geomorphology. GSA Rev. Eng. Geol. 16, 137–147. https://doi.org/10.1130/2005.4016(12)

Toimil, A., Camus, P., Losada, I.J., Alvarez-Cuesta, M., 2021. Visualising the Uncertainty Cascade in Multi-Ensemble Probabilistic Coastal Erosion Projections. Front. Mar. Sci. 8,

1–19. https://doi.org/10.3389/fmars.2021.683535

Tseng, K.H., Kuo, C.Y., Lin, T.H., Huang, Z.C., Lin, Y.C., Liao, W.H., Chen, C.F., 2017. Reconstruction of time-varying tidal flat topography using optical remote sensing imageries. ISPRS J. Photogramm. Remote Sens. 131, 92–103. https://doi.org/10.1016/j.isprsjprs.2017.07.008

van der Lugt, M.A., Quataert, E., van Dongeren, A.R., van Ormondt, M., Sherwood, C.R., 2019. Morphodynamic modeling of the response of two barrier islands to Atlantic hurricane forcing. Estuar. Coast. Shelf Sci. 229. https://doi.org/10.1016/j.ecss.2019.106404

van Wiechen, P.P.J., de Vries, S., Reniers, A.J.H.M., Aarninkhof, S., 2023. Dune erosion during storm surges: A review of the observations, physics and modelling of the collision regime. Coast. Eng. 186, 104383. https://doi.org/10.1016/j.coastaleng.2023.104383

Vellinga, P., 1986. Beach and dune erosion during storm surges.

Vousdoukas, M.I., Ferreira, Ó., Almeida, L.P.M., Pacheco, A., 2012. Toward reliable storm-hazard forecasts: XBeach calibration and its potential application in an operational early-warning system. Ocean Dyn. 62, 1001–1015. https://doi.org/10.1007/s10236-012-0544-6

Vousdoukas, M.I., Mentaschi, L., Voukouvalas, E., Verlaan, M., Jevrejeva, S., Jackson, L.P., Feyen, L., 2018. Global probabilistic projections of extreme sea levels show intensification of coastal flood hazard. Nat. Commun. 9, 1–12. https://doi.org/10.1038/s41467-018-04692-w

Wechsler, S.P., 2007. Uncertainties associated with digital elevation models for hydrologic applications: A review. Hydrol. Earth Syst. Sci. 11, 1481–1500. https://doi.org/10.5194/hess-11-1481-2007

Wesselman, D., de Winter, R.C., Engelstad, A., McCall, R.T., van Dongeren, A.R., Hoekstra, P., Oost, A., van der Vegt, M., 2018. The effect of tides and storms on the sediment transport across a Dutch barrier island. Earth Surf. Process. Landforms 43, 579–592. https://doi.org/10.1002/esp.4235

Williams, J.J., de Alegría-Arzaburu, A.R., McCall, R.T., Van Dongeren, A.R., 2012. Modelling gravel barrier profile response to combined waves and tides using XBeach: Laboratory and field results. Coast. Eng. 63, 62–80. https://doi.org/10.1016/j.coastaleng.2011.12.010

Wölfl, A.C., Snaith, H., Amirebrahimi, S., Devey, C.W., Dorschel, B., Ferrini, V., Huvenne, V.A.I., Jakobsson, M., Jencks, J., Johnston, G., Lamarche, G., Mayer, L., Millar, D., Pedersen, T.H., Picard, K., Reitz, A., Schmitt, T., Visbeck, M., Weatherall, P., Wigley, R., 2019. Seafloor mapping - The challenge of a truly global ocean bathymetry. Front. Mar. Sci. 6, 1–16. https://doi.org/10.3389/fmars.2019.00283

Chapter 2 Improved estimates of extreme wave conditions in coastal areas from calibrated global reanalyses

Fanti, V., Ferreira, Ó., Kümmerer, V., & Loureiro, C. (2023). Improved estimates of extreme wave conditions in coastal areas from calibrated global reanalyses. *Communications Earth & Environment*, 4(1), 151.

Abstract

The analysis of extreme wave conditions is crucial for understanding and mitigating coastal hazards. As global wave reanalyses allow to extend the evaluation of wave conditions to periods and locations not covered by in-situ measurements, their direct use is common. However, in coastal areas, the accuracy of global reanalyses is lower, particularly for extreme waves. Here we compare two leading global wave reanalyses against 326 coastal buoys, demonstrating that both reanalyses consistently underestimate significant wave height, 50-year return period and mean wave period in most coastal locations around the world. Different calibration methods applied to improve the modelled extreme waves, resulting in a 53% reduction in the underestimation of extreme wave heights. Importantly, the 50-year return period for significant wave height is improved on average by 55%. Extreme wave statistics determined for coastal areas directly from global wave reanalyses require careful consideration, with calibration largely reducing uncertainty and improving confidence.

Keywords: Global wave reanalysis, Extreme waves, Coastal wave buoys, Validation in-situ, Calibration equations

2.1 Introduction

Extreme wave conditions cause large disruption in coastal areas (Coco and Ciavola, 2017) and their impacts are likely to increase due to climate change (Lobeto et al., 2021; Meucci et al., 2020), including sea level rise (Vitousek et al., 2017), while also being enhanced by expanding coastal populations (Neumann et al., 2015; van Dongeren et al., 2018). Therefore,

characterising the nearshore wave climate is fundamental for present and future coastal management, as extreme wave events can potentially affect a wide range of socio-economic activities. Storms or extreme wave events enhance sediment transport (Wesselman et al., 2018) and modify coastal geomorphology (Houser et al., 2008; Morton and Sallenger, 2003), cause erosion and flooding (Leaman et al., 2021) and must be considered when designing and implementing coastal structures or marine energy devices (Guillou et al., 2020; Neary et al., 2020). Knowledge of the extreme wave climate is also necessary to characterize coastal hazards, quantify the risks associated with different return periods, and propose management actions as a function of the expected consequences (Ferreira et al., 2018). If the extreme wave parameters used in such analyses are biased (i.e. underestimated or overestimated), the error is propagated to the estimation of the related coastal hazards and risks. This can lead to incorrect coastal risk assessments, affecting and compromising the planning, the mitigation efforts, and ultimately the adoption of risk reduction measures.

At a global level, reliable in-situ measurements of waves in coastal areas (e.g. buoys) are still scarce, comprise records with relatively short duration (often only a few years or decades), have limited geographical distribution (Data Buoy Cooperation Panel, 2018) and are subject to errors (Gemmrich et al., 2011; Janssen et al., 2007) that require appropriate quality control. Comprehensive characterization of extreme wave conditions derived from satellite altimetry data is also irregular in time and space, scarcely available in coastal regions and high latitudes, and requires complex post-processing techniques for retrieving accurate information in coastal areas (Vignudelli et al., 2019). Wave hindcast models are a powerful alternative for wave climate analysis, allowing to minimise the lack of data by providing consistent global datasets of past wave conditions, including coastal areas, and temporally and spatially augmenting wave observations.

Several global and regional wave reanalyses, derived from the assimilation of atmospheric and oceanographic data from models, satellites and in-situ observations, have been developed and improved in the last decades, and their reliability and use for coastal hazard analysis increased substantially (Almar et al., 2021b; Muis et al., 2016, 2020; Michalis I. Vousdoukas et al., 2018). Until recently, the most widely used wave reanalyses on a global scale were the 1.5° spatial resolution ERA40 (Uppala et al., 2005) and 1° ERA-Interim (Dee et al., 2011) produced by the European Centre for Medium-Range Weather Forecasts (ECMWF), the CFSR/NCAR

(0.5°/0.07°) produced by NCEP/NOAA (Chawla et al., 2013) and GOW2 (Perez et al., 2017) (0.5°/0.25°) from IH Cantabria. In the past few years, new global wave reanalyses have been produced, including the 0.5° ERA5 (Hersbach et al., 2018) by ECMWF and 0.2° WAVERYS (Law-Chune et al., 2021) by the Copernicus Marine Environment Monitoring Service (CMEMS). These last generation and up-to-date wave reanalyses are becoming the most commonly used reanalyses globally, and several studies have demonstrated the accuracy and improvements they have achieved (Hersbach et al., 2020, 2019; Hoffmann et al., 2019; Sharmar and Markina, 2020; Wang and Wang, 2021). Compared to wave buoys, reanalyses have the advantage of being a physically consistent reconstruction of past wave climate, with no gaps in space and time. However, they have coarse resolutions (Feng et al., 2006) that cannot fully resolve the complexity of coastlines, accurately incorporate regional coastal winds, simulate depth-limited wave propagation processes across shallow parts of the continental shelf, or entirely incorporate local processes such as bottom friction, wave breaking and sub-grid island shadowing (Cavaleri et al., 2018, 2007). Despite being quite reliable in the open ocean, wave reanalyses can still exhibit systematic errors and thus consistently over or under predict wave parameters in coastal areas with respect to in-situ observations (Baordo et al., 2020; Bidlot et al., 2002; Lemos et al., 2020; Stopa and Cheung, 2014). Consequently, modelled outputs from wave reanalysis might not be directly applicable to coastal areas without previous validation and calibration (Hisaki, 2020; Kumar and Naseef, 2015; Shi et al., 2021).

To address this limitation, several bias correction methodologies (Aguiar et al., 2021; Haerter et al., 2011; Lemos et al., 2020; Maraun, 2016) and improved calibration methods (Caires and Sterl, 2005a, 2005b; Espejo et al., 2011; Mínguez et al., 2011; Neary et al., 2020; Tomas et al., 2008) have been developed to produce wave time series that better fit observations. Some authors focused on finding linear relationships between buoy and reanalysis data for the n-year return period (Caires and Sterl, 2005b; Neary et al., 2020; Sterl and Caires, 2005), others proposed spatial calibration that considers multiple observations (Tomas et al., 2008), while more recently a calibration that depends on mean wave direction was proposed (Espejo et al., 2011; Mínguez et al., 2011). At regional and local scales, downscaling has also been used to better resolve the physical processes and improve reanalysis accuracy (Bellotti et al., 2021; Vannucchi et al., 2021). However, this method does not correct systematic errors and instead propagates the errors of the global reanalyses (Bertotti et al., 2014), which are normally used as boundary conditions to force the downscaled local wave propagation models. Despite these

limitations, wave data from global reanalyses have been routinely and increasingly applied in coastal studies without validation and/or calibration (Almar et al., 2021b; Fernández-Montblanc et al., 2020; Kirezci et al., 2020; Marcos et al., 2019; Mentaschi et al., 2017; Nienhuis et al., 2020; Vousdoukas et al., 2016b, 2016a, 2020) due to their easiness of use and because measured data are often not available. The systematic errors of global reanalyses are often amplified for extreme values (Baordo et al., 2020; Cavaleri, 2009), resulting in greater under or over prediction (Campos and Soares, 2016; Stopa and Cheung, 2014) and potentially causing large errors and uncertainties in the determination of the return periods of extreme events (Morim et al., 2023; Neary et al., 2020), incorrectly estimating consequences and potentially misrepresenting coastal risks and influencing the subsequent coastal management decisions.

Aiming to improve the characterization of extreme wave conditions and associated return periods for coastal areas based on validated and calibrated global wave reanalysis data, this work evaluates ERA5 and WAVERYS reanalysis against a database of 326 coastal buoys. Results indicate a globally consistent underestimation of extreme wave conditions and associated return periods, which can be considerably reduced using a range of calibration approaches based on in-situ observations. To overcome data limitations in many coastal areas worldwide, a global calibration is proposed and shown to improve accuracy and reduce uncertainty in estimates of extreme wave conditions in coastal areas. The findings of this work provide an improved understanding of the limitations of global wave reanalyses and enhance their applicability around the world's coasts.

2.2 Materials and methods

Two of the most recent and advanced wave reanalyses were selected for evaluation: ERA5 (Hersbach et al., 2020), the latest reanalysis released by the European Centre for Medium-Range Weather Forecasts (ECMWF) with 0.5° resolution, and WAVERYS (Law-Chune et al., 2021), a 0.2° resolution reanalysis by the Copernicus Marine Environment Monitoring Service (CMEMS). The reanalyses have different resolutions, dissipation terms, and white capping terms. WAVERYS includes wave-current interactions but is not coupled with an atmospheric model like ERA5. Both reanalyses have been extensively validated against buoy and satellite data (e.g., Hisaki, 2020; Law-Chune et al., 2021; Shi et al., 2021; Stefanakos, 2019). In this

work, the calibration of H_s, T_m, T_p and Dir_m was performed for 326 buoys located in distinct coastal areas around the world (Supplementary Table 1).

2.2.1 Wave reanalysis data

ERA5 (Hersbach et al., 2020) is produced by the ECMWF, covers the period from 1950 to the present at hourly intervals, and it has improved spatial and temporal resolution and performance in comparison to its predecessors (ERA-40 and ERA-Interim) (Hersbach et al., 2020; Hoffmann et al., 2019). ERA5 provides records of the atmosphere, land surface, and ocean waves. The atmospheric model is coupled to WAM, a third-generation spectral WAve Model developed by the WAMDI Group (Group, 1988). ERA5 also assimilates H_s measured from satellites (ERS1, ERS2, SARAL, CryoSat2, Jason1, Envisat) into the predicted wave spectra (Hersbach et al., 2020). The ERA5 wave data are available from the Copernicus Climate Data Store (https://cds.climate.copernicus.eu/). For the present study, synthetic parameters, derived from the wave spectra, were used. The parameters considered are the H_s of combined wind waves and swell, T_p, T_m, and Dir_m.

WAVERYS is the first global wave reanalysis produced by CMEMS (Law-Chune et al., 2021) and released in December 2019. It has a spatial resolution of 0.2° and covers the period from 1993 to 2019 with a temporal resolution of 3 hours. WAVERYS is not coupled with an atmospheric model but includes the 3 hours surface currents from GLORYS12V1 (Lellouche et al., 2018) global physical reanalysis. The altimeter wave data from ERS1 until Sentinel-3A missions (Law-Chune et al., 2021) were assimilated into the model. WAVERYS is forced with the ERA5 10-m wind fields and the wave model used is MF-WAM version 4 implemented by Météo-France, which differs from the version used in ERA5 for the input and dissipation terms (Baordo et al., 2020).

For both reanalyses, the data from the cell closer to the mooring location of each buoy were considered, unless the location was beyond a radius of 0.099° (0.249°) for WAVERYS (ERA5). In those cases, the data from adjacent cells were interpolated using a weighted approach based on the distance between the buoy location and adjacent grid cells centre. Regardless of the use of weighted averages or the values for individual grid cells, it must be recognized that reanalysis data are estimates of the average conditions for entire grid cells (Caires et al., 2004). This has implications for the consistency between buoy and reanalysis data, not only because of the

spatial scale but also because the grid cell depth will not represent exactly the buoy depth. This may contribute to differences in wave parameters between wave reanalysis and coastal buoys, particularly as depth influences wave transformation. However, the improved resolution of both reanalysis datasets, the developments in model source terms and quality of bathymetric grids, as well as improved assimilation of a larger range of observations (Hersbach et al., 2020; Law-Chune et al., 2021), provides increased confidence that buoy datasets are spatially consistent with the reanalysis datasets. In addition, the buoy data were linearly interpolated to a 1-hour temporal resolution (as described below), and such averaging over time is considered to bring the temporal and spatial scales of buoy and reanalysis data closer together (Caires and Sterl, 2003).

2.2.2 Wave buoy data

Buoys are available for limited locations around the world, with the majority in the Northern Hemisphere, particularly in the North Pacific and North Atlantic, and large data gaps in the Southern Hemisphere (Data Buoy Cooperation Panel, 2018). In addition, buoy data are often discontinuous or cover only short periods, which makes the analysis of the return periods unfeasible in many locations (Neary et al., 2020). This work used buoy measurements to evaluate and calibrate the two wave reanalyses. The in-situ wave observations were extracted from the global network of buoys provided by the CMEMS, with product name INSITU_GLO_WAV_REP_OBSERVATIONS_013_045 (Copernicus Marine in situ TAC, 2022), supplemented by additional buoys sourced from hydrographic agencies for underrepresented areas. The CMEMS database includes 1489 buoys with information about latitude, longitude and time series of H_s and in some cases T_m, T_p and Dir_m, together with quality flags (from 0 to 9, more details in the product user manual (Loic et al., 2021)) for each parameter. In cases where only the 1D wave spectra were available, the synthetic parameters were computed from the spectral moments. The criteria for selecting coastal buoys from the database included: i) water depth, only buoys in water depths of less than 100 m were considered (water depth was estimated using the global GEBCO2022 bathymetry); and ii) record length, only buoys with more than one complete year of data and including the winter months were considered. Buoys in lagoonal areas, small enclosed basins, protected by headlands or around small islands (less than ~22 km in length, which is the spatial resolution of WAVERYS) were removed, as their setting is not properly resolved by the relatively coarse

resolution of global reanalyses. The buoys situated in coastal locations where both reanalyses had empty cells were also automatically excluded. All buoy records were inspected to remove spikes, quality control flags, flat lines, wrongly assigned variables and values outside the acceptance range (Bushnell, 2019). The criteria and filters used reduced the set of buoys considered in this study to 326 (Supplementary Table 1). The time series from the buoys were interpolated at 1-hour intervals to ensure consistency with model outputs and homogenise variable temporal resolutions (e.g., some buoys increase the sampling frequency to 30 minutes during storm events) or fill in missing records for data gaps of less than 6 hours. Gaps longer than 6 hours were excluded from the analysis. The records from the buoys ranged from 1 year to 42 years, with 83 buoys including more than 12 years of data. These 83 buoys were used for the estimation of return periods, as described below. The number of buoys used for comparison with WAVERYS and ERA5 differs depending on the presence of a reanalysis cell at the buoy location and on the temporal range of the reanalysis, as WAVERYS only covers the period from 1993 to 2019. Moreover, while 326 buoys have records for H_s, only 210 also recorded T_m, 270 T_p and 183 Dir_m.

2.2.3 Evaluation

The performance of wave reanalysis was evaluated against wave data (for H_s, T_m, T_p and Dir_m) from the in-situ buoy records for each of the selected coastal locations (Supplementary Table 2). Standard error metrics were used to evaluate the hourly time series, namely the Pearson's correlation coefficient (R), scatter index (SI), root mean square error (RMSE) and relative bias (bias):

$$R = \frac{\sum_{i=1}^{N}(M_i-\bar{M})(O_i-\bar{O})}{\sqrt{\sum_{i=1}^{N}(M_i-\bar{M})^2 \sum_{i=1}^{N}(O_i-\bar{O})^2}} \quad (2.1)$$

$$SI = \frac{\sqrt{\frac{1}{N}\sum_{i=1}^{N}[(O_i-\bar{O})-(M_i-\bar{M})]^2}}{\frac{1}{N}\sum_{i=1}^{N} O_i} \quad (2.2)$$

$$RMSE = \sqrt{\frac{1}{N}\sum_{i=1}^{N}(M_i - O_i)^2} \quad (2.3)$$

$$bias = \frac{\sum_{i=1}^{N}(M_i - O_i)}{\sum_{i=1}^{N} O_i} * 100 \quad (2.4)$$

Where O_i represents the observations, M_i the modelled data from the wave reanalysis and N is the number of measurements. The overbar refers to the mean. A negative (positive) bias represents an underestimation (overestimation) from the wave reanalysis. For the wave directions circular *R*, SI, RMSE and bias were estimated taking into consideration the fact that when comparing two angular variables in the sector from -90° to 90° the values ranging from 270° to 360° need to be corrected to -90° and 0°.

2.2.4 Calibration

2.2.4.1 Calibration for individual buoy locations

To calibrate the wave reanalysis (*y*) against the buoy observations (*x*) four transfer functions were tested to better represent the behaviour of wave data from buoys with different locations around the world. The functions were applied to H_s, T_m and T_p of each buoy. The selection of the best fit function was performed automatically by finding the fit that optimizes both the standard error metrics for the entire time series and for the extremes (i.e. the values above the 95th percentile). This was done by estimating the improvement obtained with each fit (in terms of *R*, RMSE, SI, mean absolute difference, and bias) and finding the fit that would optimize the most parameters (Supplementary Table 3). The transfer functions used were a first-degree polynomial without and with intercept (Eq. 2.5 and Eq. 2.6), a power function (Eq. 2.7), and a rotation around the mean (Eq. 2.8), from which Eq. 2.9 is derived:

$$y' = ay, \quad (2.5)$$

$$y' = ay + b, \quad (2.6)$$

$$y' = ay^b, \quad (2.7)$$

$$\begin{bmatrix} x' \\ y' \end{bmatrix} = \begin{bmatrix} \cos(1-a) & -\sin(1-a) \\ \sin(1-a) & \cos(1-a) \end{bmatrix} \begin{bmatrix} x - x_c \\ y - y_c \end{bmatrix}, \quad (2.8)$$

$$y' = sin\beta(x - x_c) + cos\beta(y - y_c),\ with\ \beta = (1 - a) \quad (2.9)$$

Linear regression methods, such as Eq. 2.5 and Eq. 2.6, have been widely used to correct modelled wave data against observations, and have been applied to the full H_s time series (Lemos et al., 2020), to the extreme H_s (Stephens and Gorman, 2006) or to correct the H_s associated with specific return periods (Caires and Sterl, 2005b; Neary et al., 2020; Sterl and Caires, 2005). Here, the equations are applied to the entire original reanalysis wave time series from WAVERYS and ERA5 to obtain a calibrated time series (y') and as a result, the bias is corrected. The power function has also been used in previous studies (Espejo et al., 2011; Lemos et al., 2020; Mínguez et al., 2011), with the correction parameters a and b varying with the direction of wave propagation. In this study, the parameters were instead constant variables for the entire time series. The rotation around the mean (x_c, y_c) was, to the authors' knowledge, applied here for the first time in wave data calibration. For this purpose, a rotation matrix was used (Eq. 2.8), which depends on the angular coefficient found through the first-degree polynomial fit with intercept. This method was deemed appropriate to correct both the underestimation of the higher H_s values from the reanalysis and the overestimation of the lower H_s values. The bias is not modified. The rotation matrix in Eq. 2.8 refers to a counterclockwise rotation, which corresponds to cases where the model underestimates the H_s compared to the observations. In case of overestimation, a clockwise rotation matrix is required, which can be obtained by changing the sign of both sines in Eq. 2.8.

For calibrating the wave directions, a different method was implemented. First, the wave roses from the buoys and from the reanalysis were compared visually. If differences between the observed and modelled wave direction distributions were observed, a calibration was performed. This was done by dividing wave direction data into 2, 3 or 4 sectors depending on the number of peaks present in the distribution. For each sector, the difference between the model and buoy averaged directions was determined and subtracted/added to the reanalysis data, according to the need to rotate each sector in a counterclockwise/clockwise direction.

2.2.4.2 Global calibration

A global calibration was implemented to improve the wave reanalyses time series where these are known to underestimate H_s and T_m, particularly above the 95th percentile of the wave height and period distributions. The buoys where reanalyses overestimate the extreme bias were excluded from the global calibration, as these locations correspond to areas of complex coastal configuration, poorly resolved in global wave reanalyses models. Such locations are found mainly in areas sheltered by islands (e.g., Hawaii, Azores, Sardinia), headlands (e.g., Cape Cod) or reefs (e.g., Great Barrier Reef), as well as in sections of enclosed basins (e.g., parts of the Baltic and North Sea), as global reanalysis models have known limitations in resolving sheltering effects (Cavaleri et al., 2018).

From the buoy datasets identified for the global calibration, 70% were randomly selected and used to derive the equations for the global calibration while the remaining 30% were used to independently validate the approach. A sensitivity analysis (Supplementary Figure S2.16, S2.17) was performed by selecting different percentages of buoys for the derivation of the equations and for the validation, as well as different random groups, which did not result in observable differences in the error statistics. After combining the data from the randomly selected buoys and calibrating ERA5 and WAVERYS reanalysis for those locations as a unique time series, Eq. 2.5, Eq. 2.6 and Eq. 2.7 were applied to find the best-fit calibration equations to be used globally to correct the underestimation of the H_s and T_m values above the 95th percentile. The equations found were then validated against the data from the remaining 30% of buoys.

2.2.5 Calculation of return periods

The calculation of the return periods of H_s was based on the Peak-Over Threshold method (Ferreira and Guedes-Soares, 1998) and a de-clustering algorithm to characterize extreme H_s events (Ferro and Segers, 2003), following the approach proposed by Oikonomou et al. (2020). Independently and identically distributed extreme value datasets were obtained by applying a threshold based on the 95th percentile value (Harley, 2017) of the H_s distribution and an independence criterion for separating consecutive events based on the extremal index calculation. Each extreme value dataset was then fitted to the Generalized Pareto Distribution

to determine the return periods of an extreme occurrence in H_s. This was performed for each location using the wave buoy data (for buoys with more than 12 years of complete data), the original, individually calibrated and globally calibrated reanalysis data.

2.3 Results

2.3.1 Overview

The evaluation of the ERA5 and WAVERYS reanalysis time series for significant wave height (H_s), mean wave period (T_m), peak wave period (T_p) and mean wave direction (Dir_m), was performed against data from 326 globally distributed coastal buoys using standard errors metrics (Eq. 2.1, Eq. 2.2, Eq. 2.3 and Eq. 2.4). Independent calibration of the wave reanalysis data for each individual buoy location was performed using four transfer functions, improving estimates of wave parameters in areas where in-situ data is available. Considering all the locations where a negative relative bias in extreme wave conditions was identified (94% of buoy locations for WAVERYS, 78% for ERA5) in the reanalyses as a single time series, the same transfer functions were applied to determine and validate a global calibration for extreme wave conditions (Eq. 2.5, Eq. 2.6, Eq. 2.7 and Eq. 2.8).

2.3.2 Evaluation of global wave reanalysis

When compared against the 326 coastal buoys, both reanalyses show a very strong correlation for H_s, with a mean Pearson correlation coefficient (R, Eq. 2.1) of 0.91 for WAVERYS and 0.90 for ERA5 (all R values reported are statistically significant for p-value < 0.01). Overall, WAVERYS performed better than ERA5, presenting higher or identical R coefficients for H_s, T_m, T_p and Dir_m (Supplementary Figure S2.5a,b). On average, the lower scatter index (SI, Eq. 2.2) for H_s, 22% for WAVERYS and 25% for ERA5, and smaller root mean square error (RMSE, Eq. 2.3), 0.33 m and 0.37 m respectively (Supplementary Figure S2.6a,b and S2.7a,b), confirm the improved performance of WAVERYS, reinforcing the findings of Law-Chune et al. (2021). Although the reanalyses display both negative and positive relative biases (Eq. 2.4) for H_s (Supplementary Figure S2.8a,b), there is a consistent underestimation of H_s in the upper quantiles, above the 95th percentile for over 95% of the buoy locations (Figure 2.1a,g for Belmullet in Ireland and Supplementary Figure S2.9a,b) and above the 99th percentile for 98%

of the 326 locations considered (Supplementary Figure S2.10a,b). Positive biases were found around islands (e.g., in the Azores, Canary Islands, Caribbean Islands and Taiwan) and channels (e.g., Strait of Gibraltar and English Channel), which evidences the limitations of global reanalyses to resolve the sheltering effects of small islands and complex coastal configurations. The relative bias computed using only data from the higher percentiles (>95th percentile) is negative for 94% (78%) of the buoy locations in WAVERYS (ERA5), with results indicating an average underprediction of -16% (-9%) in the two reanalyses (Figure 2.2a,b). Given the underestimation of the extreme wave heights, the resulting H_s 50-year return periods are underestimated on average by 1.11 m for WAVERYS and 0.80 m for ERA5 (Supplementary Figure S2.11a,b). Return periods were only determined for locations with more than 12 years of observations, which corresponds to 30% of the 326 buoys used for calculation of the error metrics. Underestimation is highest in enclosed basins or sheltered locations: specifically the Sea of Japan with deviations of 3.08 m for the H_s 50-year return period determined using WAVERYS; and coastal areas in South Korea and the Balearic Sea with 2.95 m deviation for ERA5 (Supplementary Figure S2.11a,b). Overall, the H_s value for the 50-year return period is underestimated in 89% (80%) of the locations considered for extreme value analysis in WAVERYS (ERA5).

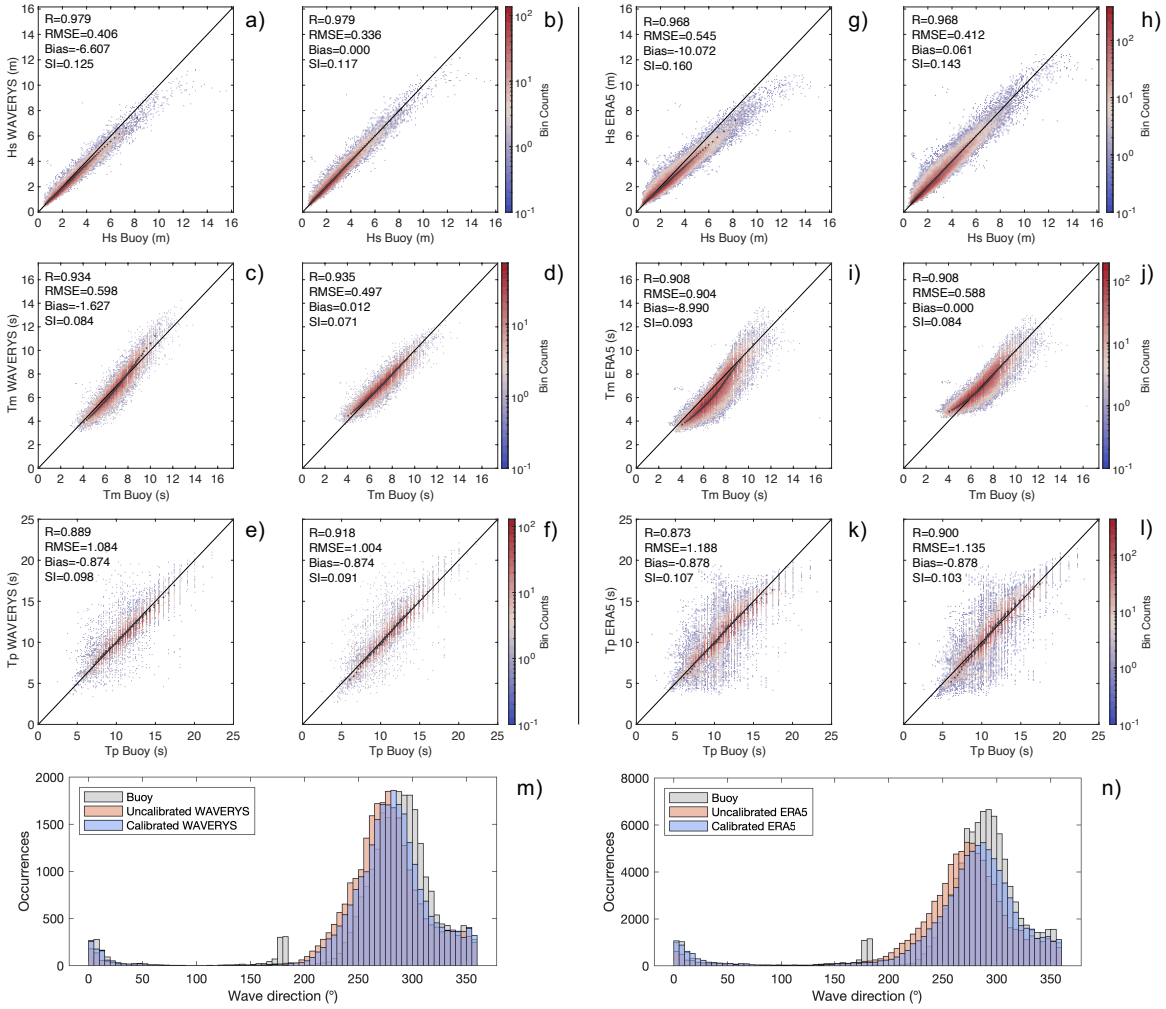

Figure 2.1 Example of original (a, c, e, g, i, k) wave parameters (H_s, T_m and T_p) and calibrated for individual buoy locations (b, d, f, h, j, l). Results shown for the Belmullet buoy location, in western Ireland, for WAVERYS (a, b, c, d, e, f) and ERA5 (g, h, i, j, k, l). Results for mean wave direction (in °) are shown for original (light red) and calibrated for individual buoy locations (light blue) for WAVERYS (m) and ERA5 (n) and compared to the buoy data (grey). The black dots indicate the percentiles (from 1st to 99th).

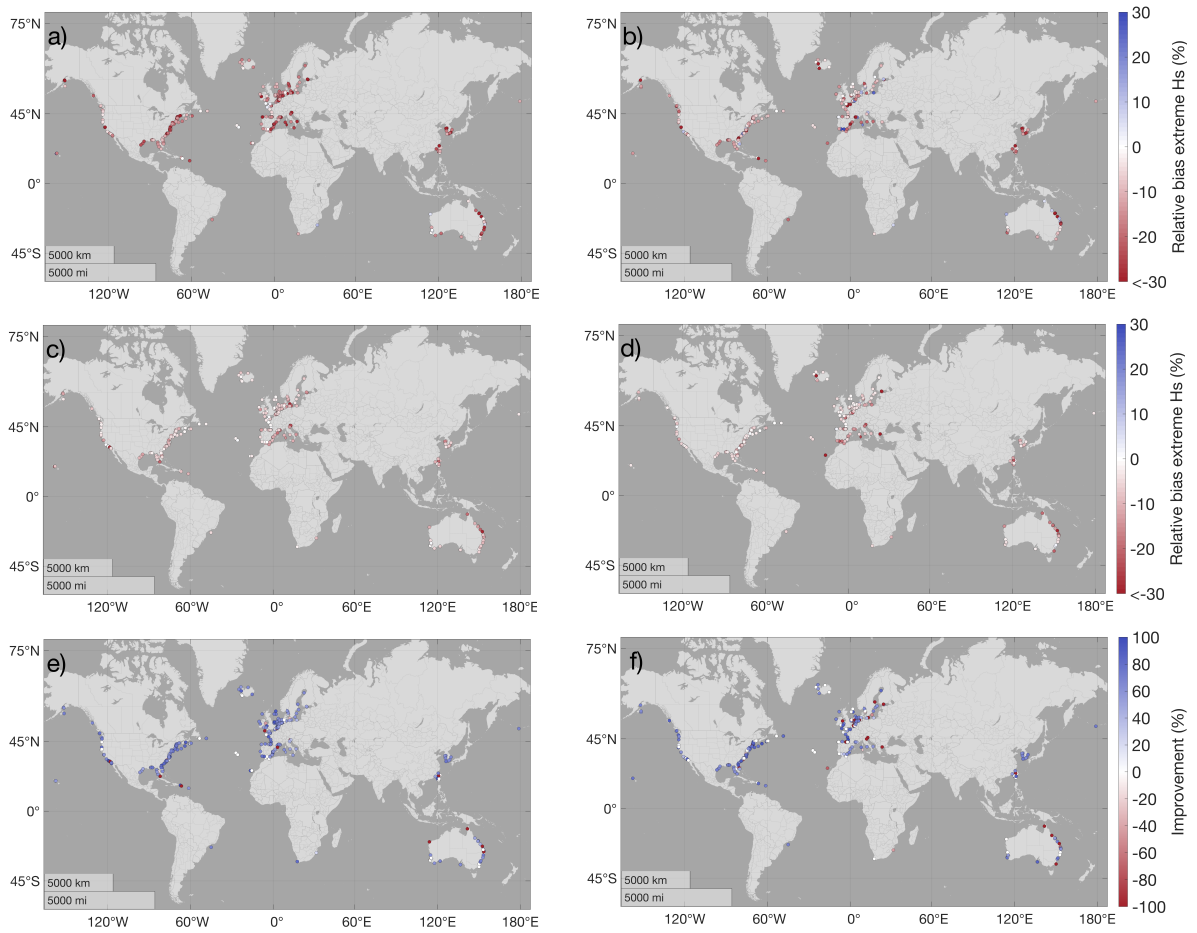

Figure 2.2 Global distribution of relative bias (in %) for extreme (above the 95th percentile) values of H_s between wave buoys and original reanalysis data (a-b), individual calibration (c-d) and percentual improvement obtained with the calibration (e-f) for WAVERYS (a, c, e) and ERA5 (b, d, f). Red (blue) values represent an underestimation (overestimation) from the reanalysis (in a, b, c, d).

Regarding T_m and T_p, results indicate strong correlation for both reanalyses, with an average R of 0.80 and 0.61 for WAVERYS and 0.79 and 0.59 for ERA5, respectively (Supplementary Figure S2.5c,d,e,f). Underestimation was generally observed for T_m, with higher values identified in ERA5 around islands and channels (Supplementary Figure S2.8c,d). The average relative bias for T_m is -9% (-13%) for WAVERYS (ERA5), increasing to -12% (-18%) when calculated for the data above the 95th percentile (Supplementary Figure S2.12a,b). The underestimation of T_p in both reanalyses is observed mostly in the higher percentiles (Supplementary Figure S2.12c,d). In fact, while the average relative bias for T_p is 1% (-1%) in WAVERYS (ERA5), it increases to -15% (-20%) when considering only the values above the 95th percentile, with both reanalyses showing underestimation for 95% of the buoy locations (Supplementary Figure S2.12c,d). This is reflected in the mean difference between buoy and

reanalysis data for the extreme T_m and T_p values (Supplementary Figure S2.9c,d,e,f and Supplementary Figure S2.10c,d,e,f). A total of 183 buoys incorporated in this analysis included directional information, allowing a comparison of Dir_m between buoy and reanalysis data. From the Dir_m histograms, the dominant wave regimes are well reproduced by both reanalyses, although with some deviation in directional peaks (Figure 2.1m,n). The average absolute difference between the circular mean direction of the buoys and the reanalyses is 17° (20°) for WAVERYS (ERA5), with the largest differences identified in the Azores islands, Strait of Gibraltar and areas of the Baltic sea (Supplementary Figure S2.13a,b). Overall, both reanalyses evidence a strong correlation of Dir_m with buoy data, with an average R of 0.64 (0.62) for WAVERYS (ERA5) (Supplementary Figure S2.5g,h). The highest R values (> 0.90) were obtained along the West coast of the USA and the North coast of the Netherlands, while the lowest were in sheltered locations in the Caribbean, Azores and Strait of Gibraltar ($R < 0.2$ for both reanalyses). The average RMSE of Dir_m was 40° (44°) for WAVERYS (ERA5), with the lowest performance in the same sheltered locations, where RMSE exceeds 80° (Supplementary Figure S2.6g,h). The relative bias for Dir_m is positive for 63% (61%) of buoy locations for WAVERYS (ERA5), indicating that reanalysis waves are dominantly biased in a counter-clockwise direction, with an average circular bias of less than 2° in both reanalyses (Supplementary Figure S2.8g,f). The deviations in Dir_m between buoy and reanalysis data are consistent in both reanalyses for 85% of the cases. These results highlight a similar performance between both reanalyses in terms of Dir_m with differences in buoy and reanalysis likely due to the complex interaction between wind-sea and swell components (Baordo et al., 2020) and coastal configuration.

2.3.3 Calibration of reanalyses for individual buoy locations

Depending on the method applied to calibrate the reanalysis data, different improvements between R and relative bias are achieved. When the first-degree polynomial (Eq. 2.5 and Eq. 2.6) is used, R is unmodified, and the bias is corrected. When rotation around the mean is applied instead (Eq. 2.8), the time series rotates and the bias remains the same, but R is improved. When a power function is used (Eq. 2.7), R remains identical while the bias is improved. Additionally, in a limited number of cases (1% to 15% depending on the model/variable considered), the original reanalysis data were already accurate, and no calibration was applied. In 71% of the cases, either a power function (Eq. 2.7) or rotation (Eq.

2.8) was applied to correct H_s in the reanalyses, with R improving by 34% (26%) for WAVERYS (ERA5) (Supplementary Figure S2.14a,b). For the locations that required bias correction (i.e., the reanalyses were corrected with a first-degree polynomial (Eq. 2.5 and Eq. 2.6) or a power function (Eq. 2.7)), changes in the relative bias resulted in an average improvement of 99% (97%) for WAVERYS (ERA5). SI and RMSE improved with all the calibration methods applied, with SI reduced on average by 18% for both reanalyses, while the RMSE for H_s improved by 18% (20%) for WAVERYS (ERA5) (Supplementary Figure S2.14a,b). The reanalysis time series for T_m were calibrated with a first-degree polynomial (Eq. 2.6) in 49% of the cases. The calibration of T_m resulted in a relative bias improvement of 86% (69%) for WAVERYS (ERA5). Calibration of T_p was performed using the rotation around the mean (Eq. 2.8) for 59% of the cases, with 15% not requiring calibration. Overall, T_p calibration contributed to an improvement of 36% (24%) in relative bias for WAVERYS (ERA5). It is important to note that in some cases the bias value in T_p is related to the presence of secondary swells with longer wave period, which are not correctly captured in either reanalysis. In terms of Dir_m, the difference in the circular mean computed between the buoys and the reanalyses was reduced from an average of 17° to 10° for WAVERYS and from 20° to 13° for ERA5. The relative bias decreased by approximately 21% (16%) on average for WAVERYS (ERA5), but no significant improvements were obtained for R, SI and RMSE. While no calibration of the directions was deemed necessary for 50% of the buoy locations, results obtained for the calibrated sites show considerable improvements (e.g., Belmullet, Figure 2.1m,n).

For extreme wave conditions, i.e. H_s above the 95th percentile, the calibration of H_s reduced the average underestimation by 0.30 m (0.15 m) for WAVERYS (ERA5) (Supplementary Figure S2.14b). When considering H_s above the 99th percentile, the calibration improves results further, with a reduction in the average underestimation of 0.45 m (0.22 m) for WAVERYS (ERA5) (Supplementary Figure S2.14). The relative bias for H_s values above the 95th percentile (Figure 2.2c,d) was reduced to -7% (-8%), which corresponds to an average improvement of 56% (36%) for WAVERYS (ERA5) (Figure 2.2e,f and Supplementary Figure S2.15a,b). The calibration for individual buoy locations allowed for relevant improvements in the H_s return period values, with differences in the 50-year return period estimated with buoy observations and with reanalysis data reduced by approximately 0.68 m (0.37 m) for WAVERYS (ERA5), corresponding to a 61% (46%) average improvement (Figure 2.3b and Figure 2.4a,b). This included areas like the southeast coast of Spain, where the underestimation of the 50-year return

period in WAVERYS was corrected by 2.5 m with the calibration for individual buoy locations. The underestimation of the relative bias for the extreme (above the 95th percentile) T_m (T_p) was reduced to -11 % (-12%) for both reanalyses, while the average underestimation of the extreme T_m (T_p) values was reduced to 0.8 s (1.5 s).

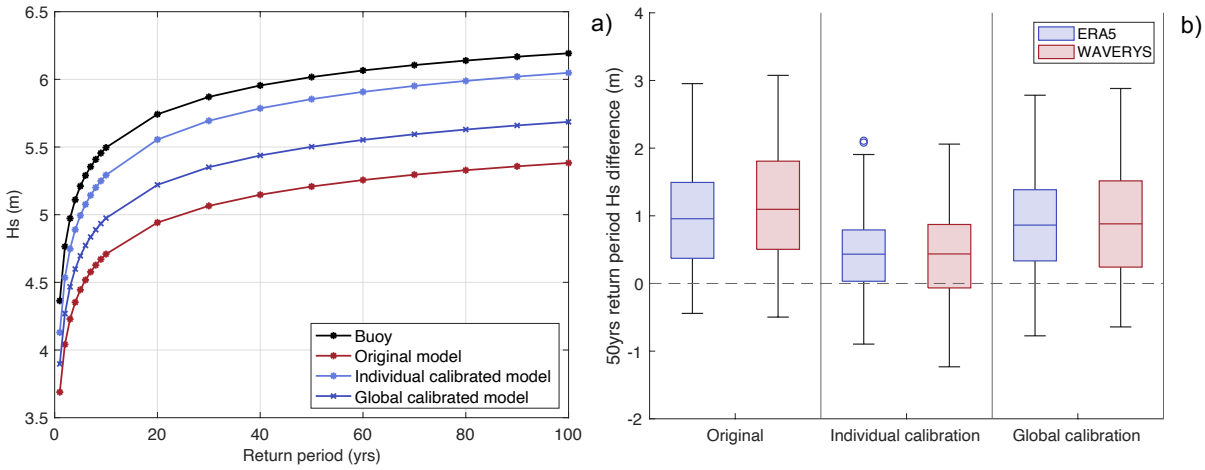

Figure 2.3 Effect of individual and global calibration on H_s 50-year return periods. a) Return period values for original WAVERYS reanalysis (red) and buoy data (black), and with the individual (light blue) and global (dark blue) calibration for the location in the coast of South Carolina, USA. b) Box plot of differences in H_s 50-years return period between buoy data (only buoys with negative relative bias for extreme H_s) and reanalysis data, estimated with the original reanalysis data, individual calibration, and global calibration for WAVERYS and ERA5. The bottom and top of each box plot are the 25th and 75th percentile, the line in the middle the median, the whiskers correspond to 99.3% of the data and the outliers are reported as circles.

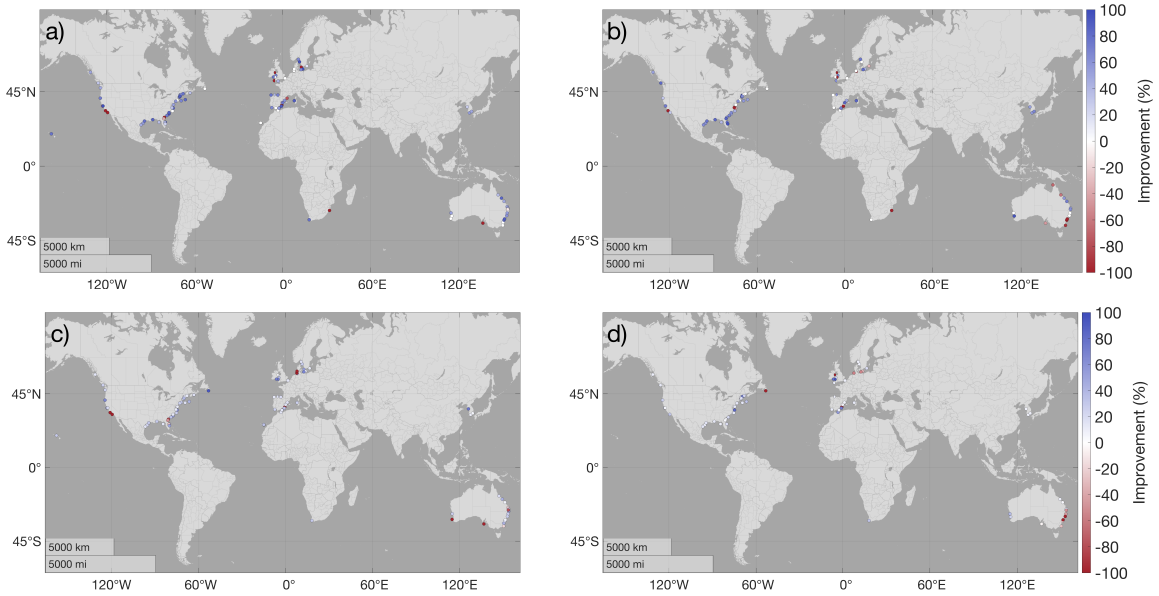

Figure 2.4 Global distribution of the relative improvement (in %) for the 50-year return period H_s calculated for the wave buoys and individual calibration (a-b) and global calibration (c-d) for WAVERYS (a-c) and ERA5 (b-d).

2.3.4 Global reanalysis calibration

Based on the common underestimation of H_s and T_m in both reanalyses for most coastal areas, a global calibration for each reanalysis dataset is proposed. The equations for the global calibration of H_s and T_m were determined by identifying the best-fit parameters considering the entire dataset as a unique time series, but excluding the data from buoys located in areas where extreme wave heights are overestimated by the reanalyses. These are areas where the extreme relative bias is positive (Figure 2.2a,b), and can be found in sheltered coasts and areas with complex coastal configurations, which represent 6% (22%) of buoy locations for WAVERYS (ERA5). For both reanalyses, a first-degree polynomial performed better for the global calibration of H_s, indicated by Eq. 2.10 for WAVERYS and Eq. 2.11 for ERA5, while a first-degree polynomial with intercept provided the best correction for T_m, shown in Eq. 2.12 for WAVERYS and Eq. 13 for ERA5. No calibration method provided a significant improvement for T_p, in the reanalysis datasets.

Based on the data from a group of randomly selected buoys (30% of the dataset) excluded from the global reanalysis calibration, a validation of the global calibration equations using the error metrics (detailed in Materials and Methods) was performed (Table 2.1). The mean difference between buoy observations and the globally calibrated reanalysis data for H_s values above the 95th percentile improved on average by 0.14 m (0.10 m) for WAVERYS (ERA5), while the

relative bias for H_s above the 95th percentile, was reduced to -12% (-11%) (Table 2.1). The averaged relative bias for extreme T_m was reduced by 4% (12%) for WAVERYS (ERA5), indicating that the underestimation was partially corrected. After applying the global calibration to all the buoy locations where a negative relative bias for extreme wave conditions was identified, the 50-years return period H_s values were corrected on average by 0.30 m (0.16 m) for WAVERYS (ERA5) (Figure 2.3b) and improvements in the overall return period estimates were observed in 90% (70%) of the locations for WAVERYS (ERA5) (Figure 2.4c,d).

$$H_{s_{CWYS}} = 1.077 * H_{s_{WYS}} \tag{2.10}$$

$$H_{s_{CERA5}} = 1.045 * H_{s_{ERA5}} \tag{2.11}$$

$$T_{m_{CWYS}} = 0.870 * T_{m_{WYS}} + 1.124 \tag{2.12}$$

$$T_{m_{CERA5}} = 0.928 * T_{m_{ERA5}} + 1.156 \tag{2.13}$$

Table 2.1 Error metrics for original and calibrated WAVERYS and ERA5 global wave reanalyses. Calibration results including the correlation coefficient R, relative bias of the values above the 95th percentile, mean differences for values above the 95th and 99th percentiles determined from the buoys and the original, individual and global calibrated reanalysis data, considering the randomly selected 70% of buoys used to find the global equations and the remaining 30% buoys used to validate the equations.

Significant Wave Height (m)								
Average of all buoys with extreme bias < 0	*R*		Relative Bias for H_s (T_m) > 95th percentile (%)		Mean difference for values >95th percentile		Mean difference for values >99th percentile	
	WAVERYS	ERA5	WAVERYS	ERA5	WAVERYS	ERA5	WAVERYS	ERA5
Original reanalysis	0.91	0.91	-17	-14	0.55	0.54	0.86	0.78
Individual Calibration	0.94	0.93	-7	-6	0.21	0.19	0.36	0.32
Global Calibration (30%)	0.91	0.90	-12	-11	0.41	0.44	0.65	0.72
Global Calibration (70%)	0.91	0.91	-12	-12	0.39	0.38	0.66	0.66
Mean Wave Period (s)								
Original reanalysis	0.80	0.80	-13	-20	0.92	1.61	1.25	2.13
Individual Calibration	0.83	0.87	-11	-11	0.83	0.87	1.24	1.28
Global Calibration (30%)	0.80	0.81	-9	-8	0.86	0.69	1.11	1.21
Global Calibration (70%)	0.80	0.80	-8	-9	0.68	0.76	1.10	1.18

2.4 Discussion

In the past decade, the performance of global reanalyses to estimate (hindcast) past wave conditions has improved significantly, and reanalysis data are now widely applied in different fields. They are highly reliable in the open ocean (Hersbach et al., 2020; Law-Chune et al., 2021; Stefanakos, 2019), while their inaccuracies have been increasingly reported in coastal areas (Cavaleri et al., 2018; Hisaki, 2020; Shi et al., 2021). Here, the evaluation of global reanalysis against data from 326 buoys distributed around the world's coasts allowed to determine that the higher-resolution WAVERYS reanalysis performed better than the more widely used ERA5 reanalysis. These results are consistent across most error metrics (R, RMSE, and SI) and for the most used wave parameters (H_s, T_m, T_p and Dir_m) in coastal areas. Law-Chune et al. (2021) also compared these reanalyses with buoy observations from the Copernicus Marine Service observations database, and although a different set of coastal buoys was considered (up to 200 m water depth), WAVERYS performed better than ERA5, regardless of from the coastal setting and geographical location of the buoys (Law-Chune et al., 2021). Spatially, lower SI values (Supplementary Figure S2.7a,b) are found on the north-eastern Pacific coast and larger SI, up to 30%, is observed in semi-enclosed regions such as the Mediterranean Sea (Law-Chune et al., 2021). In terms of wave direction, the mean differences for Dir_m are consistent with previous research (Law-Chune et al., 2021), with higher values found in enclosed basins and around small islands. So far, comparisons of the global performance of WAVERYS and ERA5 against coastal buoy observations are limited, but a recent regional assessment by Crespo et al. (2022) for the south-western Atlantic Ocean, an area underrepresented in terms of wave buoy data, also identified improved performance by WAVERYS for mean and extreme H_s.

The main contribution of this work is the detailed analysis of the errors in the estimation of extreme wave conditions in global wave reanalyses and the impact this has on the determination of return period values, which are fundamental for coastal risk analysis. A main finding is the overall underestimation of coastal H_s in global reanalyses, especially for extreme wave heights ($H_s > 95^{th}$ percentile), as highlighted by average negative biases of -16% (-9%) in WAVERYS (ERA5). Underestimation of extreme H_s in ERA5 based on comparison with buoy data was also found in Chinese waters (Shi et al., 2021), around Japan (Hisaki, 2020), and in the Mediterranean sea (Vannucchi et al., 2021; Kardakaris et al., 2021). Cases of extreme H_s

overestimation were identified for 6% (22%) of the buoy locations when compared to WAVERYS (ERA5). The overestimation in WAVERYS occurred mainly in coastal areas where the reanalysis resolution is insufficient to resolve nearshore wave changes across complex shelf bathymetries (in the presence of reefs, headlands, sheltering land), while ERA5 was found to overestimate extreme H_s for buoy locations that are closer to the coastline due to its coarser resolution. Previous work evidenced the overestimation of wave heights in ERA5 for locations in the Arabian Sea (Bruno et al., 2020), as well as its precursor ERA-Interim in several coastal locations around India (Haripriya et al., 2021; Kumar et al., 2020; Kumar and Naseef, 2015). However, no regional patterns were identified in the present study for overestimated values of H_s. Instead, such cases corresponded to very specific locations, often surrounded by cases of underestimation in extreme waves and most likely related to the limitations of coarse resolution global models to resolve local wave propagation and transformation.

Underestimation of T_m was also found in most coastal areas analysed, with an average relative bias of -9% (-13%) for WAVERYS (ERA5). T_m was overestimated in less than 10% of the buoy locations considered in both reanalyses, mostly coincident with the sites where H_s was also overestimated, and for very long wave periods (> 95th percentile). Overestimation of T_m in ERA5 is not uncommon and has been reported along the Chinese coast (Shi et al., 2021), Arabian Sea, Bay of Bengal (Muhammed Naseef and Sanil Kumar, 2020) and in the Mediterranean Sea (Vannucchi et al., 2021). T_p was also consistently underestimated by global reanalyses for 90% of the buoy locations and for conditions above the 95th percentile, with average relative biases of -15% (-20%) for WAVERYS (ERA5), confirming previous results for the North Indian Ocean (Muhammed Naseef and Sanil Kumar, 2020) and in the Greek seas (Kardakaris et al., 2021).

Assessments of the performance of global wave reanalysis rarely consider wave direction, mainly because in coastal areas the wave direction is highly dependent on the model resolution and the ability to simulate small scale processes (Vannucchi et al., 2021). However, accurately determining wave direction is extremely important for coastal studies related to sediment transport (Harley et al., 2017) and coastal erosion (Mortlock et al., 2017). Although the calibration of wave direction cannot be applied at a global scale and instead requires local buoy

data, application of a shift in the distribution of wave directions as demonstrated in this work, allows to improve the representation of the peaks in the directional distribution and achieve a better average direction in the reanalysis datasets (see Figure 2.1n,m as an example). Furthermore, WAVERYS and ERA5 present similar wave direction distributions, and this is likely due to the use of the same 2-minute ETOPO2 bathymetric grid and the fact that WAVERYS is forced with the ERA5 10-m wind conditions.

The systematic underestimation of wave parameters in the ERA reanalysis products developed by ECMWF is not new. It was reported for the previous reanalysis, ERA-Interim, when compared to buoy data from the National Data Buoy Centre in the USA (Stopa and Cheung, 2014), in the Atlantic coast of Spain and the Italian coast (Dentale et al., 2018). It is widely known that global wave models, such as WAM used by both WAVERYS and ERA5 in different versions, tend to underestimate extremes in H_s, and hence T_p (Cavaleri, 2009). This is mostly due to uncertainties in wind forcing (Baordo et al., 2020), but also because of limitations in the computation of various wave processes (bottom friction, wave breaking, island shadowing, and fetch length) (Cavaleri, 2009; Cavaleri et al., 2007). However, more than the numeric errors in reanalysis datasets, the potential risks associated with using model outputs for coastal applications that systematically under or overpredict wave conditions lay in the likely under or overestimation of the outcome. This includes assessments of wave energy and impact, erosional potential, flooding severity, amongst others. For example, deviations in the modelled H_s are propagated quadratically in terms of wave energy calculation (or linearly in the case of T_p). This is particularly relevant for extreme H_s conditions, as the higher percentiles are poorly estimated by wave models (Cavaleri, 2009).

Coastal hazard and risk assessments are often based on the definition of extreme values for different return periods (Ferreira et al., 2018). The widespread global underestimation of the wave parameters associated with a given return period based on original reanalysis data, highlighted in the results presented here for most coastal locations, will result in a potential minimisation of the hazard or risk level. Despite this limitation, global wave reanalyses have and continue to be widely used for coastal studies without calibration or without quantifying their uncertainties. The applications of uncalibrated reanalyses include analysis of wave climate (Bergsma et al., 2022; Kumar et al., 2020) and extreme events (Marcos et al., 2019; Mentaschi

et al., 2017), coastal wave energy assessments (Haripriya et al., 2021; Hemer et al., 2017; Sanil Kumar and Anoop, 2015), estimation of overtopping (Almar et al., 2021b), shoreline retreat (Vousdoukas et al., 2020) and coastal flooding (Kirezci et al., 2020). As the recognition of the limitations of global reanalyses increases, it becomes evident that it is fundamental to improve return period estimates from global reanalyses (Morim et al., 2023) to ensure the accurate definition of coastal hazards and risk analysis at local to global scales.

To minimize the underestimation that is common in global wave models, particularly for extreme conditions, different calibration techniques have been developed to correct wave reanalysis (Espejo et al., 2011; Lemos et al., 2020; Mínguez et al., 2011) or explicitly the extreme wave heights (Stephens and Gorman, 2006) and their return periods (Caires and Sterl, 2005b; Neary et al., 2020; Sterl and Caires, 2005). Although directional calibration techniques exist (Espejo et al., 2011; Mínguez et al., 2011) for H_s, the calibration of the direction itself, and the periods, have not been addressed. Underestimation of H_s extremes occurs randomly in wave models and not all extreme H_s values need correction (Caires and Sterl, 2005a). Thus, the application of simple parametric corrections can also lead to errors and uncertainties, since many complex factors influence the prediction of extreme events (Cavaleri, 2009). However, the results obtained by applying four different transfer functions to calibrate time series of wave parameters, demonstrated that it is possible to improve the estimation of extreme wave conditions by correcting the overall underestimation of H_s, T_m and T_p in reanalysis datasets. Substantial improvements were observed (Figure 2.3a and Figure 2.4a,b) in the estimation of the H_s values associated with long return periods (50 years), which are often used for hazard and risk assessments in coastal areas (Ferreira et al., 2018), demonstrating the importance of calibrating wave reanalyses before their use in coastal applications.

In ideal conditions, calibration should be performed against wave buoy data from a location close to the reanalysis grid node. This not only improves the reanalysis but allows extending, with higher accuracy, the often limited temporal coverage of wave buoy time series. Once a reanalysis is calibrated for a specific location, the results can be extended to adjacent areas with similar morphology and wave climate. However, when in-situ observations are not available, this work proposes a global calibration equation for H_s and T_m, to be applied in coastal areas where ERA5 and WAVERYS reanalyses are known to underestimate wave heights and mean

periods. This excludes locations with complex coastal configurations, sheltered by islands, headlands or reefs, as well as nearshore areas where shallow water processes cannot be properly captured by global coarse resolution reanalyses. In those cases, calibrated reanalysis could be used after downscaling with a regional wave model that better resolves the impacts of complex coastal configurations on wave propagation. Based on the validation performed with the buoys that were not included in the global calibration equations, the estimation of H_s for different return periods using the global calibration achieves improvements for 90% (70%) of the buoys compared to WAVERYS (ERA5), although the calibration for individual buoy locations allows a greater improvement. The main potential of the global equations proposed is their broader applicability when compared to the individual calibration, which require in-situ data to be applied. The underestimation of the widely used H_s 50-years return period was reduced on average by 25% (15%) for WAVERYS (ERA5). This allows more reliable results in any coastal engineering application that requires the use of return periods, whether for design purposes, coastal hazard and protection analysis or evaluation of wave energy devices. Although global calibration equations have the merit of being a simple method to correct wave reanalysis data, their use should consider the specific characteristics of the wave climate in the study areas. In areas where the overall H_s time series is commonly overestimated by global reanalyses, such as in extremely shallow or sheltered areas, the global equation would further increase the error (i.e. the overestimation). Future work can potentially explore the development of basin scale calibrations to be applied for areas where reanalyses have clear and distinct regional patterns. This would allow a regionally consistent calibration for those areas where a global calibration may not be suitable.

In conclusion, by comparing two of the most recent and widely used global wave reanalyses, WAVERYS and ERA5, with observations from 326 coastal buoys in different areas of the world, this work demonstrates that global reanalyses have important limitations in the determination of extreme wave parameters in coastal areas, including widely used return period estimates. This highlights the need to perform site specific validation and calibration before using wave reanalyses in coastal areas in order to reduce their uncertainties. Such limitations can be problematic, particularly when assessing coastal hazards and associated risks. To address this, this work proposes efficient and reproducible calibration approaches to improve wave reanalyses in coastal areas, either using site-specific observations where available, or globally derived approximations.

2.5 References

Aguiar, D.F., McInnes, K., Filho, E.M., Romeu, M.A.R., Fontoura, J.A.S., 2021. Extreme Wave Analysis Based on 31 years Data from WW3 Model: Study off Southern Brazilian Coast. An. Acad. Bras. Cienc. 93, 1–17. https://doi.org/10.1590/0001-3765202120190011

Almar, R., Ranasinghe, R., Bergsma, E.W.J., Diaz, H., Melet, A., Papa, F., Vousdoukas, M., Athanasiou, P., Dada, O., Almeida, L.P.M., Kestenare, E., 2021. A global analysis of extreme coastal water levels with implications for potential coastal overtopping. Nat. Commun. 12, 1–9. https://doi.org/10.1038/s41467-021-24008-9

Baordo, F., Clementi, E., Iovino, D., Masina, S., 2020. Intercomparison and assessement of wave models at global scale, CMCC Research Paper.

Bellotti, G., Franco, L., Cecioni, C., 2021. Regional Downscaling of Copernicus ERA5 Wave Data for Coastal Engineering Activities and Operational Coastal Services. Water 13, 859.

Bergsma, E.W.J., Almar, R., Anthony, E.J., Garlan, T., Kestenare, E., 2022. Waves variability along the world's continental shelves and coasts: monitoring opportunities from satellite Earth observation. Adv. Sp. Res. 69, 3236–3244. https://doi.org/10.1016/j.asr.2022.02.047

Bertotti, L., Cavaleri, L., Soret, A., Tolosana-Delgado, R., 2014. Performance of global and regional nested meteorological models. Cont. Shelf Res. 87, 17–27. https://doi.org/10.1016/j.csr.2013.12.013

Bidlot, J.R., Holmes, D.J., Wittmann, P.A., Lalbeharry, R., Chen, H.S., 2002. Intercomparison of the performance of operational ocean wave forecasting systems with buoy data. Weather Forecast. 17, 287–310. https://doi.org/10.1175/1520-0434(2002)017<0287:IOTPOO>2.0.CO;2

Bruno, M.F., Molfetta, M.G., Totaro, V., Mossa, M., 2020. Performance assessment of ERA5 wave data in a swell dominated region. J. Mar. Sci. Eng. 8. https://doi.org/10.3390/jmse8030214

Bushnell, 2019. Manual for Real-Time Quality Control of In-Situ Surface Wave Data: A Guide to Quality Control and Quality Assurance of In-Situ Surface Wave Observations Version 2.1. https://doi.org/10.25923/7yc5-vs69

Caires, S., Sterl, A., 2005a. A new nonparametric method to correct model data: Application to significant wave height from the ERA-40 re-analysis. J. Atmos. Ocean. Technol. 22, 443–459. https://doi.org/10.1175/JTECH1707.1

Caires, S., Sterl, A., 2005b. 100-Year Return Value Estimates for Ocean Wind Speed and Significant Wave Height from the ERA40 Data. J. Clim. 18. https://doi.org/10.1175/JCLI-3312.1

Caires, S., Sterl, A., 2003. Validation of ocean wind and wave data using triple collocation. J. Geophys. Res. Ocean. 108, 1–16. https://doi.org/10.1029/2002jc001491

Caires, S., Sterl, A., Bidlot, J.R., Graham, N., Swail, V., 2004. Intercomparison of different wind-wave reanalyses. J. Clim. 17, 1893–1913. https://doi.org/10.1175/1520-0442(2004)017<1893:IODWR>2.0.CO;2

Campos, R.M., Soares, C.G., 2016. Comparison and assessment of three wave hindcasts in the North Atlantic Ocean. J. Oper. Oceanogr. 9, 26–44. https://doi.org/10.1080/1755876X.2016.1200249

Cavaleri, L., 2009. Wave modeling-Missing the peaks. J. Phys. Oceanogr. 39, 2757–2778. https://doi.org/10.1175/2009JPO4067.1

Cavaleri, L., Abdalla, S., Benetazzo, A., Bertotti, L., Bidlot, J.R., Breivik, Ø., Carniel, S., Jensen, R.E., Portilla-Yandun, J., Rogers, W.E., Roland, A., Sanchez-Arcilla, A., Smith, J.M., Staneva, J., Toledo, Y., van Vledder, G.P., van der Westhuysen, A.J., 2018. Wave modelling in coastal and inner seas. Prog. Oceanogr. 167, 164–233. https://doi.org/10.1016/j.pocean.2018.03.010

Cavaleri, L., Alves, J.H.G.M., Ardhuin, F., Babanin, A., Banner, M., Belibassakis, K., Benoit, M., Donelan, M., Groeneweg, J., Herbers, T.H.C., Hwang, P., Janssen, P.A.E.M., Janssen, T., Lavrenov, I. V., Magne, R., Monbaliu, J., Onorato, M., Polnikov, V., Resio, D., Rogers, W.E., Sheremet, A., McKee Smith, J., Tolman, H.L., van Vledder, G., Wolf, J., Young, I., 2007. Wave modelling - The state of the art. Prog. Oceanogr. 75, 603–674. https://doi.org/10.1016/j.pocean.2007.05.005

Chawla, A., Spindler, D.M., Tolman, H.L., 2013. Validation of a thirty year wave hindcast using the Climate Forecast System Reanalysis winds. Ocean Model. 70, 189–206. https://doi.org/10.1016/j.ocemod.2012.07.005

Coco, G., Ciavola, P., 2017. Coastal storms: processes and impacts.

Copernicus Marine in situ TAC, 2022. Copernicus Marine In Situ - Global Ocean Wave Observations Reanalysis [WWW Document]. SEANOE. https://doi.org/10.17882/70345

Crespo, N.M., Silva, N.P. da, Palmeira, R.M. de J., Cardoso, A.A., Kaufmann, C.L.G., Lima, J.A.M., Andrioni, M., de Camargo, R., da Rocha, R.P., 2022. Western South Atlantic Climate Experiment (WeSACEx): extreme winds and waves over the Southeastern Brazilian sedimentary basins. Clim. Dyn. 60, 571–588. https://doi.org/10.1007/s00382-022-06340-y

Data Buoy Cooperation Panel, 2018. Global Data Buoy Observations, a DBCP Implementation Strategy.

Dee, D.P., Uppala, S.M., Simmons, A.J., Berrisford, P., Poli, P., Kobayashi, S., Andrae, U., Balmaseda, M.A., Balsamo, G., Bauer, P., Bechtold, P., Beljaars, A.C.M., van de Berg, L., Bidlot, J.R., Bormann, N., Delsol, C., Dragani, R., Fuentes, M., Geer, A.J., Haimberger, L., Healy, S.B., Hersbach, H., Hólm, E. V., Isaksen, L., Kållberg, P., Köhler, M., Matricardi, M., Mcnally, A.P., Monge-Sanz, B.M., Morcrette, J.J., Park, B.K., Peubey, C., de Rosnay, P., Tavolato, C., Thépaut, J.N., Vitart, F., 2011. The ERA-Interim reanalysis: Configuration and performance of the data assimilation system. Q. J. R. Meteorol. Soc. 137, 553–597. https://doi.org/10.1002/qj.828

Dentale, F., Furcolo, P., Carratelli, E.P., Reale, F., Contestabile, P., Tomasicchio, G.R., 2018. Extremewave analysis by integrating model and wave buoy data. Water (Switzerland) 10, 1–15. https://doi.org/10.3390/w10040373

Espejo, A., Mínguez, R., Tomás, A., Menéndez, M., Méndez, F.J., Losada, I.J., 2011. Directional calibrated wind and wave reanalysis databases using instrumental data for optimal design of off-shore wind farms, in: OCEANS 2011 IEEE - Spain. pp. 1–9. https://doi.org/10.1109/Oceans-Spain.2011.6003592

Feng, H., Vandemark, D., Quilfen, Y., Chapron, B., Beckley, B., 2006. Assessment of wind-forcing impact on a global wind-wave model using the TOPEX altimeter. Ocean Eng. 33, 1431–1461. https://doi.org/10.1016/j.oceaneng.2005.10.015

Fernández-Montblanc, T., Vousdoukas, M.I., Mentaschi, L., Ciavola, P., 2020. A Pan-

European high resolution storm surge hindcast. Environ. Int. 135. https://doi.org/10.1016/j.envint.2019.105367

Ferreira, J.A., Guedes-Soares, C., 1998. An application of the peaks over threshold method to predict extremes of significant wave height. J. Offshore Mech. Arct. Eng. 120, 165–176. https://doi.org/10.1115/1.2829537

Ferreira, Ó., Viavattene, C., Jiménez, J.A., Bolle, A., das Neves, L., Plomaritis, T.A., McCall, R.T., van Dongeren, A.R., 2018. Storm-induced risk assessment: Evaluation of two tools at the regional and hotspot scale. Coast. Eng. 134, 241–253. https://doi.org/10.1016/j.coastaleng.2017.10.005

Ferro, C.A.T., Segers, J., 2003. Inference for clusters of extreme values. J. R. Stat. Soc. Ser. B Stat. Methodol. 65, 545–556. https://doi.org/10.1111/1467-9868.00401

Gemmrich, J., Thomas, B., Bouchard, R., 2011. Observational changes and trends in northeast Pacific wave records. Geophys. Res. Lett. 38, 1–5. https://doi.org/10.1029/2011GL049518

Group, T.W., 1988. The WAM Model - A Third Generation Ocean Wave Prediction Model. J. Phys. Oceanogr. 18, 1775–1810.

Guillou, N., Lavidas, G., Chapalain, G., 2020. Wave energy resource assessment for exploitation-A review. J. Mar. Sci. Eng. 8. https://doi.org/10.3390/JMSE8090705

Haerter, J.O., Hagemann, S., Moseley, C., Piani, C., 2011. Climate model bias correction and the role of timescales. Hydrol. Earth Syst. Sci. 15, 1065–1079. https://doi.org/10.5194/hess-15-1065-2011

Haripriya, R., Misra, A., Jeyaraj, S., Ramakrishnan, B., 2021. Wave energy assessment for 39 years along the Exclusive Economic Zone (EEZ) of India. Reg. Stud. Mar. Sci. 45, 101809. https://doi.org/10.1016/j.rsma.2021.101809

Harley, M.D., 2017. Coastal Storm Definition, in: Coastal Storms: Processes and Impacts. pp. 1–21.

Harley, M.D., Turner, I.L., Kinsela, M.A., Middleton, J.H., Mumford, P.J., Splinter, K.D., Phillips, M.S., Simmons, J.A., Hanslow, D.J., Short, A.D., 2017. Extreme coastal erosion enhanced by anomalous extratropical storm wave direction. Sci. Rep. 7, 1–9. https://doi.org/10.1038/s41598-017-05792-1

Hemer, M.A., Zieger, S., Durrant, T., O'Grady, J., Hoeke, R.K., McInnes, K.L., Rosebrock, U., 2017. A revised assessment of Australia's national wave energy resource. Renew. Energy 114, 85–107. https://doi.org/10.1016/j.renene.2016.08.039

Hersbach, H., Bell, B., Berrisford, P., Biavati, G., Horányi, A., Muñoz Sabater, J., Nicolas, J., Peubey, C., Radu, R., Rozum, I., Schepers, D., Simmons, A., Soci, C., Dee, D.P., Thépaut, J.-N., 2018. ERA5 hourly data on single levels from 1979 to present [WWW Document]. Copernicus Clim. Chang. Serv. Clim. Data Store. https://doi.org/10.24381/cds.adbb2d47

Hersbach, H., Bell, B., Berrisford, P., Hirahara, S., Horányi, A., Muñoz-Sabater, J., Nicolas, J., Peubey, C., Radu, R., Schepers, D., Simmons, A., Soci, C., Abdalla, S., Abellan, X., Balsamo, G., Bechtold, P., Biavati, G., Bidlot, J.R., Bonavita, M., De Chiara, G., Dahlgren, P., Dee, D.P., Diamantakis, M., Dragani, R., Flemming, J., Forbes, R., Fuentes, M., Geer, A., Haimberger, L., Healy, S., Hogan, R.J., Hólm, E., Janisková, M., Keeley, S., Laloyaux, P., Lopez, P., Lupu, C., Radnoti, G., de Rosnay, P., Rozum, I., Vamborg, F., Villaume, S., Thépaut, J.N., 2020. The ERA5 global reanalysis. Q. J. R. Meteorol. Soc. 146, 1999–2049. https://doi.org/10.1002/qj.3803

Hersbach, H., Bell, B., Berrisford, P., Horányi, A., Sabater, J.M., Nicolas, J., Radu, R., Schepers, D., Simmons, A., Soci, C., Dee, D.P., 2019. Global reanalysis: goodbye ERA-Interim, hello ERA5. ECMWF Newsl. 17–24. https://doi.org/10.21957/vf291hehd7

Hisaki, Y., 2020. Intercomparison of assimilated coastal wave data in the Northwestern Pacific Area. J. Mar. Sci. Eng. 8. https://doi.org/10.3390/JMSE8080579

Hoffmann, L., Günther, G., Li, D., Stein, O., Wu, X., Griessbach, S., Heng, Y., Konopka, P., Müller, R., Vogel, B., Wright, J.S., 2019. From ERA-Interim to ERA5: The considerable impact of ECMWF's next-generation reanalysis on Lagrangian transport simulations. Atmos. Chem. Phys. 19, 3097–3214. https://doi.org/10.5194/acp-19-3097-2019

Houser, C., Hapke, C., Hamilton, S., 2008. Controls on coastal dune morphology, shoreline erosion and barrier island response to extreme storms. Geomorphology 100, 223–240. https://doi.org/10.1016/j.geomorph.2007.12.007

Janssen, P.A.E.M., Abdalla, S., Hersbach, H., Bidlot, J.R., 2007. Error estimation of buoy, satellite, and model wave height data. J. Atmos. Ocean. Technol. 24, 1665–1677. https://doi.org/10.1175/JTECH2069.1

Kardakaris, K., Boufidi, I., Soukissian, T., 2021. Offshore wind and wave energy complementarity in the greek seas based on ERA5 data. Atmosphere (Basel). 12, 1–17. https://doi.org/10.3390/atmos12101360

Kirezci, E., Young, I.R., Ranasinghe, R., Muis, S., Nicholls, R.J., Lincke, D., Hinkel, J., 2020. Projections of global-scale extreme sea levels and resulting episodic coastal flooding over the 21st Century. Sci. Rep. 10, 1–12. https://doi.org/10.1038/s41598-020-67736-6

Kumar, V.S., George, J., Joseph, D., 2020. Hourly maximum individual wave height in the Indian shelf seas—its spatial and temporal variations in the recent 40 years. Ocean Dyn. 70, 1283–1302. https://doi.org/10.1007/s10236-020-01395-z

Kumar, V.S., Naseef, T.M., 2015. Performance of ERA-interim wave data in the nearshore waters around India. J. Atmos. Ocean. Technol. 32, 1257–1269. https://doi.org/10.1175/JTECH-D-14-00153.1

Law-Chune, S., Aouf, L., Dalphinet, A., Levier, B., Drillet, Y., Drevillon, M., 2021. WAVERYS: a CMEMS global wave reanalysis during the altimetry period. Ocean Dyn. 71, 357–378. https://doi.org/10.1007/s10236-020-01433-w

Leaman, C.K., Harley, M.D., Splinter, K.D., Thran, M.C., Kinsela, M.A., Turner, I.L., 2021. A storm hazard matrix combining coastal flooding and beach erosion. Coast. Eng. 170, 104001. https://doi.org/10.1016/j.coastaleng.2021.104001

Lellouche, J.M., Greiner, E., Le Galloudec, O., Garric, G., Regnier, C., Drevillon, M., Benkiran, M., Testut, C.E., Bourdalle-Badie, R., Gasparin, F., Hernandez, O., Levier, B., Drillet, Y., Remy, E., Le Traon, P.Y., 2018. Recent updates to the Copernicus Marine Service global ocean monitoring and forecasting real-time 1/12° high-resolution system. Ocean Sci. 14, 1093–1126. https://doi.org/10.5194/os-14-1093-2018

Lemos, G., Menendez, M., Semedo, A., Camus, P., Hemer, M., Dobrynin, M., Miranda, P.M.A., 2020. On the need of bias correction methods for wave climate projections. Glob. Planet. Change 186, 103109. https://doi.org/10.1016/j.gloplacha.2019.103109

Lobeto, H., Menendez, M., Losada, I.J., 2021. Future behavior of wind wave extremes due to climate change. Sci. Rep. 11, 1–12. https://doi.org/10.1038/s41598-021-86524-4

Loic, P.D.L.V., Marta, de A., Fernando, M.-M., Sylvie, P., 2021. Product user manual. For

REProcessed IN SITU product (WAVES). CMEMS-INS-PUM-013-045. https://doi.org/https://doi.org/10.13155/54853

Maraun, D., 2016. Bias Correcting Climate Change Simulations - a Critical Review. Curr. Clim. Chang. Reports 2, 211–220. https://doi.org/10.1007/s40641-016-0050-x

Marcos, M., Rohmer, J., Vousdoukas, M.I., Mentaschi, L., Le Cozannet, G., Amores, A., 2019. Increased Extreme Coastal Water Levels Due to the Combined Action of Storm Surges and Wind Waves. Geophys. Res. Lett. 46, 4356–4364. https://doi.org/10.1029/2019GL082599

Mentaschi, L., Vousdoukas, M.I., Voukouvalas, E., Dosio, A., Feyen, L., 2017. Global changes of extreme coastal wave energy fluxes triggered by intensified teleconnection patterns. Geophys. Res. Lett. 44, 2416–2426. https://doi.org/10.1002/2016GL072488.Received

Meucci, A., Young, I.R., Hemer, M., Kirezci, E., Ranasinghe, R., 2020. Projected 21st century changes in extreme wind-wave events. Sci. Adv. 6. https://doi.org/10.1126/sciadv.aaz7295

Mínguez, R., Espejo, A., Tomás, A., Méndez, F.J., Losada, I.J., 2011. Directional calibration of wave reanalysis databases using instrumental data. J. Atmos. Ocean. Technol. 28, 1466–1485. https://doi.org/10.1175/JTECH-D-11-00008.1

Morim, J., Wahl, T., Vitousek, S., Santamaria-aguilar, S., Young, I., Hemer, M., 2023. Understanding uncertainties in contemporary and future extreme wave events for broad-scale impact and adaptation planning. Sci. Adv. 9, 1–13. https://doi.org/10.1126/sciadv.ade3170

Mortlock, T.R., Goodwin, I.D., McAneney, J.K., Roche, K., 2017. The June 2016 Australian East Coast Low: Importance of wave direction for coastal erosion assessment. Water 9, 1–22. https://doi.org/10.3390/w9020121

Morton, R.A., Sallenger, A.H., 2003. Morphological impacts of extreme storms on sandy beaches and barriers. J. Coast. Res. 19, 560–573.

Muhammed Naseef, T., Sanil Kumar, V., 2020. Climatology and trends of the Indian Ocean surface waves based on 39-year long ERA5 reanalysis data. Int. J. Climatol. 40, 979–1006. https://doi.org/10.1002/joc.6251

Muis, S., Apecechea, M.I., Dullaart, J., de Lima Rego, J., Madsen, K.S., Su, J., Yan, K., Verlaan, M., 2020. A high-resolution global dataset of extreme sea levels, tides, and storm surges, including future projections. Front. Mar. Sci. 7, 1–15. https://doi.org/10.3389/fmars.2020.00263

Muis, S., Verlaan, M., Winsemius, H.C., Aerts, J.C.J.H., Ward, P.J., 2016. A global reanalysis of storm surges and extreme sea levels. Nat. Commun. 7. https://doi.org/10.1038/ncomms11969

Neary, V.S., Ahn, S., Seng, B.E., Allahdadi, M.N., Wang, T., Yang, Z., He, R., 2020. Characterization of Extreme Wave Conditions for Wave Energy Converter Design and Project Risk Assessment. J. Mar. Sci. Eng. 8, 1–19. https://doi.org/10.3390/JMSE8040289

Neumann, B., Vafeidis, A.T., Zimmermann, J., Nicholls, R.J., 2015. Future coastal population growth and exposure to sea-level rise and coastal flooding - A global assessment. PLoS One 10. https://doi.org/10.1371/journal.pone.0118571

Nienhuis, J.H., Ashton, A.D., Edmonds, D.A., Hoitink, A.J.F., Kettner, A.J., Rowland, J.C., Törnqvist, T.E., 2020. Global-scale human impact on delta morphology has led to net land

area gain. Nature 577, 514–518. https://doi.org/10.1038/s41586-019-1905-9

Oikonomou, C.L.G., Gradowski, M., Kalogeri, C., Sarmento, A.J.N.A., 2020. On defining storm intervals: Extreme wave analysis using extremal index inferencing of the run length parameter. Ocean Eng. 217. https://doi.org/10.1016/j.oceaneng.2020.107988

Perez, J., Menendez, M., Losada, I.J., 2017. GOW2: A global wave hindcast for coastal applications. Coast. Eng. 124, 1–11. https://doi.org/10.1016/j.coastaleng.2017.03.005

Sanil Kumar, V., Anoop, T.R., 2015. Wave energy resource assessment for the Indian shelf seas. Renew. Energy 76, 212–219. https://doi.org/10.1016/j.renene.2014.11.034

Sharmar, V., Markina, M., 2020. Validation of global wind wave hindcasts using ERA5, MERRA2, ERA-Interim and CFSRv2 reanalyzes. IOP Conf. Ser. Earth Environ. Sci. 606. https://doi.org/10.1088/1755-1315/606/1/012056

Shi, H., Cao, X., Li, Q., Li, D., Sun, J., You, Z., Sun, Q., 2021. Evaluating the Accuracy of ERA5 Wave Reanalysis in the Water Around China. J. Ocean Univ. China 20, 1–9. https://doi.org/10.1007/s11802-021-4496-7

Stefanakos, C., 2019. Intercomparison of wave reanalysis based on ERA5 and WW3 databases. Proc. Int. Offshore Polar Eng. Conf. 3, 2506–2512.

Stephens, S.A., Gorman, R.M., 2006. Extreme wave predictions around New Zealand from hindcast data. New Zeal. J. Mar. Freshw. Res. 40, 399–411. https://doi.org/10.1080/00288330.2006.9517431

Sterl, A., Caires, S., 2005. Climatology, variability and extrema of ocean waves: The web-based KNMI/ERA-40 wave atlas. Int. J. Climatol. 25, 963–977. https://doi.org/10.1002/joc.1175

Stopa, J.E., Cheung, K.F., 2014. Intercomparison of wind and wave data from the ECMWF Reanalysis Interim and the NCEP Climate Forecast System Reanalysis. Ocean Model. 75, 65–83. https://doi.org/10.1016/j.ocemod.2013.12.006

Tomas, A., Mendez, F.J., Losada, I.J., 2008. A method for spatial calibration of wave hindcast data bases. Cont. Shelf Res. 28, 391–398. https://doi.org/10.1016/j.csr.2007.09.009

Uppala, S.M., Kållberg, P.W., Simmons, A.J., Andrae, U., da Costa Bechtold, V., Fiorino, M., Gibson, J.K., Haseler, J., Hernandez, A., Kelly, G.A., Li, X., Onogi, K., Saarinen, S., Sokka, N., Allan, R.P., Andersson, E., Arpe, K., Balmaseda, M.A., Beljaars, A.C.M., van de Berg, L., Bidlot, J.R., Bormann, N., Caires, S., Chevallier, F., Dethof, A., Dragosavac, M., Fisher, M., Fuentes, M., Hagemann, S., Hólm, E., Hoskins, B.J., Isaksen, L., Janssen, P.A.E.M., Jenne, R., McNally, A.P., Mahfouf, J.F., Morcrette, J.J., Rayner, N.A., Saunders, R.W., Simon, P., Sterl, A., Trenberth, K.E., Untch, A., Vasiljevic, D., Viterbo, P., Woollen, J., 2005. The ERA-40 re-analysis. Q. J. R. Meteorol. Soc. 131, 2961–3012. https://doi.org/10.1256/qj.04.176

van Dongeren, A.R., Ciavola, P., Martinez, G., Viavattene, C., Bogaard, T., Ferreira, Ó., Higgins, R., McCall, R.T., 2018. Introduction to RISC-KIT: Resilience-increasing strategies for coasts. Coast. Eng. 134, 2–9. https://doi.org/10.1016/j.coastaleng.2017.10.007

Vannucchi, V., Taddei, S., Capecchi, V., Bendoni, M., Brandini, C., 2021. Dynamical downscaling of era5 data on the north-western mediterranean sea: From atmosphere to high-resolution coastal wave climate. J. Mar. Sci. Eng. 9, 1–29. https://doi.org/10.3390/jmse9020208

Vignudelli, S., Birol, F., Benveniste, J., Fu, L.L., Picot, N., Raynal, M., Roinard, H., 2019.

Satellite Altimetry Measurements of Sea Level in the Coastal Zone, Surveys in Geophysics. Springer Netherlands. https://doi.org/10.1007/s10712-019-09569-1

Vitousek, S., Barnard, P.L., Fletcher, C.H., Frazer, N., Erikson, L., Storlazzi, C.D., 2017. Doubling of coastal flooding frequency within decades due to sea-level rise. Sci. Rep. 7, 1–9. https://doi.org/10.1038/s41598-017-01362-7

Vousdoukas, M.I., Mentaschi, L., Voukouvalas, E., Verlaan, M., Jevrejeva, S., Jackson, L.P., Feyen, L., 2018. Global probabilistic projections of extreme sea levels show intensification of coastal flood hazard. Nat. Commun. 9, 1–12. https://doi.org/10.1038/s41467-018-04692-w

Vousdoukas, M.I., Ranasinghe, R., Mentaschi, L., Plomaritis, T.A., Athanasiou, P., Luijendijk, A., Feyen, L., 2020. Sandy coastlines under threat of erosion. Nat. Clim. Chang. 10, 260–263. https://doi.org/10.1038/s41558-020-0697-0

Vousdoukas, M.I., Voukouvalas, E., Annunziato, A., Giardino, A., Feyen, L., 2016a. Projections of extreme storm surge levels along Europe. Clim. Dyn. 47, 3171–3190. https://doi.org/10.1007/s00382-016-3019-5

Vousdoukas, M.I., Voukouvalas, E., Mentaschi, L., Dottori, F., Giardino, A., Bouziotas, D., Bianchi, A., Salamon, P., Feyen, L., 2016b. Developments in large-scale coastal flood hazard mapping. Nat. Hazards Earth Syst. Sci. Discuss. 0, 1–24. https://doi.org/10.5194/nhess-2016-124

Wang, J., Wang, Y., 2021. Evaluation of the ERA5 Significant Wave Height against NDBC Buoy Data from 1979 to 2019. Mar. Geod. 1–15. https://doi.org/10.1080/01490419.2021.2011502

Wesselman, D., de Winter, R.C., Engelstad, A., McCall, R.T., van Dongeren, A.R., Hoekstra, P., Oost, A., van der Vegt, M., 2018. The effect of tides and storms on the sediment transport across a Dutch barrier island. Earth Surf. Process. Landforms 43, 579–592. https://doi.org/10.1002/esp.4235

2.6 Data availability

The ERA5 data were provided by ECMWF and downloaded from the Copernicus Climate Change Service Climate Data Store (https://cds.climate.copernicus.eu) dataset “ERA5 hourly data on single levels from 1979 to present”. The WAVERYS data were downloaded from the CMEMS Portal (https://resources.marine.copernicus.eu) dataset “GLOBAL_REANALYSIS_WAV_001_032”. Wave buoy data were retrieved from the “INSITU_GLO_WAVE_REP_OBSERVATIONS_013_045” dataset distributed by CMEMS (https://doi.org/10.48670/moi-00022 and https://doi.org/10.17882/70345); the Portuguese Hydrographic Institute (IH, https://www.hidrografico.pt); the EMODnet-Physics portal (https://map.emodnet-physics.eu) with the data originators being the Rijkswaterstaat Ministry of Infrastructure and Water Management and the German Federal Maritime and Hydrographic Agency (BSH); the NOAA’s National Data Buoy Center (NDBC, https://www.ndbc.noaa.gov);

the Queensland Government Open Data Portal (https://www.data.qld.gov.au/dataset); the UK's Centre for Environment Fisheries and Aquaculture Science (CEFAS) WaveNet (https://wavenet.cefas.co.uk/map, © Crown copyright, 2022); the TRANSNET & African Council for Scientific and Industrial Research (http://wavenet.csir.co.za/), collected on behalf of the Transnet National Port Authority (TNPA); the Irish Marine Institute (http://www.marine.ie/Home/site-area/data-services/real-time-observations/wave-buoys); the Italian Data Buoy Network (RON, http://dati.isprambiente.it/id/website/ronRmn).

2.7 Code availability

The custom MATLAB code written for the calibration of wave reanalysis is publicly available at https://github.com/ValeriaFanti93/Wave-Reanalysis-Calibration.git or via a request to the corresponding author.

2.8 Acknowledgments

Valeria Fanti and Vincent Kümmerer are funded through the FCT PhD Research Scholarships program (ref. 2020.07553.BD and 2020.07497.BD, respectively). This work was supported by the Portuguese Foundation of Science, under the projects LA/P/0069/2020 (granted to the Associate Laboratory ARNET) and UIDP/00350/2020 CIMA. Access to the wave datasets used in this study was kindly provided by several institutions, as detailed in the data availability statement.

2.9 Appendix A. Supplementary figures

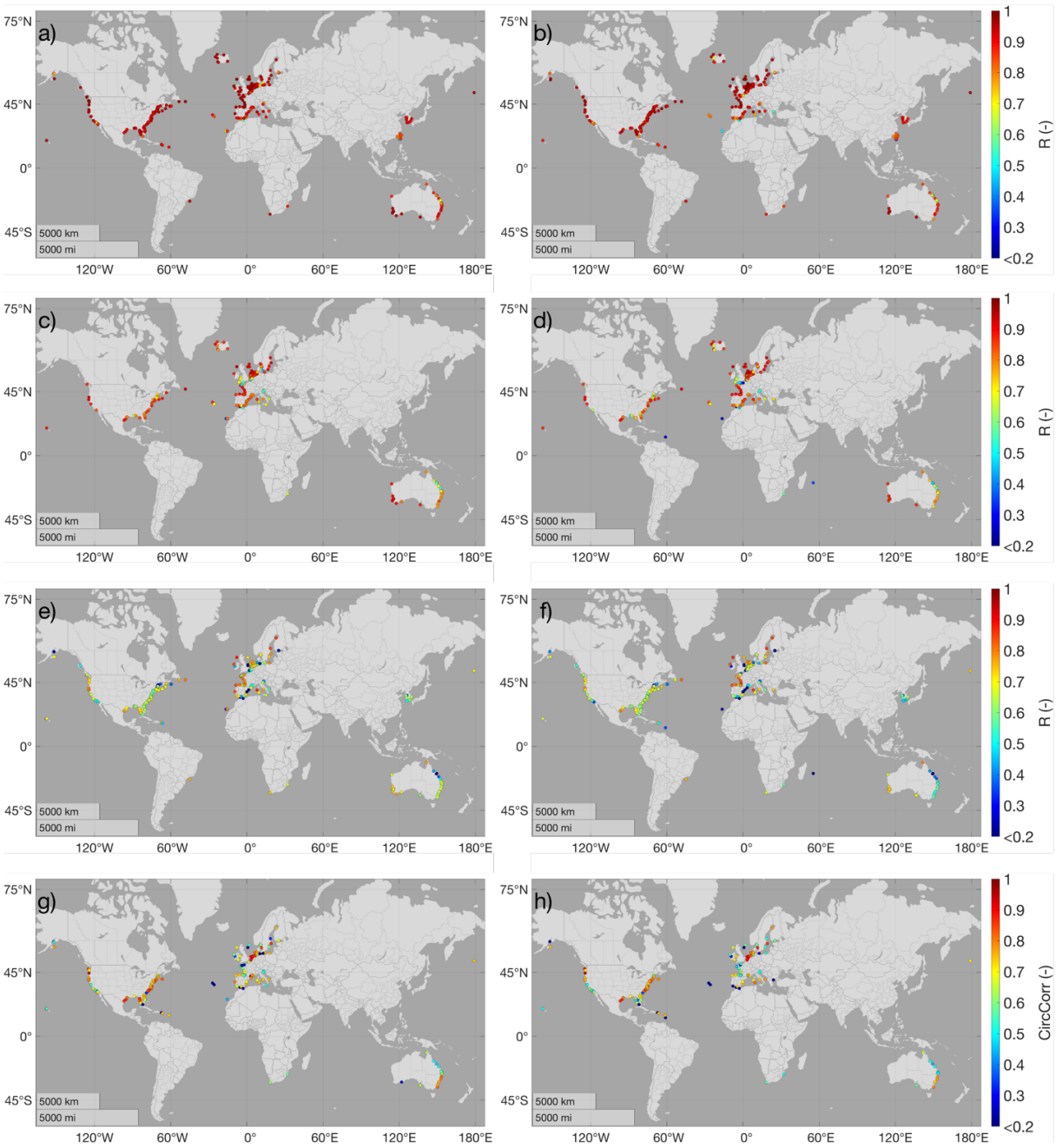

Figure S2.5 Correlation coefficient. Global distribution of Pearson's correlation coefficient (R) for H_s (a-b), Tm (c-d), T_p (e-f) and Dir_m (g-h) between the wave buoys and WAVERYS (left column, a-c-e-g) and ERA5 (right column, b-d-f-h) reanalyses.

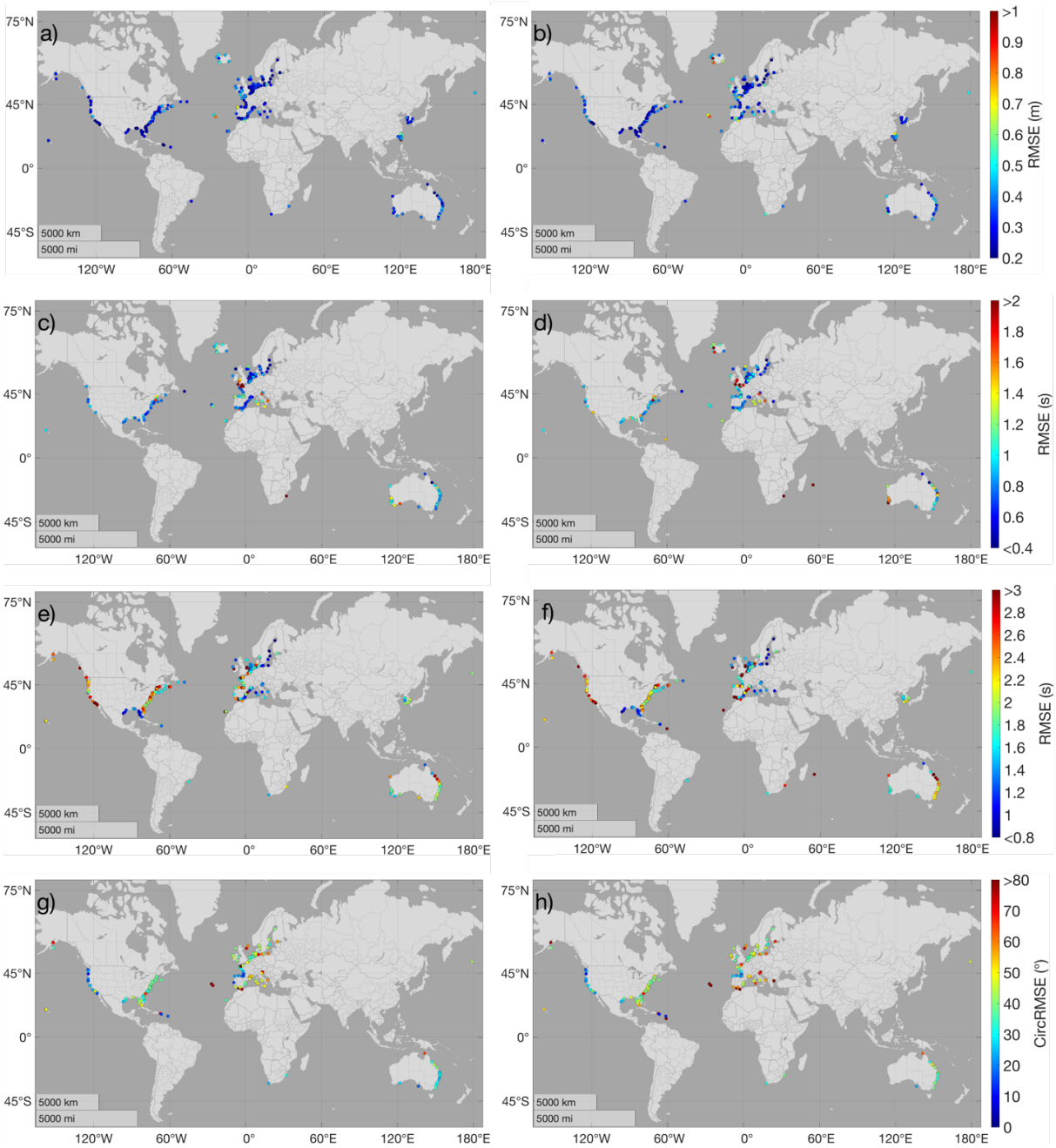

Figure S2.6 Global distribution of RMSE for H_s (a-b, in meters), T_m (c-d, in seconds), T_p (e-f, in seconds) and Dir_m (g-h, in degrees) between wave buoys and WAVERYS (left column, a-c-e-g) and ERA5 (right column, b-d-f-h) reanalyses.

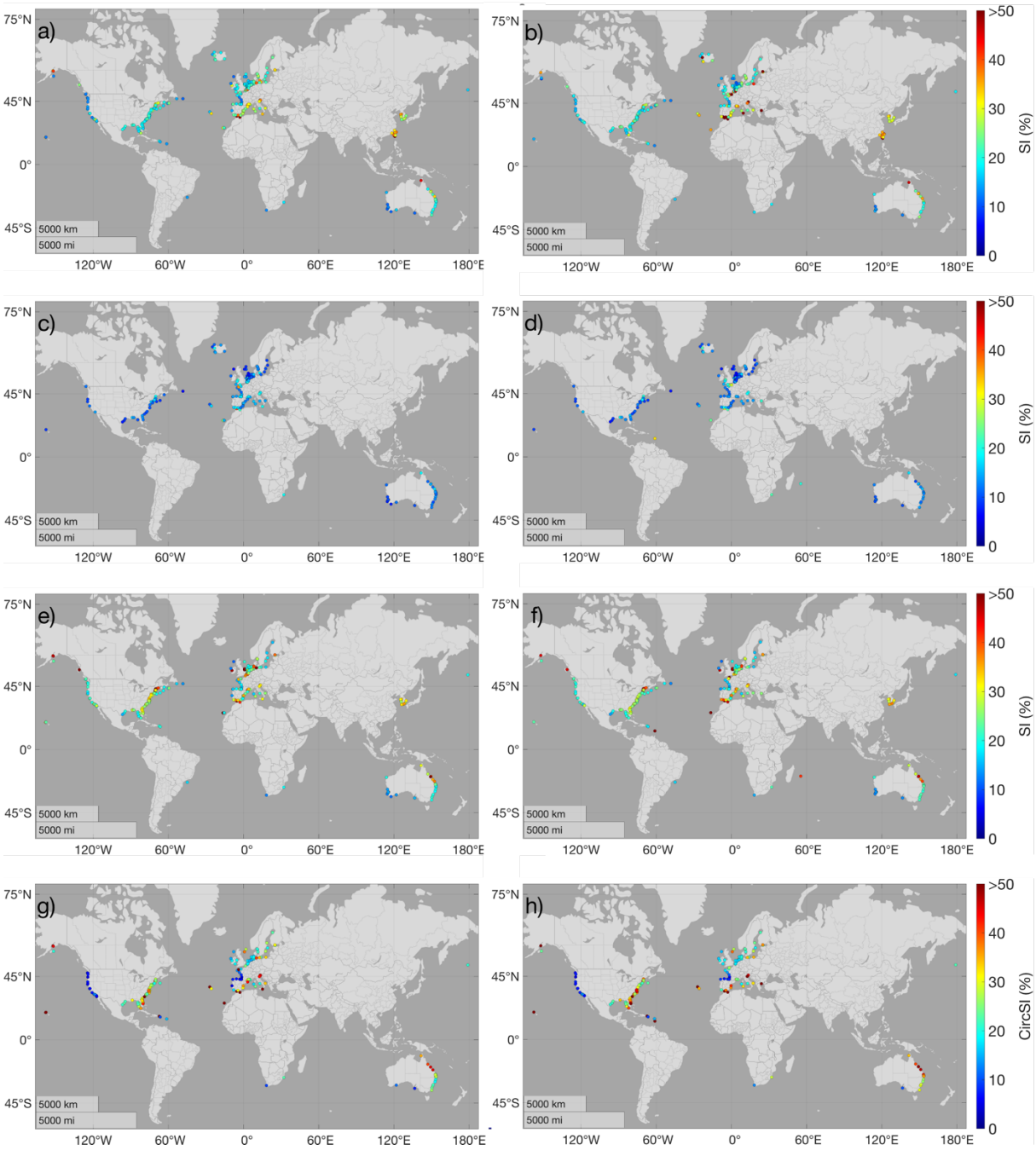

Figure S2.7 Global distribution of SI (in %) for H_s (a-b), T_m (c-d), T_p (e-f) and Dir_m (g-h) between wave buoys and WAVERYS (left column, a-c-e-g) and ERA5 (right column, b-d-f-h) reanalyses.

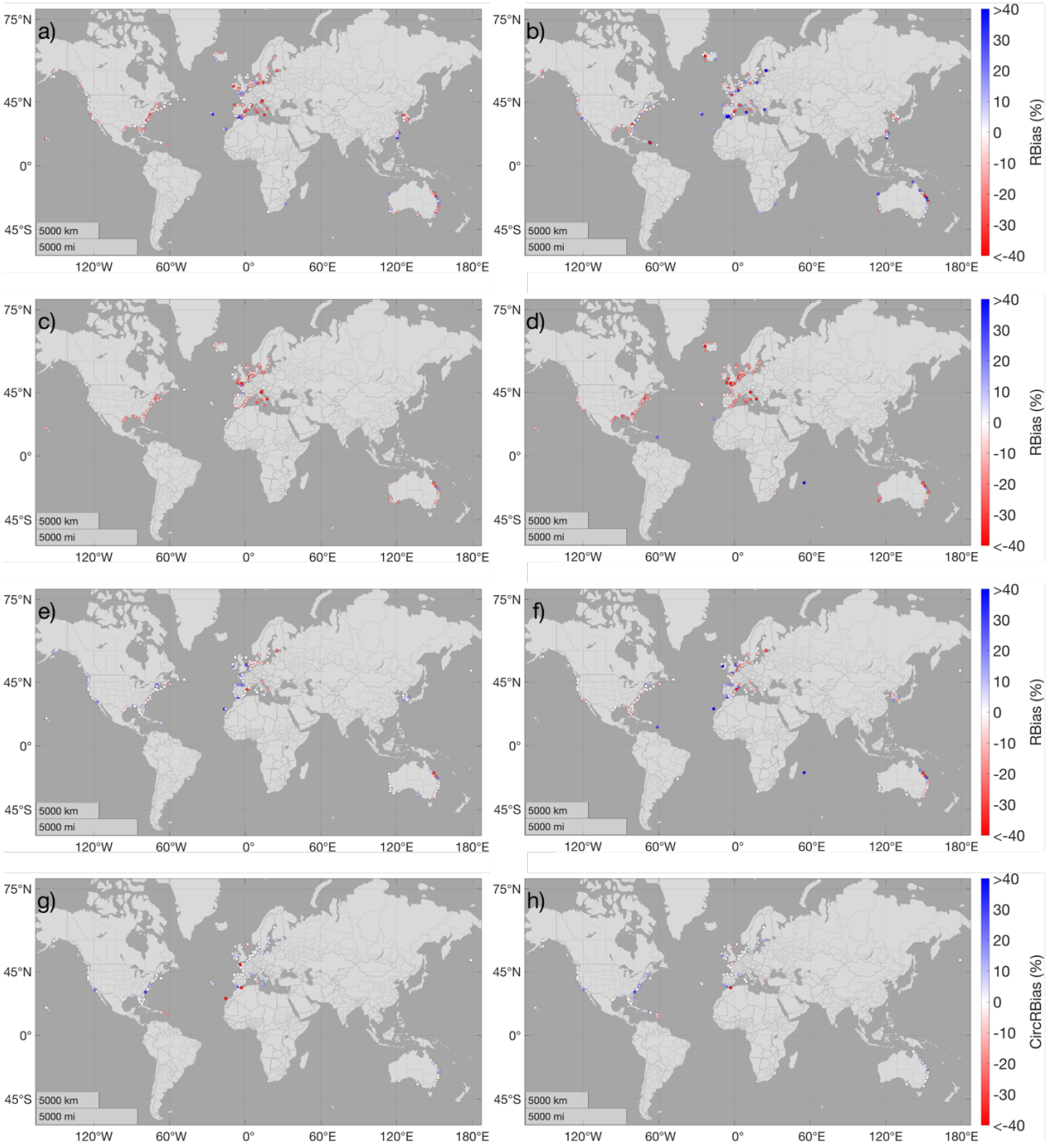

Figure S2.8 Global distribution of relative bias (in %) for H_s (a-b), T_m (c-d), T_p (e-f) and Dir_m (g-h) between wave buoys and WAVERYS (left column, a-c-e-g) and ERA5 (right column, b-d-f-h) reanalysis. Red (blue) values represent an underestimation (overestimation) from the reanalysis.

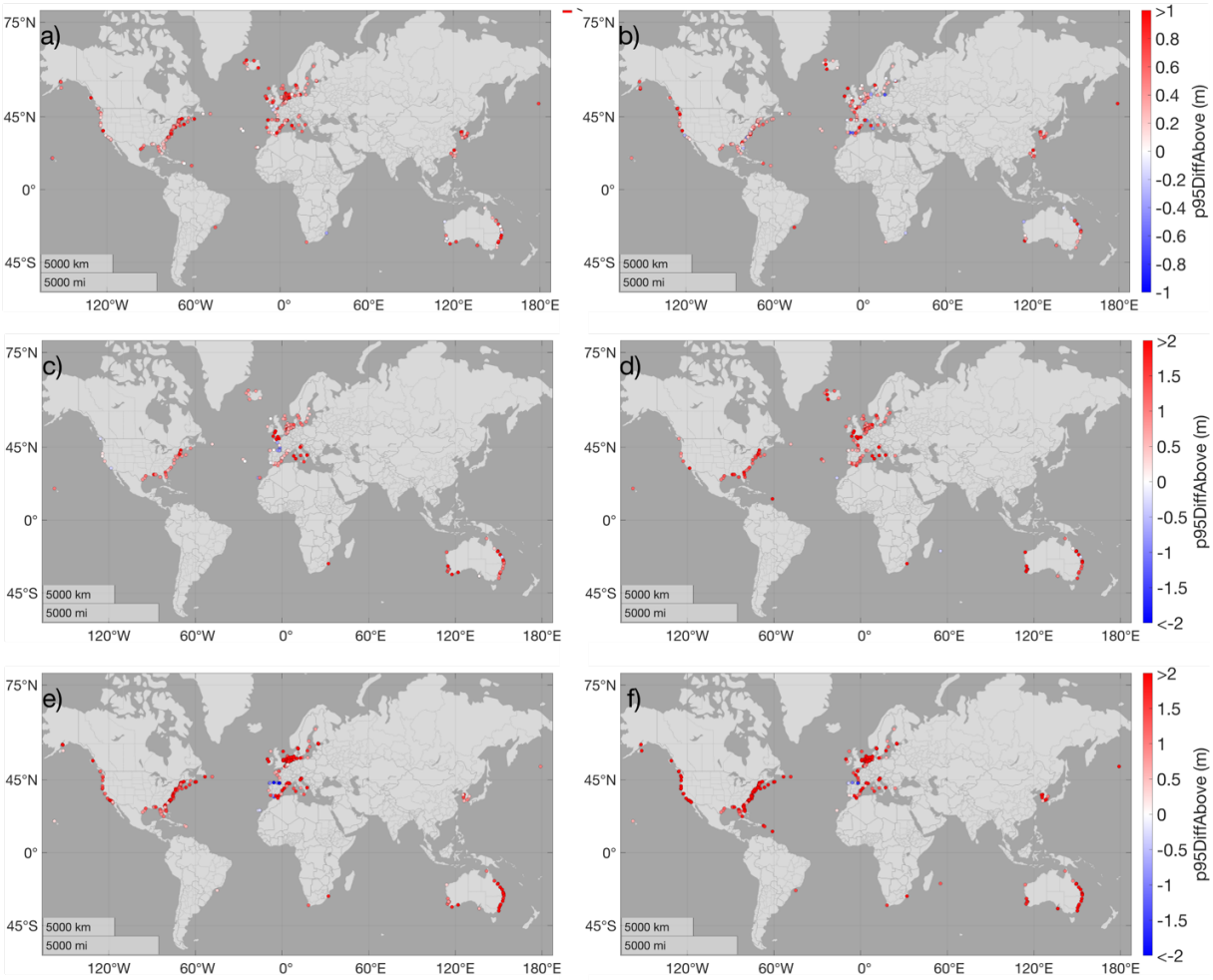

Figure S2.9 Global distribution of the mean difference for extreme values (above the 95th percentile) values of H_s (a-b in meters), T_m (c-d, in seconds) and T_p (e-f, in seconds) between wave buoys and WAVERYS (left column, a-c) and ERA5 (right column, b-d) reanalysis. Red (blue) values represent an underestimation (overestimation) from the reanalysis.

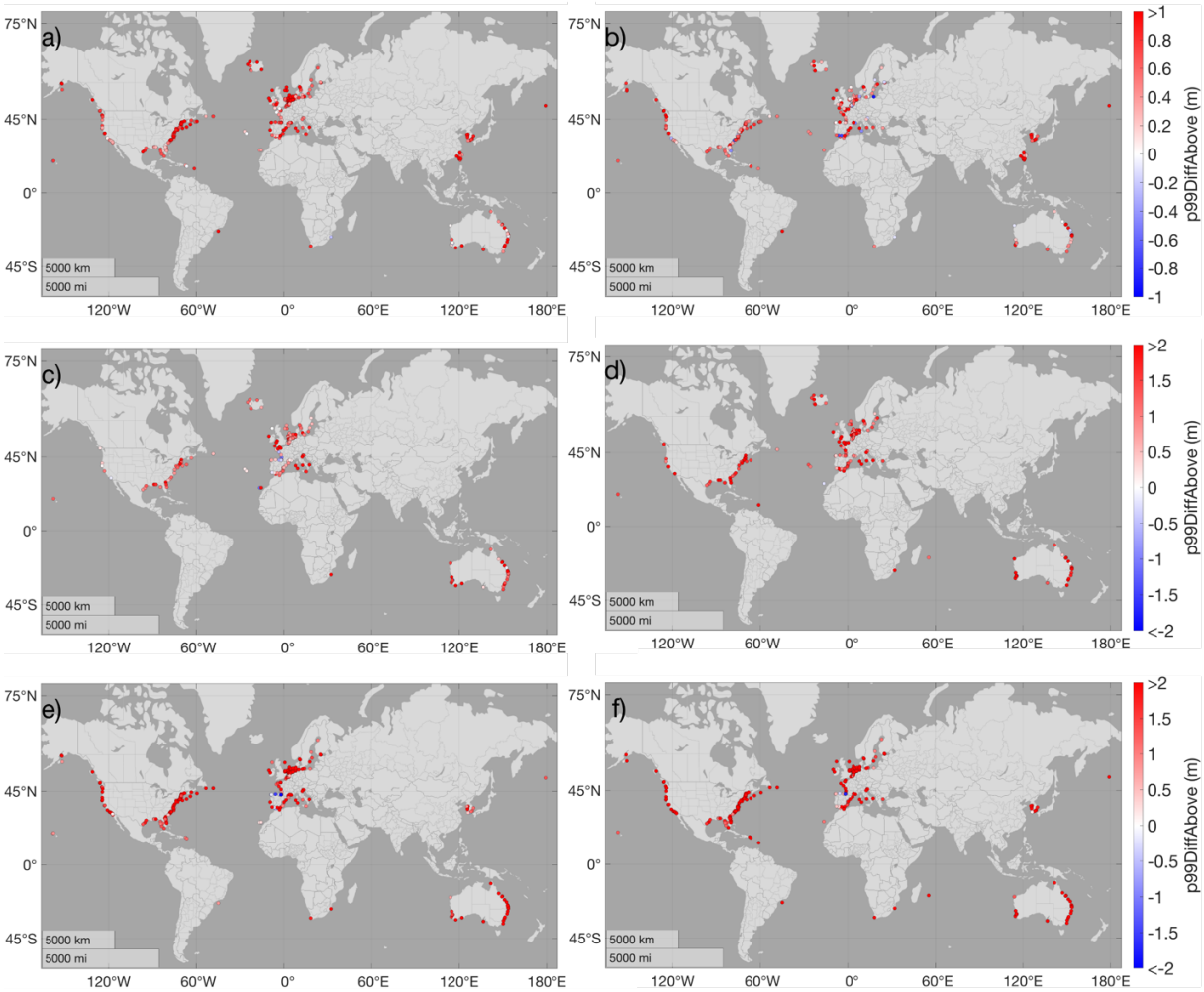

Figure S2.10 Global distribution of the mean difference for extreme values (above the 99th percentile) values of H_s (a-b in meters), T_m (c-d, in seconds) and T_p (e-f, in seconds) between wave buoys and WAVERYS (left column, a-c) and ERA5 (right column, b-d) reanalysis. Red (blue) values represent an underestimation (overestimation) from the reanalysis.

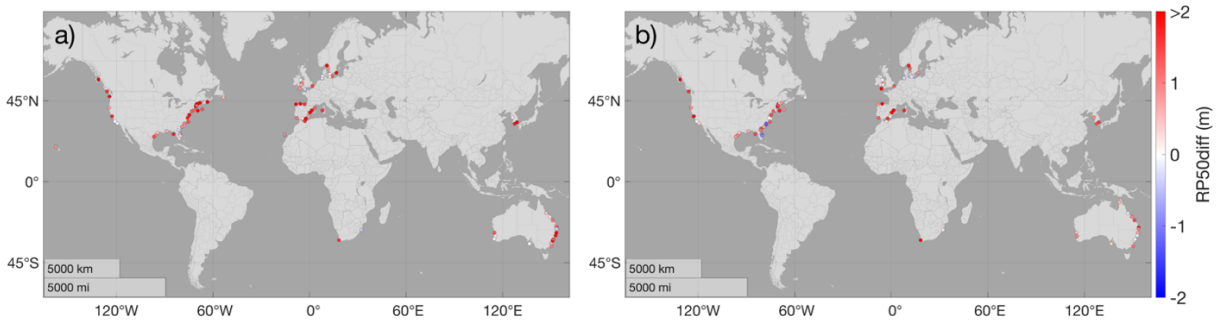

Figure S2.11 Global distribution of H_s 50-year return period difference between wave buoy data and WAVERYS (a) and ERA5 (b) reanalysis. Red (blue) values represent an underestimation (overestimation) from the reanalysis.

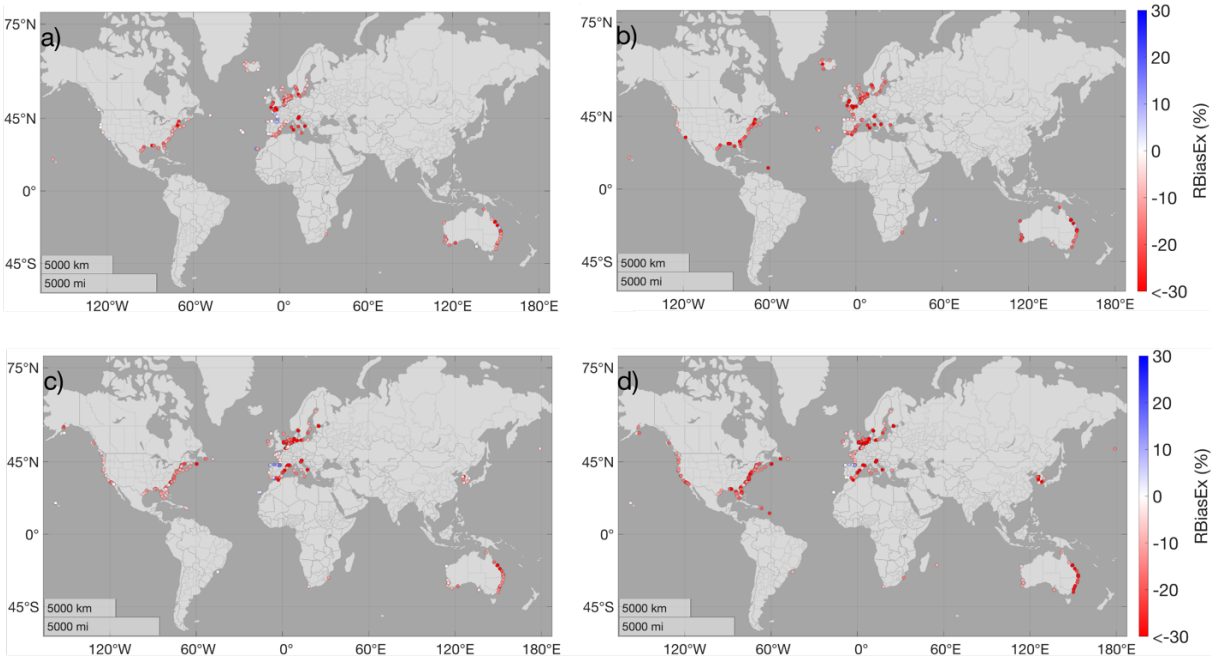

Figure S2.12 Global distribution of relative bias (in %) for extreme (>95th percentile) values of T_m (a-b) and T_p (c-d) between wave buoys and WAVERYS (left column, a-c-e) and ERA5 (right column, b-d-f) reanalyses. Red (blue) values represent an underestimation (overestimation) from the reanalysis.

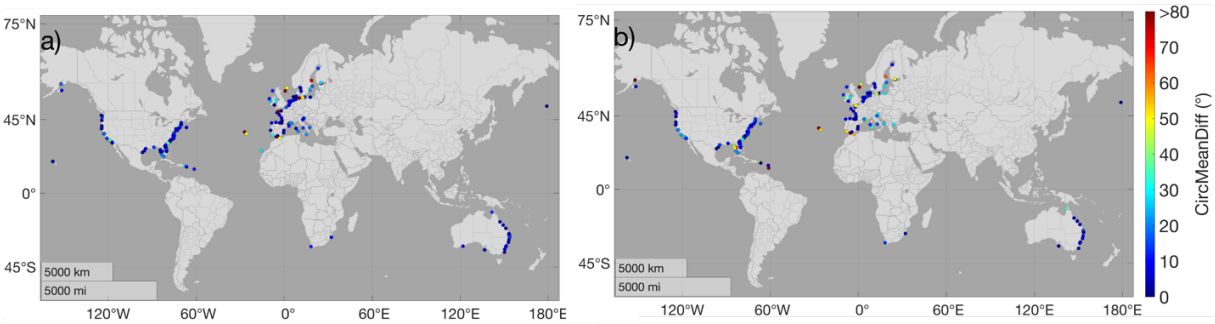

Figure S2.13 Global distribution of difference (in degrees) between mean direction estimated with wave buoys data and with WAVERYS (a) or ERA5 (b) reanalysis data.

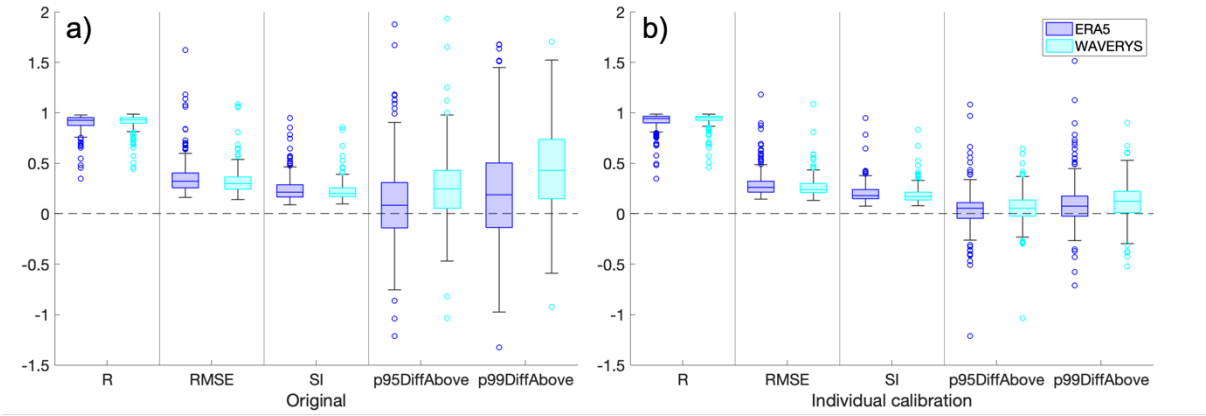

Figure S2.14 Box plot of R, RMSE (in meters), SI (in meters) and difference of extreme H_s (in meters) estimated with buoy data and original (a) and calibrated (b) reanalysis data from WAVERYS and ERA5.

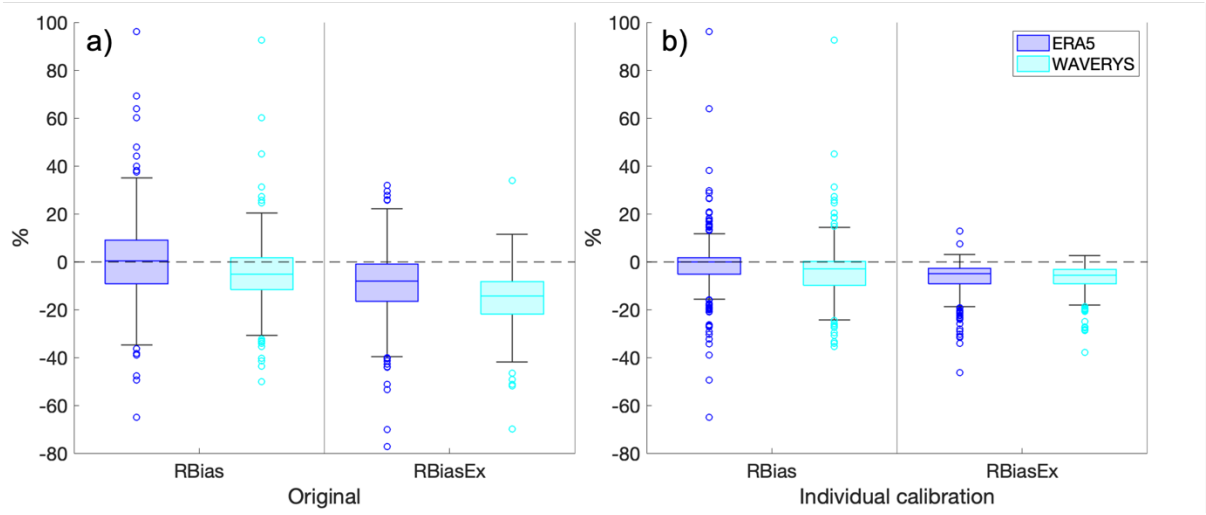

Figure S2.15 Box plot of relative bias (in %) for H_s and for the extreme H_s (above the 95th percentile) estimated with buoy data and original (a) and calibrated (b) reanalysis data from WAVERYS and ERA5.

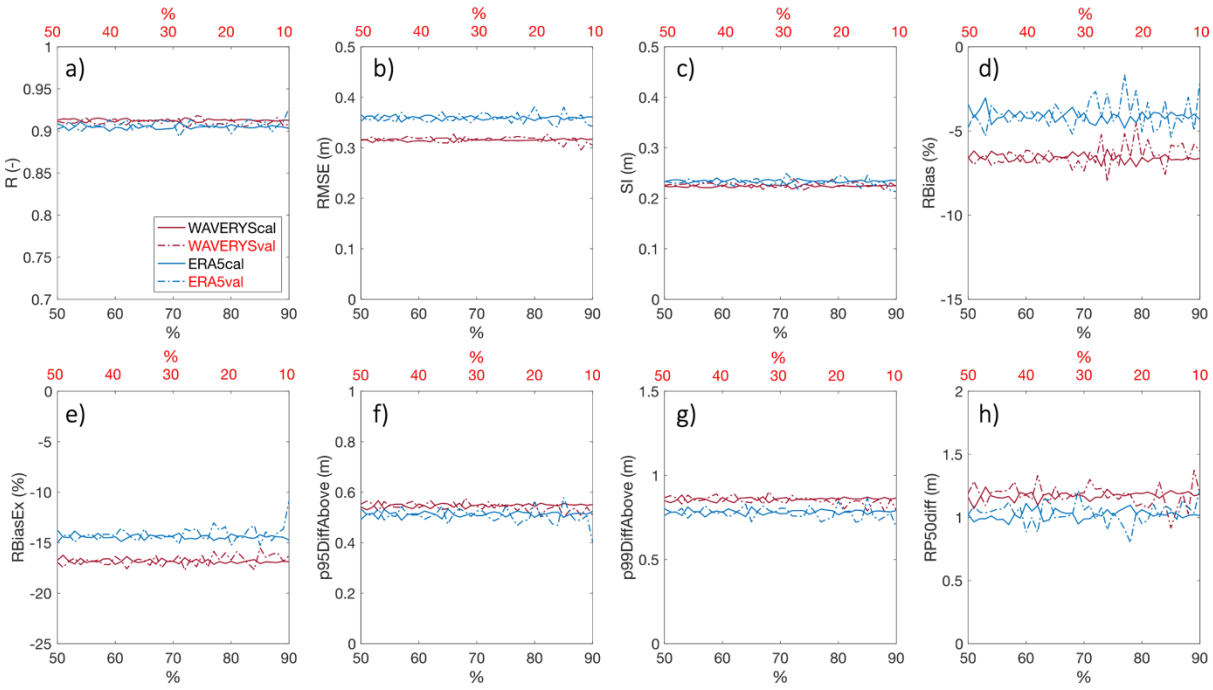

Figure S2.16 Sensitivity analysis of global calibration for H_s. Error metrics for the comparison of H_s between the buoys and global calibration of WAVERYS and ERA5 applied to the validation group (in red, ranging from 50% to 10% of the total buoys in bins of 0.01%) and the group of buoys used to determine the global calibration equations (in black, ranging from 50% to 90% of the total buoys). The parameters represented are R (a), RMSE (b), SI (c), relative bias (d), extreme (>95th percentile) relative bias (e), mean difference between buoy and reanalysis for values above the 95th (f) and 99th (g) percentile and difference between the H_s 50-years return period (h).

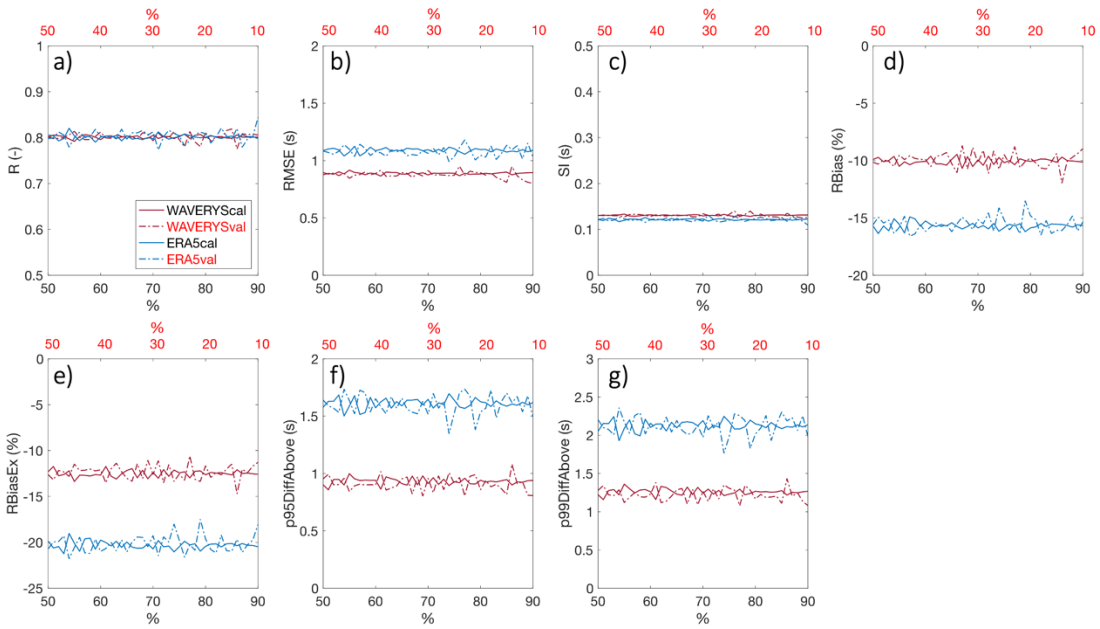

Figure S2.17 Sensitivity analysis of global calibration for T_m. Error metrics for the comparison of T_m between the buoys and global calibration of WAVERYS and ERA5 applied to the validation group (in red, ranging from 50% to 10% of the total buoys in bins of 0.01%) and the group of buoys used to determine the global calibration equations (in black, ranging from 50% to 90% of the total buoys). The parameters represented are R (a), RMSE (b), SI (c), relative bias (d), extreme (>95th percentile) relative bias (e), mean difference between buoy and reanalysis for values above the 95th (f) and 99th (g) percentile.

2.10 Appendix B. Supplementary tables

Supplementary Table 1 – Geographical and temporal coverage details of the 326 coastal buoys used in this study. Available at https://doi.org/10.6084/m9.figshare.22357441.v2

Supplementary Table 2 – Statistical results of validation of wave parameters (H_s, T_m, T_p and Dir_m) from WAVERYS and ERA5 wave reanalyses evaluated at 326 coastal buoy locations. Available at https://doi.org/10.6084/m9.figshare.22357450.v3

Supplementary Table 3 – Statistical results of comparison of wave parameters (H_s, T_m, T_p and Dir_m) from calibrated WAVERYS and ERA5 wave reanalysis at 326 coastal buoy locations. Available at https://doi.org/10.6084/m9.figshare.22357459.v1

Chapter 3 Development of topo-bathymetric continuum profiles for coastal barriers with global open-access data

Fanti, V., Loureiro, C. & Ferreira, Ó. (2025). Development of topo-bathymetric continuum profiles for coastal barriers with global open-access data. *Remote Sensing Applications: Society and Environment*, 38, 101528.

Abstract

Coastal barriers are dynamic and vulnerable coastal environments exposed to storms and rising sea levels, requiring a thorough understanding of their physical and geomorphological characteristics. Despite this, high-resolution topo-bathymetric data are not openly available for most of the world's coastal areas, preventing accurate estimation of the exposure to storms and associated risks. Global models of topography and bathymetry, derived from remote sensing techniques, are available worldwide as an open-source solution to characterise coastal morphology. However, their coarse resolution, limited vertical and horizontal accuracy, alongside inconsistencies in the transition from land to the shallow nearshore zone, make their use in coastal areas challenging, requiring careful evaluation. This study investigates the potential and limitations of four recent open-access satellite-derived topographic models (Copernicus GLO-30 DEM, AW3D30, TanDEM-X, Euro-Maps 3D) and three bathymetric models (GEBCO_2023, SRTM15+, ETOPO 2022) in five coastal barriers. It proposes a new approach to integrate global models to provide a consistent representation of the topo-bathymetric continuum profile in coastal areas characterised by a barrier morphology. Coastal barrier profiles, representative of natural sectors and characterized by morphological homogeneity, were derived by merging global topographic and bathymetric digital elevation models and implementing an equilibrium profile in the transition zone. The profiles obtained from the global models were compared with higher resolution local or regional topo-bathymetry. The global topographies tend to underestimate the dune top, with TanDEM-X giving the best results in terms of dune crest height and beach slope. The barrier continuum profiles that merged TanDEM-X and ETOPO 2022 global models were found to have the lowest error, with a vertical RMSE of 0.76 m. Based on integration of these remotely sensed

models, it is possible to determine average representative coastal barrier profiles suitable for use in global to regional coastal studies or in data-poor areas, potentially serving as a cost-effective tool for preliminary coastal hazard assessments and early warning systems at wide spatial scales.

Keywords: Barrier profiles, Global models, Satellite topography, Nearshore bathymetry, Coastal hazards

3.1 Introduction

Coastal barriers are dynamic, valuable, yet vulnerable coastal environments (e.g., McBride et al., 2022), and are strongly affected by storm events and sea level rise (e.g., Gharagozlou et al., 2020; Irish et al., 2010). To understand and model their morphological response to coastal processes, it is necessary to characterise not only the forcing agents but also the geomorphological properties of these coastal systems (Cooper et al., 2018). Such properties are also paramount for the definition of morphological geo-indicators (see Carapuço et al. 2016) or process-based indicators (Ferreira et al., 2017), which can be used in coastal hazard and risk assessments (e.g. Torresan et al. 2008; Nguyen et al. 2016). Several methods have been developed to derive high-resolution land topography and ocean bathymetry data at local scales (see Melet et al., 2020) and to extract coastal barrier characteristics (Wernette et al., 2016). These include airborne Light Detection and Ranging (LiDAR), structure from motion photogrammetry using imagery from unmanned aerial vehicles and multibeam echo sounding. However, high-resolution topo-bathymetry is still not available in many coastal areas around the world (e.g., Archer et al., 2018; Simpson et al., 2015; Wechsler, 2007), and there is a global lack of data in intertidal and shallow water coastal regions (Tseng et al., 2017). This is particularly relevant in areas where water clarity is suboptimal and wave breaking restricts direct surveying. Moreover, data collected in coastal waters are often under national jurisdiction, outdated, and not freely accessible (Wölfl et al., 2019). Despite major international seafloor mapping initiatives (e.g. SEABED 2030, EMODnet, ETOPO), more than fifty percent of the world's coastal waters shallower than 200 m depth remain unsurveyed (IHO, 2023), with less than 10% of the seafloor covered by high-resolution multibeam data (Mayer et al., 2018), mostly collected in economically relevant areas and often confidential (Wölfl et al., 2019).

Given these limitations, Global Digital Elevation Models (GDEMs) and Global Bathymetric Models (GBMs), generated using remote sensing techniques, are increasingly becoming the data of choice for many coastal applications from global to local scales. The first GDEM was produced in 2003 by the Shuttle Radar Topography Mission (SRTM, Farr et al. 2007), with 90 m horizontal resolution, after which several open source GDEMs options derived from Synthetic Aperture Radar (SAR) technologies or optical satellite imagery became available (Hawker et al., 2018a; Proietti et al., 2017). Between 2009 and 2020 several 30 m resolution GDEMs were released: the Advanced Spaceborne Thermal Emission and Reflection Radiometer (ASTER, Yamaguchi et al. 1998), the NASADEM derived from reprocessing and improving SRTM (Crippen et al., 2016), the World3D based on stereo-imagery from the Advanced Land Observing Satellite (ALOS) (AW3D30, Tadono et al. 2016), the SAR-derived TanDEM-X (Rizzoli et al., 2017) and, from the TanDEM-X terrain correction and hydrological editing, the Copernicus GLO-30 DEM (Fahrland et al., 2020). Recently, commercial GDEMs have also been developed, generally with a higher spatial resolution and better accuracy, such as the CoastalDEM (Kulp and Strauss, 2019) at 30m resolution, WorldDEM (i.e. the commercial TanDEM-X) at 12 m resolution, the stereo-derived Euro-Maps 3D (Uttenthaler et al., 2013) at 5 m resolution and Vricon at 0.5 m resolution.

Regarding global ocean bathymetry and starting in the mid-1990s with Smith and Sandwell (1994, 1997), the advent of satellite altimetry led to major advances in the estimation of bathymetry from space to complement the sparse and scarce high-resolution bathymetric surveys (Wölfl et al., 2019). Since then, several GBMs obtained from satellite-derived gravity anomalies, integrated with marine remote sensing techniques (single and multibeam echo sounding, bathymetric LiDAR) and existing nautical charts have been produced using a range of interpolation techniques, and released at increasingly higher resolutions (Tozer et al., 2019). The most recent GBMs are SRTM15+V2.0 (Tozer et al., 2019), ETOPO 2022 (NOAA National Centers for Environmental Information, 2022) and GEBCO_2023 (GEBCO Bathymetric Compilation Group, 2023), all providing global coverage on a 15 arcsecond grid (~460 m). Despite providing elevation data for land and depth data for the ocean, bathymetry and topography in these GBMs are not merged but rather separated by the shoreline boundary, defined using the World Vector Shorelines (WVS) dataset. This can result in a misalignment in the order of a few hundred meters (Tozer et al., 2019), which, together with their coarser

resolution than freely available GDEMs, makes GBMs use challenging for nearshore and coastal areas.

Despite years of progress and increasing vertical and horizontal accuracies, GDEMs still have systematic to random errors (Hawker et al., 2018a) with various authors pointing to the need for up-to-date, freely available and high-resolution GDEMs (Hawker et al., 2018a; Schumann and Bates, 2018; Simpson et al., 2015). The current GDEMs are considered to be uncertain in terms of vertical accuracy for high-confidence evaluations of sea level rise and coastal flooding impacts (Gesch, 2018), leading to errors in coastal hazard assessments (Melet et al., 2020; Serafin et al., 2019) and underestimation of coastal vulnerability (Kulp and Strauss, 2016; Parodi et al., 2020; Simpson et al., 2015). Similarly, global compilations of ocean bathymetry are still incomplete (Li et al., 2023), have insufficient vertical and spatial resolution, interpolation errors, and inaccuracies in shallow waters (Cesbron et al., 2021). Moreover, their vertical consistency is seldom guaranteed when merging multiple data sources (GEBCO Bathymetric Compilation Group, 2023) due to the lack of detailed information on the vertical datums (Weatherall et al., 2015). Therefore, it is crucial to recognise their limitations, errors, and inconsistencies but also to develop approaches to improve their quality and guarantee a suitable use as freely available global databases are an advantageous alternative to costly and sparsely available high-resolution data sources, particularly in remote and/or data poor regions where more accurate local data is not available and collection is not feasible. Careful evaluation of GDEMs and GBMs is required to ensure appropriate consideration of data uncertainties, especially in coastal areas where more detailed and accurate information is fundamental for effective management and decision-making (Gesch, 2018; Parodi et al., 2020; Sepúlveda et al., 2020; Simpson et al., 2015), and where remote sensing techniques present greater challenges.

Although better remote sensing solutions for estimating bathymetry in coastal areas are beginning to emerge both locally (Bergsma et al., 2021; Caballero and Stumpf, 2019; Cesbron et al., 2021; Li et al., 2023; Pacheco et al., 2015; Pleskachevsky et al., 2011), regionally (Bishop-Taylor et al., 2019) and globally (Almar et al., 2021a; Ashphaq et al., 2021; Salameh et al., 2019), as well as algorithms for editing and improving GDEMs (González et al., 2020; Hawker et al., 2018a, 2018b), global models are still commonly used without fully acknowledging their inaccuracies and errors or requiring in-situ data for calibration. In particular, GBMs have been used without corrections to assess tsunami hazards (Sepúlveda et

al., 2020), storm surges and extreme sea levels (Muis et al., 2020), shoreline retreat due to sea level rise (Vousdoukas et al., 2020), and coastal flooding (Parodi et al., 2020). Similarly, space-borne GDEMs have been widely applied in coastal areas for hydrogeomorphological risk assessment and damage estimation for natural hazards such as coastal flooding and inundation (Archer et al., 2018; Gesch, 2018; Hawker et al., 2018b, 2018a; Mason et al., 2016, 2015; Neumann et al., 2015; Michalis Ioannis Vousdoukas et al., 2018; Vousdoukas et al., 2016b), also considering the effect of sea level rise (Almar et al., 2021b; Bove et al., 2020; Fandé et al., 2022; Gesch, 2018; Kulp and Strauss, 2019; Parodi et al., 2020; Vousdoukas et al., 2022). Results from such analyses have been incorporated in key findings in the IPCC Sixth Assessment Report (IPCC, 2022). A fundamental challenge for the correct use of GDEMs and GBMs is to understand and quantify their errors and then, as they propagate through the analysis, incorporate these uncertainties into the models and projections (Bove et al., 2020; Leon et al., 2014; Sepúlveda et al., 2020; Michalis Ioannis Vousdoukas et al., 2018). Moreover, it is also necessary to develop tools and methods that minimise errors and allow the definition of representative coastal profiles from GDEMs and GBMs that are suitable for coastal hazard and risk analysis. This paper presents a new approach to determine continuous topo-bathymetric barrier profiles from GDEMs and GBMs and proposes a novel solution to minimise the challenges associated with the absence of shallow nearshore and intertidal data, robustly evaluating the performance for estimating coastal barrier profiles. These profiles can be widely applied in regional to global scale analysis that evaluate the vulnerability of coastal barriers to coastal hazards, as well as in impact and disaster risk reduction assessments for present and future scenarios.

3.2 Materials and Methods

3.2.1 Topography

In this work, four recent freely available satellite-derived GDEMs were analysed: Copernicus GLO-30 DEM (Fahrland et al., 2020) and AW3D30 (Tadono et al., 2014) with 30 m resolution, TanDEM-X (Rizzoli et al., 2017) with 12 m resolution and Euro-Maps 3D with 5 m resolution (Uttenthaler et al., 2013) (Table 3.1). Euro-Maps 3D is derived from IRS-P5 CartoSat-1 in-flight stereo data and was selected because it is the highest resolution GDEM, although with a free download for Copernicus-related institutional users limited to an area of 1400 km^2, which limited the availability across the study sites. The TanDEM-X GDEM was generated using

SAR interferometry and allows for more accurate topographic data by measuring the phase differences between multiple SAR acquisitions from two satellites (TerraSAR-X and TanDEM-X) and is openly available at 12 m for non-commercial research purposes. TanDEM-X has been shown to outperform previously commonly used GDEMs, such as ASTER, SRTM and AW3D30, in terms of accuracy in a wide variety of areas such as mountainous, coastal, urban and vegetated (Chu and Lindenschmidt, 2017; Gdulová et al., 2021; Gesch, 2018; Li et al., 2021; Parodi et al., 2020; Vassilaki and Stamos, 2020). The Copernicus GLO-30 DEM was derived from TanDEM-X after terrain correction and hydrological processing by removing spikes, gap filling and identifying systematic and random errors (Collins et al. 2015), thus representing an improvement to the native TanDEM-X (Marešová et al., 2021), although it has lower horizontal resolution (Table 3.1). Finally, AW3D30 was derived from images acquired by the panchromatic remote sensing instrument for stereo mapping onboard of the ALOS and it proved to be a robust and accurate DEM for multiple geographic regions (Uuemaa et al., 2020) and specifically for maximum coastal elevations (Almar et al., 2021b).

Table 3.1 Specifications for global topographic models.

GDEMs	Pixel Spacing	Horizontal Datum	Vertical Datum	Absolute Horizontal Accuracy[1]	Absolute Vertical Accuracy[2]	Relative Vertical Accuracy	Acquisition window	Coverage
TanDEM-X	0.4 arcsec (~12 m @ equator[3])	WGS84-G1150 EPSG:4979	WGS84-G1150 ellipsoid	<10m	<10m	2m (slope <= 20%) 4m (slope > 20%)	2010-2015	Global (-180°W to 180°E, -90°S to 84°N)
Copernicus GLO-30 DEM	1 arcsec (~30 m @ equator)	WGS84-G1150 EPSG:4326	EGM2008 EPSG:3855	<6m	<4m	<2m (slope <= 20%) <4m (slope > 20%)	2010-2015	Global (-180°W to 180°E, -90°S to 90°N)
Euro-Maps 3D	5 m	WGS84 EPSG:4326	EGM96	5-10 m	5-10 m	< 3m	2007-2016	Global, cloud limited (Proietti et al., 2017)
AW3D30	1 arcsec (~30 m @ equator)	WGS84 EPSG:4326	EGM96	7 m	7 m	5m RMSE	2006-2011	Global, gap filled (Takaku et al., 2020)

[1] 90% circular error (CE90)

[2] 90% linear error (LE90)

[3] The north-south resolution remains consistent, while the east-west resolution decreases with increasing latitude.

All GDEMs analysed represent the actual surface of the terrain (i.e. they are digital surface models), including infrastructures and vegetation. Since the main objective of this work is to define the uncertainties of the models for coastal barriers, only natural areas were selected, avoiding heavily vegetated or built-up areas. The analysis was performed on five natural coastal barriers sectors specifically, the Ria Formosa in Portugal, Pamlico Sound and Fire Island in the USA, Terschelling in the Netherlands, and Myalup in Australia (see section 2.3 for details of study sites), for which high-resolution LiDAR-derived DEMs were also available (Table 3.2).

Table 3.2 Specifications for local topographic models.

Location	**Local DEM**	**Pixel Spacing**	**Horizontal Datum**	**Vertical Datum**	**Absolute Horizontal Accuracy**	**Absolute Vertical Accuracy**	**Acquisition window**
Faro, Portugal	LiDAR 2011	2 m	PT-TM06/ETRS89 EPSG:3763	Cascais Helmert 38, GeodPT08	RMSE 0.16 m (Direcção-Geral do Território, 2011)		November/ December 2011
Outer Banks, USA	2019 USACE NCMP Topobathy Lidar DEM: East Coast (NC)	1 m	EPSG:3631 NAD83 (2007)	NAVD88	100 cm (95% confidence level)	20 cm (95% confidence level)	2019
Fire Island, USA	2020 USACE NAN Topobathy Lidar DEM: New Jersey and New York	1 m	EPSG:6318 NAD83(2011)	EPSG:5703 NAVD88	100 cm (95% confidence level)	20 cm (95% confidence level)	2012
Terschelling, Netherlands	AHN3	0.5 m	EPSG:28992 - Amersfoort / RD New Ellipsoid: Bessel 1841	EPSG:5709 NAP height (Normaal Amsterdams Peil)	objects of 2 x 2 m have a maximum position deviation of 50 cm (PDOK L., 2017)	Standard deviation <15 cm for 99.7% of points (PDOK L., 2017)	2014-2019
Myalup, Australia	LiDAR DEM	5 m	EPSG:4283 GDA94	AHD – using AUSGeoid98	80 cm (95% confidence interval)	30 cm (95% confidence interval)	2001-2015

3.2.2 Bathymetry

Among all the available GBMs, the most recent and commonly used were analysed in this work and include SRTM15+ (Tozer et al., 2019), GEBCO_2023 (GEBCO Bathymetric Compilation Group, 2023) and ETOPO 2022 (NOAA National Centers for Environmental Information, 2022) (Table 3.3). These were compared with high-resolution LiDAR-derived bathymetric DEMs to approximately 10 m water depth and, at greater depths, with regional bathymetric models (RBMs) such as the CUDEM for the USA (Amante et al., 2023), EMODnet for Europe (Thierry et al., 2019) and the 2023 Australian Bathymetry and Topography grid (Beaman, 2023) (Table 3.4). The SRTM15+ bathymetry was developed following the methodology outlined by Smith and Sandwell (1997, 1994) and has recently been augmented in shallow areas with bathymetric datasets developed by the Seabed 2030 Regional Centers for the production of GEBCO 2023. The GEBCO 2023 grid is augmented through a blending "remove-restore" procedure (Weatherall et al., 2015) with SRTM15+ and regional bathymetric datasets based on multibeam, singlebeam and other individual surveys from EMODnet and additional sources. ETOPO 2022 integrates bathymetric data from GEBCO 2022 and GMRTv4.0, as well as land topography from Copernicus GLO-30 and other data sources (NOAA National Centers for Environmental Information, 2022). The RBMs also include GBMs, for instance, ETOPO and SRTM are incorporated in the Australian RBM in areas where higher resolution sounding data are not available (Whiteway, 2009), GEBCO in EMODnet (Thierry et al., 2019) and SRTM15+ in CUDEM (Amante et al., 2023).

While these datasets are related and have interdependencies due to shared high-resolution data, their comparison is important to consistently assess their accuracy and performance in different coastal areas. The fact that they are derived from the assimilation of heterogeneous data types has implications in terms of vertical datum, as surface models in shallow water areas are often assumed to be referred to MSL, even when they have distinct vertical references (GEBCO Bathymetric Compilation Group, 2023; NOAA National Centers for Environmental Information, 2022). The GEBCO 2023 grid is accompanied by a Type Identifier file (TID, GEBCO Bathymetric Compilation Group, 2023) while each ETOPO 2022 tile has an associated Source ID (SID, NOAA National Centers for Environmental Information, 2022) with information on the source data merged into the final grid. However, detailed information on each specific dataset used and the vertical datum are unavailable.

To evaluate the accuracy of the GBMs and RBMs, detailed bathymetry was extracted at each site from LiDAR-derived DEMs (Table 3.4). For the study sites in the USA and Australia,

multibeam data were available and integrated with the LiDAR data, while for the other sites the GBMs could only be compared with LiDAR-derived DEMs down to 10 m water depths due to the lack of high-resolution offshore surveys, and with RBMs for deeper parts of the profiles.

Table 3.3 Specifications for global and regional bathymetric models.

GBMs	**Pixel Spacing**	**Horizontal Datum**	**Vertical Datum**	**Accuracy**	**Acquisition window**	**Coverage**
GEBCO_2023	15 arcsec (~460 m @ equator)	WGS84 EPSG:4326	MSL	Multiple data contributors (https://www.gebco.net/about_us/acknowledgements/our_data_contributors/)		Global (89° 59' 52.5"N to 89° 59' 52.5"S, 179° 59' 52.5"W to 179° 59' 52.5"E)
SRTM15+V2.0	15 arcsec (~460 m @ equator)	WGS84 EPSG:4326	EGM96 EPSG:5171	RMSE ±150 m in the deep oceans and ±180 m near coasts (Tozer et al., 2019)	Multiple data contributors (Table 2, Tozer et al. 2019)	Global (-180°W to 180°E, -90°S to 90°N)
ETOPO 2022	15 arcsec (~460 m @ equator)	WGS84 EPSG:4326	EGM2008	Multiple data contributors (NOAA National Centers for Environmental Information, 2022)		Global (-180°W to 180°E, -90°S to 90°N)
RBMs	**Pixel Spacing**	**Horizontal Datum**	**Vertical Datum**	**Accuracy**	**Acquisition window**	**Coverage**
NCEI's Continuously Updated DEM (CUDEM)	1/9th-1/3rd arcsec (~3-10 m @ equator)	EPSG:4269 NAD83	NAVD88	Horizontal accuracy: 100 cm Vertical accuracy: 50 cm	Multiple data contributors (Amante et al., 2023)	U.S. Atlantic; Gulf of Mexico Coasts; portions of Alaska, Washington, Oregon and California Coasts; Hawaii; Guam and Common- wealth of the Northern Mariana Islands; Puerto Rico and U.S. Virgin Islands; American Samoa (Amante et al., 2023)
EMODnet Bathymetry World Base Layer	115 m	WGS84 EPSG:4326	MSL	Multiple data contributors (Thierry et al., 2019)		Europe (36°W to 43°W, 15°N to 90°N)
Australian Bathymetry and Topography 2023	250 m	WGS84 EPSG:4326	MSL	Multiple data contributors (Beaman, 2023)		Australia (92°E to 172°E, -8°S to -60° S)

Table 3.4 Specifications for local bathymetric models (N/A where not available).

Location	Local DEMs	Pixel Spacing	Horizontal Datum	Vertical Datum	Horizontal Accuracy	Vertical Accuracy	Acquisition window
Faro, Portugal	LiDAR 2011	2 m	PT-TM06/ETRS 89 EPSG:3763	Cascais Helmert 38, GeodPT08	< 5 m + 5% of depth (IHO 2022, 1a)	RMSE 30 cm (DGT, 2011)	June/August 2011
Outer Banks, USA	2019 USACE NCMP Topobathy Lidar DEM: East Coast (NC)	1 m	EPSG:3631 NAD83 (NSRS 2007)	NAVD88	100 cm at 95% confidence level	$\sqrt{0.25^2 + (0.0075}$ m at 95% confidence level (d is depth)	2019
	NOAA/NCEI Multibeam bathymetry mosaic (Varner et al., 2017)	3 arcsec (~90 m @ equator)	WGS84 EPSG:4326	MSL	N/A	N/A	Multiple dates (from 1998 to 2020)
Fire Island, USA	2020 USACE NAN Topobathy Lidar DEM: New Jersey and New York	1 m	EPSG:6318 NAD83(2011)	EPSG:5703 NAVD88	$3.5 + 0.05 * d$ m at 95% confidence level	$\sqrt{0.25^2 + (0.0075}$ m at 95% confidence level (d is depth)	2020
	NOAA/NCEI Multibeam bathymetry mosaic	3 arcsec (~90 m @ equator)	WGS84 EPSG:4326	MSL	N/A	N/A	Multiple dates (1993 to 2019)
Terschelling, Netherlands	Jarkus grid	5 m	EPSG:28992	NAP (Normaal Amsterdams Peil)	0.4 m (Wiegmann et al., 2002)	0.25 m (Wiegmann et al., 2002)	2020
Myalup, Australia	Multibeam Dataset of Australia 2018	50 m	EPSG:7850	MSL	N/A	N/A	Multiple dates (1989 to 2018)

3.2.3 Study sites

Coastal barriers are accumulations of unconsolidated sediments deposited by waves, tides and wind occurring along ocean coastlines that act as important natural buffers against coastal hazards (McBride et al., 2022). They are valuable coastal environments but because they are at the land-water interface, data from satellite sensors in these areas are subject to greater uncertainty. Five coastal barriers were selected from diverse locations around the world (Figure

3.1), namely the Ria Formosa in southern Portugal, the Outer Banks and Fire Island in the USA, Terschelling in the Netherlands, and Myalup in Australia. This selection was made based on the availability of high resolution and accurate topo-bathymetric data, but also to include systems with complex morphology associated with different oceanographic and atmospheric forcing (i.e. wind intensity, wave energy and tidal range). All sites are wave-dominated natural coastal barriers with a semi-diurnal mesotidal regime, with Faro and Terschelling presenting a few houses in the backbarrier area that were avoided when extracting the profiles. The GDEMs and GBMs were evaluated at these diverse coastal barrier sites to assess their performance and accuracy in capturing complex topo-bathymetric features. The barrier sections analysed extended from the barrier area behind the primary dune to an offshore depth of approximately 30 m below mean sea level.

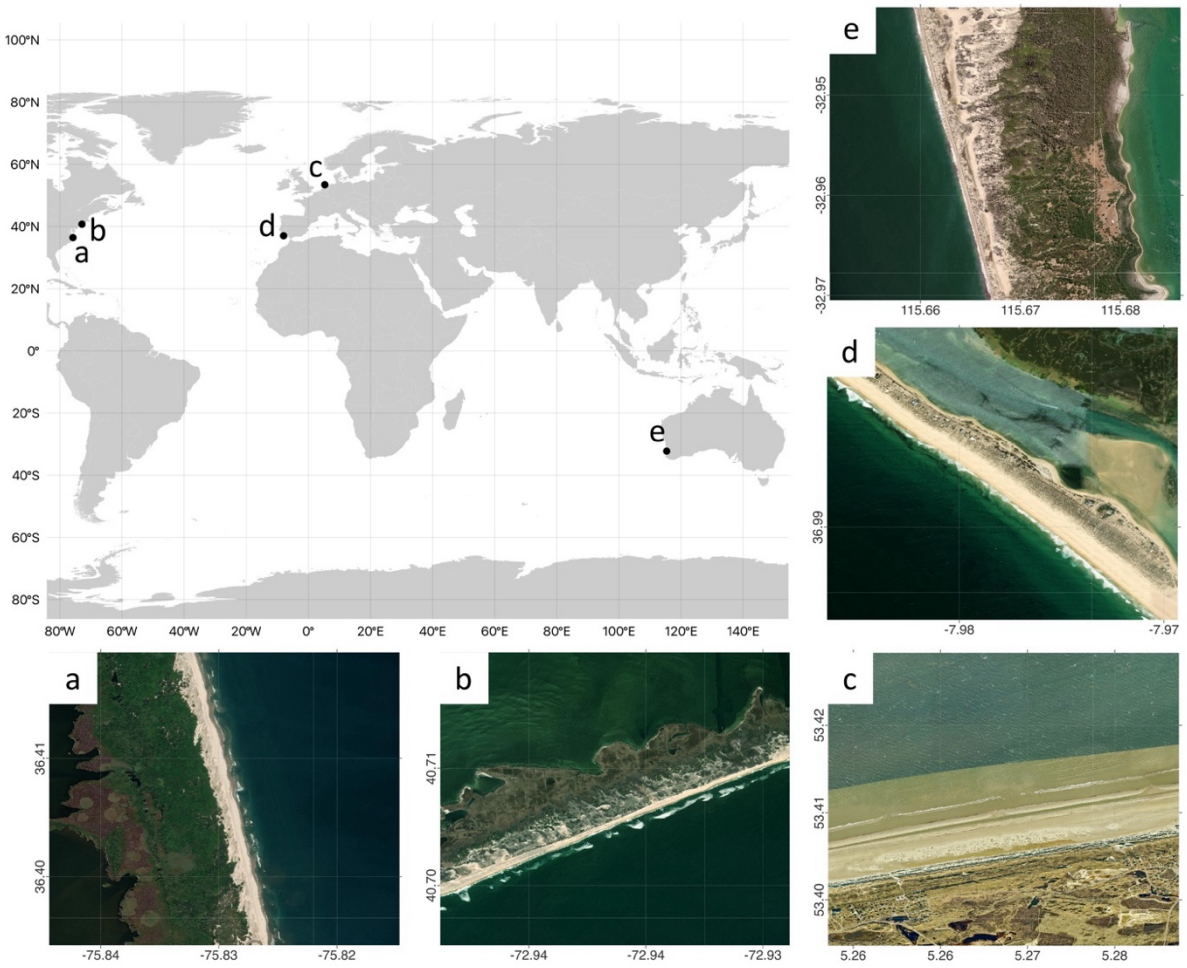

Figure 3.1 Location of coastal barriers and analysed 2 km-long sectors in: a) the Outer Banks in the USA, b) Fire Island in the USA, c) Terschelling in the Netherlands, d) Ria Formosa in southern Portugal and e) Myalup in Australia. Source: ESRI World Imagery.

3.2.4 Horizontal and vertical datum correction

To ensure a consistent comparison of the datasets, the GDEMs and GBMs (Table 3.1 and Table 3.3) were reprojected to the horizontal datum of the high-resolution data (Table 3.2 and Table 3.4). The vertical datums for the DEMs in the USA were corrected using the National Oceanic and Atmospheric Administration (NOAA) Vertical Datum Transformation VDatum software version v4.4.2, in the Netherlands using the RDNAPTRANS 2018 parameters in combination with PROJ6, in Australia with the AUSGeoid2020 and in the Ria Formosa with the local mean sea level from the openly available dataset by Cyrille et al. (2021).

3.2.5 Cleaning of spikes and water bodies removal

A preliminary analysis was carried out across entire sectors of the coastal barriers to detect gaps and remove inaccuracies and spikes. A visual inspection of the spikes against ESRI satellite imagery revealed that most spikes were located near water bodies or associated with the presence of buildings in backbarrier areas (for Faro and Terschelling). In the case of buildings, even if these were avoided through the careful selection of profile locations, their influence can still affect the surrounding area due to the coarse resolution of the GDEMs. The Euro-Maps 3D, Copernicus GLO-30 and AW3D30 datasets have already been processed with gap filling and error detection algorithms (Marešová et al., 2021; Takaku et al., 2020) and didn't require further correction. However, TanDEM-X presented several spikes, mostly at the ocean-land interface, and these were manually removed (Figure 3.2). The Water Indication Mask included in the TanDEM-X auxiliary files (Wendleder et al., 2012; Wessel, 2018) was used to remove water bodies from the GDEM, excluding pixels with a low interferometric coherence (mask values greater than 33) from the analysis. For Euro-Maps 3D, Copernicus GLO-30 and AW3D30, the water pixels were already flagged as zero.

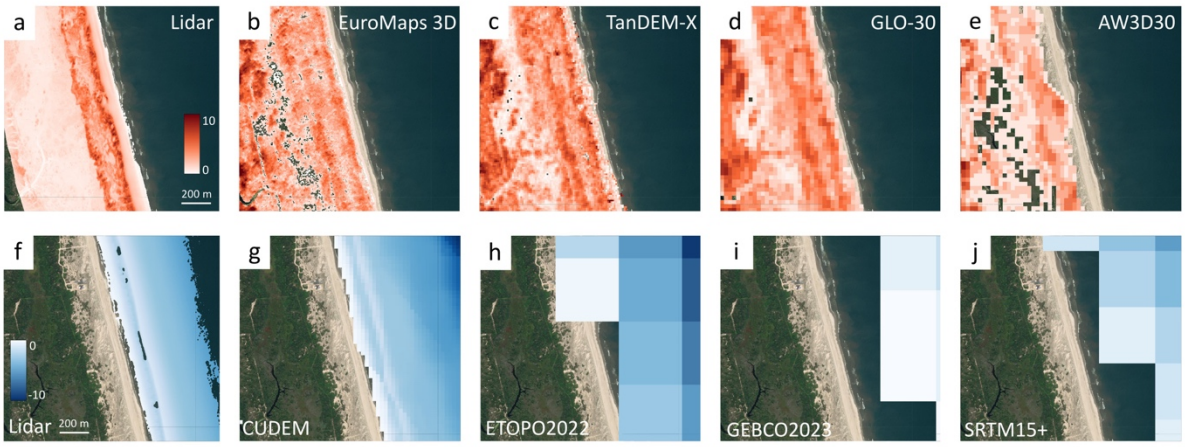

Figure 3.2 Visualisation of topographic (a-e) and bathymetric (f-j) data at the Outer Banks, USA, displaying the different resolutions according to the data source. All GDEMs and GBMs are reprojected into the same horizontal (EPSG:3631 NAD83) and vertical (NAVD88) datum.

3.2.6 DEM resampling

To better compare the cross-shore profiles of the coastal barriers, all GDEMs and GBMs were resampled using the QGIS SAGA "Resampling" tool to match the LiDAR's resolution and obtain a smoother profile. A bilinear interpolation method was tested using a weighted average of the nearest 4 cells, alongside a bicubic spline interpolation, which fits a smooth curve through the nearest 16 cell centres, and a B-spline interpolation, which is a smooth surface passing through the input points, minimizing the total curvature. Previous studies on spatial interpolation methods for DEMs have shown that higher-order interpolation methods, such as bicubic and biquadratic (Kidner, 2003; Shi et al., 2014, 2005) or spline (Her et al., 2015), are more accurate than bilinear interpolation. However, other authors suggested that case-specific interpolation methods should be employed (El-Quilish et al., 2018; Smith et al., 2004). The differences in the DEMs obtained from the three interpolation methods tested at the sites of interest were not relevant, and the bilinear method was chosen because of its better performance when compared to the LiDAR data.

3.2.7 Error metrics

The vertical error of the GDEMs and GBMs was evaluated by subtracting the LiDAR-derived reference elevation (h_{LiDAR}) from the topographic or bathymetric DEM (h_{DEM}) at each pixel (*i*) along a ~2 km natural sector of the coastal barriers (1 km for Praia de Faro due to the presence of buildings):

$$\Delta h_i = h_{i,LiDAR} - h_{i,DEM} \tag{3.1}$$

The vertical accuracy of the GDEMs and GBMs was assessed using the root mean square error (RMSE), Pearson's correlation coefficient (R), standard deviation (STD), mean absolute error (MAE), bias and the linear error at the 90th percentile (LE90), calculated as:

$$RMSE = \sqrt{\frac{1}{N}\sum_{i=1}^{N} \Delta h_i^2} \tag{3.2}$$

$$R = \frac{\sum_{i=1}^{N}(h_{i,LiDAR} - \overline{h_{i,LiDAR}})(h_{i,DEM} - \overline{h_{i,DEM}})}{\sqrt{\sum_{i=1}^{N}(h_{i,LiDAR} - \overline{h_{i,LiDAR}})^2 \sum_{i=1}^{N}(h_{i,DEM} - \overline{h_{i,DEM}})^2}} \tag{3.3}$$

$$STD = \sqrt{\frac{1}{N-1}\sum_{i=1}^{N}(\Delta h_i - ME)^2} \tag{3.4}$$

$$MAE = \frac{1}{N}\sum_{i=1}^{N} |h_{i,LiDAR} - h_{i,DEM}| = \frac{1}{N}\sum_{i=1}^{N} |\Delta h_i| \tag{3.5}$$

$$Bias = \frac{1}{N}\sum_{i=1}^{N} h_{i,LiDAR} - h_{i,DEM} = \frac{1}{N}\sum_{i=1}^{N} \Delta h_i \tag{3.6}$$

$$LE90 = Q_{|\Delta h|}(0.9) \tag{3.7}$$

where N is the total number of pixels considered when extracting the profiles from the LiDAR and the interpolated GDEMs and GBMs.

3.2.8 Merging of topo-bathymetry

After assessing the overall accuracy of the GDEMs and GBMs along a ~2 km natural sector of the coastal barriers, an area of ~300 m alongshore was selected for each site to extract cross-shore barrier profiles. These areas were defined as having homogeneous characteristics in terms of dune and beach morphology, and areas with either high (arboreal) vegetation or infrastructure (roads, walls or small buildings scattered among the natural dunes) were avoided. Along the natural areas selected, cross-shore profiles were extracted at 30 m intervals (chosen to match the resolution of the coarser GDEM), aligned at the dune crest (i.e. profile origin) and averaged to obtain a single profile representative of the selected area. After averaging, a local regression smoothing method (*LOESS interpolation*) was applied to preserve the peaks while smoothing any spike at the tails of the profiles. The bathymetry was also extracted along the same profiles, extending offshore to approximately 30 m water depth. To ensure spatial agreement between topographic and bathymetric datasets, the same horizontal shift used for aligning the topographic profiles to the dune crest was applied to the corresponding bathymetric profiles, and the GBMs and RBMs were also averaged into a single profile representative of the selected sector for each coastal barrier.

To merge the LiDAR-derived topographies with the RBMs, the most seaward intersecting point was chosen to prioritise the dataset with higher resolution, i.e. the LiDAR-derived topo-bathymetries. An equilibrium profile was then implemented to merge the topographic and bathymetric profiles, as there is high topographic variability in the upper shoreface and inaccurate or absent bathymetric information in the shallow nearshore area in the GDEMs and GBMs, respectively. The equilibrium profile was applied under the assumption that the selected areas have sufficient sediment supply and are in equilibrium conditions with the hydrodynamic forcing. The concept of an equilibrium profile configuration on sandy beaches was first developed by Bruun (1954) as a simple empirical relationship between the cross-shore profile depth (y) and the distance offshore from the shoreline (x), and later modified by Dean (1991):

$$y = Ax^{2/3} = 0.067 * w_s^{0.44} \tag{3.8}$$

where A is the sediment-dependent scale parameter obtained from the sediment fall velocity w_s, determined according to the median sediment grain size (*D50*) (Soulsby, 1997). The use of Dean's (1991) equilibrium profile has the advantage of simplicity as it depends on a single site-

specific parameter, the *D50*, and it represents the concave-up nearshore shape typically found on wave-dominated barriers. However, due to the lack of sediment information in many coastal areas, in this case the Dean profile was derived by fitting the equilibrium curve from the mean sea level (z ~ 0) to the point where the GBM intersects the depth of closure (d_c). This is the depth beyond which the bottom changes and sediment transport become negligible at an annual scale, which Dean (2003) considered to be the limit of the equilibrium profile. For defining the d_c the formula proposed by Hallermeier (1981) for sandy beaches was used:

$$d_c = 2.28H_{12h/y} - 68.5(H_{12h/y}^2/gT_{12h/y}^2) \quad (3.9)$$

where $H_{12h/y}$ is the significant wave height that is exceeded for 12 hours per year (or the wave height with 0.137% probability of occurrence in one year), $T_{12h/y}$ is the associated wave period and g is the acceleration of gravity. Wave data (significant wave height and peak period) were retrieved from the WAVERYS global wave reanalysis (Law-Chune et al., 2021) for the nearshore area of each study site. This reanalysis has a temporal resolution of 3 hours for the years 1993 to 2021 and a spatial resolution of 0.2°x0.2°. The extracted significant wave heights were first calibrated to account for WAVERYS underestimation in coastal areas (Eq. 10 in Fanti et al., 2023). In this way, instead of first selecting a specific *D50* value, which is often neither available nor clearly specified from where it was obtained in the field (Aragonés et al., 2016), and only then estimating the equilibrium profile, the depth of closure is used to determine the extent of the equilibrium profile and thus the A parameter in Eq. (3.8). The corresponding values of *D50* were then compared to values retrieved from the literature (Table S3.4) to check plausibility of the result obtained and were considered acceptable if in the range of fine to medium sand (0.125 mm to 0.5 mm, Wentworth, 1922).

3.3 Results

3.3.1 Evaluation of GDEMs' elevation accuracy

The vertical errors of the GDEMs were assessed across the study sites and showed varying levels of accuracy compared to the high-resolution DEMs (Figure 3.3), with the largest gaps observed in the intertidal zone (Figure 3.2), where land and water surfaces dynamically interact. Copernicus GLO-30 exhibited vertical RMSE values between 1.11 m and 2.54 m, while

AW3D30 showed RMSE values between 1.59 m and 2.76 m. For TanDEM-X the range of RMSE values was lower, between 1.19 m and 1.84 m, while Euro-Maps 3D had similar RMSE values for the Outer Banks and Ria Formosa study sites (1.32 m and 1.20 m, respectively). The LE90 values were found to be consistent with those reported by the data providers (Table 3.1) but also showed variability across sites, ranging from 1.81 m to 3.90 m for Copernicus GLO-30, 2.61 m to 4.72 m for AW3D30, 1.82 m to 2.73 m for TanDEM-X and remaining relatively consistent for Euro-Maps 3D (2.09 m and 1.92 m). In comparison, TanDEM-X outperformed the other GDEMs with an average RMSE of 1.41 m, a correlation coefficient R of 0.84, an MAE of 1.06 m and an LE90 of 2.29 m (Table 3.5). For the sites where the higher resolution Euro-Maps 3D data were available (the Outer Banks and the Ria Formosa) TanDEM-X remained the most accurate, followed by Euro-Maps 3D and Copernicus GLO-30 that showed similar accuracy, while AW3D30 presented the highest RMSE, MAE and STD (Table S3.1). AW3D30 and Copernicus GLO-30 evidence a consistent tendency to underestimate the elevation of coastal barriers, while TanDEM-X is found to have lower and overall positive bias (Figure 3.4). A general underestimation of the dune crest height was observed for all GDEMs.

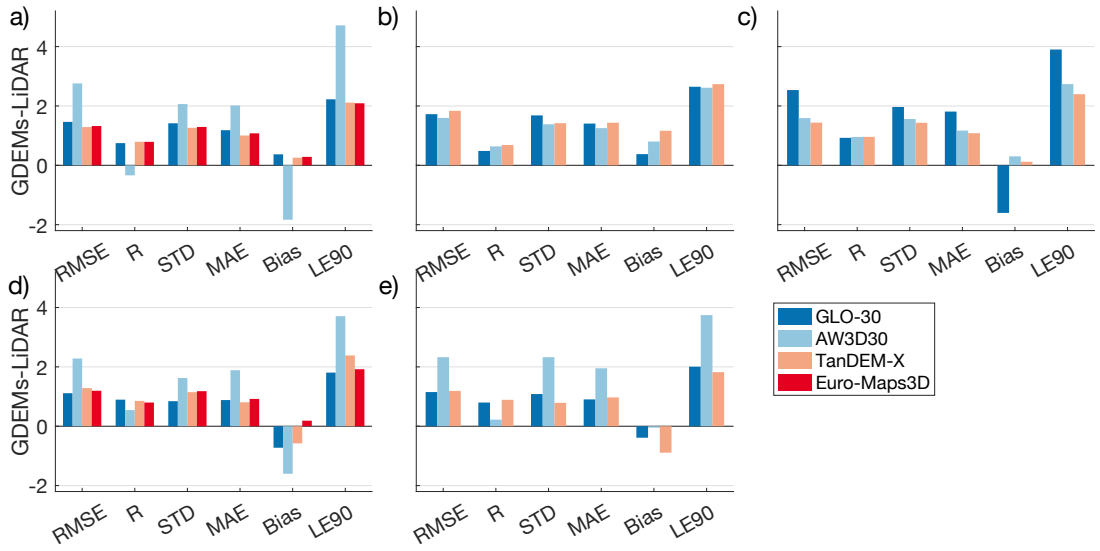

Figure 3.3 Error metrics between GDEMs and high-resolution LiDAR-derived DEMs for cross-shore profiles extracted at the Outer Banks in the USA (a), Fire Island in the USA (b), Terschelling in the Netherlands (c), Ria Formosa in southern Portugal (d) and Myalup in Australia (e).

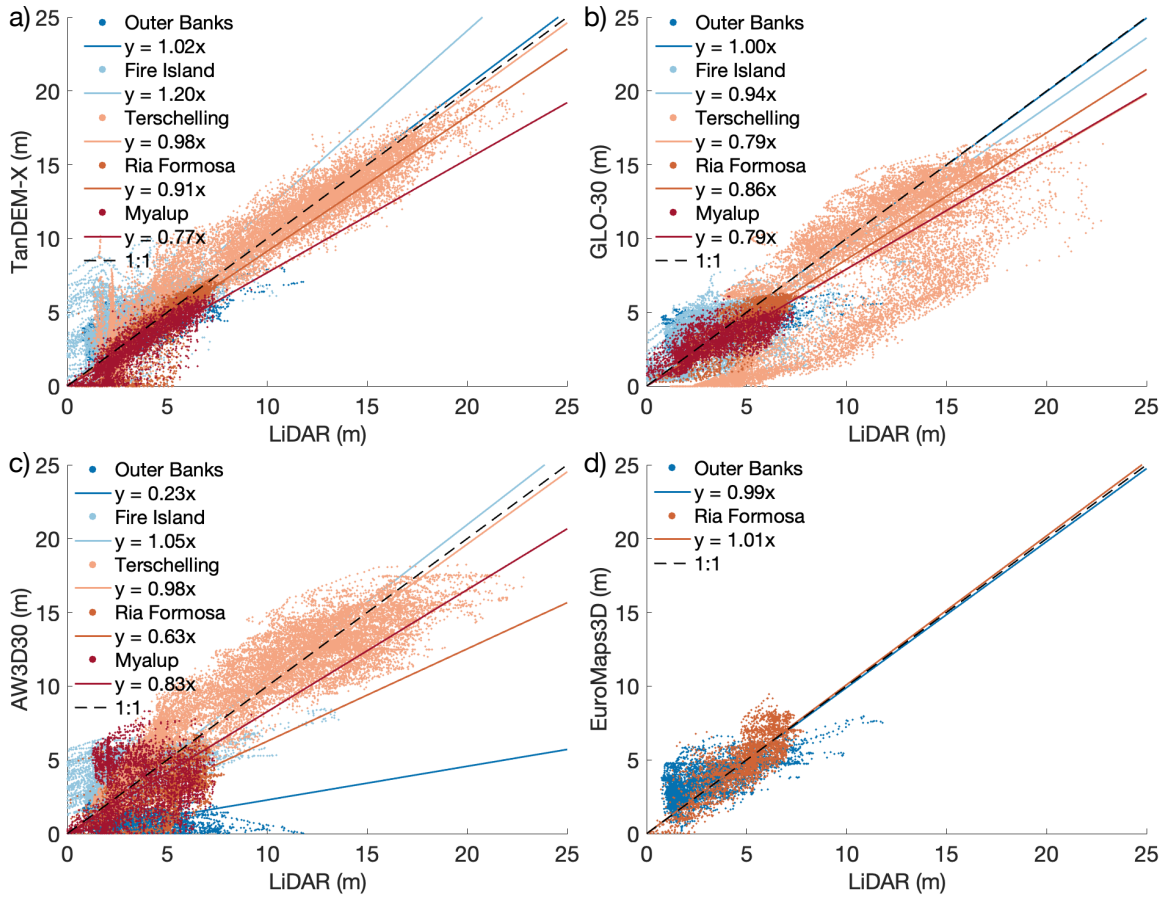

Figure 3.4 Comparison between LiDAR-derived elevation and GDEMs for a) TanDEM-X, b) Copernicus GLO-30), c) AW3D30 and d) Euro-Maps 3D. Linear regression lines (forced through the origin) are shown along with their equation for each location. The dashed black line represents a perfect fit.

When averaging alongshore the profiles, the average profile derived from TanDEM-X provided a better representation of the dune crest height, dune face slope, dune leeward slope (Figure 3.5) and the overall topographic profile at all locations, with an average correlation coefficient of 0.95 and a RMSE of 0.98 m, while those derived from AW3D30 consistently underestimated the dune top and slope with an average bias of -0.55 m and a RMSE of 1.54 m (Table 3.5). The profiles derived from Euro-Maps 3D performed similarly to those derived from TanDEM-X, with larger errors on the dune face.

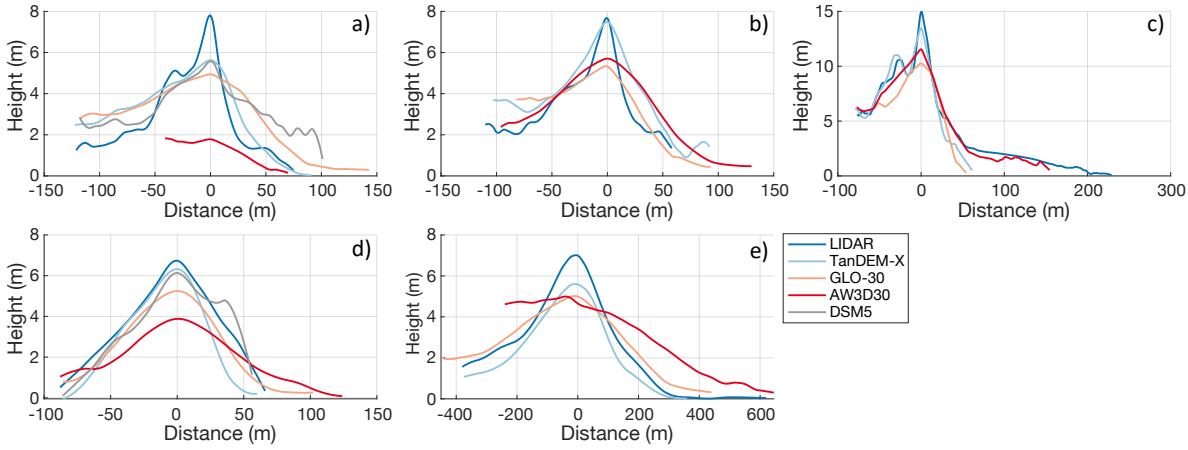

Figure 3.5 Averaged topographic profiles aligned at the dune top (x = 0 m) derived from LiDAR and GDEMs at the Outer Banks in the USA (a), Fire Island in the USA (b), Terschelling in the Netherlands (c), Ria Formosa in southern Portugal (d) and Myalup in Australia (e). The ocean is to the right of the profiles.

Table 3.5 Statistical comparison of LiDAR-derived topography and bathymetry against GDEMs/GBMs (from 0 m to ~10 m depth) averaged over all study sites for three cases: a) estimated for all profiles, b) for the average profiles and c) for the merged topo-bathymetric profile obtained from TanDEM-X and ETOPO 2022. Euro-Maps 3D is not included here as data were only available for 2 of the 5 sites.

Dataset			**RMSE (m)**	**R (-)**	**STD (m)**	**MAE (m)**	**Bias (m)**	**LE90 (m)**
All profiles	**Topography**	Copernicus GLO-30	1.60	0.77	1.40	1.24	-0.39	2.52
		AW3D30	2.11	0.40	1.79	1.66	-0.48	3.50
		TanDEM-X	1.41	0.84	1.21	1.06	0.01	2.29
	Bathymetry	SRTM15+V2.0	3.43	0.86	1.80	2.88	1.18	4.78
		GEBCO_2023	2.01	0.98	1.04	1.73	1.58	3.01
		ETOPO 2022	1.81	0.96	1.42	1.27	0.98	2.90
Average profiles	**Topography**	Copernicus GLO-30	1.20	0.91	0.95	1.00	-0.32	1.97
		AW3D30	1.54	0.91	1.14	1.25	-0.55	2.56
		TanDEM-X	0.98	0.95	0.69	0.80	-0.12	1.62
	Bathymetry	SRTM15+V2.0	2.93	0.97	1.31	2.54	2.01	3.75
		GEBCO_2023	1.96	0.99	0.92	1.74	1.64	3.03
		ETOPO 2022	1.83	0.97	1.42	1.32	0.87	2.78
Merged profile	**Topo-bathymetry**	TanDEM-X + ETOPO 2022	0.76	0.99	0.75	0.55	0.01	1.25

3.3.2 Evaluation of GBMs' depth accuracy

Similarly to remotely sensed topographic data, GBMs have increased uncertainties in shallow coastal areas compared to the open ocean. This is related to the dynamic nature of the nearshore morphology, and to the fact that GBMs are derived from merging of bathymetric data from different years. From a visual inspection, the GBMs showed larger deviations between each other from 0 m to ~15 m depth, while converging towards a more consistent bathymetric profile with increasing water depth.

The vertical errors of the GBMs vary considerably between the study sites (Figure 3.6), with SRTM15+ displaying the largest errors overall, with RMSE values ranging from 1.25 m at Fire Island to 4.87 m at the Outer Banks and a strong bias in the Ria Formosa. Conversely, ETOPO 2022 and GEBCO 2023 were found to have similar and better overall performance compared to SRTM15+ when averaged over the five coastal barriers, with ETOPO 2022 showing higher accuracy (Table 3.5). The RBMs, such as CUDEM in the USA sites, EMODnet in Europe and the 2023 bathymetric grid of Australia, display high accuracy, with lower RMSE, STD, MAE, Bias and LE90 values compared to the GBMs (Figure 3.6, Table S3.2 and Table S3.3).

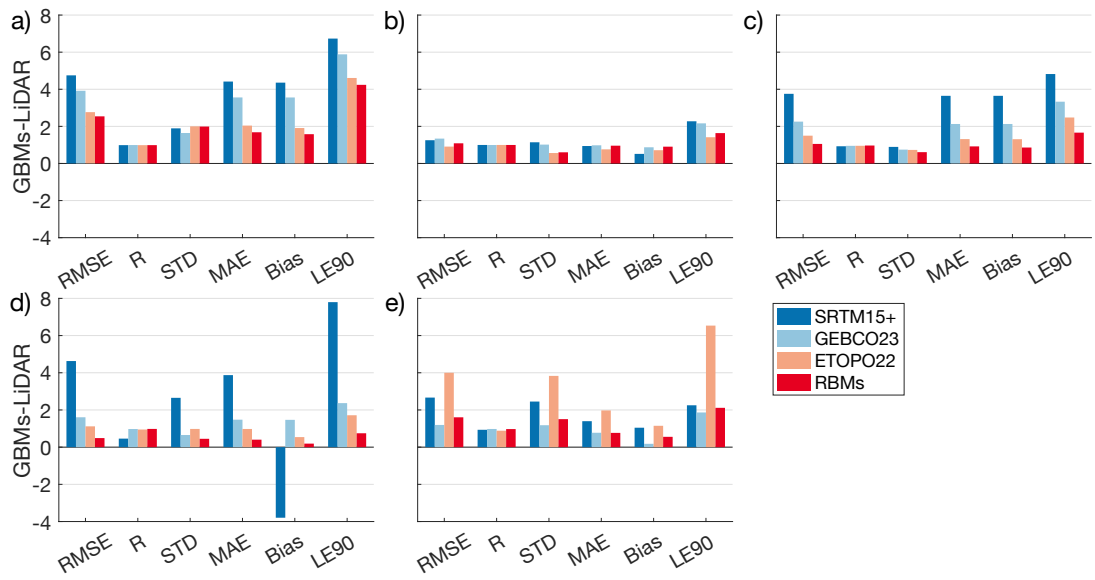

Figure 3.6 Error metrics between GBMs and RBMs (CUDEM, EMODnet, 2023 bathymetry of Australia) and high-resolution LiDAR-derived DEMs for cross-shore profiles extracted at the Outer Banks in the USA (a), Fire Island in the USA (b), Terschelling in the Netherlands (c), Ria Formosa in southern Portugal (d) and Myalup in Australia (e).

The regional differences in the accuracy of GBMs were partially explained by the information available in the TID grid for GEBCO 2023 (which is identical to GEBCO 2022 TID) and SID for ETOPO 2022 (Figure S3.9).

The largest errors in ETOPO 2022 were found at Myalup, where the GEBCO_2022 was used, with 50% of the data coming from an unknown source. For GEBCO_2023 the largest error was observed in the Outer Banks, where 21% of the sampled data were based on multiple indirect measurements (satellite-derived gravity data or interpolated bathymetric soundings) that were merged in a relatively small region. In contrast, data from the remaining sites were mostly derived from direct measurements and therefore more accurate. The statistical accuracy of the average bathymetric profiles (Figure 3.7) showed a slight improvement compared to the single profiles (Table 3.5), with ETOPO 2022 showing the highest accuracy across the study sites and SRTM15 v2.0 the lowest.

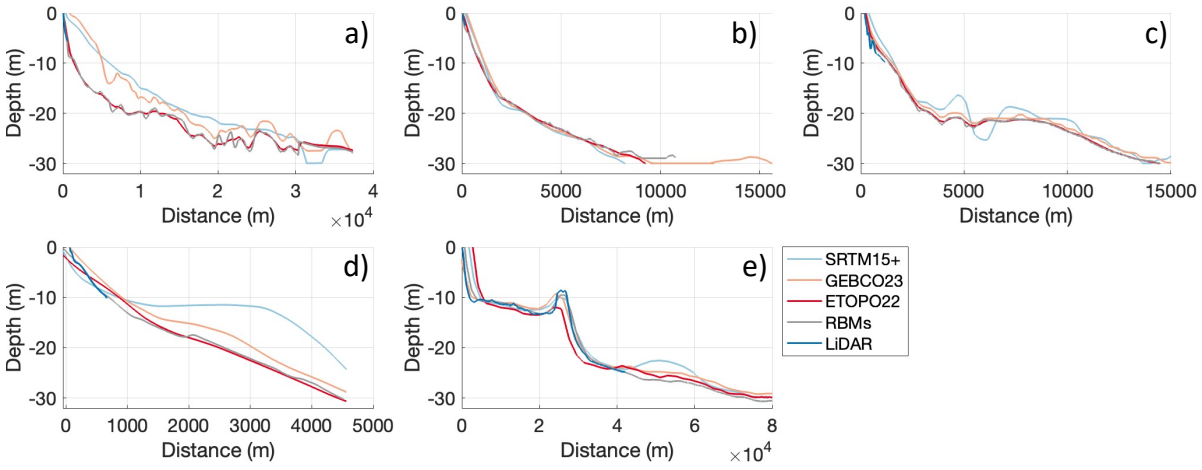

Figure 3.7 Averaged bathymetric profiles derived from LiDAR, RBMs and GBMs at the Outer Banks in the USA (a), Fire Island in the USA (b), Terschelling in the Netherlands (c), Ria Formosa in southern Portugal (d) and Myalup in Australia (e).

3.3.3 Merging of topo-bathymetry and profile elevation accuracy

The merged averaged profiles derived from the GDEMs and GBMs were compared with averaged profiles obtained by merging the LiDAR-derived DEMs with the RBMs. The profile derived from merging TanDEM-X and ETOPO 2022 (Figure 3.8 and Table S3.4) showed a high performance in terms of statistical fit (low values of MAE, RMSE and bias), although with larger deviations in Myalup. The values estimated for D50 based on profiles derived from

merging ETOPO 2022 bathymetry with any GDEM evidence better agreement with the values obtained from the literature (Table S3.4), while the profiles derived from merging SRTM15+V2.0 and the GDEMs showed the worst performance (Table S3.4).

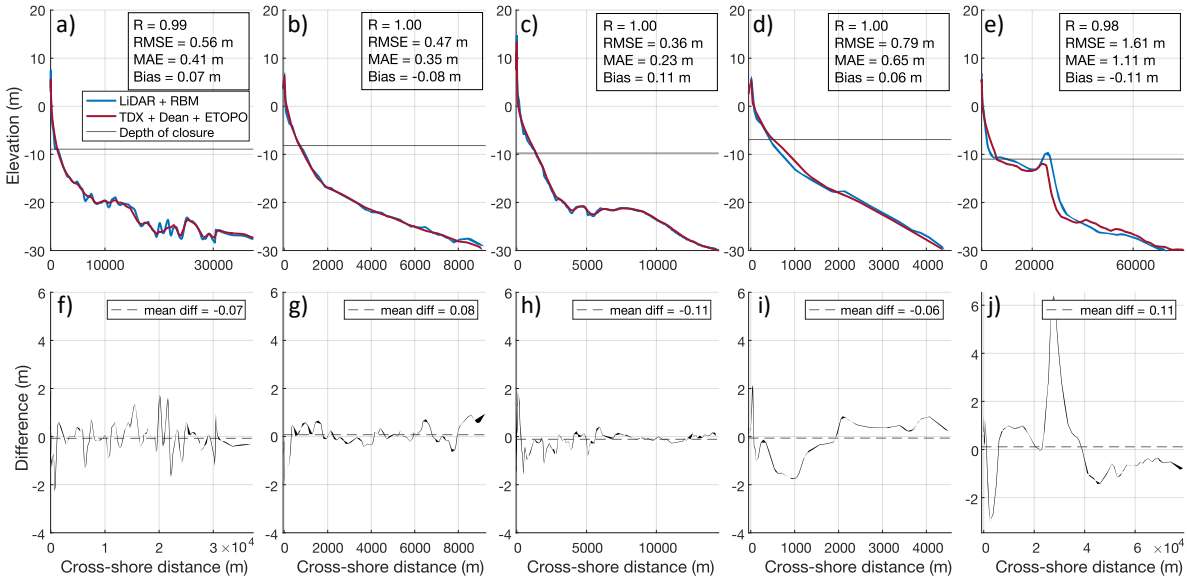

Figure 3.8 Top (a to e): Merged topo-bathymetric profiles obtained from LiDAR topography and regional bathymetries (blue line) compared with profiles obtained from merging the equilibrium profile with the TanDEM-X topography and ETOPO 2022 bathymetry (red line). Bottom (f to j): Plot of differences (in meters) between the higher resolution topo-bathymetry derived from merging LiDAR and RBMs and the topo-bathymetry derived from merging TanDEM-X GDEM with ETOPO 2022 GBM. The profiles refer to the coastal barriers at the Outer Banks in the USA (a, f), Fire Island in the USA (b, g), Terschelling in the Netherlands (c, h), Ria Formosa in southern Portugal (d, i) and Myalup in Australia (e, j).

3.4 Discussion

3.4.1 Performance of global and regional models

The vertical error assessment of the GDEMs revealed varying levels of accuracy across the study sites. Overall, the RMSE, STD, LE90 and ME determined in the present study are consistent with previous accuracy assessments for the 12 m-resolution TanDEM-X (Chu and Lindenschmidt, 2017; Gesch, 2018; Li et al., 2021; Vassilaki and Stamos, 2020; Wessel et al., 2018; Zhang et al., 2019), AW3D30 (Ding et al., 2023; Gesch, 2018; Li et al., 2022; Takaku et al., 2020; Vassilaki and Stamos, 2020), Copernicus GLO-30 (Hawker et al., 2022; Li et al., 2022) and Euro-Maps 3D (Proietti et al., 2017), with L90 within the range disclosed by each

DEM provider (Table 3.1). However, the errors found in this study were shown to be generally lower than previous assessments. This occurs for several reasons: the evaluation was performed after removing water bodies and spikes in intertidal areas and resampling GDEMs to the LiDAR-derived DEM resolution; the study areas correspond to natural sectors of coastal barriers where buildings and tall vegetation are absent, so there are fewer artefacts in the GDEMs (Gdulová et al., 2021; Wessel et al., 2018; Zhang et al., 2019); areas with lower slopes are normally associated to higher GDEM accuracy (Li et al., 2022). The largest gaps in the data were found in the intertidal area, where SAR processing is more challenging due to the low backscatter combined with complex coastal morphology, resulting in noisy relief data (Rizzoli et al., 2017; Wendleder et al., 2012). Moreover, cloud cover and homogeneous surfaces such as sand can hinder the processing of optical stereo imagery (Gesch, 2012; Takaku et al., 2020).

According to the statistical evaluation, TanDEM-X outperformed other GDEMs for the characterised coastal barriers (Table 3.5), in line with previous work by Vassilaki and Stamos (2020) for a range of latitudes, terrain types and land cover classes, and by Li et al. (2021) for different slopes. The performance of Euro-Maps 3D was slightly worse than TanDEM-X, possibly due to the superiority of the SAR sensors over optical sensors (Vassilaki and Stamos, 2020). This was followed by Copernicus GLO-30, which outperformed the other 30 m resolution GDEM, AW3D30, as already verified in Greece (Grigoriadis et al., 2023) and China (Li et al., 2022).

Beyond standard error metrics, when analysing the performance of GDEMs in coastal barriers with a focus on coastal hazards assessments, the dune crest height and beach slope have a critical role in the selection of the best GDEM. An overall underestimation of the dune crest was observed for all GDEMs (Figure 3.5), as well as a tendency to overestimate the beach slope, as previously observed for several GDEMs (Almar et al., 2021b; Diaz et al., 2019). Considering this, TanDEM-X was shown to be the GDEM of choice for representing coastal barrier morphology, as it was found to outperform all other GDEMs, including the Euro-Maps 3D commercial dataset. TanDEM-X also provides a better representation of the dune morphology, possibly because Euro-Maps 3D data are stored as integers, which can lead to the flattening of peak values.

Regarding the nearshore bathymetry, which has a fundamental role in wave transformation processes near the coast and, therefore, on coastal flooding (Parodi et al., 2020), storm impact and sea level assessments, or even for the definition of process-based indicators for coastal hazards (Ferreira et al., 2017), there are fewer intercomparisons between GBMs and a higher uncertainty on their overall quality. Moreover, the footprint of altimeter pulses is relatively large, resulting in a limited ability to capture fine-scale details of the seafloor in nearshore areas, while at the same time this dynamic coastal environment is subject to complex morphological features (sandbars, rhythmic forms, channels) and processes (tides, wave action, currents, and sediment transport).

To quantify the uncertainties in the bathymetric data for the selected coastal barriers, three GBMs and three RBMs were evaluated against higher resolution bathymetric data available for areas shallower than -10 m. The GBMs considered here showed lower RMSE, STD and MAE values (Figure 3.6) compared to previous assessments (Li et al., 2023; Vrdoljak, 2021). This is likely explained by the smoothing that resulted from the interpolation applied to resample the GBM cell size to that of the LiDAR-derived DEMs, as well as by the fact that in some areas GBMs integrate higher resolution data, as is the case for GEBCO 2023. The GBMs tend to agree with each other in deeper areas most likely because they are based on the same source for those depths (GEBCO Bathymetric Compilation Group, 2023; NOAA National Centers for Environmental Information, 2022). ETOPO 2022 outperformed all other GBMs across the five locations (Table 3.5). It was followed by GEBCO 2023, which had a similar performance, while SRTM15+V2.0 showed the largest errors. This may be due to the fact that GEBCO 2023 is based on SRTM15+V2.0 and augmented by direct soundings and ETOPO 2022 is based on GEBCO 2022, also augmented with local higher resolution data. When available, RBMs should be the bathymetric dataset of choice. Otherwise, and considering the frequent updates of GBMs, the latest versions and models should be preferred.

3.4.2 Challenges for the topo-bathymetric continuum in poorly surveyed areas

The coastal topo-bathymetric continuum can be derived from different sensors, with different levels of accuracy and resolution (Li et al., 2023) and presenting different challenges (Eakins and Grothe, 2014). New products have recently been developed to map the intertidal area at higher resolution from space-borne data (Cesbron et al., 2021), including from Pleiades satellite imagery (Almar et al., 2019; Almeida et al., 2019), but also from Sentinel imagery (Almar et

al., 2021a; Darmanin et al., 2023; Fitton et al., 2021; Khan et al., 2019) and from VENμS (Bergsma et al., 2021). However, only altimeter-derived gravity data from satellites can currently provide global coverage of the ocean floor, although with lower resolution, and therefore most of the published GBMs are still based on this technology. For this reason, the use of GBMs and GDEMs is inevitable for global (e.g. Muis et al., 2020; Parodi et al., 2020; Sepúlveda et al., 2020; Vousdoukas et al., 2020) and regional assessments (e.g. Bove et al., 2020; Gesch, 2009), and they remain a valuable option in remote or poorly surveyed areas where high quality alternatives are absent (Parodi et al., 2020; Vousdoukas et al., 2022).

This study complements previous assessments of large-scale remote sensing-based DEM products proposing a new method to improve the application of GDEMs and GBMs in coastal barriers, characterized by the presence of dune morphologies. The methodology was developed by averaging topo-bathymetric DEMs along homogeneous sectors and replacing missing or inaccurate data in the shallow coastal area with an equilibrium nearshore profile. Given the lack of site-specific grain size information in many coastal areas around the world, an indirect method was applied to derive an empirical fitting by forcing it from the mean sea level to the offshore location where the bathymetry reaches the depth of closure, similar to Holman et al. (2014). The depth of closure was estimated using 28 years of wave data from WAVERYS global wave reanalysis, averaged to avoiding tying the analysis to a specific year or event. The depth of closure formulation from Hallermeier (1981) was adopted, which does not account for non-wave forces (such as the tide) but is a suitable approximation to define the limit of the active coastal zone. The equilibrium profile based on Dean (1991) represents a simplification, and more accurate formulations have been developed to account for the tide (de Villar et al., 2019) and sandbanks (Holman et al., 2014), but these require detailed local data and cannot be generalised to data poor areas. Therefore, the approach proposed in this study represents an improvement given the lack of accurate bathymetric data from the GBMs and an equilibrium profile that represents wave energy dissipation across the surf zone better than a linear slope. Nevertheless, given the impossibility of accounting for dynamic sandbars that are relevant for specific events and areas, it is an adequate approximation for engineering to geological scales and idealised simulations.

Furthermore, previous studies have found equilibrium profiles to be a valuable approximation for nearshore bathymetry, for example when pre-storm bathymetric data are lacking (Matheen et al., 2021). The equilibrium profiles obtained using the method described above were

compared with equilibrium profiles obtained using actual D50 values found in the literature for the same coastal areas, except for Myalup where the existence of rocky outcrops on part of the nearshore may justify the large differences between GBMs and multibeam data in the nearshore area. Based on the combinations of GDEMs and GBMs tested, the ones with ETOPO 2022 consistently outperformed other GBMs (Table S3.4).

The newly developed method proposed in this work involves the merging of multiple barrier profiles, resulting in the transformation of the existing data from global models into a single simplified and representative profile for a given coastal sector (Figure 3.8). The comparison of the seamless topo-bathymetric profiles derived from the global models with the LiDAR-derived topo-bathymetries demonstrates that the combination of TanDEM-X GDEM and ETOPO 2022 GBM delivered the best results. This is evident both in terms of statistical comparison to the higher-resolution LiDAR-derived profiles, with an average RMSE of 0.76 m, and in terms of an accurate representation of the dune morphology, with a lower average underestimation of the dune crest by TanDEM-X of only 1.14 m. An overall underestimation of the dune height is observed for all GDEMs (with an average underestimation of 2.68 m for Copernicus GLO-30, 3.25 m for AW3D30 and 6.50 m for Euro-Maps 3D), as well as the absence of a beach berm due to their coarse resolution (Figure 3.5). Such underestimation of morphological features that determine the protective role of coastal barriers can lead to an overestimation of the vulnerability for natural coastal barriers in regional to global studies (Vousdoukas et al., 2018, 2016). This can result, for example in the lowering of thresholds that determine the occurrence of storm-induced overwash or inundation (Sallenger, 2000). The use of the best possible approach (TanDEM-X) is therefore essential in the application of global models for the definition of coastal hazards and risks. Nevertheless, hazard evaluations derived using GDEMs and GBMs could be considered as worst-case estimates of the possible coastal hazards. Moreover, given the overall RMSE found (Figure 3.8), the use of the barrier profiles derived from GDEMs and GBMs for coastal flooding assessments due to a sea level rise of less than one meter is severely limited.

The findings in this study highlight the critical importance of incorporating a range of vertical uncertainties associated with GDEMs, both when considered individually and when used as merged topo-bathymetric profiles. All GBMs showed an overall positive bias (Table 3.5), as previously demonstrated in the case of SRTM (Bove et al. 2020 and references therein),

resulting in a shallower coastal profile and contributing to an inaccurate consideration of the wave energy dissipation by wave models. A shallower nearshore bathymetry also influences the calculation of storm surge and water levels, increasing the uncertainty in the determination of coastal flooding and erosion hazards. The errors in the GDEMs and GBMs were found to be spatially variable and mainly dependent on slope (Diaz et al., 2019; Li et al., 2022), land cover and terrain type (Leon et al., 2014; Li et al., 2022, 2021), and therefore not easily represented by a single dispersion parameter, such as the RMSE (Leon et al., 2014). For this reason, in coastal barriers it is important to consider the overall RMSE of the topo-bathymetric merged profile, but also the bias and underestimation of the dune crest in GDEMs and nearshore slope in GBMs.

An intrinsic limitation of the barrier profiles obtained by the integration of GDEMs and GBMs is related to the fact that these are neither time nor event-specific. The data were collected over several years and seasons (Wendleder et al., 2012), and therefore cannot be used to infer variability over time. The interpolation, first in the resampling of the GBMs and GDEMs and then in the alongshore averaging, introduces errors for length scales smaller than the resolution of the original data. The profiles must be considered as generalized morphologies that can be easily implemented to identify and prioritize flooding and erosion hotspots or to estimate geoindicators, such as dune elevation, volume and width as proposed by Carapuço et al. (2016) and dune stability factors (Armaroli et al., 2012; Turner et al., 2024). These profiles can also be useful for rapid assessments at large scales (global, national, or regional), or in areas where higher resolution topo-bathymetric data does not exist. The approach proposed in this study is meant for morphologically homogeneous areas along coastal barriers but could be also implemented in all sandy coasts fronted by sparsely vegetated dunes. The main advantage of the presented methodology is that it allows to extract continuous coastal barrier profiles from which profile indicators can be readily extracted as in Athanasiou et al. (2023). The topo-bathymetric coastal barrier profiles derived in this work, together with their associated errors, offer a valuable, coherent and sufficiently accurate solution for quantifying exposure to coastal hazards at global scales. They can support first order assessments that help to identify and prioritize coastal risk areas that can then be further studied using higher-resolution data.

3.5 Conclusion

Topo-bathymetric profiles of coastal barriers were developed by merging GDEMs and GBMs with an equilibrium beach profile derived by estimating the averaged depth of closure. The combination of TanDEM-X and ETOPO 2022 performed better in terms of statistical accuracy when compared to high-resolution LiDAR-derived profiles and in terms of morphological characterisation of the coastal barrier, particularly the dune crest height and beach slope. LiDAR-derived DEMs can provide accurate results at the centimetre scale to capture small changes in topo-bathymetry, but have limitations in terms of spatial coverage, cost, and other logistical challenges. Therefore, the integrated topo-bathymetric profiles proposed here, derived from global open-access remotely sensed datasets, can provide a cost-effective and readily available solution for coastal hazard assessments over large geographical areas on a global scale, provided their uncertainties are considered. They can be used across wide areas as a preliminary tool for managing coastal zones, contributing to identifying areas potentially vulnerable to coastal flooding, storm-induced erosion, and sea level rise. Ultimately, they can enable the understanding and mitigation of the impacts of natural hazards on society and risk analysis, which detailed local scale assessments can later address.

3.6 Acknowledgements

Valeria Fanti is funded through the FCT PhD Research Scholarships program (ref. 2020.07553.BD). This work was supported by the Portuguese Foundation of Science, under the projects LA/P/0069/2020 granted to the Associate Laboratory ARNET, UIDP/00350/2020 granted to CIMA (https://doi.org/10.54499/UIDP/00350/2020), and CEECINST/00052/2021/CP2792/CT0011 granted to Carlos Loureiro (https://doi.org/10.54499/CEECINST/00052/2021/CP2792/CT0011).

The TanDEM-X DEM tiles were provided by the German Aerospace Center (Proposal ID: DEM_HYDR3317). COP-DEM-GLO-30-R and EURO-MAPS 3D DSM products © DLR e.V. (2014-2018) and © Airbus Defence and Space GmbH (2021) provided under COPERNICUS by the European Union and ESA.WAVERYS data were downloaded from the CMEMS Portal (https://resources.marine.copernicus.eu) dataset "GLOBAL_REANALYSIS_WAV_001_032".

3.7 Appendix A. Supplementary data

Table S3.6 Average GDEM performance statistics. All GDEMs are averaged only for two sites, Outer Banks in the USA and Ria Formosa in Portugal due to the restricted availability of Euro-Maps3D.

GDEM	RMSE (m)	R (-)	STD (m)	MAE (m)	Bias (m)	LE90 (m)
Copernicus GLO-30	1.29	0.82	1.13	1.03	-0.18	2.02
AW3D30	2.52	0.10	1.84	1.95	-1.72	4.21
TanDEM-X	1.29	0.82	1.21	0.91	-0.16	2.25
Euro-Maps3D	1.26	0.79	1.24	1.00	0.24	2.01

Table S3.7 Average GBM performance statistics. All GBMs are averaged only for two sites, Outer Banks and Fire Islands in the USA due to the availability of CUDEM data only for the USA.

GBM	RMSE (m)	R (-)	STD (m)	MAE (m)	Bias (m)	LE90 (m)
SRTM15+V2.0	3.00	0.99	1.52	2.68	2.44	4.50
GEBCO_2023	2.63	0.99	1.33	2.27	2.21	4.02
ETOPO 2022	1.84	0.99	1.28	1.40	1.31	3.01
CUDEM	1.81	0.99	1.30	1.32	1.24	2.94

Table S3.8 Average GBM performance statistics. All GBMs are averaged only for two sites, Praia de Faro in Portugal and Terschelling in the Netherlands due to the availability of EMODnet data only for the European coast.

GBM	RMSE (m)	R (-)	STD (m)	MAE (m)	Bias (m)	LE90 (m)
SRTM15+V2.0	4.19	0.69	1.77	3.76	-0.07	6.31
GEBCO_2023	1.93	0.96	0.70	1.80	1.80	2.85
ETOPO 2022	1.31	0.95	0.85	1.15	0.92	2.10
EMODnet	0.77	0.97	0.53	0.66	0.52	1.20

Table S3.9 Depth of closure (Dc) calculated with wave height and peak period from the entire WAVERYS series ($H_{12h/y}$, $T_{12h/y}$), median grain size (D50) from the literature and statistical results from the comparison of the profiles obtained merging of GDEMs and GBMs and the profile obtained from LiDAR-derived DEMs and RBMs. D50 values in red are out of the acceptable range of fine (0.125 - 0.25 mm) to medium (0.25 - 0.5 mm) sand. The colour scale (blue for higher accuracy, red for lower accuracy) of the mean absolute error (MAE) and root mean squared error (RMSE) is based on the highest and lowest values amongst all sites. The colour scale of the bias is based on the highest and lowest absolute values.

Location	Depth of closure	D50 literature	GDEM	GBM	D50 (mm)	R (-)	MAE (m)	RMSE (m)	Bias (m)
Outer Banks, USA	$H_{12h/y}$ = 4.30 m $T_{12h/y}$ = 12.04 s Dc = -8.92 m	D50 = 0.2-0.3 mm (CSE, 2015; Grasso et al., 2009; Safak et al., 2017; Splinter et al., 2014)	TanDEM-X	GEBCO 2023	0.06	0.97	2.99	3.58	2.82
				ETOPO 2022	0.18	0.99	0.41	0.56	0.07
				SRTM15+V2.0	0.05	0.94	3.83	4.59	3.28
			Copernicus GLO-30	GEBCO 2023	0.06	0.97	3.04	3.66	2.87
				ETOPO 2022	0.20	0.99	0.42	0.59	0.08
				SRTM15+V2.0	0.06	0.94	3.77	4.47	3.21
			AW3D30	GEBCO 2023	0.06	0.97	2.99	3.59	2.82
				ETOPO 2022	0.18	0.99	0.41	0.57	0.07
				SRTM15+V2.0	0.05	0.94	3.84	4.60	3.28
Fire Island, USA	$H_{12h/y}$ = 4.07 m $T_{12h/y}$ = 10.18 s Dc = -8.17 m	D50 = 0.2-0.4 mm (Kana et al., 2011)	TanDEM-X	GEBCO 2023	0.22	1.00	0.75	0.93	-0.06
				ETOPO 2022	0.33	1.00	0.35	0.47	-0.08
				SRTM15+V2.0	0.22	1.00	0.90	1.07	-0.29
			Copernicus GLO-30	GEBCO 2023	0.20	1.00	0.75	0.94	-0.07
				ETOPO 2022	0.30	1.00	0.34	0.45	-0.09
				SRTM15+V2.0	0.21	1.00	0.88	1.05	-0.33
			AW3D30	GEBCO 2023	0.22	1.00	0.76	0.96	-0.05
				ETOPO 2022	0.35	1.00	0.36	0.51	-0.07
				SRTM15+V2.0	0.22	1.00	0.91	1.10	-0.28
Terschelling, Netherlands	$H_{12h/y}$ = 5.03 m $T_{12h/y}$ = 10.13 s Dc = -9.74 m	D50 = 0.18-0.21 mm (Athanasiou et al., 2021; Pilarczyk et al., 1989)	TanDEM-X	GEBCO 2023	0.17	1.00	0.83	0.89	0.78
				ETOPO 2022	0.18	1.00	0.23	0.36	0.11
				SRTM15+V2.0	0.16	0.98	1.65	1.93	1.15
			Copernicus GLO-30	GEBCO 2023	0.16	1.00	0.84	0.91	0.78
				ETOPO 2022	0.18	1.00	0.22	0.39	0.08
				SRTM15+V2.0	0.16	0.97	1.64	1.94	1.12
			AW3D30	GEBCO 2023	0.18	1.00	0.84	0.91	0.83
				ETOPO 2022	0.20	1.00	0.23	0.37	0.15

				SRTM15+V2.0	0.17	0.98	1.66	1.95	1.19
Ria Formosa, Portugal	$H_{12h/y}$ = 3.38 m $T_{12h/y}$ = 10.10 s Dc = -6.93 m	D50 = 0.5 mm (Kombiadou et al., 2021; Poelhekke et al., 2016)	TanDEM-X	GEBCO 2023	0.25	1.00	1.98	2.08	1.93
				ETOPO 2022	0.33	1.00	0.65	0.79	0.06
				SRTM15+V2.0	0.53	0.92	6.15	7.19	5.97
			Copernicus GLO-30	GEBCO 2023	0.27	1.00	2.01	2.09	1.97
				ETOPO 2022	0.36	1.00	0.67	0.80	0.09
				SRTM15+V2.0	0.94	0.92	6.16	7.19	5.97
			AW3D30	GEBCO 2023	0.31	1.00	2.06	2.13	1.98
				ETOPO 2022	0.43	1.00	0.72	0.87	0.10
				SRTM15+V2.0	1.27	0.93	6.18	7.18	5.96
Myalup, Australia	$H_{12h/y}$ = 5.71 m $T_{12h/y}$ = 14.10 s Dc = -11.87 m	D50 = 0.22 mm (Short, 2022)	TanDEM-X	GEBCO 2023	0.06	0.99	1.15	1.33	0.89
				ETOPO 2022	0.06	0.98	1.11	1.61	-0.11
				SRTM15+V2.0	0.06	0.99	1.24	1.68	1.05
			Copernicus GLO-30	GEBCO 2023	0.06	0.99	1.17	1.37	0.93
				ETOPO 2022	0.07	0.98	1.08	1.58	-0.13
				SRTM15+V2.0	0.06	0.99	1.26	1.71	1.09
			AW3D30	GEBCO 2023	0.06	0.99	1.20	1.41	0.97
				ETOPO 2022	0.07	0.98	1.11	1.61	-0.10
				SRTM15+V2.0	0.06	0.99	1.29	1.74	1.12

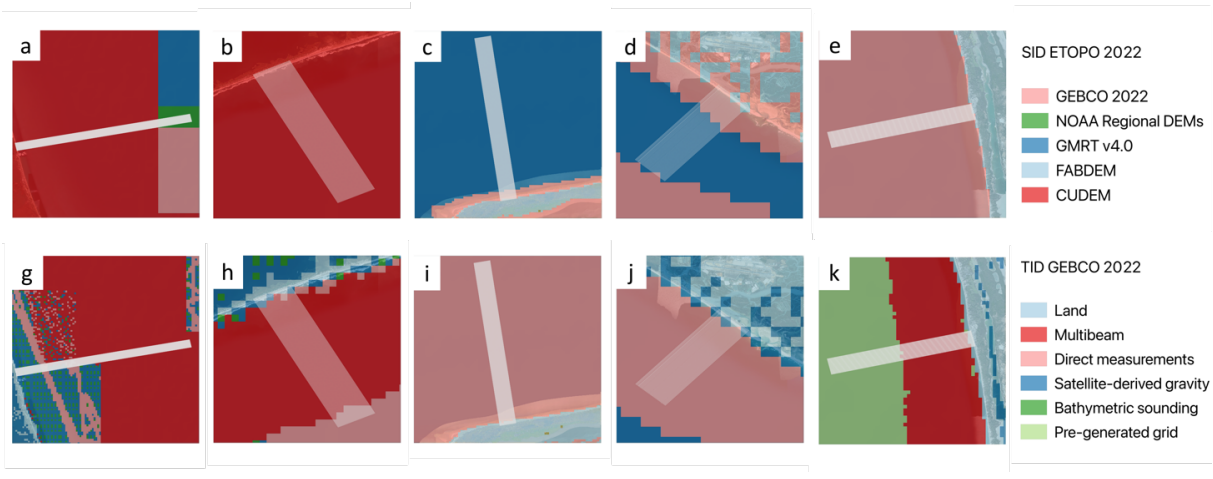

Figure S3.9 Source ID grids from ETOPO 2022 (a to e) and Type Identifier grids from GEBCO 2022 (f to j) for the Outer Banks in the USA (a-f), Fire Island in the USA (b-g), Terschelling in the Netherlands (c-h), Ria Formosa in Portugal (d-i), Myalup in Australia (e-j). For each coastal barrier the extracted cross-shore profiles until 30 m depth are represented in white.

3.8 References

Almar, R., Bergsma, E.W.J., Maisongrande, P., de Almeida, L.P.M., 2019. Wave-derived coastal bathymetry from satellite video imagery: A showcase with Pleiades persistent mode. Remote Sens. Environ. 231, 111263. https://doi.org/10.1016/j.rse.2019.111263

Almar, R., Bergsma, E.W.J., Thoumyre, G., Baba, M.W., Cesbron, G., Daly, C., Garlan, T., Lifermann, A., 2021a. Global satellite-based coastal bathymetry from waves. Remote Sens. 13, 1–13. https://doi.org/10.3390/rs13224628

Almar, R., Ranasinghe, R., Bergsma, E.W.J., Diaz, H., Melet, A., Papa, F., Vousdoukas, M., Athanasiou, P., Dada, O., Almeida, L.P., Kestenare, E., 2021b. A global analysis of extreme coastal water levels with implications for potential coastal overtopping. Nat. Commun. 12, 1–9. https://doi.org/10.1038/s41467-021-24008-9

Almeida, L.P., Almar, R., Bergsma, E.W.J., Berthier, E., Baptista, P., Garel, E., Dada, O.A., Alves, B., 2019. Deriving high spatial-resolution coastal topography from sub-meter satellite stereo imagery. Remote Sens. 11, 590. https://doi.org/10.3390/rs11050590

Amante, C.J., Love, M., Carignan, K., Sutherland, M.G., MacFerrin, M., Lim, E., 2023. Continuously updated digital elevation models (CUDEMs) to support coastal inundation modeling. Remote Sens. 15, 1702. https://doi.org/10.3390/rs15061702

Aragonés, L., Serra, J.C., Villacampa, Y., Saval, J.M., Tinoco, H., 2016. New methodology for describing the equilibrium beach profile applied to the Valencia's beaches. Geomorphology 259, 1–11. https://doi.org/10.1016/j.geomorph.2015.06.049

Archer, L., Neal, J., Bates, P., House, J., 2018. Comparing TanDEM-X data with frequently-used DEMs for flood inundation modeling. Water Resour. Res. 54, 10–205. https://doi.org/https://doi.org/10.1029/2018WR023688

Armaroli, C., Ciavola, P., Perini, L., Calabrese, L., Lorito, S., Valentini, A., Masina, M., 2012. Critical storm thresholds for significant morphological changes and damage along the Emilia-Romagna coastline, Italy. Geomorphology 143–144, 34–51. https://doi.org/10.1016/j.geomorph.2011.09.006

Ashphaq, M., Srivastava, P.K., Mitra, D., 2021. Review of near-shore satellite derived bathymetry: Classification and account of five decades of coastal bathymetry research. J. Ocean Eng. Sci. 6, 340–359. https://doi.org/10.1016/j.joes.2021.02.006

Athanasiou, P., van Dongeren, A., Giardino, A., Vousdoukas, M.I., Antolinez, J.A.A., Ranasinghe, R., 2021. A clustering approach for predicting dune morphodynamic response to storms using typological coastal profiles: a case study at the dutch coast. Front. Mar. Sci. 8, 1–20. https://doi.org/10.3389/fmars.2021.747754

Athanasiou, P., van Dongeren, A., Pronk, M., Giardino, A., Vousdoukas, M.I., Ranasinghe, R., 2023. Global Coastal Characteristics (GCC): A global dataset of geophysical, hydrodynamic and socioeconomic coastal indicators (submitted for publication). Earth Syst. Sci. Data Discuss.

Beaman, R., 2023. AusBathyTopo 250m (Australia) 2023 - A High-resolution Depth Model for Australia. https://doi.org/https://dx.doi.org/10.26186/148758

Bergsma, E.W.J., Almar, R., Rolland, A., Binet, R., Brodie, K.L., Bak, A.S., 2021. Coastal morphology from space: A showcase of monitoring the topography-bathymetry continuum. Remote Sens. Environ. 261, 112469. https://doi.org/10.1016/j.rse.2021.112469

Bishop-Taylor, R., Sagar, S., Lymburner, L., Beaman, R.J., 2019. Between the tides: Modelling the elevation of Australia's exposed intertidal zone at continental scale. Estuar. Coast. Shelf Sci. 223, 115–128. https://doi.org/10.1016/j.ecss.2019.03.006

Bove, G., Becker, A., Sweeney, B., Vousdoukas, M.I., Kulp, S., 2020. A method for regional estimation of climate change exposure of coastal infrastructure: Case of USVI and the influence of digital elevation models on assessments. Sci. Total Environ. 710, 136162. https://doi.org/10.1016/j.scitotenv.2019.136162

Bruun, P., 1954. Coast erosion and the development of beach profiles, US Beach Erosion Board. Washington DC.

Caballero, I., Stumpf, R.P., 2019. Retrieval of nearshore bathymetry from Sentinel-2A and 2B satellites in South Florida coastal waters. Estuar. Coast. Shelf Sci. 226, 106277. https://doi.org/10.1016/j.ecss.2019.106277

Carapuço, M.M., Taborda, R., Silveira, T.M., Psuty, N.P., Andrade, C., Freitas, M.C., 2016. Coastal geoindicators: Towards the establishment of a common framework for sandy coastal environments. Earth-Science Rev. 154, 183–190. https://doi.org/10.1016/j.earscirev.2016.01.002

Cesbron, G., Melet, A., Almar, R., Lifermann, A., Tullot, D., Crosnier, L., 2021. Pan-European Satellite-derived coastal bathymetry—review, user needs and future services. Front. Mar. Sci. 8, 1–15. https://doi.org/10.3389/fmars.2021.740830

Chu, T., Lindenschmidt, K.E., 2017. Comparison and validation of digital elevation models derived from InSAR for a flat inland delta in the high latitudes of Northern Canada. Can. J. Remote Sens. 43, 109–123. https://doi.org/10.1080/07038992.2017.1286936

Collins, J., Riegler, G., Schrader, H., Tinz, M., 2015. Applying terrain and hydrological editing to TanDEM-X data to create a consumer-ready WorldDEM product. Int. Arch. Photogramm. Remote Sens. Spat. Inf. Sci. 40, 1149–1154. https://doi.org/10.5194/isprsarchives-XL-7-W3-1149-2015

Cooper, J.A.G., Green, A.N., Loureiro, C., 2018. Geological constraints on mesoscale coastal barrier behaviour. Glob. Planet. Change 168, 15–34. https://doi.org/10.1016/j.gloplacha.2018.06.006

Crippen, R., Buckley, S., Agram, P., Belz, E., Gurrola, E., Hensley, S., Kobrick, M., Lavalle, M., Martin, J., Neumann, M., Nguyen, Q., Rosen, P., Shimada, J., Simard, M., Tung, W., 2016. NASADEM global elevation model: Methods and progress. Int. Arch. Photogramm. Remote Sens. Spat. Inf. Sci. 41, 125–128. https://doi.org/10.5194/isprsarchives-XLI-B4-125-2016

CSE, 2015. APPENDIX C - GEOTECHNICAL DATA REPORT Beach Restoration to Protect NC Highway 12 at Buxton, Dare County, North Carolina.

Cyrille, P., Gael, B., Anthony, S., 2021. Global estimated surfaces of Lowest Astronomical Tide (LAT) and Mean Sea Level (MSL) [WWW Document]. SEANOE. https://doi.org/https://doi.org/10.17882/85408

Darmanin, G., Gauci, A., Deidun, A., Galone, L., D'Amico, S., 2023. Satellite-derived bathymetry for selected shallow Maltese coastal zones. Appl. Sci. 13, 5238. https://doi.org/10.3390/app13095238

de Villar, A.C., Gómez-Pina, G., Muñoz-Pérez, J.J., Contreras, F., López-García, P., Ruiz-Ortiz, V., 2019. New design parameters for biparabolic beach profiles (SW Cadiz, Spain). Rev. la Constr. 18, 432–444. https://doi.org/10.7764/RDLC.18.3.432

Dean, Robert G, 1991. Equilibrium beach profiles: Characteristics and applications. J. Coast. Res. 7, 53–84.

Dean, R.G., 2002. Beach nourishment: theory and practice, Vol. 18. ed. World scientific. https://doi.org/https://doi.org/10.1142/2160

Diaz, H., Almar, R., Bergsma, E.W.J., Leger, F., 2019. On the use of satellite-based Digital Elevation Models to determine coastal topography. Int. Geosci. Remote Sens. Symp. 8201–8204. https://doi.org/10.1109/IGARSS.2019.8899189

Ding, H., Liu, J., Yang, S., Luo, J., Liu, Y., Jiang, S., Fu, Y., Liang, X., Na, J., 2023. Performance assessment of global open-access digital elevation models in China mainland coastal region. Earth Surf. Process. Landforms 48, 2133–2140. https://doi.org/10.1002/esp.5677

Direcção-Geral do Território, 2011. Modelo Digital do Terreno das Zonas Costeiras de Portugal Continental com resolução de 2 m (600 m mar , 400 m terra) - LiDAR. Lisboa.

Eakins, B.W., Grothe, P.R., 2014. Challenges in building coastal digital elevation models. J. Coast. Res. 30, 942–953. https://doi.org/10.2112/JCOASTRES-D-13-00192.1

El-Quilish, M., El-Ashquer, M., Dawod, G., El-Fiky, G., 2018. Development and accuracy assessment of high-resolution digital elevation model using GIS approaches for the Nile Delta Region, Egypt. Am. J. Geogr. Inf. Syst. 7, 107–117. https://doi.org/10.5923/j.ajgis.20180704.02

Fahrland, E., Jacob, P., Schrader, H., Kahabka, H., 2020. Copernicus digital elevation model product handbook, Airbus Defence and Space—Intelligence: Potsdam. Germany.

Fandé, M.B., Lira, C.P., Penha-Lopes, G., 2022. Using TanDEM-X Global DEM to Map Coastal Flooding Exposure under Sea-Level Rise : Application to Guinea-Bissau. Int. J. Geo-Information 11, 1–20.

Fanti, V., Ferreira, Ó., Kuemmerer, V., Loureiro, C., 2023. Improved estimates of extreme wave conditions in coastal areas from calibrated global reanalyses. Commun. Earth Environ. 4, 151. https://doi.org/https://doi.org/10.1038/s43247-023-00819-0

Farr, T.G., Rosen, P.A., Caro, E., Crippen, R., Duren, R., Hensley, S., Kobrick, M., Paller, M., Rodriguez, E., Roth, L., Seal, D., 2007. The shuttle radar topography mission. Rev. Geophys. 45, 1–33. https://doi.org/10.1007/3-540-44818-7_11

Ferreira, Ó., Plomaritis, T.A., Costas, S., 2017. Process-based indicators to assess storm induced coastal hazards. Earth-Science Rev. 173, 159–167. https://doi.org/10.1016/j.earscirev.2017.07.010

Fitton, J.M., Rennie, A.F., Hansom, J.D., Muir, F.M.E., 2021. Remotely sensed mapping of the intertidal zone: A Sentinel-2 and Google Earth Engine methodology. Remote Sens. Appl. Soc. Environ. 22, 100499. https://doi.org/10.1016/j.rsase.2021.100499

Gdulová, K., Marešová, J., Barták, V., Szostak, M., Červenka, J., Moudrý, V., 2021. Use of tandem-x and srtm-c data for detection of deforestation caused by bark beetle in central european mountains. Remote Sens. 13, 1–17. https://doi.org/10.3390/rs13153042

GEBCO Bathymetric Compilation Group, 2023. The GEBCO_2023 Grid. https://doi.org/doi:10.5285/f98b053b-0cbc-6c23-e053-6c86abc0af7b

Gesch, D.B., 2018. Best practices for elevation-based assessments of sea-level rise and coastal flooding exposure. Front. Earth Sci. 6. https://doi.org/10.3389/feart.2018.00230

Gesch, D.B., 2012. Global digital elevation model development from satellite remote-sensing data, in: Advances in Mapping from Remote Sensor Imagery: Techniques and Applications. pp. 92–109. https://doi.org/10.1201/b13770-5

Gesch, D.B., 2009. Analysis of lidar elevation data for improved identification and delineation of lands vulnerable to sea-level rise. J. Coast. Res. 2009, 49–58. https://doi.org/10.2112/SI53-006.1

Gharagozlou, A., Dietrich, J.C., Karanci, A., Luettich, R.A., Overton, M.F., 2020. Storm-driven erosion and inundation of barrier islands from dune-to region-scales. Coast. Eng. 158, 103674. https://doi.org/10.1016/j.coastaleng.2020.103674

González, C., Bachmann, M., Bueso-Bello, J.L., Rizzoli, P., Zink, M., 2020. A fully automatic algorithm for editing the TanDEM-X global DEM. Remote Sens. 12, 1–23. https://doi.org/10.3390/rs12233961

Grasso, F., Michallet, H., Barthélemy, E., Certain, R., 2009. Physical modeling of intermediate cross-shore beach morphology: Transients and equilibrium states. J. Geophys. Res. Ocean. 114, 1–15. https://doi.org/10.1029/2009JC005308

Grigoriadis, V.N., Andritsanos, V.D., Natsiopoulos, D.A., 2023. Validation of Recent DSM/DEM/DBMs in Test Areas in Greece Using Spirit Leveling, GNSS, Gravity and Echo Sounding Measurements. ISPRS Int. J. Geo-Information 12. https://doi.org/10.3390/ijgi12030099

Hallermeier, R., 1981. A profile zonation for seasonal sand beaches from wave climate. Coast. Eng. 4, 253–277.

Hawker, L., Bates, P., Neal, J., Rougier, J., 2018a. Perspectives on digital elevation model (DEM) simulation for flood modeling in the absence of a high-accuracy open access global DEM. Front. Earth Sci. 6, 1–9. https://doi.org/10.3389/feart.2018.00233

Hawker, L., Rougier, J., Neal, J., Bates, P., Archer, L., Yamazaki, D., 2018b. Implications of simulating global digital elevation models for flood inundation studies. Water Resour. Res. 54, 7910–7928. https://doi.org/10.1029/2018WR023279

Hawker, L., Uhe, P., Paulo, L., Sosa, J., Savage, J., Sampson, C., Neal, J., 2022. A 30 m global map of elevation with forests and buildings removed. Environ. Res. Lett. 17. https://doi.org/10.1088/1748-9326/ac4d4f

Her, Y., Heatwole, C.D., Kang, M.S., 2015. Interpolating SRTM elevation data to higher resolution to improve hydrologic analysis. J. Am. Water Resour. Assoc. 51, 1072–1087. https://doi.org/10.1111/jawr.12287

Holman, R.A., Lalejini, D.M., Edwards, K., Veeramony, J., 2014. A parametric model for barred equilibrium beach profiles. Coast. Eng. 90, 85–94. https://doi.org/10.1016/j.coastaleng.2014.03.005

IHO, 2023. Status of Hydrographic Surveying and Charting Worldwide.

IHO, 2022. Standards for Hydrographic Surveys.

IPCC, 2022. Climate Change 2022: Impacts, Adaptation and Vulnerability. Contribution of Working Group II to the Sixth Assessment Report of the Intergovernmental Panel on Climate Change. Cambridge University Press, Cambridge, UK and New York, NY, USA, Cambridge, UK and New York, NY, USA. https://doi.org/doi:10.1017/9781009325844

Irish, J.L., Frey, A.E., Rosati, J.D., Olivera, F., Dunkin, L.M., Kaihatu, J.M., Ferreira, C.M., Edge, B.L., 2010. Potential implications of global warming and barrier island degradation

on future hurricane inundation, property damages, and population impacted. Ocean Coast. Manag. 53, 645–657. https://doi.org/10.1016/j.ocecoaman.2010.08.001

Kana, T.W., Rosati, J.D., Traynum, S.B., 2011. Lack of evidence for onshore sediment transport from deep water at decadal time scales: Fire Island, New York. J. Coast. Res. 59, 61–75. https://doi.org/10.2307/29783103

Khan, M.J.U., Ansary, M.N., Durand, F., Testut, L., Ishaque, M., Calmant, S., Krien, Y., Saifu, A.K.M., Papa, F., 2019. High-resolution intertidal topography from Sentinel-2 multi-spectral imagery: synergy between remote sensing and numerical modeling. Remote Sens. 11, 1–20. https://doi.org/10.3390/rs11242888

Kidner, D.B., 2003. Higher-order interpolation of regular grid digital elevation models. Int. J. Remote Sens. 24, 2981–2987. https://doi.org/10.1080/0143116031000086835

Kombiadou, K., Costas, S., Roelvink, D., 2021. Simulating destructive and constructive morphodynamic processes in steep beaches. J. Mar. Sci. Eng. 9, 1–19. https://doi.org/10.3390/jmse9010086

Kulp, S., Strauss, B., 2019. New elevation data triple estimates of global vulnerability to sea-level rise and coastal flooding. Nat. Commun. 10, 1–12. https://doi.org/10.1038/s41467-019-12808-z

Kulp, S., Strauss, B., 2016. Global DEM errors underpredict coastal vulnerability to sea level rise and flooding. Front. Earth Sci. 4, 1–8. https://doi.org/10.3389/feart.2016.00036

Law-Chune, S., Aouf, L., Dalphinet, A., Levier, B., Drillet, Y., Drevillon, M., 2021. WAVERYS: a CMEMS global wave reanalysis during the altimetry period. Ocean Dyn. 71, 357–378. https://doi.org/10.1007/s10236-020-01433-w

Leon, J.X., Heuvelink, G.B.M., Phinn, S.R., 2014. Incorporating DEM uncertainty in coastal inundation mapping. PLoS One 9, e108727. https://doi.org/10.1371/journal.pone.0108727

Li, H., Zhao, J., Yan, B., Yue, L., Wang, L., 2022. Global DEMs vary from one to another: an evaluation of newly released Copernicus, NASA and AW3D30 DEM on selected terrains of China using ICESat-2 altimetry data. Int. J. Digit. Earth 15, 1149–1168. https://doi.org/10.1080/17538947.2022.2094002

Li, P., Li, Z., Dai, K., Al-Husseinawi, Y., Feng, W., Wang, H., 2021. Reconstruction and evaluation of DEMs from bistatic TanDEM-X SAR in mountainous and coastal areas of china. IEEE J. Sel. Top. Appl. Earth Obs. Remote Sens. 14, 5152–5170. https://doi.org/10.1109/JSTARS.2021.3073782

Li, Z., Peng, Z., Zhang, Z., Chu, Y., Xu, C., Yao, S., García-Fernández, Á.F., Zhu, X., Yue, Y., Levers, A., Zhang, J., Ma, J., 2023. Exploring modern bathymetry: A comprehensive review of data acquisition devices, model accuracy, and interpolation techniques for enhanced underwater mapping. Front. Mar. Sci. 10, 1–22. https://doi.org/10.3389/fmars.2023.1178845

Marešová, J., Gdulová, K., Pracná, P., Moravec, D., Gábor, L., Prošek, J., Barták, V., Moudrý, V., 2021. Applicability of data acquisition characteristics to the identification of local artefacts in global digital elevation models: Comparison of the Copernicus and TanDEM-X DEMs. Remote Sens. 13, 1–18. https://doi.org/10.3390/rs13193931

Mason, D.C., Garcia-Pintado, J., Cloke, H.L., Dance, S.L., 2015. The potential of flood forecasting using a variable-resolution global digital terrain model and flood extents from synthetic aperture radar images. Front. Earth Sci. 3, 1–14. https://doi.org/10.3389/feart.2015.00043

Mason, D.C., Trigg, M., Garcia-Pintado, J., Cloke, H.L., Neal, J.C., Bates, P.D., 2016. Improving the TanDEM-X Digital Elevation Model for flood modelling using flood extents from Synthetic Aperture Radar images. Remote Sens. Environ. 173, 15–28. https://doi.org/10.1016/j.rse.2015.11.018

Matheen, N., Harley, M.D., Turner, I.L., Splinter, K.D., Simmons, J.A., Thran, M.C., 2021. Bathymetric data requirements for operational coastal erosion forecasting using xbeach. J. Mar. Sci. Eng. 9. https://doi.org/10.3390/jmse9101053

Mayer, L., Jakobsson, M., Allen, G., Dorschel, B., Falconer, R., Ferrini, V., Lamarche, G., Snaith, H., Weatherall, P., 2018. The Nippon Foundation-GEBCO seabed 2030 project: The quest to see the world's oceans completely mapped by 2030. Geosci. 8. https://doi.org/10.3390/geosciences8020063

McBride, R.A., Anderson, J.B., Buynevich, I. V., Byrnes, M.R., Cleary, W., Fenster, M.S., FitzGerald, D.M., Hapke, C.J., Harris, M.S., Hein, C.J., Johnson, C.L., Klein, A.H.F., Liu, B., De Menezes, J.T., Mulhern, J.S., Oliver, T.S.N., Pejrup, M., Riggs, S.R., Roberts, H.H., Rodriguez, A.B., Seminack, C.T., Short, A.D., Stone, G.W., Tamura, T., Wallace, D.J., Wang, P., 2022. Morphodynamics of modern and ancient barrier systems: an updated and expanded synthesis, Treatise on Geomorphology. Elsevier. https://doi.org/10.1016/B978-0-12-818234-5.00153-X

Melet, A., Teatini, P., Le Cozannet, G., Jamet, C., Conversi, A., Benveniste, J., Almar, R., 2020. Earth observations for monitoring marine coastal hazards and their drivers, Surveys in Geophysics. Springer Netherlands. https://doi.org/10.1007/s10712-020-09594-5

Muis, S., Apecechea, M.I., Dullaart, J., de Lima Rego, J., Madsen, K.S., Su, J., Yan, K., Verlaan, M., 2020. A high-resolution global dataset of extreme sea levels, tides, and storm surges, including future projections. Front. Mar. Sci. 7, 1–15. https://doi.org/10.3389/fmars.2020.00263

Neumann, B., Vafeidis, A.T., Zimmermann, J., Nicholls, R.J., 2015. Future coastal population growth and exposure to sea-level rise and coastal flooding - A global assessment. PLoS One 10. https://doi.org/10.1371/journal.pone.0118571

Nguyen, T.T.X., Bonetti, J., Rogers, K., Woodroffe, C.D., 2016. Indicator-based assessment of climate-change impacts on coasts : A review of concepts , methodological approaches and vulnerability indices. Ocean Coast. Manag. 123, 18–43. https://doi.org/10.1016/j.ocecoaman.2015.11.022

NOAA National Centers for Environmental Information, 2022. ETOPO 2022 15 Arc-Second Global Relief Model. https://doi.org/https://doi.org/10.25921/fd45-gt74

Pacheco, A., Horta, J., Loureiro, C., Ferreira, Ó., 2015. Retrieval of nearshore bathymetry from Landsat 8 images: A tool for coastal monitoring in shallow waters. Remote Sens. Environ. 159, 102–116. https://doi.org/10.1016/j.rse.2014.12.004

Parodi, M.U., Giardino, A., Van Dongeren, A., Pearson, S.G., Bricker, J.D., Reniers, A.J.H.M., 2020. Uncertainties in coastal flood risk assessments in small island developing states. Nat. Hazards Earth Syst. Sci. 20, 2397–2414. https://doi.org/10.5194/nhess-20-2397-2020

PDOK L., 2017. Besteksvoorwaarden inwinning landsdekkende dataset AHN2014–2019: Technical Report 3.0 Final.

Pilarczyk, K.W., Verhagen, H.J., Roelse, P., Adriaanse, L., Consemulder, J., 1989. Handboek Zandsuppleties, uitgever waltman.

Pleskachevsky, A., Lehner, S., Heege, T., Mott, C., 2011. Synergy and fusion of optical and

synthetic aperture radar satellite data for underwater topography estimation in coastal areas. Ocean Dyn. 61, 2099–2120. https://doi.org/10.1007/s10236-011-0460-1

Poelhekke, L., Jäger, W.S., van Dongeren, A., Plomaritis, T.A., McCall, R., Ferreira, Ó., 2016. Predicting coastal hazards for sandy coasts with a Bayesian Network. Coast. Eng. 118, 21–34. https://doi.org/10.1016/j.coastaleng.2016.08.011

Proietti, S., Lorenzon, F., Uttenthaler, A., Klaus, A., Probeck, M., 2017. Overview of Global DEM: Assessment of the current global DEMs and requirements for an updated global DEM.

Rizzoli, P., Martone, M., Gonzalez, C., Wecklich, C., Borla Tridon, D., Bräutigam, B., Bachmann, M., Schulze, D., Fritz, T., Huber, M., Wessel, B., Krieger, G., Zink, M., Moreira, A., 2017. Generation and performance assessment of the global TanDEM-X digital elevation model. ISPRS J. Photogramm. Remote Sens. 132, 119–139. https://doi.org/10.1016/j.isprsjprs.2017.08.008

Safak, I., List, J.H., Warner, J.C., Kumar, N., 2017. Observations and 3D hydrodynamics-based modeling of decadal-scale shoreline change along the Outer Banks, North Carolina. Coast. Eng. 120, 78–92. https://doi.org/10.1016/j.coastaleng.2016.11.014

Salameh, E., Frappart, F., Almar, R., Baptista, P., Heygster, G., Lubac, B., Raucoules, D., Almeida, L.P., Bergsma, E.W.J., Capo, S., De Michele, M.D., Idier, D., Li, Z., Marieu, V., Poupardin, A., Silva, P.A., Turki, I., Laignel, B., 2019. Monitoring beach topography and nearshore bathymetry using spaceborne remote sensing: A review. Remote Sens. 11. https://doi.org/10.3390/rs11192212

Sallenger, J., 2000. Storm impact scale for barrier islands. J. Coast. Res. 16, 890–895.

Schumann, G.J.-P., Bates, P.D., 2018. The need for a high-accuracy, open-access global DEM. Front. Earth Sci. 6, 225. https://doi.org/10.3389/feart.2018.00225

Sepúlveda, I., Tozer, B., Haase, J.S., Liu, P.L.F., Grigoriu, M., 2020. Modeling uncertainties of bathymetry predicted with satellite altimetry data and application to tsunami hazard assessments. J. Geophys. Res. Solid Earth 125, 1–25. https://doi.org/10.1029/2020JB019735

Serafin, K.A., Ruggiero, P., Barnard, P.L., Stockdon, H.F., 2019. The influence of shelf bathymetry and beach topography on extreme total water levels: Linking large-scale changes of the wave climate to local coastal hazards. Coast. Eng. 150, 1–17. https://doi.org/10.1016/j.coastaleng.2019.03.012

Shi, W.Z., Li, Q.Q., Zhu, C.Q., 2005. Estimating the propagation error of DEM from higher-order interpolation algorithms. Int. J. Remote Sens. 26, 3069–3084. https://doi.org/10.1080/01431160500057905

Shi, W.Z., Wang, B., Tian, Y., 2014. Accuracy analysis of digital elevation model relating to spatial resolution and terrain slope by bilinear interpolation. Math. Geosci. 46, 445–481. https://doi.org/10.1007/s11004-013-9508-8

Short, A., 2022. Sediment size dataset for Australia, in: Springer Cham (Ed.), Australian Coastal Systems. https://doi.org/doi: 10.5281/zenodo.7127184

Simpson, A.L., Balog, S., Moller, D.K., Strauss, B.H., Saito, K., 2015. An urgent case for higher resolution digital elevation models in the world's poorest and most vulnerable countries. Front. Earth Sci. 3, 50. https://doi.org/10.3389/feart.2015.00050

Smith, S., Holland, D., Longley, P.A., 2004. The importance of understanding error in Lidar

digital elevation models. Int. Arch. Photogramm. Remote Sens. Spat. Inf. Sci. 35, 996–1001.

Smith, W.H.F., Sandwell, D.T., 1997. Global sea floor topography from satellite altimetry and ship depth soundings. Science (80-.). 277, 1956–1962. https://doi.org/10.1126/science.277.5334.1956

Smith, W.H.F., Sandwell, D.T., 1994. Bathymetric prediction from dense satellite altimetry and sparse shipboard bathymetry. J. Geophys. Res. 99. https://doi.org/10.1029/94jb00988

Soulsby, R.L., 1997. Dynamics of marine sands: a manual for practical applications. Oceanogr. Lit. Rev. 9, 947.

Splinter, K.D., Turner, I.L., Davidson, M.A., Barnard, P., Castelle, B., Oltman-Shay, J., 2014. A generalized equilibrium model for predicting daily to interannual shoreline response. J. Geophys. Res. Earth Surf. 119, 1936–1958. https://doi.org/10.1002/2014JF003106

Tadono, T., Ishida, H., Oda, F., Naito, S., Minakawa, K., Iwamoto, H., 2014. Precise global DEM generation by ALOS PRISM. ISPRS Ann. Photogramm. Remote Sens. Spat. Inf. Sci. II–4, 71–76. https://doi.org/10.5194/isprsannals-ii-4-71-2014

Tadono, T., Nagai, H., Ishida, H., Oda, F., Naito, S., Minakawa, K., Iwamoto, H., 2016. Generation of the 30 M-MESH global digital surface model by alos prism. Int. Arch. Photogramm. Remote Sens. Spat. Inf. Sci. - ISPRS Arch. 41, 157–162. https://doi.org/10.5194/isprsarchives-XLI-B4-157-2016

Takaku, J., Tadono, T., Doutsu, M., Ohgushi, F., Kai, H., 2020. Updates of "AW3D30" ALOS global digital surface model with other open access datasets. Int. Arch. Photogramm. Remote Sens. Spat. Inf. Sci. 43, 183–190. https://doi.org/10.5194/isprs-archives-XLIII-B4-2020-183-2020

Thierry, S., Dick, S., George, S., Benoit, L., Cyrille, P., 2019. EMODnet bathymetry a compilation of bathymetric data in the European waters. Ocean. 2019 - Marseille 2019-June. https://doi.org/10.1109/OCEANSE.2019.8867250

Torresan, S., Critto, A., Dalla Valle, M., Harvey, N., Marcomini, A., 2008. Assessing coastal vulnerability to climate change: Comparing segmentation at global and regional scales. Sustain. Sci. 3, 45–65. https://doi.org/10.1007/s11625-008-0045-1

Tozer, B., Sandwell, D.T., Smith, W.H.F., Olson, C., Beale, J.R., Wessel, P., 2019. Global Bathymetry and Topography at 15 Arc Sec: SRTM15+. Earth Sp. Sci. 6, 1847–1864. https://doi.org/10.1029/2019EA000658

Tseng, K.H., Kuo, C.Y., Lin, T.H., Huang, Z.C., Lin, Y.C., Liao, W.H., Chen, C.F., 2017. Reconstruction of time-varying tidal flat topography using optical remote sensing imageries. ISPRS J. Photogramm. Remote Sens. 131, 92–103. https://doi.org/10.1016/j.isprsjprs.2017.07.008

Turner, I.L., Leaman, C.K., Harley, M.D., Thran, M.C., David, D.R., Splinter, K.D., Matheen, N., Hansen, J.E., Cuttler, M.V.W., Greenslade, D.J.M., Zieger, S., Lowe, R.J., 2024. A framework for national-scale coastal storm hazards early warning. Coast. Eng. 192, 104571. https://doi.org/10.1016/j.coastaleng.2024.104571

Uttenthaler, A., Barner, F., Hass, T., Makiola, J., D'Angelo, P., Reinartz, P., Carl, S., Steiner, K., 2013. Euro-Maps 3D – a Transnational, High-Resolution Digital Surface Model for Europe. Spec. Publ. SP-722.

Uuemaa, E., Ahi, S., Montibeller, B., Muru, M., Kmoch, A., 2020. Vertical accuracy of freely

available global digital elevation models (Aster, aw3d30, merit, tandem-x, srtm, and nasadem). Remote Sens. 12, 1–23. https://doi.org/10.3390/rs12213482

Varner, J.D., Cartwright, J., Rosenberg, A.M., Amante, C., Sutherland, M., Jencks, J.H., 2017. New Multibeam Bathymetry Mosaic at NOAA/NCEI. AGU Fall Meet. Abstr. 2017, OS41A-1371.

Vassilaki, D.I., Stamos, A.A., 2020. TanDEM-X DEM: Comparative performance review employing LIDAR data and DSMs. ISPRS J. Photogramm. Remote Sens. 160, 33–50. https://doi.org/10.1016/j.isprsjprs.2019.11.015

Vousdoukas, M.I., Bouziotas, D., Giardino, A., Bouwer, L.M., Mentaschi, L., Voukouvalas, E., Feyen, L., 2018. Understanding epistemic uncertainty in large-scale coastal flood risk assessment for present and future climates. Nat. Hazards Earth Syst. Sci. 18, 2127–2142. https://doi.org/10.5194/nhess-18-2127-2018

Vousdoukas, M.I., Clarke, J., Ranasinghe, R., Reimann, L., Khalaf, N., Duong, T.M., Ouweneel, B., Sabour, S., Iles, C.E., Trisos, C.H., Feyen, L., Mentaschi, L., Simpson, N.P., 2022. African heritage sites threatened as sea-level rise accelerates. Nat. Clim. Chang. 12, 256–262. https://doi.org/https://doi.org/10.1038/s41558-022-01280-1

Vousdoukas, M.I., Ranasinghe, R., Mentaschi, L., Plomaritis, T.A., Athanasiou, P., Luijendijk, A., Feyen, L., 2020. Sandy coastlines under threat of erosion. Nat. Clim. Chang. 10, 260–263. https://doi.org/10.1038/s41558-020-0697-0

Vousdoukas, M.I., Voukouvalas, E., Mentaschi, L., Dottori, F., Giardino, A., Bouziotas, D., Bianchi, A., Salamon, P., Feyen, L., 2016. Developments in large-scale coastal flood hazard mapping. Nat. Hazards Earth Syst. Sci. Discuss. 0, 1–24. https://doi.org/10.5194/nhess-2016-124

Vrdoljak, L., 2021. Comparison and analysis of publicly available bathymetry models in the east adriatic sea. Nase More 68, 110–119. https://doi.org/10.17818/NM/2021/2.7

Weatherall, P., Marks, K.M., Jakobsson, M., Schmitt, T., Tani, S., Arndt, J.E., Rovere, M., Chayes, D., Ferrini, V., Wigley, R., 2015. A new digital bathymetric model of the world's oceans. Earth Sp. Sci. 2, 331–345. https://doi.org/10.1002/ 2015EA000107

Wechsler, S.P., 2007. Uncertainties associated with digital elevation models for hydrologic applications: A review. Hydrol. Earth Syst. Sci. 11, 1481–1500. https://doi.org/10.5194/hess-11-1481-2007

Wendleder, A., Wessel, B., Roth, A., Breunig, M., Martin, K., Wagenbrenner, S., 2012. TanDEM-X water indication mask: Generation and first evaluation results. IEEE J. Sel. Top. Appl. Earth Obs. Remote Sens. 6, 171–179. https://doi.org/10.1109/JSTARS.2012.2210999

Wentworth, C.K., 1922. A scale of grade and class terms for clastic sediments. J. Geol. 30, 377–392.

Wernette, P., Houser, C., Bishop, M.P., 2016. An automated approach for extracting Barrier Island morphology from digital elevation models. Geomorphology 262, 1–7. https://doi.org/10.1016/j.geomorph.2016.02.024

Wessel, B., 2018. TanDEM-X Ground Segment - DEM Products Specification Document. EOC, DLR, Oberpfaffenhofen, Ger. Public Doc. TD-GS-PS-0, 49.

Wessel, B., Huber, M., Wohlfart, C., Marschalk, U., Kosmann, D., Roth, A., 2018. Accuracy assessment of the global TanDEM-X Digital Elevation Model with GPS data. ISPRS J.

Photogramm. Remote Sens. 139, 171–182. https://doi.org/10.1016/j.isprsjprs.2018.02.017

Whiteway, T.G., 2009. Australian Bathymetry and Topography Grid, June 2009, Geoscience Australia. https://doi.org/http://dx.doi.org/10.4225/25/53D99B6581B9A

Wiegmann, N., Perluka, R., Boogaard, K., 2002. Onderzoek naar efficiency verbetering kustlodingen. Rijkswaterstaat, RIKZ.

Wölfl, A.C., Snaith, H., Amirebrahimi, S., Devey, C.W., Dorschel, B., Ferrini, V., Huvenne, V.A.I., Jakobsson, M., Jencks, J., Johnston, G., Lamarche, G., Mayer, L., Millar, D., Pedersen, T.H., Picard, K., Reitz, A., Schmitt, T., Visbeck, M., Weatherall, P., Wigley, R., 2019. Seafloor mapping - The challenge of a truly global ocean bathymetry. Front. Mar. Sci. 6, 1–16. https://doi.org/10.3389/fmars.2019.00283

Yamaguchi, Y., Kahle, A.B., Tsu, H., Kawakami, T., Pniel, M., 1998. Overview of advanced spaceborne thermal emission and reflection radiometer (ASTER). IEEE Trans. Geosci. Remote Sens. 36, 1062–1071. https://doi.org/10.1109/36.700991

Zhang, K., Gann, D., Ross, M., Biswas, H., Li, Y., Rhome, J., 2019. Comparison of TanDEM-X DEM with LiDAR data for accuracy assessment in a coastal urban area. Remote Sens. 11. https://doi.org/10.3390/RS11070876

Chapter 4 Barrier island response to energetic storms: a global view

Fanti, V., Ferreira, Ó., & Loureiro, C. (2023). Application of global datasets for storm impact assessment in barrier island systems. In: *Coastal Sediments 2023: The Proceedings of the Coastal Sediments 2023* (pp. 12-23).

Fanti, V., Ferreira, Ó., Kümmerer V., & Loureiro, C. (submitted). Barrier island response to energetic storms using global models.

Abstract

During extreme coastal storm events, barrier islands are vulnerable to both erosion and flooding. These can be assessed with high accuracy using process-based models that capture morphodynamic and hydrodynamic processes. However, such models require detailed boundary and input conditions that are often not available. An emerging alternative is the use of open-access global datasets for waves, water levels and topo-bathymetry. The methodology developed exploits the coverage of such datasets to develop a global assessment of barrier island response to a synthetic storm with a 50-year return period wave height. Topo-bathymetric data are merged to derive a synthetic barrier island profile, and the storm is propagated with the wave model SWAN to the nearshore boundary and the morphodynamic model XBeach until the beach/dune system. XBeach surfbeat was used to simulate the erosional response and XBeach non-hydrostatic for the flooding. The results indicate that the use of global datasets and process-based modelling allowed to capture the global variability in barrier island morphology, hydrodynamic forcing and subsequent storm response. Furthermore, the variability of the erosion response was found to be dominated by the maximum offshore wave height and water level, while the flooding response was also controlled by the total volume of the barrier island.

Keywords: Barrier islands, Storm hazards, Global datasets, XBeach, Process-based indicators

4.1 Introduction

Barrier islands are narrow, shore-parallel dynamic landforms that cover more than 10% of the world's coastline (Stutz and Pilkey, 2011). They act as an important natural protection for the mainland and the backbarrier ecosystem by lessening storm damage by hampering storm surge and wave energy. As dynamic buffers that adapt to changes in sea level and sediment supply, they are able to evolve under a changing climate (Miselis and Lorenzo-Trueba, 2017). More than 2,000 barrier islands have been identified worldwide, spanning approximately 21,000 km. Of these, 63% are located along trailing edge coasts, 21% along marginal sea coasts, and only 16% along collision coasts (Stutz and Pilkey, 2011). In terms of their geographic distribution, 74% of barrier islands are located in the Northern Hemisphere, with 24% situated in the USA, where approximately 1.4 million people reside (Zhang and Leatherman, 2011), a number projected to grow in the coming decades (Neumann et al., 2015).

Barrier islands are exposed to a combination of hazards during coastal storms, including erosion and flooding (Leaman et al., 2021; Sallenger, 2000), but also hazards related to sea level rise (Oppenheimer et al., 2019). The morphological response to these hazards can be categorized by the interactions between hydrodynamic forcing and barrier morphology. Sallenger (2000) identified four barrier island storm response regimes: the swash regime, where mild storm conditions lead to beach erosion; the collision regime, characterized by dune erosion and scarping under more severe storm conditions; the overwash regime, when the total water level during a storm reaches the dune crest, causing erosion and landward sediment transport; and the inundation regime, where storm-induced continuous overland flow can cause island breaching. Leaman et al. (2021) later complemented Sallenger's framework by proposing a classification that combines coastal flooding and erosion hazards. Such frameworks are crucial for determining and classifying storm impacts but require detailed in-situ data, alongside considerable computational resources for modelling coastal erosion and flooding effectively.

Quantifying the erosional response of coastal barriers under extreme coastal storm forcing has evolved significantly in the past decades. This evolution has been driven by the need to mitigate coastal hazards and establish setback lines and risk areas for coastal infrastructure. Understanding the complex dynamics of barrier islands, including sediment transport, hydrodynamics, structures and vegetation interactions across multiple temporal and spatial

scales (Zinnert et al., 2017), has led to the development of several methods and models to estimate barrier's response to storms. Process-based models like SBEACH (Larson and Kraus, 1989) and XBeach (Roelvink et al., 2009) have considerably advanced the field by simulating dune erosion, overwash, and breaching under extreme storm conditions, integrating both hydrodynamic and morphodynamic processes. Probabilistic approaches (Plant and Stockdon, 2012) have also been developed to assess dune evolution during storms. XBeach has undergone extensive validation and calibration worldwide, becoming a preferred model for simulating storm-induced erosion and/or overwash (Elsayed and Oumeraci, 2017; McCall et al., 2010), breaching and/or inundation (Harter and Figlus, 2017; van der Lugt et al., 2019), and beach recovery (Roelvink and Costas, 2019). It has been applied not only to local scales, but nationally and regionally along the entire coastline of the Netherlands (Wilmink et al., 2022), on selected sites along the European coastline with the MICORE and RISC-KIT projects (Ciavola et al., 2011; van Dongeren et al., 2018), the Gulf of Mexico and Atlantic coasts of the USA for hurricane forecasting (van Dongeren et al., 2024), the west coast of the USA in the CoSMoS approach (O'Neill et al., 2018), and has been integrated into Australia's (Turner et al., 2024) and Emilia Romagna's (Harley et al., 2016) early warning systems. XBeach is commonly implemented using two primary modes: surfbeat (XB-SB), that averages short-waves but resolves long-wave motions, and non-hydrostatic (XB-NH), that resolves all wave motions including the short-waves. In particular, modelling based on the SandyDuck '97 field experiment on a range of beach conditions from dissipative to reflective showed that XB-SB underpredicts run-up on reflective beaches, while XB-NH provides better accuracy in such conditions (de Beer et al., 2021). Despite the advances, currently no single mode is able to accurately capture storm-induced erosional and flooding responses simultaneously (Roelvink et al., 2018). Moreover, these modelling approaches rely on pre-storm measurements for input and post-storm observations for validation and calibration (Sherwood et al., 2022).

At the local scale, high-resolution topo-bathymetric surveys and in-situ observations from wave buoys and tide gauges, have enabled detailed characterizations of storm impacts on barrier islands (e.g., Cañizares and Irish, 2008; Gharagozlou et al., 2020; Passeri et al., 2020; Schambach et al., 2018; Sherwood et al., 2022), supported by further investigation with morphodynamic numerical models (e.g., Hoagland et al., 2023; Sherwood et al., 2022). Yet, most high-resolution implementations of XBeach for storm impact analysis have focused on the Northern Hemisphere (Dziwnow Spit in Poland, Bugajny et al., 2013; Fire Island in New

York, De Vet et al., 2015; Praia de Faro in Portugal, Garzon et al., 2022; Santa Rosa Island in Florida, Gharagozlou et al., 2021; Trabucador in Spain, Gracia et al., 2013; Duck in North Carolina, Matheen et al., 2021; Chandeleur Islands in Louisiana, Mickey et al., 2017 and Lindemer et al., 2010; Charlestown in Rhode Island, Schambach et al., 2018; Schiermonnikoog in the Netherlands, Wesselman et al., 2018; Matanzas in Florida, van der Lugt et al., 2019). The disproportionate focus on the Northern Hemisphere in both studies and datasets, alongside the absence of data in vast areas of the Southern Hemisphere, hinders wider model calibration, validation and application, including in many remote and data-poor regions.

Although not using morphodynamic models such as XBeach, recent studies have sought to address these data challenges by utilizing open-access global datasets to quantify the exposure of coastal areas to erosion (e.Athanasiou et al., 2020; Luijendijk et al., 2018; Mentaschi et al., 2018; Vousdoukas et al., 2020) or flooding (e.g., Bove et al., 2020; Eilander et al., 2022; Gesch, 2018; Kirezci et al., 2020), proving these datasets can be valuable tools for first-level assessments and hotspot identification. The numerous global models available allow the description of different aspects of the environment, such as elevation (TanDEM-X; Copernicus GLO-30; AW3D30; SRTM15+; ETOPO 2022; GEBCO 2024), land use and land cover (Copernicus Global Dynamic Land Cover; GLAD Landsat), waves (ERA5; WAVERYS; WW3; GOW2), water levels (GTSM), and, more specifically, coastal characteristics (Athanasiou et al., 2024) at a coarse but global scale. This large amount of information can be translated into hazard scales (Leaman et al., 2021; Sallenger, 2000) and process-based indicators (Carapuço et al., 2016; Ferreira et al., 2017), which can be determined using models like XBeach, providing a framework for comparing storm impacts across different regions and developing risk assessment frameworks to identify vulnerable areas.

However, two critical issues persist: the lack of high-resolution data for validating and calibrating global and local models and the coarse spatial and temporal resolution of global datasets, which introduces errors and limits detailed local assessments. While advancements in satellite technologies are already contributing to improved data resolution (Vitousek et al., 2023), the potential of existing global models for meaningful storm impact analysis has not been yet explored. The aim of this work is to assess storm impacts on barrier islands globally, using global datasets and a morphodynamic model implemented using synthetic topo-bathymetric barrier island profiles. The morphological and hydrodynamic characteristics of

barrier islands are also analyzed alongside the modelled storm responses in order to identify morphological patterns in barrier islands response on a global scale. In particular, the erosion and flooding impacts of a storm with a significant wave height with a 50-year return period were simulated using the XBeach process-based numerical model. While recognizing the uncertainties inherent in global models, this approach aims to explore the possibility of overcoming data limitations for data poor coastal areas, such as some coasts of the Southern Hemisphere, through the use of global, openly available datasets. At the same time, the applicability of these datasets in the development of process-based indicators of coastal storm impacts was tested.

4.2 Methods

4.2.1 Selection of barrier islands

Barrier islands (and peninsulas) were selected according to a number of specific morphological criteria to ensure their suitability for analysis (Figure 4.1 and Table S4.3 in Appendix A for the exact coordinates). First, barriers were selected to represent a broad global distribution, avoiding locations fronted by small islands or with complex topo-bathymetric features that could negatively impact wave propagation given the coarse resolution of the global bathymetric models. The presence of a sandy dune with low vegetation that could be clearly identified from the satellite-derived global digital elevation models (DEMs), was a prerequisite for selection, in addition to having a morphologically homogeneous natural sector of approximately 200 meters, free of any infrastructure or buildings. Wherever possible, efforts were also made to ensure that the barrier islands had not undergone any nourishment or human modification. This rigorous selection process ensured that a total of 30 barrier islands and peninsulas met all the necessary criteria for reliable and meaningful comparison.

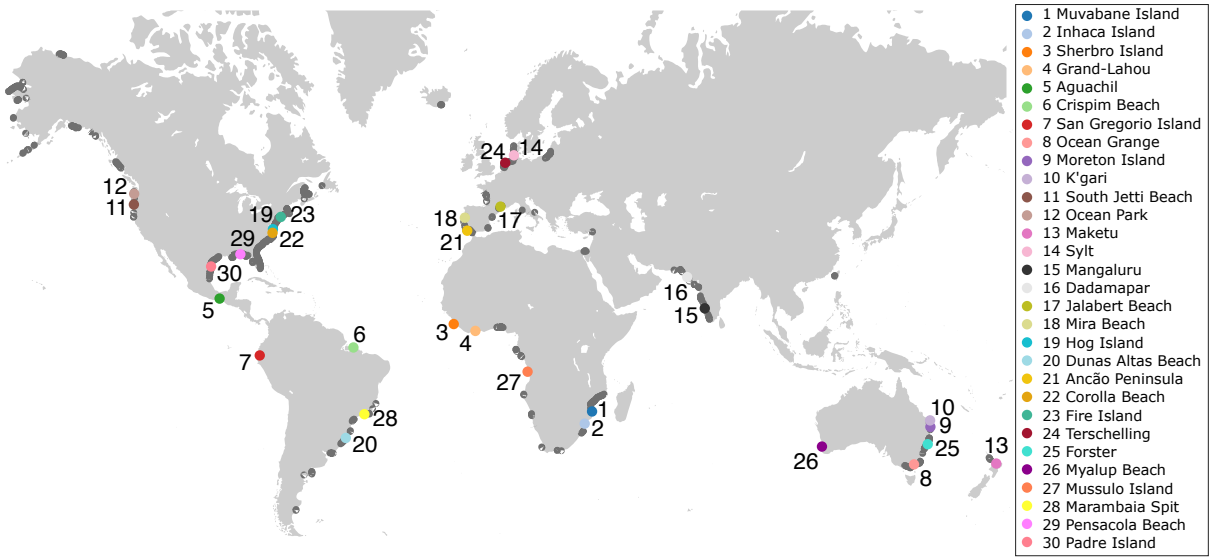

Figure 4.1 Global distribution of modern barrier islands from the Mulhern et al. (2021) database (dark grey) and 30 barrier islands selected for the present study (black).

4.2.2 Synthetic barrier island profiles

Storm impact assessments in remote and data-poor locations can be challenging due to the lack of accurate pre- and post-storm topo-bathymetric information. A common and practical approximation for XBeach applications is to assume averaged or synthetic bathymetries based on equilibrium profiles (Matheen et al., 2021). In this approach, a synthetic barrier island profile was developed by merging the TanDEM-X global DEM (0.4 arcsec resolution, ~12 m; Rizzoli et al., 2017) and the ETOPO 2022 global bathymetric model (15 arcsec resolution, ~460 m; NOAA National Centers for Environmental Information, 2022). These two global datasets were selected because previous analysis demonstrated that these had the lowest error compared to similar global models (Fanti et al., 2025). To consistently combine the datasets, these were reprojected to a common vertical (mean sea level, MSL) and horizontal datum (EPSG:4979 – WGS84) in QGIS. In particular, the TanDEM-X ellipsoidal height was vertically corrected using the Earth Gravitational Model of 2008 (EGM2008) geoid model and the water bodies were removed with the Water Indication Mask auxiliary file. Remaining spikes were visually identified and removed manually. The bathymetry from ETOPO 2022 is already provided as vertically referenced to the EGM2008 geoid surface (EPSG:3855).

For each of the 30 barrier islands, cross-shore profiles of the beach and dune for the ~200 m long natural sector were extracted from TanDEM-X with ~10 m spacing between profiles. The

cross-shore profiles were aligned at the dune crest, averaged and merged with the averaged bathymetric profiles extracted along the same cross-shore positions until an offshore water depth of ~30 m. The Dean equilibrium profile (Dean, 1991) was used to merge the topography and bathymetry averaged profiles in the section between MSL and the depth of closure. This was estimated according to Hallermeier (1981), an empirical indirect method for determining the depth of closure based on wave parameters, which were retrieved from the WAVERYS global wave reanalysis (Law-Chune et al., 2021). The profile merging is detailed in Fanti et al. (2025) and Chapter 3, and the resulting synthetic topo-bathymetric profiles are represented in Figure 4.2.

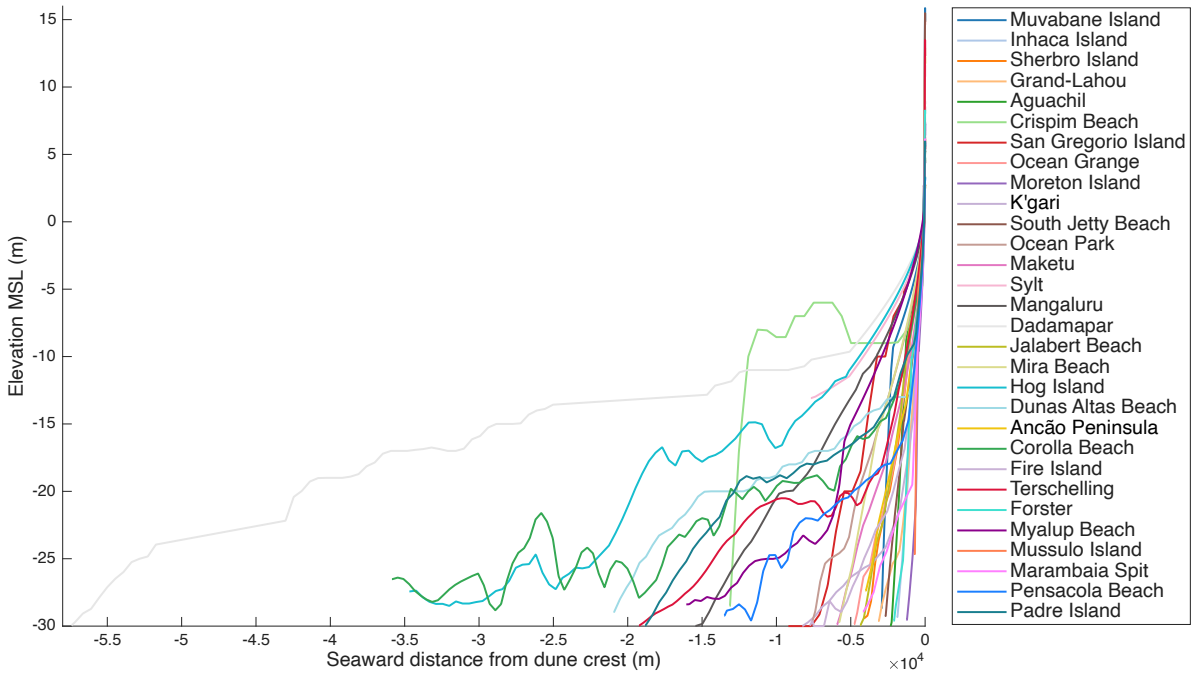

Figure 4.2 Topo-bathymetric profiles of the barrier islands aligned at the dune crest (x = 0). Negative values represent distances seaward the dune crest and depths below mean sea level.

4.2.3 Synthetic storm identification

The characterization of the offshore wave conditions for each barrier island location was performed using the data from the WAVERYS global wave reanalysis (Law-Chune et al., 2021). This reanalysis has 0.2° spatial resolution and 3 hours temporal resolution and it showed a good performance when compared to coastal wave buoys (Fanti et al., 2023). The water level information was extracted from the Global Tide and Surge Model (GTSM v3.0, Muis et al.,

2022) developed by Deltares, that has a spatial resolution at coastal areas of 2.5 km (1.25 km in Europe) and 1 hour temporal resolution.

To model the erosional response for comparable high-magnitude storm events at each barrier island, the 50-year return period storm conditions were selected, and a synthetic storm forcing developed. Symmetric triangular shapes representing storm forcing have been widely used for their simplicity (e.g., Mackay and Johanning, 2018; Martín-Hidalgo et al., 2014; Martín Soldevilla et al., 2015). However, their simplicity also leads to criticism due to their assumptions and uncertainties (Duo et al., 2020). In this work, a simple methodology was employed to preserve the storm shape characteristic of each location and scaling it to the 50-year return period wave height.

The significant wave height (H_s), peak wave period (T_p) and mean direction (Dir_m) were extracted from WAVERYS at an offshore location, with H_s being calibrated if the location was in water depths of less than 100 m. The calibration procedure is detailed in Fanti et al. (2023) and was derived from the analysis of a global dataset of coastal wave buoys (see Chapter 2). Independent storm events were identified with a de-clustering algorithm that was applied to the winter months (i.e. when 95% of the storms occurred) and that uses the 95th percentile of H_s as the storm threshold, 6-hour minimum storm duration and an independent duration statistically estimated (according to the method proposed by Kümmerer et al., 2024). Homogeneity and independence tests were then performed on the dataset of storm events and a Generalized Pareto Distribution was fitted to the de-clustered storm H_s time series to determine the return periods of H_s (Figure 4.3a).

From the storms identified, events with H_s higher than the 2-year return period were then selected, aligned at the storm peak and averaged to obtain a synthetic storm shape that would preserve the characteristics of each location better than a simplified triangular shape. The synthetic shape obtained was then scaled so that the peak H_s corresponds to the 50-year return period H_s (Figure 4.3f). The duration of the synthetic 50-year return period storm was determined from the linear relationship with the maximum H_s during each storm (Figure 4.3b), a methodology used by other authors (e.g., Almeida et al., 2011). Similarly, the linear relationship between the maximum H_s for each storm and the corresponding T_p (Figure 4.3c), was used to determine a synthetic storm T_p (Figure 4.3g). As for the direction, the modal

direction of the de-clustered independent storms was associated with the synthetic storm, representing the most commonly occurring storm direction for each location.

The water levels, including tidal elevation and storm surge, were extracted from the GTSM at the closest point to the barrier island's locations. After removing the sea level rise component (also provided in the dataset), the tidal elevations from the global reanalysis were split into tidal cycles of 14 days, aligned to the peak of each spring tide, and averaged to obtain an averaged spring tide cycle where the peak was aligned with the peak storm H_s by shifting the phase (Figure 4.3e). A linear fit between the maximum storm surge and the maximum H_s for each storm was also calculated (Figure 4.3d) and used to determine a synthetic storm surge (Figure 4.3h), which was added to the tidal level to obtain the water level (tide + surge) during the storm. The synthetic storm forcing developed for the 50-year return period storm H_s represents a worst-case scenario, where there is a coincidence of the storm's peak H_s, T_p, storm surge and astronomical high tide.

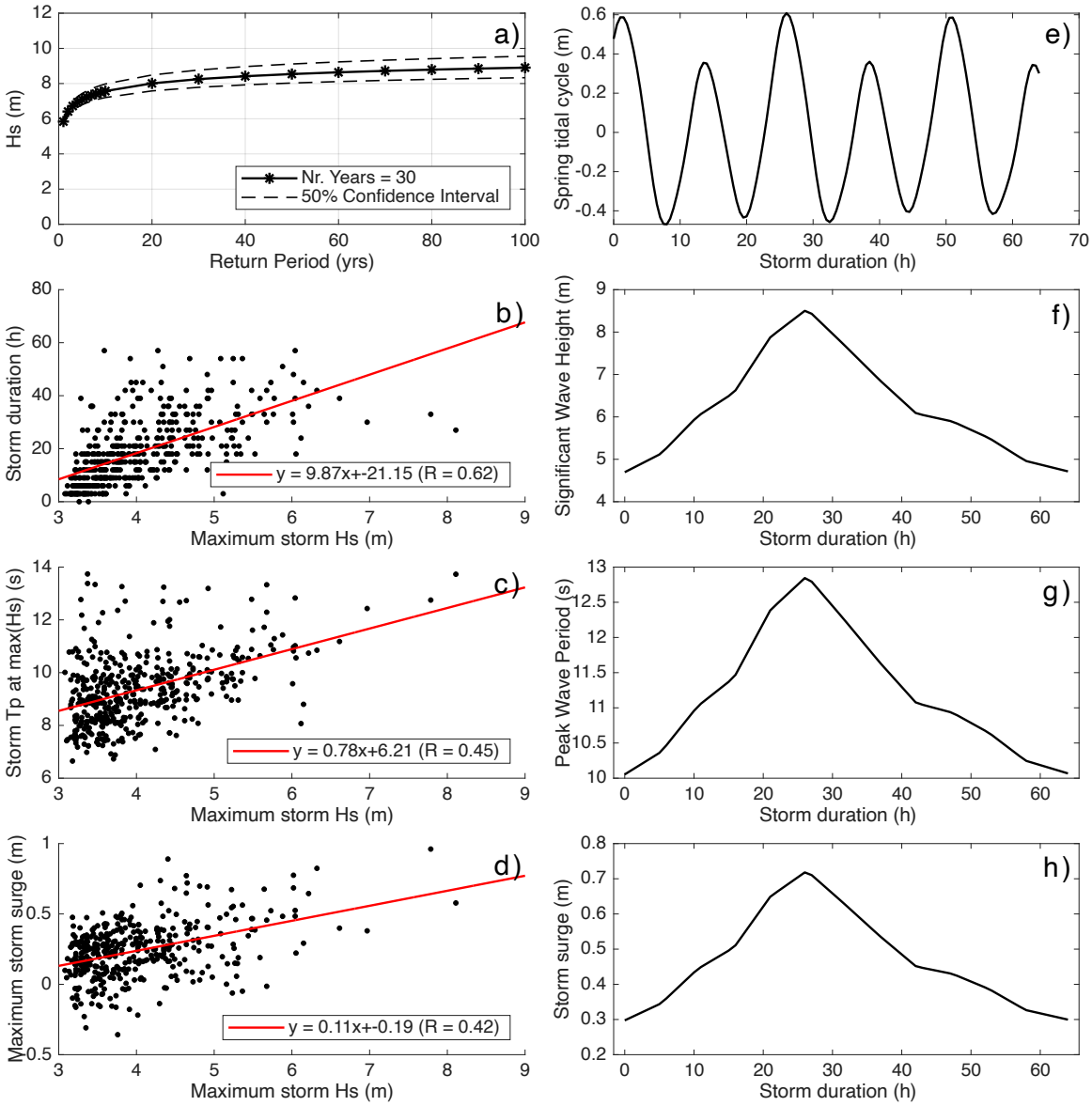

Figure 4.3 Parameters used to determine the synthetic storm forcing for Hog Island from WAVERYS and GTSM global data. (a) Return period for H_s. (b) Linear relationship between storm H_s and storm duration, (c) T_p and (d) storm surge (d). (e) Average spring tidal cycle and synthetic profile of the 50-year return period storm, including (f) H_s (g), T_p and (h) storm surge.

4.2.4 Nearshore downscaling

To obtain the nearshore wave conditions at the XBeach offshore boundary the third-generation spectral wave propagation model SWAN (Simulating WAves Nearshore: Booij et al., 1999) was implemented in 2D nonstationary mode, using a JONSWAP spectral shape to represent the synthetic storm extracted from WAVERYS with 10° directional discretization and 24 logarithmic distributed frequency classes from 1 Hz to 0.04 Hz. The bathymetric grid was

extracted from ETOPO 2022, and the rectilinear computational grid resolution retained the 15 arc-second resolution of the bathymetric data. SWAN was run with default parameters for wave breaking, diffraction, bottom friction dissipation and triad wave-wave interactions. The depth of the computational offshore boundary was at least half of the maximum wavelength of the incoming waves to ensure deep water conditions. The parameters extracted from WAVERYS and used to force the offshore boundary model were the synthetic storm time series of H_s, T_p, modal direction and directional spreading (set to 20°) for every hour.

4.2.5 Storm impact modelling

The 2D hourly spectral output from SWAN, together with the synthetic water levels and averaged topo-bathymetry, were used as the input for estimating the morphodynamic response to the synthetic storm events for the 30 barrier islands with the open-source process-based model XBeach v1.24 Halloween release (Roelvink et al., 2009). XBeach was run both in 1D surfbeat (hydrostatic) mode and 1D non-hydrostatic mode, as each served a distinct purpose in the study. The XB-SB mode, which solves short-wave variations on the wave group scale in a phase-averaged manner separately from the long waves, was used to model erosion processes by incorporating sediment transport and morphological changes. In contrast, the XB-NH mode, which resolves both short and long waves with higher computational expense, was employed to model flooding by predicting run-up over a fixed, non-evolving bed, with sediment transport and morphological modules deactivated to focus on hydrodynamic processes. Infragravity band swash was shown to be lower in XB-SB mode than in XB-NH mode (de Beer et al., 2021), highlighting the different capabilities of the two approaches.

Both XBeach modes were run with default parameters, random set to 0 and morfac of 1. The offshore boundary was located at approximately 30 m water depth and, for each barrier island, the depth restrictions were verified (no wave breaking near the boundary $H_s/h < \sim 1/3$ and realistic long waves at the boundary $c_g/c < \sim 0.8$, where h is the water depth, c_g the group velocity and c the wave celerity).

The two-layer non-hydrostatic mode (de Ridder et al., 2021) was used because the XBeach offshore boundary is located in intermediate water depth. The maximum relative depth kh (where $k = 2\pi/L$ is the wave number and L the wavelength) in the 1-layer non-hydrostatic model is restricted to shallow waters ($kh \sim 1$), while in the 2-layer model, the approximation is

effective up to intermediate relative depths (kh ~ 4). The model was set up with spatially varying grid resolution in the cross-shore domain, optimized according to the water depth and mean wave period. The output variables were saved at 1-hour intervals, with the exception of the run-up gauge that had a time-step of 100 s. The wave directions from SWAN runs were modified to ensure they were cross-shore to the barrier island profile, which is considered to be oriented along an ideal x-axis with land on the right side and ocean on the left side.

4.2.6 Statistical analysis of barrier island characteristics and storm response

To investigate the relationships between the morphological and hydrodynamic characteristics of barrier islands and their response to storms, an extensive classification of relevant variables was performed. This classification aimed to capture the complex interplay between barrier features and storm-induced forces, providing a basis for understanding and predicting barrier island behavior under extreme conditions. Many of the variables considered are consistent with the geoindicators previously outlined by Carapuço et al. (2016) and with the process-based indicators defined by Ferreira et al. (2017), ensuring consistency with established frameworks.

4.2.6.1 Barrier island morphological and hydrodynamic variables

Applying the methodology described in sections 4.2.2 and 4.2.3, the morphological and hydrodynamic characteristics of the barrier islands were systematically defined, using data exclusively derived from global models. These variables represent key aspects of the islands' structure, such as beach and dune geometries, and the forces acting upon them during storm events, such as storm power and tidal influences. The variables are summarized in Table 4.1 and a detailed description of each variable can be found in the Appendix B.

Table 4.1 Selected morphological and hydrodynamic variables characterizing the barrier islands.

Morphological variables	**Hydrodynamic variables**
Latitude (°)	Maximum offshore H_s (m)
Depth of closure (m)	Maximum offshore T_p (s)
Nearshore slope (-)	Relative storm direction (-)
Total barrier volume (m^3/m)	Storm duration (h)
Beach slope (-)	Storm power (MWh/m)
Beach width (m)	Wave energy at the depth of closure (Nm/m^2)
Berm volume (m^3/m)	Wave energy at 2 m depth (Nm/m^2)
Dune half width (m)	Maximum water level (m)
Dune height (m)	Tide range (m)
Dune volume (m^3/m)	Mean annual H_s (m)
D50 (mm)	Mean annual tide range (m)
Dimensionless fall velocity (-)	

4.2.6.2 Process-based indicators of storm response

To characterize the barrier island's behavior and vulnerability during storm events, a set of process-based indicators, including both the forcing mechanisms and the morphological response to those forcings (Ferreira et al., 2017), were extracted and summarized in Table 4.2. The indicators were derived from the pre- and post-storm profile difference simulated with XBeach and used to characterize the barrier islands' erosional (XB-SB) and flooding (XB-NH) response to a synthetic 50-year return period storm. The erosional response indicators quantify changes such as sediment loss, dune and berm retreat. Meanwhile, the flooding response indicators focused on the overwash. Further details on the derivation of each parameter are provided in the Appendix C.

Table 4.2 Process-based indicators of barrier island erosion and flooding response to an extreme storm, derived with XB-SB and XB-NH respectively.

Erosional response	**Flooding response**
Collision hours (%)	Overwash hours (%)
Maximum run-up XB-SB (m)	Maximum run-up XB-NH (m)
Dune eroded volume (m^3/m)	Overtopping volume (m^3)
Berm eroded volume (m^3/m)	Average overtopping discharge (l/s/m)
Total eroded volume (m^3/m)	Number of overtopping waves (-)
Maximum retreat (m)	Mean overtopping event duration (s)
Mean retreat (m)	Overwash extent (m)
Dune toe retreat (m)	
Shoreline retreat (m)	
Relative volume loss (%)	

4.2.6.3 Correlation analysis

The Pearson correlation coefficient (R) was estimated between all explanatory and both erosional and flooding response variables to measure their linear correlation, even though not all variables follow a normal distribution. A high coefficient (1 or -1) indicates a high correlation (positive or negative) between the two variables, while a coefficient near zero indicates no correlation. To assess the significance of the correlations, the p-value was calculated, with levels above 0.95 and 0.99 used to determine the statistical reliability of the observed relationships. For a variable x and a variable y with i sample values, it is estimated as:

$$R = \frac{\sum(x_i - \bar{x})(y_i - \bar{y})}{\sqrt{\sum(x_i - \bar{x})^2 (y_i - \bar{y})^2}} \quad (4.1)$$

4.2.6.4 Multilinear regression

The differences in the morphological setting and hydrodynamic forcing between the various barrier islands result in differences in the morphodynamic and flooding response. To evaluate the relative contribution of the morphologic and hydrodynamic variables to the erosion and flooding response, a multilinear regression analysis was performed. The explanatory variables

(Table 4.1) that showed a statistically significant correlation with each other were removed to avoid multicollinearity and ensure reliable regression models. The remaining explanatory variables that showed statistically significant correlation with the response variables (Table 4.2) were divided into two groups: morphologic variables, representing the physical characteristics of the coastal system, and hydrodynamic variables, representing storm-related forcing conditions. Using these groups, three separate multilinear regression models (Eq. 4.2) were developed to estimate the variance explained by the predictors. The first model used only the morphologic variables, the second used only the hydrodynamic variables, and the third combined both morphologic and hydrodynamic variables. This setup allowed for an analysis of the variance explained by each group individually and in combination. The multilinear regression model between the response variables (Y) and the different groups of explanatory variables (X) is defined as:

$$Y = a_o + \sum_{i=1}^{n} a_i X_i \tag{4.2}$$

where a_i are the coefficients of n variables and a_0 is the intercept. The variance explained by each group was estimated with the adjusted coefficient of determination (R^2).

4.3 Results

4.3.1 Storm hydrodynamic forcing

The storm hydrodynamic forcing scaled to the 50-year return period H_s for each of the 30 barrier islands distributed along the global coastline evidences a latitudinal pattern for most variables (Figure 4.4). The distribution of the 50-year return period H_s ranges from 2.9 m (Crispim Beach in Brazil and San Gregorio Island in Ecuador) to 10.1 m (South Jetty Beach and Ocean Park on the west coast of the USA), with the higher H_s values estimated for extratropical latitudes of both the Northern and Southern Hemispheres and the lower values in the equatorial region (Figure 4.4a). The distribution of T_p corresponding to a storm with a 50-year return period H_s shows longer periods on the open coasts from the extratropical regions affected by the propagation of energetic swells (Figure 4.4b), such as in Mexico (19.9 s in Aguachil), the Pacific coast of the USA (15.4 s at Ocean Park), the Atlantic-facing west coast of Portugal (17.5 s at Mira Beach) and the Ivory Coast (18.3 s at Grand-Lahou). The smaller storm T_p was found

in enclosed basins, including Gulf of Mexico (Padre Island, 9.6 s), the Mediterranean Sea (Jalabert Beach, 11.2 s) and the North Sea (Terschelling, 11.6 s, and Sylt, 12.8 s). In terms of duration, longer storms were found in areas exposed to monsoon winds (Figure 4.4c), including the Arabian Sea at Mangaluru (300 h) and Dadamapar (232 h), and at Padre Island (144 h) in the north-eastern Gulf of Mexico, as it is directly exposed to tropical cyclones (TCs). The higher total water levels were found in the North Sea (Figure 4.4d), specifically for the barrier islands of Terschelling (3.0 m) and Sylt (3.5 m). This area is exposed to larger tidal ranges and the semi-enclosed and shallow nature of the basin contributes to intense storm surges. All the selected barrier islands are wave-dominated, with a relative tidal range, estimated as the mean annual tidal range divided by the mean annual H_s (see Appendix A), ranging from 0.1 m (Myalup Beach in Australia) to 1.9 m (Ancão Peninsula in Portugal).

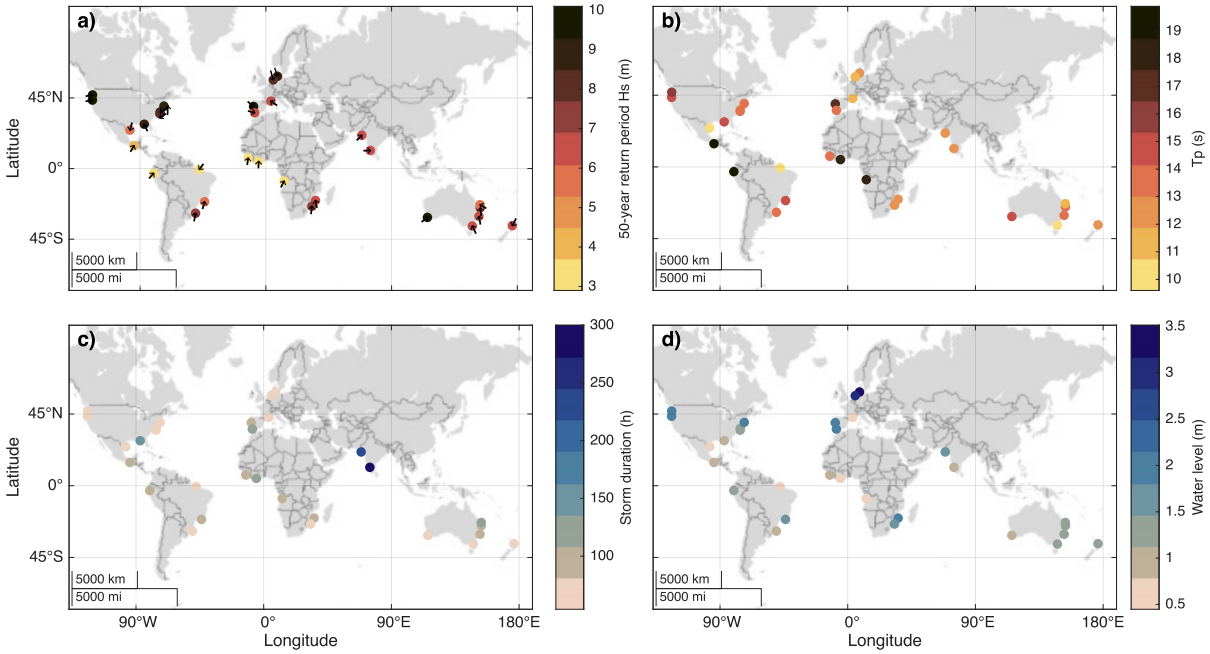

Figure 4.4 Storm hydrodynamic forcing scaled to the 50-year return period H_s. (a) 50-year return period H_s (in m) and modal storm direction; (b) T_p (in s), (c) storm duration (in h), (d) total water level (in m).

4.3.2 Barrier island morphology

The topo-bathymetric morphological characteristics of the 30 barrier islands analyzed vary widely, particularly in terms of dune height (Figure 4.5a), dune volume (Figure 4.5b), nearshore and offshore slopes (Figure 4.2). Based on the dimensionless fall velocity (Ω), barrier islands with steeper nearshore slopes were consistently classified as reflective (Inhaca Island, Grand-

Lahou, Crispim Beach, Moreton Island, K'gari, Dunas Altas Beach, Fire Island, Forster, Mussulo Island, Marambaia Spit, Pensacola Beach, Padre Island), those with gentler slopes as dissipative (Sylt, Mangaluru, Dadamapar, Hog Island), and all others as intermediate. Dune height (Figure 4.5a), calculated from the pre-storm dune toe to the dune crest, was highest at Muvabane Island in Mozambique (15.3 m), known to be one of the highest dune systems in the world (Cooper and Pilkey, 2002), followed by South Jetty Beach (15.0 m), Ocean Grange (13.9 m) and Grand-Lahou (11.6 m), all areas of abundant sand availability, while the lowest dunes were found at San Gregorio Island in Ecuador (1.3 m) and Jalabert Beach in the south of France (2.2 m).

The dunes with the largest sedimentary volumes (Figure 4.5b), estimated by integrating the area from the dune toe to the dune crest, were found in south-east Africa (Muvabane Island, 640 m^3/m) and south-east Australia (Ocean Grange, 616 m^3/m), in the west coast of the USA (South Jetty Beach, 555 m^3/m, and Ocean Park, 488 m^3/m) and the west coast of Portugal (Mira Beach, 512 m^3/m). Consistent with lower dune heights, the smaller dune volumes were identified in Ecuador (San Gregorio Island, 58 m^3/m) and France (Jalabert Beach, 70 m^3/m).

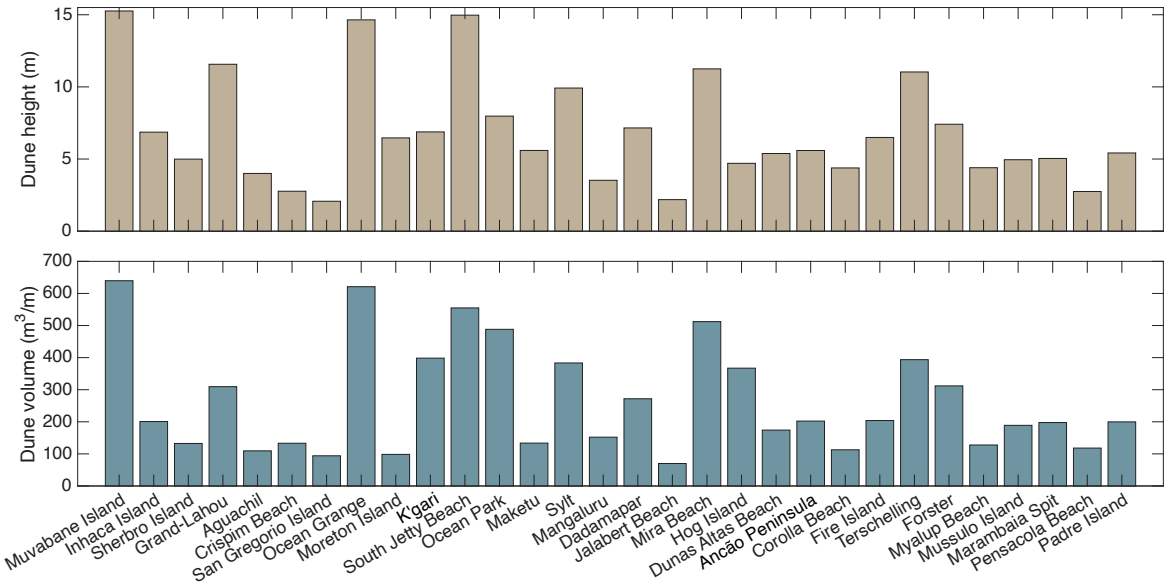

Figure 4.5 Morphologic characteristics of barrier islands: (a) dune height (in m) and (b) dune volume (in m^3/m), both estimated from the dune toe to the dune crest.

4.3.3 Relationships between morphological, hydrodynamic and process-based variables

4.3.3.1 Cross-correlation between explanatory variables

Variables with no statistically significant correlations, which include *D50*, beach width and berm volume, maximum T_p, relative storm direction, storm duration, wave energy at depth of closure and at 2 m depth, were excluded from the analysis and from Figure 4.6. The same applies to variables that depend directly on other variables, such as the storm power, which depends on the maximum offshore H_s, overtopping discharge, which correlates with the overtopping volume, and hours of overwash, which correlate with the number of overtopping waves. Following the findings of Lobeto et al. (2024) that outline a latitudinal gradient in storminess patterns along the global coastline, a significant correlation was found between latitude and the offshore maximum H_s during a 50-year return period storm (R = 0.38, p-value < 0.05) and the maximum total water level (R = 0.43, p-value < 0.05). The dune volume correlated with the maximum offshore H_s (R = 0.37, p-value < 0.05) and even more significantly with the maximum water level (0.52, p-value < 0.01). While these correlations don't have any physical meaning, a correlation was also found between the mean annual H_s and mean annual tide range with the dune height (R = 0.38 and R = 0.45, p-value < 0.05), not shown in Figure 4.6.

4.3.3.2 Cross-correlation between response and explanatory variables

Four of the explanatory variables (dune height; dune volume; maximum offshore H_s; maximum water level) were significantly correlated with most of the erosion response variables (maximum run-up estimated both with XB-SB and XB-NH; dune and total eroded volume; shoreline retreat) (Figure 4.6). Inversely, the berm eroded volume was significantly negatively correlated with the same explanatory variables, which results from the accumulation of sediment eroded from the dune in the beach face/berm. The dune toe retreat wasn't significantly correlated with the variables analyzed, except for the maximum offshore water level (R = 0.55, p-value < 0.01) and with the dune half width (R = 0.63, p-value < 0.01), with the last being an intrinsic correlation due to the fact that both parameters were defined according to the same dune toe position. This lack of correlation for the dune toe retreat is probably due to the difficulty of identifying an exact dune toe position on profiles extracted from a global topographic dataset with coarse resolution like TanDEM-X. The total eroded volume and the

mean retreat were positively correlated with the beach slope (R = 0.45 and R = 0.41, p-value < 0.05), reflecting the fact that steeper beaches allow more energetic swash which allows run-up to reach the dune toe and erode the dune. The maximum run-up simulated with XB-SB was correlated with the latitude (R = 0.39, p-value < 0.05), and an even stronger correlation was found between the accumulated berm volume and the latitude (R = -0.54, p-value < 0.01). Run-up values obtained with both XBeach modes are also well correlated with dune height (R = 0.56 for XB-SB and R = 0.71 for XB-NH, p-value < 0.01), with the storm power (R = 0.54 and R = 0.50, p-value < 0.01) and maximum water level (R = 0.80 and R = 0.50, p-value < 0.01). Overall, the explanatory variables that had strongest correlations with the erosional response was the maximum offshore H_s.

When analyzing the results from XB-NH, the number of overtopping events was negatively correlated with dune height (R = -0.37, p-value < 0.05). The overtopping volume was negatively correlated with the dune volume (R = -0.38, p-value < 0.05), meaning that lower dunes experienced a greater number of events, and positively correlated with storm duration (R = 0.51, p-value < 0.01) and storm power (R = 0.36, p-value < 0.05), not shown in Figure 4.6, reflecting the fact that longer and stronger storms lead to an increased number of overwash events. Also, the overwash extent was positively correlated with the maximum offshore H_s (R = 0.53, p-value < 0.01), while the overtopping volume only showed significant correlation with the dune volume (R = -0.32, p-value < 0.05).

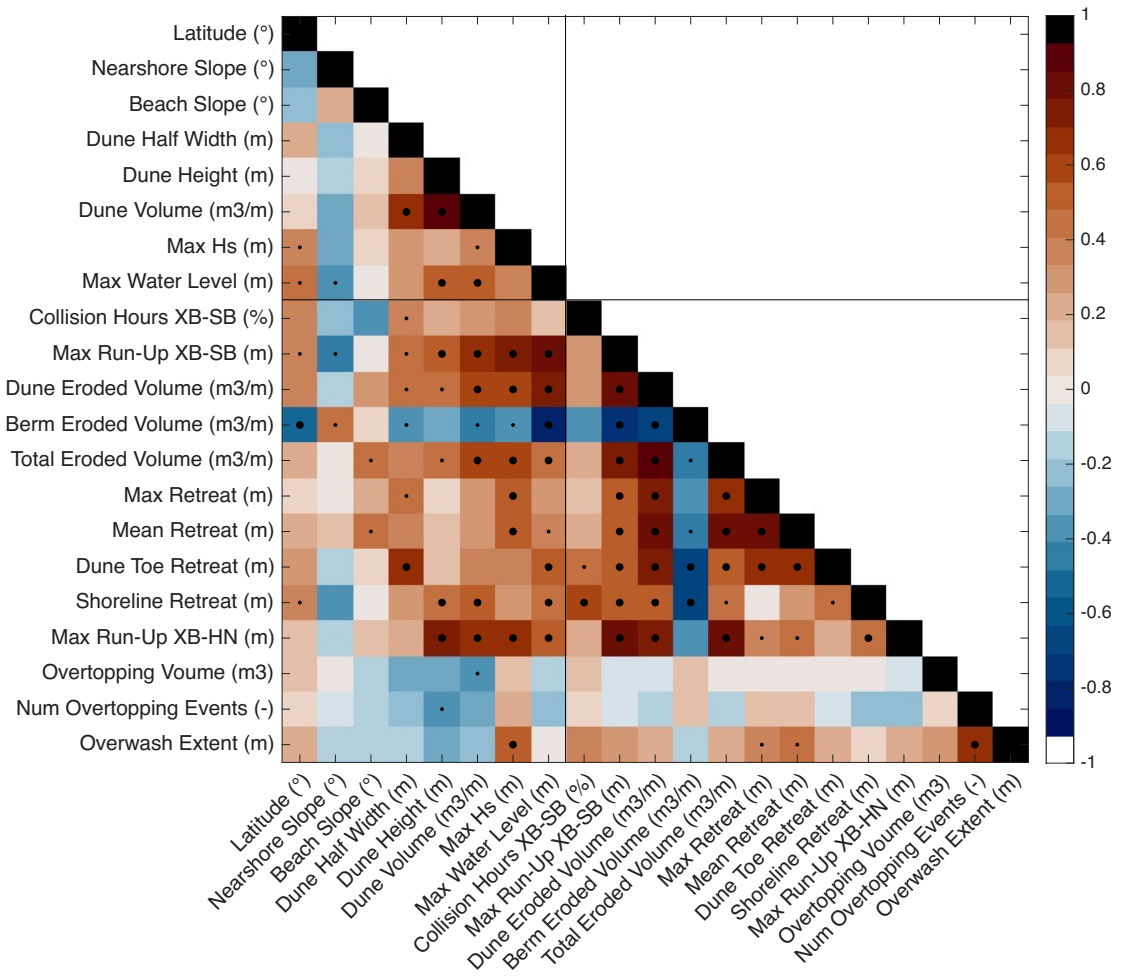

Figure 4.6 Heatmap of cross-correlations between morphological, hydrodynamic and process-based variables. All morphological parameters refer to the pre-storm conditions. The larger (smaller) black dots show relationships that are significant at the 99% (95%) significance level. The red (blue) colors represent positive (negative) correlation between variables. The vertical and horizontal lines separate the response variables from the explanatory variables.

4.3.3.3 Multilinear regression analysis

Considering that explanatory variables that were not significantly correlated with the erosion and flooding response variables or that were correlated with other explanatory variables were excluded, the set of variables that were included in the multilinear correlation analysis is composed of: the maximum offshore H_s, the maximum water level, the dune half width and the dune height. The first two were considered for the multilinear regression with hydrodynamic variables, the other two with morphological variables. For most of the erosion response variables, the multilinear regression performed with the hydrodynamic explanatory variables showed a higher correlation than the regression with the morphologic variables (Figure 4.7). This is particularly true for the maximum run-up estimated with XB-SB (87 % of variability

explained by hydrodynamic variables only); the dune, berm and total eroded volume (65 %, 73 % and 45 %); the maximum and mean retreat (30 % for both). Moreover, the regressions that were significant at the 99% confidence level were only those that included hydrodynamic variables. For the shoreline retreat and maximum run-up estimated with XB-NH, both groups had equal importance, and together they better explain the variability of the response. The overwash extent was also mostly explained by the hydrodynamic variables (p-value < 0.01) while overtopping volume and discharge were better explained by the morphologic variables, although overall poorly explained (low correlation values).

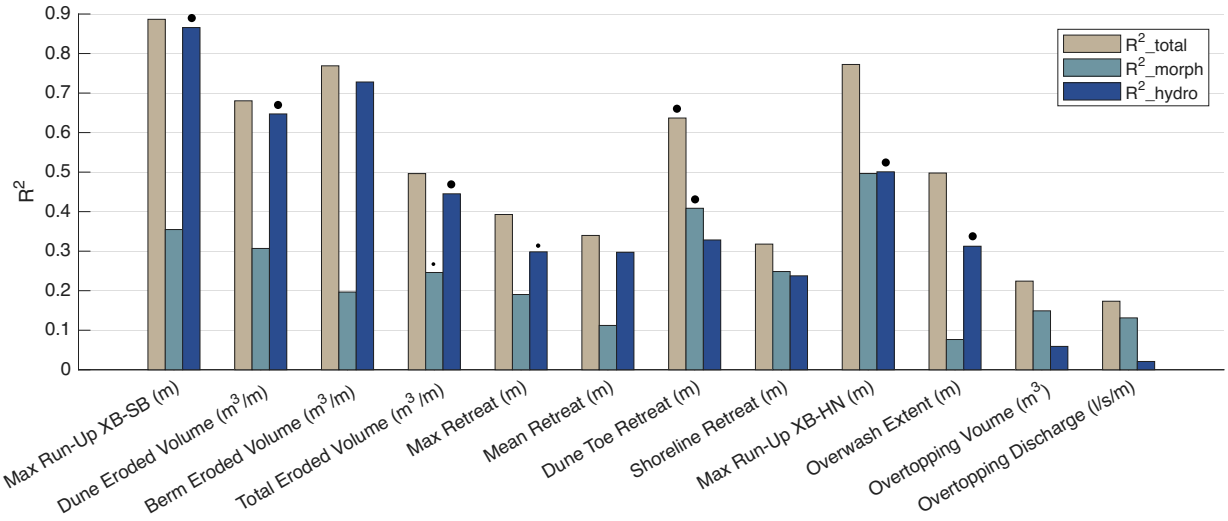

Figure 4.7 Coefficient of determination estimated through multilinear regression between the response variables (indicated in the x-axis) and the explanatory variables as a whole and separated between morphologic and hydrodynamic variables. The large (small) dots on top show when the regression is significant at 99 % (95 %) confidence level.

4.3.4 Storm-induced barrier erosion

The barrier islands with greater total eroded volume (Figure 4.8 and Figure 4.9a) due to a 50-year return period storm event included barriers that were classified as reflective to intermediate, specifically South Jetty Beach and Ocean Park in the USA (105 m^3/m and 94 m^3/m), K'gari in eastern Australia (93 m^3/m) and Mira Beach in Portugal (82 m^3/m). However, when looking at eroded volume as a percentage of total barrier volume (Figure 4.9b), the barrier islands with the highest relative volume loss were Moreton Island (32%) in eastern Australia, Marambaia Spit in Brazil (31%), Maketu in New Zealand (29%), Fire Island (26%) and Pensacola Beach (25%) on the east coast of the USA. The highest mean dune retreat (Figure

4.9d) was observed at Ocean Park, with 16.5 m, followed by K'gari (14.2 m), Pensacola Beach (13.3 m) and Marambaia Spit (13.0 m). The maximum dune toe retreat (Figure 4.9c) was also observed at Ocean Park (56 m), but this value is extremely variable and dependent on the dune toe selection choice. When applying the erosion hazard scale from Leaman et al. (2021), all the barrier islands experienced dune face erosion when exposed to a 50-year return period H_s storm, without dune crest retreat.

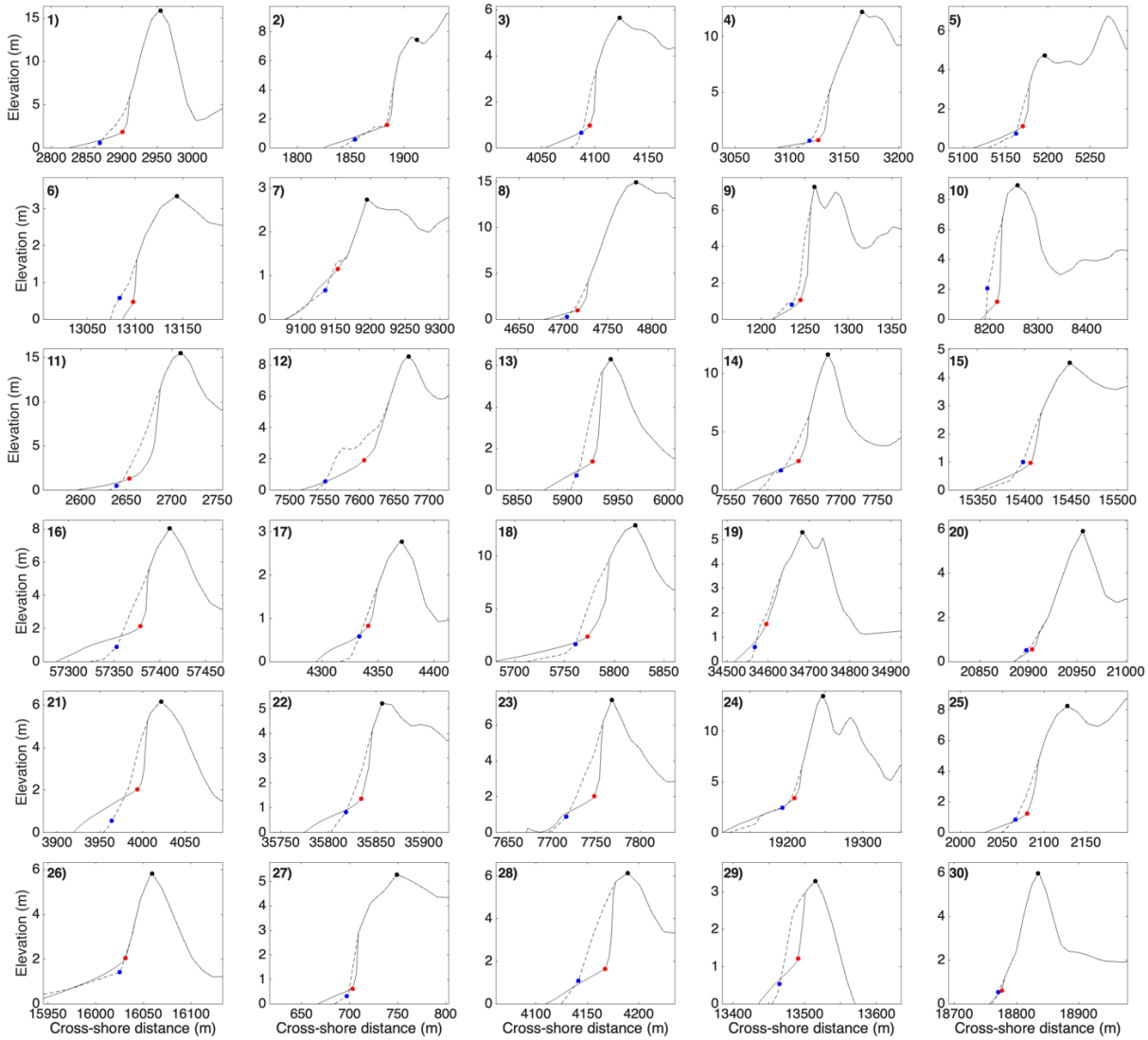

Figure 4.8 Pre- (dotted line) and post- (continuous line) storm profiles simulated with XB-SB. The dune crest (black dot), dune toe before the storm (blue dot) and dune toe after the storm (red dot) are reported.

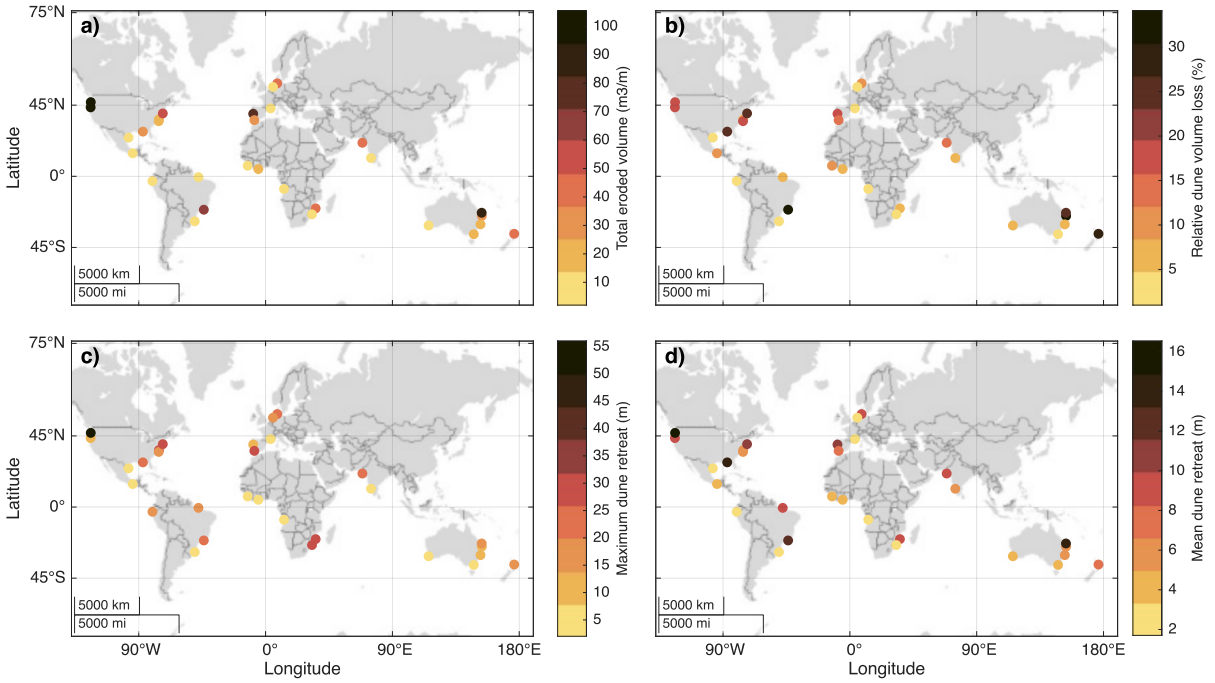

Figure 4.9 Erosional response of synthetic barrier island profiles to a 50-year return period storm simulated with XBeach in surfbeat mode. (a) Eroded volume (in m^3/m), (b) relative volume loss (in %), (c) maximum dune horizontal retreat (in m) and (d) average dune retreat (in m).

4.3.5 Storm-induced barrier flooding

Sixteen out of the thirty barrier islands experienced episodes of overwash during the XB-NH simulations of a synthetic 50-year return period storm. This means that the barrier islands analyzed can be distinguished between those experiencing only collision erosional hazard and those experiencing overwash flooding hazard regimes, as defined by Leaman et al. (2021). In terms of their geographical distribution, barriers for which overwash was modelled are concentrated in mid-latitude coasts in the North Atlantic, North Pacific and around the coast of Australia. The barrier islands that experienced greater overtopping volumes (Figure 4.10a) were Jalabert Beach (74 m^3/m), Moreton Island (68 m^3/m) and Aguachil (64 m^3/m), which are all characterized by low dunes. The number of overtopping waves (Figure 4.10b) was higher at Pensacola Beach (9311) and Mangaluru (7054), which experienced long synthetic storms (144 h and 300 h, respectively), with the former also registering the longest overwash extent (121.5 m, Figure 4.10d). The highest run-up simulated with XB-NH (Figure 4.10c) was in South Jetty Beach (15.6 m) and Mira Beach (12.9 m).

It was found that when the total barrier volume (estimated as the area between MSL and the dune crest) divided by the product of the maximum offshore H_s and the maximum offshore water level was less than 42, the barrier islands experienced overwash (Figure 4.11); if it was greater, then the volume of the barrier island didn't allow overwash. The exceptions were Sylt, Mangaluru and Terschelling, which didn't experience overwash, most likely due to their shallow and gently sloping nearshore area which dissipated part of the energy. Forster, on the other hand, has a steeper profile that allowed more wave energy to reach the shore, causing overwash despite the large barrier volume. Moreover, looking at the average values of the explanatory variables for the barrier islands that experienced overwash compared to the average values for the barrier islands that didn't, the average storm power (10.4 MWh/m versus 4.1 MWh/m) was higher, while the non-overwashed barrier islands had a larger dune volume (307.6 m^3/m versus 246.8 m^3/m) and dune half width (58.9 m versus 55.6 m).

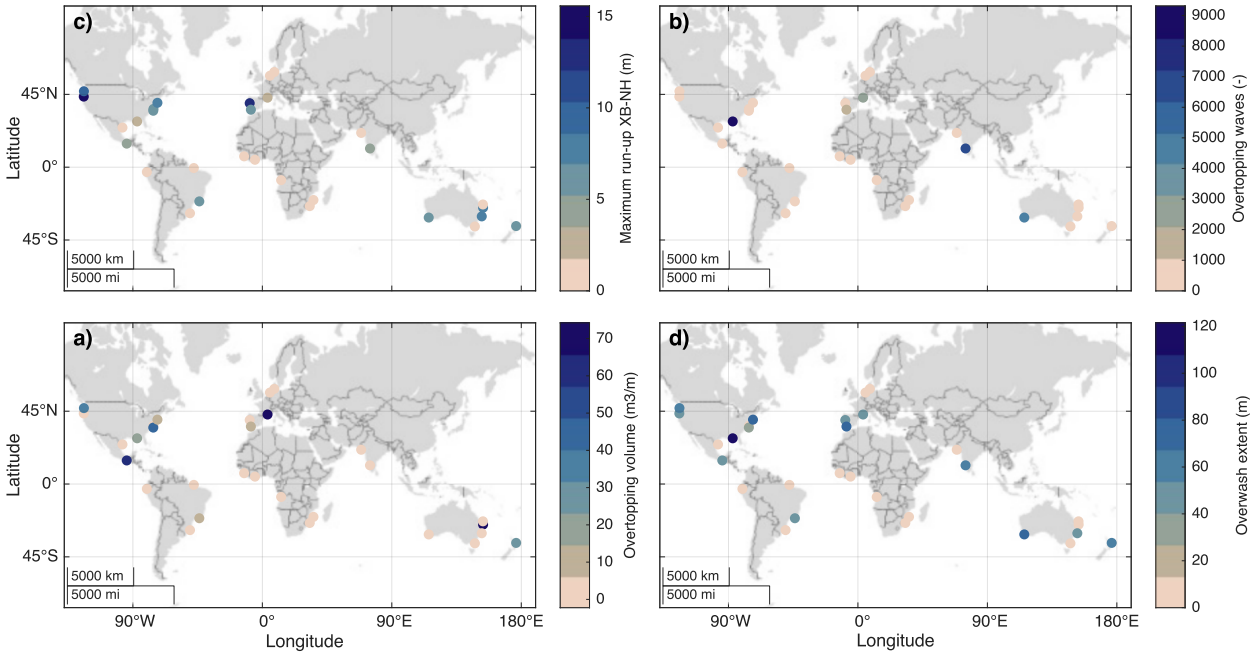

Figure 4.10 Flooding due to overwash events for a 50-year return period storm simulated with XBeach in non-hydrostatic mode. (a) Maximum run-up simulated with XB-NH only shown for overwashed barrier islands (in m), (b) number of overtopping waves, (c) overtopping volume (in m^3/m), (d) overwash extent (in m).

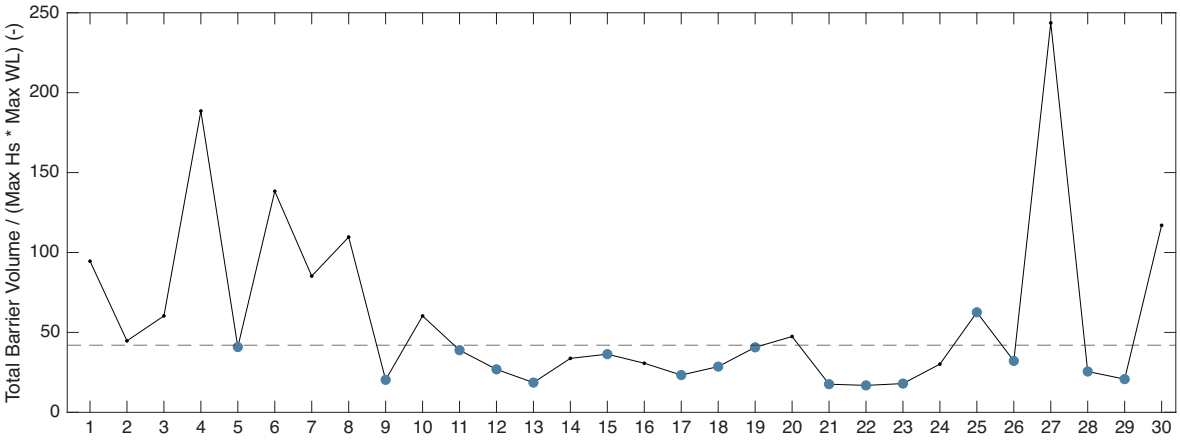

Figure 4.11 Total barrier volume (in m^3/m, calculated from MSL to the dune crest) normalized by the product of the maximum H_s (in m) and maximum water level (in m). The horizontal threshold corresponds to 42. Barrier islands that experienced overwash are highlighted with a blue dot.

4.4 Discussion

4.4.1 Assumptions of the global data and modelling-based methodology

This study focused on event-scale morphodynamic changes on barrier islands using a 1D representation and a synthetic storm with a 50-year return period H_s, employing a methodology that exclusively relies on openly available global datasets. This approach presents both strengths and weaknesses. On the one hand, the creation of a synthetic barrier island profile reduced the impact of data gaps and anomalies by averaging multiple profiles and merging nearshore gaps with an equilibrium shape. This process enabled the seamless integration of two distinct topographic and bathymetric global datasets, TanDEM-X and ETOPO 2022. On the other hand, these global datasets are sometimes limited by outdated topo-bathymetric data, often derived from heterogeneous sources. A main concern also lies in the underestimation of the dune height, as demonstrated in Chapter 3, which might lead to an overestimation of the flooding hazard. Nevertheless, with the increasing availability of satellite-derived topographic and bathymetric data, these limitations are expected to reduce in the future and the accuracy of the global datasets improve.

The hydrodynamic characterization of offshore conditions using global datasets is recognized as a feasible alternative for global to regional scale assessments. Here, data derived from the WAVERYS wave reanalysis were optimized through a calibration equation for shallow coastal areas (Fanti et al., 2023) and dynamically downscaled using SWAN, a method validated in

previous studies (Bellotti et al., 2021). WAVERYS demonstrated to be a valuable and preferable alternative to the commonly used ERA5, especially in coastal areas where a higher resolution of 0.2° instead of 0.5° can improve the representation of more complex topo-bathymetric features (Fanti et al., 2023). However, previous studies (e.g., Cavaleri, 2009; Morim et al., 2023) have shown that extreme wave heights and water levels tend to be underestimated, which can lead also to an underestimation of erosion and flooding hazards. Nevertheless, the WAVERYS-derived hydrodynamic characterization of the storm for the barrier islands analyzed aligned well with Lobeto et al. (2024) in terms of the global distribution of coastal storm H_s, T_p (although they analyzed the mean wave period), storm direction and duration (Figure 4.4). Moreover, the assumption of a synthetic storm with coinciding peak H_s, peak T_p, storm surge, and spring tide represents an idealized worst-case scenario. An improvement over previous methodologies that adopted a synthetic triangular profile (Duo et al., 2020; McCall et al., 2010; Schambach et al., 2018) was achieved by adopting an average storm shape derived from real, de-clustered storms specific to each study area. This approach, combined with linear relationships between storm parameters, allowed for more realistic storm durations in regions influenced by monsoonal winds and TCs.

A relevant part of the approach in this work is the use of models that integrate data from global datasets and use them to produce reliable morphodynamic modelled responses. Accurate erosion and flooding analyses should rely, when possible, on up-to-date information both as input to process-based models and to validate model results. However, that is not always available when using global topo-bathymetry datasets and alternatives must be found. Previous authors have proposed viable alternatives when pre- and post-storm surveys and other detailed information are not available. For instance, Matheen et al. (2021) and Splinter et al. (2011) have tested the validity of XBeach results while varying the nearshore bathymetry, supporting the feasibility of using equilibrium profiles to replace detailed and updated topo-bathymetric data. Moreover, Splinter and Palmsten (2012) found that modelled erosion volumes were more sensitive to changes in the XBeach free parameters than to offshore bathymetry variations.

While calibrating key XBeach parameters can significantly improve accuracy, calibration is both site-specific (Simmons et al., 2019) and event-specific (Rafati et al., 2021), presenting a challenge for global applications. For this global-based approach, due to the impossibility of calibrating XBeach in all coastal areas considered, the default model parameters were used,

probably leading to some additional degree of uncertainty on the results. Studies employing XBeach with default parameters have often reported a tendency of the model to overpredict the erosional response (Harley et al., 2016; Simmons et al., 2017; Splinter and Palmsten, 2012; Vousdoukas et al., 2012). In this study, the most recent version of XBeach, Halloween v1.24, was utilized, as it has been successfully validated with the updated set of default parameters based on a large range of tests for wave flumes and field cases across the Netherlands, Belgium, Germany, Denmark and in the USA (Deltares, 2023). Despite improvements in default parameters, the use of uniform values for varying beach types remains a limitation. Future efforts could focus on defining parameter ranges tailored to specific beach morphologies, such as dissipative or reflective profiles.

A further limitation lies in the use of different XBeach modes for erosion (XB-SB) and flooding (XB-NH), which introduces a level of methodological inconsistency. XB-SB is optimized for simulating long-wave dynamics and cross-shore sediment transport, making it suitable for modeling wave-driven erosion, but it showed to consistently underpredict incident and infragravity swash (de Beer et al., 2021). Conversely, XB-NH is more effective at resolving swash-zone processes and capturing overwash phenomena due to its phase-resolving capabilities, better predicting infragravity waves and therefore run-up (de Beer et al., 2021). However, the reliance on two distinct modes complicates the integration of erosion and overwash predictions, hindering a comprehensive understanding of barrier island storm responses.

4.4.2 Controls on the barrier island morphodynamic response

Large variability in the morphological characteristics of the barrier islands was observed (Figure 4.5), with no apparent latitudinal control, a finding that aligns with the global analysis of nearshore slopes by Athanasiou et al. (2019). Mulhern et al. (2017), analyzing a comprehensive database of barrier islands, demonstrated that their shape is not primarily influenced by coastal wave energy or tidal range, but rather by factors such as the sediment supply, relative sea level change, shelf morphology, tidal prism and, as further emphasized by Davidson-Arnott et al. (2018), aeolian processes, vegetation cover and human impact. Despite these complex and interconnected influences, recent regional-scale research on foredune morphology in southeast Australia (Doyle et al., 2024) highlighted the significant role of

surfzone and beach state in shaping foredune size and volume. Similarly, this study observed that barrier islands with steeper nearshore slopes tended to exhibit smaller dune volumes and lower dune heights and that the dimensionless fall velocity was an accurate proxy to define whether the barrier was dissipative, intermediate or reflective.

While it was not possible to validate the erosion and flooding resulting from the synthetic storms, the hotspots of erosion identified in this analysis (Figure 4.9) are consistent with previous analyses highlighting the vulnerability of areas such as South Jetty Beach and Ocean Park in the USA (Allan and Komar, 2006; Mull and Ruggiero, 2014; Ruggiero et al., 2013, 1998) and Mira Beach in the north-west of Portugal (Ponte Lira et al., 2016; Veloso-Gomes et al., 2004). The sites that experienced extreme erosion are located in mid-latitudes and are regularly exposed to ETCs (Figure 4.12). The intensity of extreme storms in these areas can lead to higher erosion compared to tropical storms. Moreover, these are also sites with large dunes, so while they may not be exposed to flooding, erosion is very significant. On the contrary, the areas more prone to flooding were those exposed to TCs and characterized by lower dunes and volumes (Figure 4.11): Pensacola Beach in the Gulf of Mexico, Fire Island on the east coast of the USA and Myalup Beach in the west coast of Australia. Those are followed by the Ancão Peninsula in Southern Portugal and Maketu in New Zealand, which are locations exposed to remnants of TCs and to ETCs. The areas not exposed to either of the storm systems were those experiencing the lowest erosion and no flooding: Sherbro Island, Grand-Lahou and Mussulo Island on the west coast of Africa, Crispim Beach and San Gregorio Island in the equatorial area of Brazil and Ecuador. The exception was Jalabert Beach in southern France, which although was not exposed to large erosion experienced overwash. Besides being characterized by small and low dunes the coastline of southern France, the occurrence of overwash likely results form the fact that this beach is also impacted by tropical-like cyclones formed in the Mediterranean, know as medicanes, that are more frequent in the northwestern part of the mediteranean basin (Cavicchia et al., 2014). This highlights the different behavior of coastal areas influenced by TCs (or TC-like storms) and ETCs. TCs are intense low-pressure systems, associated with extreme winds and rain as well as high waves and storm surges that lead to extensive and damaging coastal flooding (Hu et al., 2018). ETCs are larger and slower-moving systems capable of great coastal impacts such as erosion and surge induced flooding (Harley et al., 2017; Lodise et al., 2022).

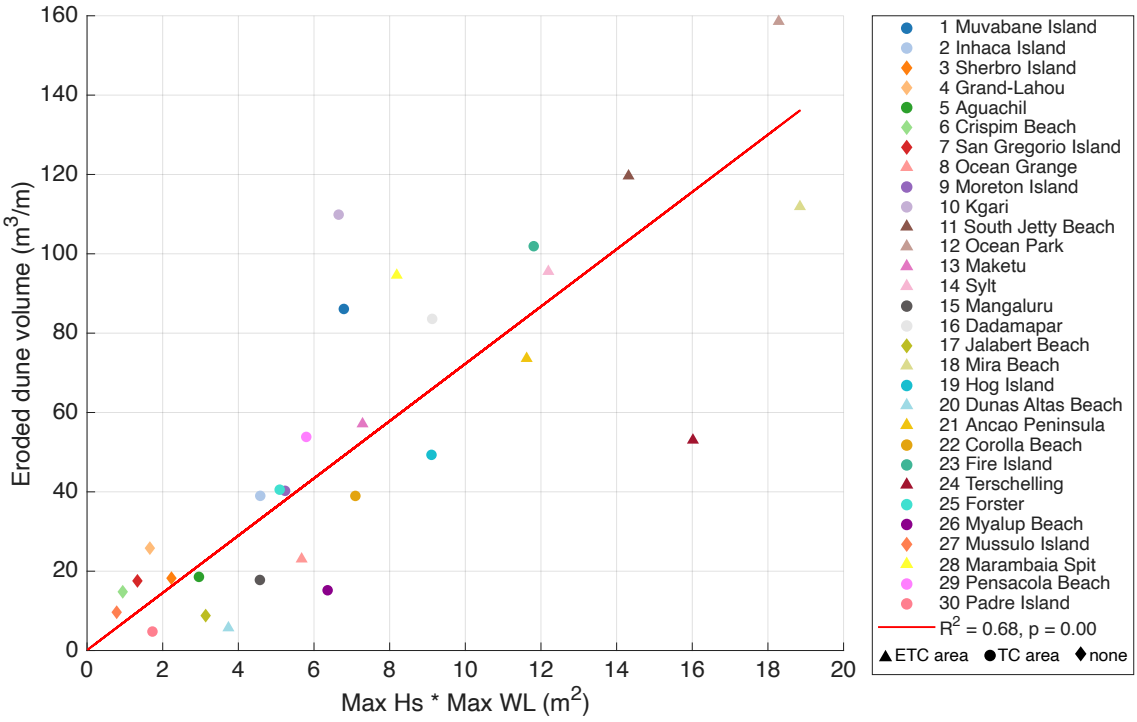

Figure 4.12 Linear regression (red line) between eroded dune volume (in m3/m) and the combination of maximum H_s (in m) and maximum water level (in m) at the offshore boundary of XBeach. The barrier islands located in areas typically affected by extratropical cyclones are represented with triangles, by tropical cyclones with dots and none of them by a diamond.

The impacts of coastal storms, as conceptualized in the Storm Impact Scale model (Sallenger, 2000) and demonstrated in this assessment, are spatially and temporally diverse, but depend primarily on the hydrodynamic forcing of the storm and the morphology of the barrier island. In this study, the relative importance of morphological and hydrodynamic variables was quantified using multilinear regression analysis. The analysis highlighted the fact that the hydrodynamic forcing (maximum H_s and maximum water level) and the morphological characteristics (dune half width and dune height) of the barrier islands derived from the global models alone could already explain a large part of the variability in the erosional response (Figure 4.7). In particular, 87 % of the variability in maximum run-up estimated with XB-SB and 65% of the variability in eroded dune volume were explained by the hydrodynamic forcing alone. Moreover, the same hydrodynamic parameters showed a significant correlation with the eroded dune volume, explaining 68% of the variability (Figure 4.12), indicating that a first estimation of the erosional response can already be obtained from the nearshore propagated hydrodynamic conditions from the global datasets, before further propagation with XBeach. Similarly, Ibaceta and Harley (2024) correlated the storm driven shoreline change with a set of

explanatory variables associated both with beach morphology and storm forcing, demonstrating that the cumulative wave energy dominated the storm response. This result was also partially confirmed by the study of Beuzen et al. (2019), that identified wave power and profile orientation as important controls on the spatial variability of both berm and dune erosion. While wave power was highly correlated with the erosion response, storm direction, and therefore the barrier island exposure to the incoming waves, was not a significant factor, which can result from the premise that only exposed barrier islands were selected for this study. Moreover, this study did not evidence a significant correlation between the dune erosion and the collision duration, possibly due to the problem of identifying the dune toe on the synthetic barrier island profile.

The variability in the flooding response was not well explained by either hydrodynamic or morphological variables, most likely because half of the barrier islands did not experience overwash and the statistical analysis was therefore performed on a smaller sample size. The exception was the maximum run-up in the XB-NH simulations, whose variability was explained equally by the hydrodynamic and morphological variables, and even more by their combination. In fact, the characteristics that exerted a stronger control on the flood response were the total barrier volume and the combined maximum offshore H_s and maximum offshore water level (Figure 4.11), demonstrating the critical role of the dune morphology. For storms with a 50-year return period H_s, overwash on most barrier islands was found to be dependent on a critical threshold: when the ratio of total barrier volume to the combined maximum wave height and water level exceeded 42, overwash was generally absent; when below 42, overwash was present. This straightforward thershold can serve as an initial screening parameter and can be tested for applicability in other regions.

While it may be useful to assess erosion and flooding hazards separately in order to distinguish the dominant processes, the reality is that they occur in combination. In fact, the barrier islands subject to overwash were also the barriers that experienced longer collision regimes in the XB-SB simulations when compared to the non-overwashed barrier islands (59 % overwash vs 37 %), and therefore larger dune erosion and horizontal retreat in the erosional response. This suggests that processes such as barrier roll-over, dune lowering and sediment deposition in the backbarrier may be present but not captured by the modelling, highlighting the need for integrated modeling approaches that do not require a high level of case-specific calibration.

4.4.3 Recommendations for assessing global erosion and flooding using global models

The interaction between the different variables involved in coastal storm impacts is inherently complex and nonlinear. However, the present analysis demonstrates that the hydrodynamic variables play a dominant role in determining the erosional response. This finding underscores the importance of prioritizing storm forcing in future assessments, emphasizing the need for rigorous validation and calibration, when feasible. A more precise representation of storm-induced hydrodynamic forcing can improve predictive accuracy and enhance the reliability of coastal vulnerability assessments.

Another critical issue identified in this study is the limitations in accurately identifying the dune toe in the pre-storm profile derived from TanDEM-X. While future advancements in global DEMs with higher resolution may mitigate this limitation, the difficulty in precisely determining the dune toe persists even with high-resolution datasets (Smith et al., 2020; Wernette et al., 2016). This limitation has significant implications for global-scale coastal erosion studies, as it restricts the ability to use the dune toe as a proxy for assessing storm-induced erosion. Given the variability and uncertainty associated with point-based measurements, a more robust approach at the global scale should rely on integrative parameters. Metrics such as total eroded volume, mean retreat, and dune volume provide a more comprehensive representation of overall erosional behavior, capturing the spatial variability of storm impacts more effectively.

Regarding flooding dynamics, the results from XB-NH simulations indicate that while hydrodynamic forcing is a key driver, its influence on overwash indicators is less distinct. For large-scale assessments using global datasets, we recommend prioritizing overtopping volume and overwash duration rather than indicators that rely also on the backbarrier morphology, such as overwash discharge or overwash extent. This is mainly due to the lower accuracy of global DEMs in the presence of vegetation.

In cases where high-resolution datasets orf hydrodynamic forcing and barrier island morphology are unavailable, the combined use of multiple global datasets offers a viable alternative for process-based assessments of coastal erosion and flooding responses. Specifically, propagating WAVERYS with SWAN, integrating TanDEM-X with ETOPO 2022

with an equilibrium profile, and using process-based modelling with XBeach provide a suitable methodological framework for capturing coastal storm impacts.

4.5 Conclusion

This study proposes an integrated methodology for assessing the impact of a synthetic storm on any natural barrier island worldwide, utilizing open-source global datasets of waves, water levels, and topo-bathymetry as input to the XBeach process-based model. While global datasets and the use of XBeach with default parameters have inherent limitations, particularly in capturing the complex and dynamic morphology and morphodynamic response of barrier island systems, the findings provide valuable insights into the key factors driving dune erosion and barrier overwash variability. Notably, the global distribution of erosion and flooding hotspots identified in this study aligns with areas exposed to ETCs and TCs. The 50-year return period H_s and the associated water level, derived from WAVERYS and GTSM models, explained a large part of the variability in the erosion response. The same hydrodynamic parameters were used to normalize the total dune volume and establish a threshold for identifying overwash occurrences. These findings highlight the potential of global models and their datasets for large-scale assessments, with the promise of even greater skill if their uncertainties are systematically included in the modelling chain to define uncertainty bounds for erosion and flooding hazards. The present study has demonstrated that XBeach can be used in combination with global datasets for global-scale assessments of erosion and overwash at coastal barriers. This approach can also be extended to incorporate future projections of global changes in extreme wave events and rising sea levels to generate future scenarios that could inform current and future management decisions.

4.6 Appendix A. Location and hydrodynamic characteristics of the barrier islands

Table S4.3 Barrier islands name, location, coordinates of the analyzed sector, depth of closure (Dc), and offshore wave characteristics extracted from WAVERYS global wave reanalysis and GTSM.

id	name	location	coordinates	Mean annual tidal range (m)	Mean annual offshore wave height (m)	Doc (m)	50-year return period offshore wave height (m)
1	Muvabane Island	Mozambique, Africa	22.197°S 35.534°E	2.40	1.74	9.31	6.66
2	Inhaca Island	Mozambique, Africa	26.043°S, 32.967°E	1.82	2.08	11.27	6.91
3	Sherbro Island	Sierra Leone, Africa	7.499°N, 12.684°W	1.04	1.28	5.79	3.02
4	Grand-Lahou	Ivory Coast, Africa	5.128°N, 5.129°W	0.86	1.34	5.86	3.19
5	Aguachil	Oxaca, Mexico	16.127°N, 94.283°W	1.34	1.77	8.54	5.46
6	Crispim Beach	Pará, Brazil	0.597°S, 47.638°W	0.56	1.20	4.64	2.94
7	San Gregorio Island	El Oro, Ecuador	3.352°S, 80.287°W	1.48	1.20	5.34	2.93
8	Ocean Grange	Victoria, Australia	37.975°S, 147.748°E	0.39	1.40	8.50	6.30
9	Moreton Island	Queensland, Australia	27.056°S, 153.457°E	1.14	1.90	8.73	7.26
10	K'gari	Queensland, Australia	25.031°S, 153.350°E	1.15	1.58	9.77	6.02
11	South Jetty Beach	Oregon, USA	43.888°N, 124.154°W	1.74	2.09	14.7	10.05
12	Ocean Park	Washington, USA	46.496°N, 124.058°W	1.91	2.33	15.15	10.10
13	Maketu	Bay of Plenty, New Zealand	37.749°S, 176.422°E	1.65	1.39	9.75	6.80
14	Sylt	Schleswig-Holstein, Germany	54.916°N, 8.303°E	2.08	1.70	11.47	9.00
15	Mangaluru	Karnataka, India	12.855°N, 74.821°E	0.89	1.30	9.7	6.40
16	Dadamapar	Gujarat, India	23.126°N, 68.702°E	1.81	1.43	9.46	6.72

17	Jalabert Beach	Sète, France	43.362°N, 3.610°E	0.17	0.77	8.15	6.40
18	Mira Beach	Coimbra, Portugal	40.495°N, 8.789°W	2.40	2.14	14.72	9.42
19	Hog Island	Virginia, USA	36.402°N, 75.698°W	0.70	1.42	10.71	8.49
20	Dunas Altas Beach	Rio Grande do Sul, Brazil	30.410°S, 50,292°W	0.20	2.00	10.67	6.93
21	Ancão Peninsula	Algarve, Portugal	36.994°N, 7.974°W	2.39	1.27	9.85	6.79
22	Corolla Beach	North Carolina, USA	36.403°N, 75.830°W	0.64	1.37	11.18	8.16
23	Fire Island	New York, USA	40.707°N, 72.941°W	1.29	1.51	12.08	8.87
24	Terschelling	West Frisian Islands, Netherlands	53.401°N, 5.258°E	2.27	1.61	11.35	8.11
25	Forster	New South Wales, Australia	32.266°S, 152.531°E	1.07	1.60	9.89	6.63
26	Myalup Beach	Western Australia	32.948°S, 115.661°E	0.23	2.89	16.18	9.89
27	Mussulo Island	Angola, Africa	8.954°S, 13.057°E	0.95	1.26	5.93	3.51
28	Marambaia Spit	Rio de Janeiro, Brazil	23.067°S, 43.820°W	2.07	1.67	8.82	5.43
29	Pensacola Beach	Florida, USA	30.345°N, 87.065°W	0.29	0.90	9.36	9.09
30	Padre Island	Texas, USA	26,464°N, 97.242°W	0.33	1.23	8.08	5.62

4.7 Appendix B. Characteristics of the morphological and hydrodynamic variables

The following is a detailed description of the morphological and hydrodynamic variables as defined in Table 4.1:

- *Latitude (°):* the latitude can be a proxy of the global climate and mean H_s distribution, specifically for coastal storms a latitudinal storminess gradient was observed by Lobeto et al. (2024), with higher values for extratropical latitudes.
- *Depth of closure (m):* the morphodynamic boundary separating the active upper shoreface from the non-active lower shoreface. It was estimated from the Hallermeier's

(1981) formulation from the H_s that is exceeded for 12 hours per year and the associated wave period.

- *Nearshore slope (-):* calculated from the depth of closure to the MSL (h = 0).
- *Total barrier volume (m^3/m):* calculated as the volume, per linear meter alongshore, between MSL and the dune crest.
- *Beach slope (-):* calculated between the MSL and the pre-storm dune toe.
- *Beach width (m):* calculated as the horizontal distance between the MSL and the pre-storm dune toe.
- *Berm volume (m^3/m):* calculated as the volume, per linear meter alongshore, between MSL and the pre-storm dune toe
- *Dune half width (m):* calculated as the horizontal distance between the pre-storm dune toe and the pre-storm dune crest. Only the half width was considered due to the presence of different morphologies of the barrier island, with some having vegetation in the backbarrier area, others a second dune, others a lagoon.
- *Dune height (m):* calculated as the vertical distance between the pre-storm dune toe and the pre-storm dune crest. Three methods to identify the dune toe location were tested: the second derivative; the farthest point from a linear fit between the position of the mean high water (average of all high tide levels in the record) and the dune crest; setting a threshold slope change. The latter was the method chosen for giving the most reasonable results after visual inspection.
- *Dune volume (m^3/m):* calculated as the volume, per linear meter alongshore, between the pre-storm dune toe and the dune crest.
- *D50 (mm)*: mean grain size obtained from fitting the Dean equilibrium profile from the MSL to the depth of closure.
- *Dimensionless fall velocity (-*): estimated as in Anthony (1998) from the breaker wave heigh H_b, which was assumed to correspond to the average storm H_s propagated to 30 m depth with SWAN; the mean storm T_p was also obtained from the SWAN propagation to 30 m water depth; while the sediment fall velocity w_s was estimated according to Soulsby (1997):

$$\Omega = H_b / W_s T \tag{4.3}$$

$$w_s = \frac{\nu}{D50}\left[(10.36^2 + 1.049 d_*^3)^{1/2} - 0.36\right] \tag{4.4}$$

Where ν is the kinematic viscosity, d_* is the nondimensional gain size. Assuming that the morphology is in equilibrium with the hydrodynamic forcing, a Ω lower than 1 is associated with a fully reflective beach, 1 < Ω < 6 intermediate and Ω > 6 dissipative.

- *Maximum offshore H_s (m):* maximum significant wave height during the synthetic storm, which corresponds to the 50-year return period H_s estimated from the WAVERYS global reanalysis and propagated to 30 m water depth with SWAN.
- *Maximum offshore T_p (s):* maximum peak period during the synthetic storm estimated from the WAVERYS global reanalysis and propagated to 30 m water depth with SWAN.
- *Relative storm direction (-):* the SWAN propagated direction is modified so that the XBeach input direction ranges from 180° to 360° (nautical convention, clockwise from the north), with 270° waves approaching perpendicularly to the coast. As wave direction is a circular variable, in order to allow its use in correlation analysis it was linearized with the sine function and referenced to 270°. This results in negative values (until -1) for storms approaching from the north and positive values (until 1) for storms from the south.

$$\sin(dir_{rel}) = \sin(dir - 270°) \tag{4.5}$$

- *Storm power (MWh/m):* cumulative storm power that takes into account both the duration and intensity of the event, calculated following Splinter et al. (2014):

$$\sum P = \int_0^N \frac{\rho g^2}{64\pi} H_s^2 T_p \Delta t \tag{4.6}$$

Where N is the duration of the storm event, ρ is the seawater density (1025 kg/m^3), g is the acceleration due to gravity and Δt is the temporal resolution of the wave data.

- *Wave energy at the depth of closure (Nm/m^2):* estimated as the sum of the wave energy (E) output parameter from XBeach at the depth of closure over the entire storm duration.
- *Wave energy at 2 m depth (Nm/m^2):* estimated as the sum of the wave energy (E) output parameter from XBeach at 2 m water depth over the entire storm duration.

- *Maximum water level (m):* calculated as the sum of the peak of the mean spring tidal cycle and the peak of the storm surge that corresponds to a 50-year return period H_s, both estimated from the GTSM database.
- *Tide range (m):* amplitude of the tidal signal during the storm (excluding the storm surge), calculated as the sum of the highest peak and lowest through.
- *Mean annual H_s (m):* estimated over the 30 years of WAVERYS H_s data.
- *Mean annual tide range (m):* estimated as the mean difference between high and low tide over the 27 years of GTSM tidal data.

4.8 Appendix C. Process-based indicators

The erosion response variables in Table 4.2 were estimated from the XB-SB runs and are defined as follows:

- *Collision hours (%):* following Sallenger's (2000) storm impact scale a collision regime is when the run-up (estimated from the run-up gauge of XB-SB) exceeds the dune toe. The percentage number of hours of collision was calculated over the total storm duration.
- *Maximum run-up XB-SB (m):* estimated using the gauge option from XBeach that moves with the waterline and gives a time-series output of locations representing the run-up at time steps of 100 s.
- *Dune eroded volume (m^3/m):* calculated as the initial dune volume minus the final dune volume, integrated from the pre-storm dune toe until the dune crest. Positive (negative) values stand for erosion (accumulation).
- *Berm eroded volume (m^3/m):* calculated as the initial berm volume minus the final berm volume, integrated from the MSL until the dune toe. Such simplification was necessary due to the lack of more accurate information on the berm location, which is not captured by the 12 m resolution global DEM TanDEM-X.
- *Total eroded volume (m^3/m):* calculated as the initial total volume minus the final total volume, integrated from MSL until the dune crest.
- *Maximum retreat (m):* maximum horizontal retreat calculated from MSL to the dune crest.
- *Mean retreat (m):* mean horizontal dune retreat calculated from MSL to the dune crest.

- *Dune toe retreat (m):* horizontal difference between pre-storm dune toe position and post-storm dune toe position.
- *Shoreline retreat (m):* horizontal difference between pre-storm shoreline position and post-storm shoreline position referenced to MSL.
- *Relative volume loss (%):* percentage of eroded volume over the total pre-storm volume (calculated from MSL to the dune crest).

From the XB-NH runs the following variables were retrieved to quantify the flooding response, as reported in Table 4.2:

- *Overwash hours (%):* following Sallenger's (2000) storm impact scale the overwash regime is when the run-up (estimated from the run-up gauge of XB-NH) exceeds the dune crest. The total number of hours when the run-up was higher than the dune crest was divided by the total storm duration, and the percentage was computed.
- *Maximum run-up XB-NH (m):* highest elevation referenced to MSL that was reached by the water during the storm determined by identifying the maximum value registered by the run-up gauge at each time step.
- *Overtopping volume (m^3):* estimated by computing the total volume of water that overtopped the dune crest. This was done using the overtopping discharge in the x-direction (parameter *qx* in the XBeach output). Specifically, for each time step, the volume of water that overtopped the dune crest was calculated as the product of the discharge (*qx* in m^2/s) and the time interval between measurements. This was then summed across all time steps to obtain the total overtopping volume in cubic meters (m^3).
- *Average overtopping discharge (l/s/m):* the average rate at which water overtops the dune crest in liters per second per meter of barrier length, computed from the total volume of overtopping water over the storm divided by the storm duration and the cross-sectional area of the overtopping basin (estimated from the profile length).
- *Number of overtopping waves (-):* determined by counting the number of events during the storm when the water level exceeded the dune crest.
- *Mean overtopping event duration (s):* calculated by first identifying the start and end times of each overtopping event (using a peak detection algorithm on the run-up data). The duration of each event was computed as the difference between the start and end

times, and the average of these durations was then taken to give the mean overtopping event duration in seconds.

- *Overwash extent (m):* most landward point reached by the run-up in the backbarrier measured from the dune crest.

4.9 Acknowledgments

Valeria Fanti is funded through the Fundação para a Ciência e Tecnologia (FCT) PhD Research Scholarships program (ref. 2020.07553.BD). This study was supported by national funds through FCT, under the institutional grants to the Associate Laboratory ARNET (LA/P/0069/2020) and CIMA (UID/00350/2020). This study has involved data acquired from many sources: Hersbach, H. et al. (2020) was downloaded from the Copernicus Climate Change Service (C3S) Climate Data Store; Copernicus Marine Service Information; https://doi.org/10.48670/moi-00022; TanDEM-X data were provided by the German Aerospace Center (DLR) under TanDEM-X Science Proposal DEM_HYDR3317.

4.10 References

Allan, J.C., Komar, P.D., 2006. Climate controls on US West Coast erosion processes. J. Coast. Res. 22, 511–529. https://doi.org/10.2112/03-0108.1

Almeida, L.P.M., Ferreira, Ó., Pacheco, A., 2011. Thresholds for morphological changes on an exposed sandy beach as a function of wave height. Earth Surf. Process. Landforms 36, 523–532. https://doi.org/10.1002/esp.2072

Anthony, E.J., 1998. Sediment-wave parametric characterization of beaches. J. Coast. Res. 14, 347–352.

Athanasiou, P., van Dongeren, A.R., Giardino, A., Vousdoukas, M.I., Gaytan-Aguilar, S., Ranasinghe, R., 2019. Global distribution of nearshore slopes with implications for coastal retreat. Earth Syst. Sci. Data 11, 1515–1529. https://doi.org/10.5194/essd-11-1515-2019

Athanasiou, P., van Dongeren, A.R., Giardino, A., Vousdoukas, M.I., Ranasinghe, R., Kwadijk, J., 2020. Uncertainties in projections of sandy beach erosion due to sea level rise: an analysis at the European scale. Sci. Rep. 10, 1–14. https://doi.org/10.1038/s41598-020-68576-0

Athanasiou, P., van Dongeren, A.R., Pronk, M., Giardino, A., Vousdoukas, M., Ranasinghe, R., 2024. Global Coastal Characteristics (GCC): A global dataset of geophysical, hydrodynamic and socioeconomic coastal indicators (submitted for publication). Earth Syst. Sci. Data Discuss. 8200199, 3433–3452.

Bellotti, G., Franco, L., Cecioni, C., 2021. Regional Downscaling of Copernicus ERA5 Wave Data for Coastal Engineering Activities and Operational Coastal Services. Water 13, 859.

Beuzen, T., Harley, M.D., Splinter, K.D., Turner, I.L., 2019. Controls of Variability in Berm and Dune Storm Erosion, Journal of Geophysical Research: Earth Surface. https://doi.org/10.1029/2019JF005184

Booij, N., Ris, R.C., Holthuijsen, L.H., 1999. A third-generation wave model for coastal regions 1. Model description and validation. J. Geophys. Res. Ocean. 104, 7649–7666. https://doi.org/10.1029/98JC02622

Bove, G., Becker, A., Sweeney, B., Vousdoukas, M.I., Kulp, S., 2020. A method for regional estimation of climate change exposure of coastal infrastructure: Case of USVI and the influence of digital elevation models on assessments. Sci. Total Environ. 710, 136162. https://doi.org/10.1016/j.scitotenv.2019.136162

Bugajny, N., Furmańczyk, K., Dudzińska-Nowak, J., Paplińska-Swerpe, B., 2013. Modelling morphological changes of beach and dune induced by storm on the Southern Baltic coast using XBeach (case study: Dziwnow Spit). J. Coast. Res. 672–677. https://doi.org/10.2112/SI65-114

Cañizares, R., Irish, J.L., 2008. Simulation of storm-induced barrier island morphodynamics and flooding. Coast. Eng. 55, 1089–1101. https://doi.org/10.1016/j.coastaleng.2008.04.006

Carapuço, M.M., Taborda, R., Silveira, T.M., Psuty, N.P., Andrade, C., Freitas, M.C., 2016. Coastal geoindicators: Towards the establishment of a common framework for sandy coastal environments. Earth-Science Rev. 154, 183–190. https://doi.org/10.1016/j.earscirev.2016.01.002

Cavaleri, L. (2009). Wave modeling-Missing the peaks. *Journal of Physical Oceanography*, *39*(11), 2757–2778. https://doi.org/10.1175/2009JPO4067.1

Cavicchia, L., von Storch, H., & Gualdi, S. (2014). A long-term climatology of medicanes. *Climate Dynamics*, *43*(5–6), 1183–1195. https://doi.org/10.1007/s00382-013-1893-7

Ciavola, P., Ferreira, Ó., Haerens, P., van Koningsveld, M., Armaroli, C., Lequeux, Q., 2011. Storm impacts along European coastlines. Part 2: Lessons learned from the MICORE project. Environ. Sci. Policy 14, 924–933. https://doi.org/10.1016/j.envsci.2011.05.009

Cooper, J.A.G., Pilkey, O.H., 2002. The Barrier Islands of Southern Mozambique. J. Coast. Res. 36, 164–172. https://doi.org/10.2112/1551-5036-36.sp1.164

Davidson-Arnott, R.G.D., Hesp, P., Ollerhead, J., Walker, I., Bauer, B., Delgado-Fernandez, I., Smyth, T., 2018. Sediment budget controls on foredune height: Comparing simulation model results with field data. Earth Surf. Process. Landforms 43, 1798–1810. https://doi.org/10.1002/esp.4354

de Beer, A.F., McCall, R.T., Long, J.W., Tissier, M.F.S., Reniers, A.J.H.M., 2021. Simulating wave runup on an intermediate–reflective beach using a wave-resolving and a wave-averaged version of XBeach. Coast. Eng. 163, 103788. https://doi.org/10.1016/j.coastaleng.2020.103788

de Ridder, M.P., Smit, P.B., van Dongeren, A.R., McCall, R.T., Nederhoff, K., Reniers, A.J.H.M., 2021. Efficient two-layer non-hydrostatic wave model with accurate dispersive behaviour. Coast. Eng. 164. https://doi.org/10.1016/j.coastaleng.2020.103808

de Vet, L., McCall, R.T., Den Bieman, J.P., Stive, M.J.F., van Ormondt, M., 2015. Modelling Dune Erosion, Overwash and Breaching At Fire Island (NY) During Hurricane Sandy 1–10. https://doi.org/10.1142/9789814689977_0006

Dean, R.G., 1991. Equilibrium beach profiles: Characteristics and applications. J. Coast. Res. 7, 53–84.

Deltares, 2023. XBeach skillbed report: XBeach 1.14 Halloween.

Doyle, T.B., Hesp, P.A., Woodroffe, C.D., 2024. Foredune morphology: Regional patterns and surfzone–beach–dune interactions along the New South Wales coast, Australia. Earth Surf. Process. Landforms 49, 3115–3138. https://doi.org/10.1002/esp.5879

Duo, E., Sanuy, M., Jiménez, J.A., Ciavola, P., 2020. How good are symmetric triangular synthetic storms to represent real events for coastal hazard modelling. Coast. Eng. 159. https://doi.org/10.1016/j.coastaleng.2020.103728

Eilander, D., Couasnon, A., Leijnse, T., Ikeuchi, H., Yamazaki, D., Muis, S., Winsemius, H.C., Ward, P.J., 2022. A globally-applicable framework for compound flood hazard modeling 1–40.

Elsayed, S.M., Oumeraci, H., 2017. Effect of beach slope and grain-stabilization on coastal sediment transport: An attempt to overcome the erosion overestimation by XBeach. Coast. Eng. 121, 179–196. https://doi.org/10.1016/j.coastaleng.2016.12.009

Fanti, V., Ferreira, Ó., Kümmerer, V., Loureiro, C., 2023. Improved estimates of extreme wave conditions in coastal areas from calibrated global reanalyses. Commun. Earth Environ. 4, 151. https://doi.org/https://doi.org/10.1038/s43247-023-00819-0

Fanti, V., Loureiro, C., Ferreira, Ó., 2025. Development of topo-bathymetric continuum profiles for coastal barriers with global. Remote Sens. Appl. Soc. Environ. 38, 101528.

Ferreira, Ó., Plomaritis, T.A., Costas, S., 2017. Process-based indicators to assess storm induced coastal hazards. Earth-Science Rev. 173, 159–167. https://doi.org/10.1016/j.earscirev.2017.07.010

Garzon, J.L., Ferreira, Ó., Plomaritis, T.A., 2022. Modeling of Coastal Erosion in Exposed and Groin-Protected Steep Beaches. J. Waterw. Port, Coastal, Ocean Eng. 148, 1–16. https://doi.org/10.1061/(asce)ww.1943-5460.0000719

Gesch, D.B., 2018. Best practices for elevation-based assessments of sea-level rise and coastal flooding exposure. Front. Earth Sci. 6. https://doi.org/10.3389/feart.2018.00230

Gharagozlou, A., Dietrich, J.C., Karanci, A., Luettich, R.A., Overton, M.F., 2020. Storm-driven erosion and inundation of barrier islands from dune-to region-scales. Coast. Eng. 158, 103674. https://doi.org/10.1016/j.coastaleng.2020.103674

Gharagozlou, A., Dietrich, J.C., Massey, T.C., Anderson, D.L., Gorski, J.F., Overton, M.F., 2021. Formation of a barrier island breach and its contributions to lagoonal circulation. Estuar. Coast. Shelf Sci. 262, 107593. https://doi.org/10.1016/j.ecss.2021.107593

Gracia, V., García, M., Grifoll, M., Sánchez-Arcilla, A., 2013. Breaching of a barrier under extreme events. The role of morphodynamic simulations. J. Coast. Res. 65, 951–956. https://doi.org/10.2112/si65-161.1

Hallermeier, R., 1981. A profile zonation for seasonal sand beaches from wave climate. Coast. Eng. 4, 253–277.

Harley, M.D., Turner, I.L., Kinsela, M.A., Middleton, J.H., Mumford, P.J., Splinter, K.D., Phillips, M.S., Simmons, J.A., Hanslow, D.J., Short, A.D., 2017. Extreme coastal erosion enhanced by anomalous extratropical storm wave direction. Sci. Rep. 7, 1–9. https://doi.org/10.1038/s41598-017-05792-1

Harley, M.D., Valentini, A., Armaroli, C., Perini, L., Calabrese, L., Ciavola, P., 2016. Can an early-warning system help minimize the impacts of coastal storms? A case study of the 2012 Halloween storm, northern Italy. Nat. Hazards Earth Syst. Sci. 16, 209–222. https://doi.org/10.5194/nhess-16-209-2016

Harter, C., Figlus, J., 2017. Numerical modeling of the morphodynamic response of a low-lying barrier island beach and foredune system inundated during Hurricane Ike using XBeach and CSHORE. Coast. Eng. 120, 64–74. https://doi.org/10.1016/j.coastaleng.2016.11.005

Hoagland, S.W.H., Jeffries, C.R., Irish, J.L., Weiss, R., Mandli, K., Vitousek, S., Johnson, C.M., Cialone, M.A., 2023. Advances in Morphodynamic Modeling of Coastal Barriers: A Review. J. Waterw. Port, Coastal, Ocean Eng. 149, 1–27. https://doi.org/10.1061/jwped5.wweng-1825

Hu, P., Zhang, Q., Shi, P., Chen, B., Fang, J., 2018. Flood-induced mortality across the globe: Spatiotemporal pattern and influencing factors. Sci. Total Environ. 643, 171–182. https://doi.org/10.1016/j.scitotenv.2018.06.197

Ibaceta, R., Harley, M.D., 2024. Data-driven modelling of coastal storm erosion for real-time forecasting at a wave-dominated embayed beach. Coast. Eng. 193. https://doi.org/10.1016/j.coastaleng.2024.104596

Kirezci, E., Young, I.R., Ranasinghe, R., Muis, S., Nicholls, R.J., Lincke, D., Hinkel, J., 2020. Projections of global-scale extreme sea levels and resulting episodic coastal flooding over the 21st Century. Sci. Rep. 10, 1–12. https://doi.org/10.1038/s41598-020-67736-6

Kümmerer, V., Ferreira, Ó., Fanti, V., Loureiro, C., 2024. Storm identification for high-energy wave climates as a tool to improve long-term analysis. Clim. Dyn. 62, 2207–2226. https://doi.org/10.1007/s00382-023-07017-w

Larson, M., Erikson, L., Hanson, H., 2004. An analytical model to predict dune erosion due to wave impact. Coast. Eng. 51, 675–696. https://doi.org/10.1016/j.coastaleng.2004.07.003

Larson, M., Kraus, N.C., 1989. SBEACH: numerical model for simulating storm-induced beach change; report 1: empirical foundation and model development. Tech. Rep. - US Army Coast. Eng. Res. Cent. 89–9.

Law-Chune, S., Aouf, L., Dalphinet, A., Levier, B., Drillet, Y., Drevillon, M., 2021. WAVERYS: a CMEMS global wave reanalysis during the altimetry period. Ocean Dyn. 71, 357–378. https://doi.org/10.1007/s10236-020-01433-w

Leaman, C.K., Harley, M.D., Splinter, K.D., Thran, M.C., Kinsela, M.A., Turner, I.L., 2021. A storm hazard matrix combining coastal flooding and beach erosion. Coast. Eng. 170, 104001. https://doi.org/10.1016/j.coastaleng.2021.104001

Lobeto, H., Semedo, A., Lemos, G., Dastgheib, A., Menendez, M., Ranasinghe, R., Bidlot, J.R., 2024. Global coastal wave storminess. Sci. Rep. 14, 1–18. https://doi.org/10.1038/s41598-024-51420-0

Lodise, J., Merrifield, S., Collins, C., Rogowski, P., Behrens, J., Terrill, E., 2022. Global Climatology of Extratropical Cyclones From a New Tracking Approach and Associated Wave Heights From Satellite Radar Altimeter. J. Geophys. Res. Ocean. 127. https://doi.org/10.1029/2022JC018925

Luijendijk, A., Hagenaars, G., Ranasinghe, R., Baart, F., Donchyts, G., Aarninkhof, S., 2018. The State of the World's Beaches. Sci. Rep. 8, 1–11. https://doi.org/10.1038/s41598-018-24630-6

Mackay, E., Johanning, L., 2018. A generalised equivalent storm model for long-term statistics of ocean waves. Coast. Eng. 140, 411–428. https://doi.org/10.1016/j.coastaleng.2018.06.001

Martín-Hidalgo, M., Martín-Soldevilla, M.J., Negro, V., Aberturas, P., López-Gutiérrez, J.S., 2014. Storm evolution characterization for analysing stone armour damage progression. Coast. Eng. 85, 1–11. https://doi.org/10.1016/j.coastaleng.2013.11.008

Martín Soldevilla, M.J., Martín-Hidalgo, M., Negro, V., López-Gutiérrez, J.S., Aberturas, P., 2015. Improvement of theoretical storm characterization for different climate conditions. Coast. Eng. 96, 71–80. https://doi.org/10.1016/j.coastaleng.2014.11.004

Matheen, N., Harley, M.D., Turner, I.L., Splinter, K.D., Simmons, J.A., Thran, M.C., 2021. Bathymetric data requirements for operational coastal erosion forecasting using xbeach. J. Mar. Sci. Eng. 9. https://doi.org/10.3390/jmse9101053

McCall, R.T., van Thiel de Vries, J.S.M., Plant, N.G., van Dongeren, A.R., Roelvink, J.A., Thompson, D.M., Reniers, A.J.H.M., 2010. Two-dimensional time dependent hurricane overwash and erosion modeling at Santa Rosa Island. Coast. Eng. 57, 668–683. https://doi.org/10.1016/j.coastaleng.2010.02.006

Mentaschi, L., Vousdoukas, M.I., Pekel, J.F., Voukouvalas, E., Feyen, L., 2018. Global long-term observations of coastal erosion and accretion. Sci. Rep. 8, 1–11. https://doi.org/10.1038/s41598-018-30904-w

Mickey, R.C., Long, J.W., Plant, N.G., Thompson, D.M., Dalyander, P.S., Werkheiser, W.H., 2017. A methodology for modeling barrier island storm-impact scenarios, USGS Open-File Report 2017-1009.

Miselis, J.L., Lorenzo-Trueba, J., 2017. Natural and Human-Induced Variability in Barrier-Island Response to Sea Level Rise. Geophys. Res. Lett. 44, 11,922-11,931. https://doi.org/10.1002/2017GL074811

Morim, J., Wahl, T., Vitousek, S., Santamaria-Aguilar, S., Young, I., & Hemer, M. (2023). Understanding uncertainties in contemporary and future extreme wave events for broad-scale impact and adaptation planning. *Science Advances*, *9*(2), 1–13. https://doi.org/10.1126/sciadv.ade3170

Muis, S., Aerts, J.C.J.H., Alvarez, A., Dullaart, J., Minh, T., Erikson, L., Haarmsa, R., Apecechea, M.I., Mengel, M., Bars, D. Le, Neill, A.O., Ranasinghe, R., Roberts, M., Ward, P.J., Yan, K., 2022. Global projections of storm surges using high-resolution CMIP6 climate models : validation , projected changes , and methodological challenges.

Mulhern, J.S., Johnson, C.L., Martin, J.M., 2017. Is barrier island morphology a function of tidal and wave regime? Mar. Geol. 387, 74–84. https://doi.org/10.1016/j.margeo.2017.02.016

Mull, J., Ruggiero, P., 2014. Estimating Storm-Induced Dune Erosion and Overtopping along U.S. West Coast Beaches. J. Coast. Res. 298, 1173–1187. https://doi.org/10.2112/jcoastres-d-13-00178.1

Neumann, B., Vafeidis, A.T., Zimmermann, J., Nicholls, R.J., 2015. Future coastal population growth and exposure to sea-level rise and coastal flooding - A global assessment. PLoS One 10. https://doi.org/10.1371/journal.pone.0118571

NOAA National Centers for Environmental Information, 2022. ETOPO 2022 15 Arc-Second Global Relief Model. https://doi.org/https://doi.org/10.25921/fd45-gt74

O'Neill, A.C., Erikson, L.H., Barnard, P.L., Limber, P.W., Vitousek, S., Warrick, J.A., Foxgrover, A.C., Lovering, J., 2018. Projected 21st century coastal flooding in the Southern California Bight. Part 1: Development of the third generation CoSMoS model. J. Mar. Sci. Eng. 6. https://doi.org/10.3390/jmse6020059

Oppenheimer, M., Glavovic, B.C., Hinkel, J., van de Wal, R., Magnan, A.K., Abd-Elgawad, A., Cai, R., Cifuentes-Jara, M., DeConto, R.M., Ghosh, T., Hay, J., Isla, F., Marzeion, B., Meyssignac, B., Sebesvaei, Z., 2019. Sea Level Rise and Implications for Low-Lying Islands,Coasts and Communities, IPCC Special Report on the Ocean and Cryosphere in a Changing Climate. https://doi.org/10.1126/science.aam6284

Passeri, D.L., Dalyander, P.S., Long, J.W., Mickey, R.C., Jenkins, R.L., Thompson, D.M., Plant, N.G., Godsey, E.S., Gonzalez, V.M., 2020. The Roles of Storminess and Sea Level Rise in Decadal Barrier Island Evolution. Geophys. Res. Lett. 47, 1–8. https://doi.org/10.1029/2020GL089370

Plant, N.G., Stockdon, H.F., 2012. Probabilistic prediction of barrier-island response to hurricanes. J. Geophys. Res. Earth Surf. 117, 1–17. https://doi.org/10.1029/2011JF002326

Ponte Lira, C., Silva, A.N., Taborda, R., De Andrade, C.F., 2016. Coastline evolution of Portuguese low-lying sandy coast in the last 50 years: An integrated approach. Earth Syst. Sci. Data 8, 265–278. https://doi.org/10.5194/essd-8-265-2016

Rizzoli, P., Martone, M., Gonzalez, C., Wecklich, C., Borla Tridon, D., Bräutigam, B., Bachmann, M., Schulze, D., Fritz, T., Huber, M., Wessel, B., Krieger, G., Zink, M., Moreira, A., 2017. Generation and performance assessment of the global TanDEM-X digital elevation model. ISPRS J. Photogramm. Remote Sens. 132, 119–139. https://doi.org/10.1016/j.isprsjprs.2017.08.008

Roelvink, D., Costas, S., 2019. Coupling nearshore and aeolian processes: XBeach and duna process-based models. Environ. Model. Softw. 115, 98–112. https://doi.org/10.1016/j.envsoft.2019.02.010

Roelvink, D., McCall, R.T., Mehvar, S., Nederhoff, K., Dastgheib, A., 2018. Improving predictions of swash dynamics in XBeach: The role of groupiness and incident-band runup. Coast. Eng. 134, 103–123. https://doi.org/10.1016/j.coastaleng.2017.07.004

Roelvink, D., Reniers, A., van Dongeren, A.R., van Thiel de Vries, J., McCall, R.T., Lescinski, J., 2009. Modelling storm impacts on beaches, dunes and barrier islands. Coast. Eng. 56, 1133–1152. https://doi.org/10.1016/j.coastaleng.2009.08.006

Ruggiero, P., Kaminsky, G.M., Komar, P.D., McDougal, W.G., 1998. Extreme waves and coastal erosion in the Pacific Northwest. Proc. Int. Symp. Ocean Wave Meas. Anal. 2, 947–961.

Ruggiero, P., Kratzmann, M.G., Himmelstoss, E.A., Reid, D., Allan, J.C., Kaminsky, G., 2013. National assessment of shoreline change: Historical shoreline change along the Pacific Northwest coast, U. S. Geological Survey Open-File Report OF 2012-1007.

Sallenger, J., 2000. Storm impact scale for barrier islands. J. Coast. Res. 16, 890–895.

Schambach, L., Grilli, A.R., Grilli, S.T., Hashemi, M.R., King, J.W., 2018. Assessing the impact of extreme storms on barrier beaches along the Atlantic coastline: Application to the southern Rhode Island coast. Coast. Eng. 133, 26–42. https://doi.org/10.1016/j.coastaleng.2017.12.004

Sherwood, C.R., van Dongeren, A.R., Doyle, J., Hegermiller, C.A., Hsu, T.J., Kalra, T.S., Olabarrieta, M., Penko, A.M., Rafati, Y., Roelvink, D., Van Der Lugt, M., Veeramony, J.,

Warner, J.C., 2022. Modeling the Morphodynamics of Coastal Responses to Extreme Events: What Shape Are We In? Ann. Rev. Mar. Sci. 14, 457–492. https://doi.org/10.1146/annurev-marine-032221-090215

Simmons, J.A., Harley, M.D., Marshall, L.A., Turner, I.L., Splinter, K.D., Cox, R.J., 2017. Calibrating and assessing uncertainty in coastal numerical models. Coast. Eng. 125, 28–41. https://doi.org/10.1016/j.coastaleng.2017.04.005

Smith, A., Houser, C., Lehner, J., George, E., Lunardi, B., 2020. Crowd-sourced identification of the beach-dune interface. Geomorphology 367, 107321. https://doi.org/10.1016/j.geomorph.2020.107321

Soulsby, R.L., 1997. Dynamics of marine sands: a manual for practical applications. Oceanogr. Lit. Rev. 9, 947.

Splinter, K.D., Carley, J.T., Golshani, A., Tomlinson, R., 2014. A relationship to describe the cumulative impact of storm clusters on beach erosion. Coast. Eng. 83, 49–55. https://doi.org/10.1016/j.coastaleng.2013.10.001

Splinter, K.D., Palmsten, M.L., 2012. Modeling dune response to an East Coast Low. Mar. Geol. 329–331, 46–57. https://doi.org/10.1016/j.margeo.2012.09.005

Splinter, K.D., Strauss, D., Tomlinson, R.B., 2011. Can we reliably estimate dune erosion without knowing pre-storm bathymetry? 20th Australas. Coast. Ocean Eng. Conf. 2011 13th Australas. Port Harb. Conf. 2011, COASTS PORTS 2011 650–655.

Stutz, M.L., Pilkey, O.H., 2011. Open-ocean barrier islands: Global influence of climatic, oceanographic, and depositional settings. J. Coast. Res. 27, 207–222. https://doi.org/10.2112/09-1190.1

Turner, I.L., Leaman, C.K., Harley, M.D., Thran, M.C., David, D.R., Splinter, K.D., Matheen, N., Hansen, J.E., Cuttler, M.V.W., Greenslade, D.J.M., Zieger, S., Lowe, R.J., 2024. A framework for national-scale coastal storm hazards early warning. Coast. Eng. 192, 104571. https://doi.org/10.1016/j.coastaleng.2024.104571

van der Lugt, M.A., Quataert, E., van Dongeren, A.R., van Ormondt, M., Sherwood, C.R., 2019. Morphodynamic modeling of the response of two barrier islands to Atlantic hurricane forcing. Estuar. Coast. Shelf Sci. 229. https://doi.org/10.1016/j.ecss.2019.106404

van Dongeren, A.R., Ciavola, P., Martinez, G., Viavattene, C., Bogaard, T., Ferreira, Ó., Higgins, R., McCall, R.T., 2018. Introduction to RISC-KIT: Resilience-increasing strategies for coasts. Coast. Eng. 134, 2–9. https://doi.org/10.1016/j.coastaleng.2017.10.007

van Dongeren, A.R., Ormondt, M. Van, Nederhoff, K., Goede, R. De, Athanasiou, P., Quataer, E., Langeraert, F., Lilly, J., 2024. Forecasting Hurricane Impacts on U.S. Coasts. https://doi.org/10.13140/RG.2.2.28728.76808

Veloso-Gomes, F., Taveira-Pinto, F., das Neves, L., Pais Barbosa, J., Coelho, C., 2004. Erosion risk levels at the NW Portuguese coast: The Douro mouth - Cape Mondego stretch. J. Coast. Conserv. 10, 43–52. https://doi.org/10.1652/1400-0350(2004)010[0043:ERLATN]2.0.CO;2

Vitousek, S., Buscombe, D., Vos, K., Barnard, P.L., Ritchie, A.C., Warrick, J.A., 2023. The future of coastal monitoring through satellite remote sensing. Cambridge Prism. Coast. Futur. 1. https://doi.org/10.1017/cft.2022.4

Vousdoukas, M.I., Ferreira, Ó., Almeida, L.P.M., Pacheco, A., 2012. Toward reliable storm-

hazard forecasts: XBeach calibration and its potential application in an operational early-warning system. Ocean Dyn. 62, 1001–1015. https://doi.org/10.1007/s10236-012-0544-6

Vousdoukas, M.I., Ranasinghe, R., Mentaschi, L., Plomaritis, T.A., Athanasiou, P., Luijendijk, A., Feyen, L., 2020. Sandy coastlines under threat of erosion. Nat. Clim. Chang. 10, 260–263. https://doi.org/10.1038/s41558-020-0697-0

Wernette, P., Houser, C., Bishop, M.P., 2016. An automated approach for extracting Barrier Island morphology from digital elevation models. Geomorphology 262, 1–7. https://doi.org/10.1016/j.geomorph.2016.02.024

Wesselman, D., de Winter, R.C., Engelstad, A., McCall, R.T., van Dongeren, A.R., Hoekstra, P., Oost, A., van der Vegt, M., 2018. The effect of tides and storms on the sediment transport across a Dutch barrier island. Earth Surf. Process. Landforms 43, 579–592. https://doi.org/10.1002/esp.4235

Wilmink, R., McCall, R.T., Van Santen, R., van Kuik, N., Pluis, S., de Bakker, A., Steetzel, H., 2022. XBEACH IMPLEMENTATION IN THE NEW NATIONAL COASTAL FLOOD RISK ASSESSMENT FRAMEWORK FOR THE DUTCH COAST, in: Coastal Engineering Proceedings (37). p. 46.

Zhang, K., Leatherman, S., 2011. Barrier Island population along the U.S. Atlantic and Gulf Coasts. J. Coast. Res. 27, 356–363. https://doi.org/10.2112/JCOASTRES-D-10-00126.1

Zinnert, J.C., Stallins, J.A., Brantley, S.T., Young, D.R., 2017. Crossing scales: The complexity of barrier-island processes for predicting future change. Bioscience 67, 39–52. https://doi.org/10.1093/biosci/biw154

Chapter 5 General conclusions

Aiming to assess the response of wave-dominated barrier islands to extreme storm events on a global scale, both in terms of erosion and flooding, this study evaluated and exploited available global datasets and process-based modelling techniques. Barrier islands are highly vulnerable to extreme events such as storm driven waves and surges due to their low elevation, high dynamics and rapid evolution, and increasing population. Coastal hazards, such as erosion, flooding and inundation, have caused environmental and social impacts worldwide. With climate change, extreme storm events may become more frequent and/or intense in many coastal areas, and there is an urgent need to prevent risks on barrier islands while preserving these fundamental coastal environments. As a solution, early warning systems are being implemented to enable preventive action and rapid response. Such systems are developed using morphological models in combination with regional to local wave datasets alongside accurate topographic information about the coastal area of interest.

The increasing development and improvement of global datasets that can describe both the storm forcing conditions and the morphological features of coastal areas, have allowed the exploration of several new options for coastal hazard assessments in combination with process-based modelling. However, despite the novel possibilities, global datasets still possess significant uncertainties, which arise from limitations in resolution, representation of physical processes, and the challenges in accurately capturing the complex variability in coastal hydrodynamics and topography. The methodologies developed in this research aim to bridge the gap between such coarse global datasets and the site-specific requirements of coastal hazard assessments. By leveraging innovative approaches to integrate global datasets and process-based modelling, this work provides a pathway to apply advanced techniques in data-scarce or remote regions. This contribution is vital in a global context where coastal erosion and flooding are intensifying, underscoring the need for easily accessible solutions at a large scale.

To address these challenges, this work firstly characterized the storm forcing and quantified errors in hydrodynamic parameters from global wave reanalysis datasets. Different methods to identify storm events have been developed, with the most recent ones relying on statistical approaches that are able to robustly distinguish between independent storms. Nevertheless, all methods rely on thresholds based on the significant wave height. The most recent and widely

used global wave reanalyses, ERA5 and WAVERYS, were therefore validated at a global scale against in-situ coastal buoys to define the accuracy of their prediction of key wave parameters, specifically during extreme events. Consistent underestimation in wave height and period was identified in this study, which proposed a straightforward calibration method to improve the accuracy of wave predictions in coastal areas. This calibration framework minimizes key limitations in current global wave datasets, enhancing their utility for coastal applications.

Following, an intercomparison of openly available topographic and bathymetric global datasets was performed, aiming to identify their differences and applicability on barrier islands. The main issue with the use of both types of datasets is the absence of information between land and the shallow nearshore zone, which makes their use in coastal areas challenging. A novel methodology was proposed to merge topographic and bathymetry data, and by integrating them to obtain a continuum cross-shore profile of barrier islands. By comparing the performance of different global datasets, the study identified those with lower errors and demonstrated the benefits of combining datasets using an equilibrium profile, rather than relying on single-point-derived nearshore slopes or other simplified approaches. This method also anticipates the rapid expansion in satellite-derived coastal data, offering a scalable solution for global applications.

Recognizing and addressing these uncertainties, as well as selecting the best performing global datasets currently available, was a critical first step in improving the reliability of the subsequent global coastal storm hazard assessment. A process-based model was applied to simulate the impact of a 50-year return period storm for wave height, on barrier island profiles derived from global topo-bathymetries using the aforementioned methodology, and forcing determined from a global wave reanalysis and a tide and surge model. In addition to uncertainties in the input data, the modelling approach itself also introduces errors, particularly when detailed, site-specific calibration is not available or feasible. The high variability of global barrier island environments and the lack of high-resolution information prevented calibration and validation of the XBeach process-based model at such a large scale, and default parameters were therefore used. However, even considering the uncertainty in the results, this study represents a pioneering effort to apply advanced process-based modelling on a global scale and demonstrates that coarse-resolution global datasets can capture physically realistic barrier island storm behaviour when coupled with process-based models. Vulnerable coastal areas were identified, alongside a threshold that can be used to predict the occurrence of overwash events based solely on hydrodynamic forcing and barrier island volume derived from the global

datasets. In addition, almost 70% of the variability in the storm erosional response, quantified using process-based indicators such as the eroded dune volume, could be explained by the nearshore hydrodynamic forcing alone.

Future research should focus on quantifying and minimizing modelling uncertainties (from global datasets to process-based model calibration), as a key step toward producing more realistic and actionable predictions of coastal storm hazards. Nevertheless, while acknowledging limitations and the need for calibration, this study has shown that, with further testing and uncertainty reduction, such methodologies could enable global-scale coastal hazard assessments that remain grounded in physical realism. Future efforts should focus on standardizing calibration approaches to improve model accuracy across diverse coastal environments. This, combined with ongoing efforts to reduce computational costs by leveraging statistical techniques, might provide a viable tool for first-level assessments in areas where local warning efforts are currently inexistent. Furthermore, while the morphological and hydrodynamic impacts of extreme storms were defined for natural sectors of globally distributed barrier islands, the hazard on urbanized and engineered barriers was not investigated. The main reason for this was the coarse resolution of the available global digital elevation models that, while representing the actual surface of the terrain (including infrastructures and vegetation), do not allow differentiation of specific built-up features at such coarse resolution. Future advances in openly available digital elevation models may help to overcome this limitation and extend the hazard assessment to urbanized or engineered barriers.